REPORT DOCUMENTATION PAGE

Form Approved OMB No. 0704-0188

Public reporting burden for this collection of information is estimated to average 1 hour per response, including the time for reviewing instructions, searching existing data sources, gathering and maintaining the data needed, and completing and reviewing the collection of information. Send comments regarding this burden estimate or any other aspect of this collection of information, including suggestions for reducing the burden, to Department of Defense, Washington Headquarters Services, Directorate for Information Operations and Reports (0704-0188), 1215 Jefferson Davis Highway, Suite 1204, Arlington, VA 22202-4302. Respondents should be aware that notwithstanding any other provision of law, no person shall be subject to any penalty for failing to comply with a collection of information if it does not display a currently valid OMB control number. **PLEASE DO NOT RETURN YOUR FORM TO THE ABOVE ADDRESS.**

1. REPORT DATE *(DD-MM-YYYY)* 16-09-2009	2. REPORT TYPE Final Report	3. DATES COVERED *(From – To)* 27 December 2004 - 07-Jan-10

4. TITLE AND SUBTITLE	5a. CONTRACT NUMBER
Roles of Tunneling, Multiphoton Ionization, and Cascade Ionization for Femtosecond Optical Breakdown in Aqueous Media	FA8655-05-1-3010
	5b. GRANT NUMBER
	5c. PROGRAM ELEMENT NUMBER

6. AUTHOR(S)	5d. PROJECT NUMBER
Dr. Alfred Vogel	
	5d. TASK NUMBER
	5e. WORK UNIT NUMBER

7. PERFORMING ORGANIZATION NAME(S) AND ADDRESS(ES) Medical Laser Center Luebeck Peter Monnik Weg #4 Luebeck D-23562 Germany	8. PERFORMING ORGANIZATION REPORT NUMBER N/A

9. SPONSORING/MONITORING AGENCY NAME(S) AND ADDRESS(ES) EOARD Unit 4515 BOX 14 APO AE 09421	10. SPONSOR/MONITOR'S ACRONYM(S)
	11. SPONSOR/MONITOR'S REPORT NUMBER(S) Grant 05-3010

12. DISTRIBUTION/AVAILABILITY STATEMENT Approved for public release; distribution is unlimited.

13. SUPPLEMENTARY NOTES

14. ABSTRACT

The interplay of the various ionization mechanisms reveals itself through the dependence of breakdown events on laser parameters such as pulse duration, wavelength, and pulse energy. In the past, the dependence of the breakdown threshold on pulse duration has attracted most attention because of the lowering of the energy threshold with decreasing pulse duration that enables precise material processing. In the present study, these aspects are included because we use pulse durations ranging from $\approx$ 300 fs to $\approx$ 10 ns. However, we go far beyond by presenting a detailed analysis of the wavelength dependence of the breakdown thresholds for nanosecond and femtosecond breakdown, and of the dependence of energy deposition on laser pulse energy. These studies are performed with unprecedented wavelength and energy resolution. They reveal previously unknown features of the optical breakdown process, and enable to assess the possibilities of controlled nonlinear energy deposition in the entire wavelength-pulse duration parameter space.

15. SUBJECT TERMS
EOARD, Femtosecond pulses, Biodynamics, Laser Protection, Laser Safety, laser-induced damage

16. SECURITY CLASSIFICATION OF:			17. LIMITATION OF ABSTRACT	18, NUMBER OF PAGES	19a. NAME OF RESPONSIBLE PERSON TAMMY SAVOIE, Lt Col, USAF
a. REPORT UNCLAS	b. ABSTRACT UNCLAS	c. THIS PAGE UNCLAS	UL	208	19b. TELEPHONE NUMBER *(Include area code)* +44 (0)1895 616459

Standard Form 298 (Rev. 8/98)
Prescribed by ANSI Std. Z39-18

Roles of tunneling, multiphoton ionization, and cascade ionization for optical breakdown in aqueous media

AFOSR International Research Initiative Project SPC 053010 / EOARD

Grant FA 8655-05-1-3010

Final Report

September 2009

Norbert Linz, Sebastian Freidank, Xiaoxuan Liang, Joachim Noack, Günther Paltauf, and Alfred Vogel

Primary Investigator:

Prof. Alfred Vogel, Ph.D.

Medical Laser Center Luebeck,

Institute of Biomedical Optics, University of Luebeck

Peter-Monnik-Weg 4, D-23562 Luebeck, Germany

Phone: + 49-451-500-6504, FAX: + 49-451-500-6546

e-mail: vogel@mll.mu-luebeck.de

AFOSR Collaboration Partner:

Benjamin A. Rockwell, Ph.D.

Air Force Research Laboratory

711 HPW/RHDO

2624 Louis Bauer Drive

Brooks City Base, TX 78235-5128, U.S.A.

Phone: (210) 536-4790 FAX:(210) 536-3903

e-mail: benjamin.rockwell@us.af.mil

CONTENTS

Summary

Our report establishes a basis for controlled nonlinear energy deposition for surgery and material processing in transparent dielectrics, exemplified on optical breakdown in aqueous media.

Background and motivation

While linear absorption of laser-light has always been seen as a means of controlled energy deposition, nonlinear absorption via optical breakdown was initially regarded as annoying and rather useless because its occurrence was often related to optical damage (see "Boulder Damage Symposium"). Later optical breakdown was employed for intraocular surgery ("photodisruption"), and, especially after the advent of reliable femtosecond laser technology, for precise material processing. However, the theoretical treatment of optical breakdown phenomena still lags behind. Most modeling approaches still focus on the determination of a "breakdown threshold" in terms of a critical free-electron density and do not attempt to model the target energy density (and distribution) as a function of incident laser energy. This is largely due to the complexity of nonlinear energy deposition. In the next paragraphs, we will shortly describe the many factors involved in nonlinear energy deposition to set the stage for the approach taken in the present report/thesis.

In linear energy deposition via one-photon absorption, the energy density reached at the end of the laser irradiation is determined by the linear absorption coefficient and scattering coefficient, and the light energy is deposited via excitation of electronic, vibrational and rotational states of the target molecules.

If the absorption and/or scattering coefficient change because of the temperature rise during the laser pulse, one-photon absorption already assumes a nonlinear character.

The next step in complexity is reached when energy is deposited through multiphoton excitation of electronic states, possibly besides one photon absorption in other molecules. Here, large irradiances and strong nonlinearrities are involved.

Finally, *free electrons* are generated by multiphoton ionization (MPI) and tunnel ionization, gain energy by inverse bremsstrahlung absorption and create additional free electrons by impact ionization, resulting in an ionization avalanche (AI). The energy of the free electrons is then thermalized by collisions and recombination.

As in linear absorption, the cross sections for the individual absorption processes change with temperature (mediated by changes in collision frequency of the free electrons), and at large T, thermal ionization (TI) comes into play as an additional ionization mechanism.

Energy losses in linear one photon absorption usually occur through heat diffusion or, after the onset of phase changes, through ablation. In nonlinear absorption, electron diffusion out of the irradiated volume comes into play as an additional loss mechanisms, and, for large energy densities, radiative losses start to play a role.

For laser beams traversing a target material, energy deposition will, furthermore, be influenced by nonlinear propagation effects such as self-focusing, self-phase modulation, plasma defocusing, and (for ns pulses) SBS. In this study, we focus on energy deposition at large numerical apertures (*NA*), because in this case nonlinear beam propagation can be neglected [Sch01], which facilitates the investigations of nonlinear energy deposition.

A key element of nonlinear energy deposition is the interaction between tunnel, multiphoton, and cascade ionization. Therefore, special emphasis will be placed on this aspect but the other above mentioned factors relevant for nonlinear energy deposition will also be considered.

The interplay between the different ionization mechanisms is still a subject of strong debate. While some researchers state that femtosecond breakdown is mainly driven by multiphoton ionization, with relatively weak support by avalanche ionization [Kai00, Ret04], others claim that the contribution of multiphoton ionization is minor, photoionization consists mainly of tunnel ionization, and the main role is played by avalanche ionization down to pulse durations well below 100 fs [Du96, Jog04]. For nanosecond breakdown, the most controversial question is whether ‚lucky' background electrons [Bas72, Blo74], impurities and defects, or multiphoton ionization across the entire bandgap [Ken95, Noa99, Vog05] initiate the ionization avalanche.

Another open question regarding the dynamics of nanosecond breakdown is the interplay between avalanche ionization, thermalization of the free electron energy by recombination, and thermal ionization. A common view is that the avalanche, once initiated, immediately progresses to full ionization [Bloe74, Stu96, Jog04]. However, it is conceivable that at short wavelengths for which the avalanche progresses slower than at longer wavelengths, it may be limited by recombination to a level below full ionization until thermal ionization overcomes recombination and full-density plasmas are produced. This stepwise increase of the degree of ionization would imply a potential for controlled, tunable nonlinear energy deposition.

Objectives

The interplay of the various ionization mechanisms reveals itself through the dependence of breakdown events on laser parameters such as pulse duration, wavelength, and pulse energy. In the past, the dependence of the breakdown threshold on pulse duration has attracted most attention because of the lowering of the energy threshold with decreasing pulse duration that enables precise material processing. In the present study, these aspects are included because we use pulse durations ranging from ≈ 300 fs to ≈ 10 ns. However, we go far beyond by presenting a detailed analysis of the wavelength dependence of the breakdown thresholds for nanosecond and femtosecond breakdown, and of the dependence of energy deposition on laser pulse energy. These studies are performed with unprecedented wavelength and energy resolution. They reveal previously unknown features of the optical breakdown process, and enable to assess the possibilities of controlled nonlinear energy deposition in the entire wavelength-pulse duration (λ-τ_L) parameter space.

Experiments

In order to achieve reproducible laser effects and precise threshold values, we use laser pulses with smooth temporal shape and good transverse beam profile that are focused by UV-VI-IR corrected water-immersion microscope objectives. Breakdown parameters determined for single-longitudinal mode (slm) nanosecond laser pulses with smooth shape are compared to the effects produced by pulses from regular laser sources exhibiting picosecond spikes due to longitudinal mode beating. All relevant laser parameters such as pulse duration, shape or spectrum, and energy are measured for each individual laser pulse, and the laser beam quality parameter M^2 is measured where appropriate.

Femtosecond- picosecond and nanosecond lasers emitting at fixed UV, visible, and IR wavelengths are used to examine $R_{max}(E_L)$, $I_{th}(NA)$, and threshold sharpness at a grid of parameters in the (λ-τ_L) space. A femtosecond OPO and a slm nanosecond OPO are used to investigate $I_{th}(\lambda)$ for pulse durations of ≈ 265 fs in the range between 330 nm and 1100 nm at 50 individual wavelengths, and ≈ 2 ns in the range between 725 nm and 1030nm at 21 wavelengths.

Acquisition of the large amount of data required to investigate the parameter dependencies listed above was made possible by a recently developed probe beam scattering technique for precise (10 nm accuracy) and rapid determination of the bubble size [Vog08]. The setup also enables photography of the plasma luminescence and cavitation bubbles with 1 µm spatial resolution. Together with transmission measurements, this capability is used to investigate the plasma energy density.

Modeling

Vogel et al. recently presented a rate equation model of optical breakdown in transparent dielectrics that considers photoionization based on the Keldysh theory [Kel65], avalanche ionization, recombination, and diffusion losses [Vog05]. This model is now extended to consider heating through linear absorption, heating via collision losses and recombination of the free electrons produced by nonlinear absorption, and its counteraction by heat diffusion out of the focal volume. Sufficiently high temperatures result in thermal ionization accelerating the ionization avalanche.

Historically, breakdown models usually aimed at calculating the irradiance necessary to produce a certain critical free-electron density that was identified with the breakdown threshold. However, this approach is not suitable for comparison with experiments that detect a phase transition such as bubble formation, or plasma luminescence, Moreover, it cannot guide the selection of laser parameters for material processing that relies on the knowledge of the volumetric energy density ε and temperature T produced by the laser pulse. Therefore, we link the theoretical analysis to energy density and temperature, and use critical temperature values to define the thresholds for bubble formation and plasma luminescence.

Wavelength dependence of breakdown thresholds

The wavelength dependence $I_{th}(\lambda)$ of nanosecond breakdown enables to distinguish between extrinsic initiation of breakdown by impurities and intrinsic breakdown. Initiation of the breakdown process by multiphoton ionization should result in a stepwise increase of the threshold irradiance, I_{th}, at wavelengths above which one more photon is required to overcome the band gap [Blo74]. Such behavior is indeed observed in our experiments, and the wavelength separation of the steps is in good agreement with literature data on the band gap of liquid water. Similar steps observed in the wavelength dependence of femtosecond breakdown would indicate a significant role of multiphoton ionization compared to tunneling. However, the scatter of the experimental data is too large to verify the small oscillations of $I_{th}(\lambda)$ predicted by model calculations.

Further information on the importance of impurities for breakdown initiation compared to intrinsic factors is obtained by examining the dependence of threshold values and sharpness on numerical aperture, $I_{th}(NA)$ for IR

nanosecond breakdown. As expected, impurities (either ions or solvated electrons) play an increasing role with decreasing NA, i.e. larger focal volume. However, these impurities just lead to local avalanche resulting in minute bubbles, while the creation of luminescent plasmas remains linked to the generation of a minimum start electron density by photoionization.

Both for nanosecond and femtosecond breakdown, the slope of the $I_{th}(\lambda)$ curves provides information about the relative importance of photoionization (threshold increases with increasing wavelength) and cascade ionization (threshold decreases with increasing wavelength). Model calculations of the $I_{th}(\lambda)$ curves are fitted to the experimentally determined $I_{th}(\lambda)$ data, using the collision time between free electrons and heavy particles, and the seed electron density provided by photoionization as fitting parameters.

Dependence of nonlinear energy deposition on laser pulse energy

Nanosecond breakdown at IR wavelengths is characterized by an abrupt threshold above which highly disruptive luminescent plasmas are produced [Vog96b]. By contrast, femtosecond breakdown first leads to low-density plasmas, at higher pulse energies to bubble formation, and finally to luminescent plasmas with large energy density [Vog05, this study]. This implies a tunability of laser effects from chemical modifications to disruptive effects that is highly desired for laser surgery and materials processing [Vog05]. The different scenarios are indicative for a different interplay of the various ionization mechanisms.

In the present study, we examine the tunability of laser effects at various points in the $(\lambda\text{-}\tau_L)$ parameter space. For this pupose, we take the size R_{max} of the laser-produced cavitation bubbles in water as a measure for the total amount of deposited energy, and use it to assess the conversion of laser energy E_L into mechanical energy. The $R_{max}(E_L)$ curves then portray the tunability.

Our results reveal that tunability is not restricted to femtosecond breakdown but exists also in nanosecond breakdown at UV and visible wavelengths. It is reflected in two separate breakdown thresholds, a lower threshold for the formation of minute cavitation bubbles and, at $3 - 30$ times larger energy, another threshold for the creation of brightly luminescent plasmas and large bubbles. This important finding is explained and confirmed by model calculations considering the interplay of all ionization mechanisms and recombination. The calculations yield good agreement between the predictted dependence of the volumetric energy density on laser pulse energy, $\varepsilon(E_L)$, with the measured dependence between cavitation bubble energy and pulse energy, $E_B(E_L)$.

Experimental results and model predictions together show that controlled, tunable nonlinear energy deposition can be achieved in a large part of the $(\lambda\text{-}\tau_L)$ space if laser pulses with smooth temporal shape and good beam profile are used to produce breakdown. We employ the model to create a map of the (λ,τ) parameter space in which the dependence of target temperature on laser energy is calculated for each (λ,τ) value. This ‚tunability' map for the magnitude of laser effects is very useful in guiding the choice of laser parameters for a large variety of applications.

Dependence of plasma energy density on laser parameters

The cavitation bubble energy reflects the total amount of deposited energy but additional information is required to determine the corresponding plasma energy density and assess its temperature and pressure. We take photographs of the plasma luminescence to determine the plasma volume, and measure the plasma transmission to assess the energy absorbed in this volume. These data, together with structural details on the photographs, provide valuable information on the plasma size dependence on incident laser energy, the average plasma energy density, and hot regions within the plasma.

For femtosecond breakdown, the energy deposition is stress confined, i.e. it occurs so rapidly that the focal volume cannot expand during the thermalization of the laser energy. Therefore, the laser-induced temperature rise leads to a large pressure rise that upon relaxation produces tensile stress in the center of the focal volume [Vog05]. The tensile stress facilitates bubble formation, and, therefore, the energy density at the bubble formation threshold is only 0.62 kJ/cm^3, about half of the value required for bubble formation in nanosecond breakdown that occurs at the spinodal limit (≈ 573 K) [Vog03].

In the regime where luminescent plasmas are produced, the energy density in bulk media is also larger for ns breakdown than for fs breakdown. The reason is that in fs breakdown only one set of free electrons is produced during the laser pulse, the energy of which is thermalized after the pulse [Noack&Vogel99]. By contrast, the duration of nanosecond pulses is 2 -3 orders of magnitude longer than the thermalization time, which implies a continuous energy flow from free electrons to heavy particles resulting in constant heating of the focal volume during the pulse and in very large energy densities. While the energy density observed in fs breakdown well above the BPL threshold is ≈ 10 kJ/cm^3, it is at least 270 kJ/cm^3 in the center of ns plasmas, and probably even higher in upstream-directed, fingered, filamentous structures along which the plasma grows.

Because the energy deposition in fs breakdown is stress-confined (isochoric), both energy density and mass density are known. This is used to determine temperature and pressure in the BPL regime using an EOS for high-energy density water [Mat06, Mat07]. We obtain $T_{average} \approx 2800$ K, $T_{peak} \approx 6000$ K, and $p_{average} \approx 4800$ MPa. The peak temperatures in ns plasmas are estimated to exceed 10^5 K.

For fs and 30- ps pulses, the dependence of plasma length on laser pulse energy agrees reasonably well with the "moving breakdown model" that correlates plasma growth with the extent of the region in which the incident laser irradiance exceeds the breakdown threshold I_{th} [Vog96b]. However, for ns breakdown, the plasmas are much larger than predicted by the moving breakdown model. The temperature above the BPL threshold would, according to the predictions of our plasma formation model that neglects plasma growth and shielding, exceed a value of 10^7 K, which is not realistic.

Such large energy density values are not reached because the deposited energy is dissipated via radiative energy transport beyond the laser cone angle and the laser focus once the volumetric energy density is sufficiently high to overcome immediate re-absorption. Radiative energy transport causes a diffusely luminescent halo that extends more than 20 µm beyond the well-defined region of original energy deposition. Since UV plasma emission in the wavelength range from 40 nm to 100 nm is reabsorbed within a distance of 10-100 nm, and only x-ray radiation in the water window of 2.5 nm < λ < 5 nm has a penetration depth corresponding to our experimental observations, we conclude that the peak energy densities in ns plasmas produced in bulk water at large numerical apertures is sufficiently high to produce soft X-rays.

How laser plasma coupling can lead to such large plasma energy densities still needs to be understood because free electron densities well above the critical density at which plasma becomes both highly reflective and absorbing are involved. We present evidence for efficient coupling into the small-scale filamentous high-density structures that, similar to the case of inertial laser fusion, may be explainable though the action of evanescent waves [God72, God79, God95].

We conclude that both femtosecond and nanosecond optical breakdown in bulk dielectrics span an enormous range of energy densities from <0.6 kJ/cm^3 below the bubble formation threshold to peak densities up to 10-40 kJ/cm^3 for fs breakdown (depending on wavelength) and up to above 270 kJ/cm^3 (more than 100x the vaporization enthalpy of water) for ns breakdown. In the range below the threshold for bright plasma luminescence at ≈ 6000 K, the energy density is readily tunable by variation of the incident laser energy. Above this value, the avalanche supported by thermal ionization progresses to full ionization, and radiative energy transfer sets in. In this regime, an increase of the incident laser energy is mainly reflected in a growth of the plasma volume rather than in a further increase of the energy density.

Implications for laser nanosurgery and materials processing

The incorporation of all ionization mechanisms including thermal ionization into the theoretical treatment of breakdown together with the consideration of losses by recombination, free electron diffusion and heat diffusion has enabled us to model the gradual increase of energy deposition with increasing laser pulse energy. The introduction of temperature-related breakdown criteria directly links plasma modeling to changes in the target relevant for laser surgery and material processing, such as bubble formation or plasma luminescence. Based on these criteria, we created a ‚tunability' map of the (λ-τ_L) parameter space presenting the dependence of the laser-produced temperature on the incident laser energy. This map can guide the choice of laser parameters appropriate for different types of applications employing nonlinear energy deposition.

The sensitive probe beam scattering technique developed for the detection of the bubble formation threshold at large numerical aperture led us to the discovery that nano-effects can be produced in a very cost-effective manner using UV- and VIS nanosecond laser pulses delivered from microchip lasers. This discovery can be used for nano-surgery of cells and tissues as well as for the modification of glass and other dielectric solids in applications such as nano-morphing and wave guide writing.

We created an algorithm for automatic evaluation of the probe beam scattering signals that presently runs at repetition rates up to 30 Hz but can be further accelerated to ≈ 1 kHz. This algorithm allows for an online dosimetry of cell and tissue surgery that complements the controlled nonlinear energy deposition.

1. Introduction

The content of this report that establishes a basis for controlled nonlinear energy deposition for surgery and material processing in transparent dielectrics, extends far beyond the initial scope of the research project "Roles of tunneling, multiphoton ionization, and cascade ionization for optical breakdown in aqueous media."

The relative importance of multiphoton and tunnel ionization compared to the role of avalanche ionization is still a matter of controversy in the research community exploring optical breakdown in condensed matter. While some theoreticians doubt that avalanche ionization plays a large role in breakdown induced by femtosecond laser pulses because of the time constraints governing the gain of kinetic energy required for impact ionization [Kai00, Ret04], the others neglect these constraints [Tien99, Jog04], claim that multiphoton ionization is strongly quenched by collisions [Du96] and conclude that avalanche ionization dominates both femtosecond and nanosecond breakdown [Jog03, Jog04]. We intended to tackle this question by investigating the wavelength dependence $I_{th}(\lambda)$ of nanosecond and femtosecond optical breakdown, using bubble formation as breakdown criterion.

These investigations required the development of a technique for bubble detection that was sufficiently sensitive to detect minute bubbles with a size below the optical diffraction limit [Vog05] and sufficiently fast to perform a large number of measurements in reasonable time. The technique was recently published in PRL [Vog08]. It was complemented by the possibility to take photographs of the laser-induced plasmas in side view with 1 μm resolution and a novel Schlieren technique that enables to visualize refractive index changes in the focal volume with high sensitivity and large dynamic range [Vog06]. This possibility offered the option to investigate the initiation mechanism of breakdown, and the plasma shape and structure.

When we applied the novel, sensitive technique to nanosecond breakdown at UV and VIS wavelengths, we made an unexpected discovery. We found that nanosecond breakdown at short wavelengths produced by laser pulses with smooth temporal shape is characterized by a gradual increase of energy deposition, in a fashion similar to femtosecond breakdown and very different from IR nanosecond breakdown where the energy density at threshold immediately rises to very large values. The gradual increase of plasma energy density with irradiance corresponds to two separate and distinct thresholds for bubble formation and bright plasma luminescence. This discovery opens new avenues for precise and cost-effective laser surgery and materials processing.

Based on the advanced theoretical model presented in section 2 of this report that includes the temperature evolution in the focal volume and thermal ionization, we can explain the two-step behavior by looking at the interplay of the underlying ionization mechanisms and recombination. The model calculations helped us realize that controlled nonlinear deposition of energy into transparent dielectrics is possible not only when using femtosecond pulses but can be achieved in a large part of the (wavelength/pulse duration) parameter space. Motivated by this insight, we extended the scope of the study from a determination of breakdown thresholds $I_{th}(\lambda)$ to include the energy dependence of the vigor of the laser effects, i.e. the tunability of nonlinear energy deposition.

Experimentally, we studied the dependence of the size of the laser-induced bubbles on pulse energy at various wavelength/pulse duration combinations, and measured plasma volume and transmission to determine the plasma energy density. In our modeling efforts, we introduced a critical temperature rise T_{cr} produced by nonlinear energy deposition as criterion to describe the threshold for bubble formation and bright plasma luminescence (BPL). The temperature criterion replaces the old criterion of a critical free electron density ρ_{cr} that is not linked to any observable experimental event and, even worse, implies a dependence of the temperature corresponding to ρ_{cr} on pulse duration and laser wavelength. The advanced model now enables us to calculate the dependence of focus temperature on laser pulse energy, $T(E_L)$, for each location in the (τ_L, λ) parameter space. We used this capability to create a „tunability map' in which we plot the normalized irradiance difference between BPL and bubble threshold as a function of (τ_L, λ). This „tunability' map can guide the choice of laser parameters for precise and cost-effective laser surgery and materials processing.

What started as enterprise to elucidate the interplay between different ionization mechanisms in aqueous media has thus brought about results that change paradigms in the theoretical analysis of nonlinear energy deposition and materials modification.

2. Theoretical description and modeling of optical breakdown

2.1 Plasma formation

In order to provide a coherent picture of our modeling efforts of fs and ns optical breakdown in aqueous media, we first summarize the classical modeling of photoionization and avalanche ionization including the full Keldysh theory, following reference [Vog05]. In section 2.1.4 we then present the modeling of thermal ionization that is coupled with Kennedy`s multiphoton approximation of the Keldysh theory.

2.1.1. Qualitative picture

The process of plasma formation through laser-induced breakdown in water is schematically depicted in **Fig. 2.1**. The generation of quasi free electrons is based on an interplay of photo-ionization and avalanche ionization. To describe the breakdown process in water, Sacchi [Sac91] has proposed that water should be treated as an amorphous semiconductor and the excitation energy (regarded as the energy required for a transition from the molecular $1b_1$ orbital into the excitation band) is 6.5 eV [Gra79, Nik83, Wil76]. We follow this approach and identify the excitation energy of 6.5 eV with the band gap energy. For simplicity, we will use the terms "free electrons" and "ionization" as abbreviations for "quasi-free electrons" and "excitation into the conduction band".

The electrons in the valence band can overcome the band gap either by photoionization (multiphoton ionization or tunneling [Amm86, Kel65]), or by impact ionization [Arn92, Rea71, Rid99, Tho81,]. In previous breakdown models, it was often assumed that a free electron could be produced as soon as the band gap energy Δ was exceeded either by the sum of the simultaneously absorbed photons, or by the kinetic energy of an impacting free electron [Fen97, Ken95, Noa99, Tie99]. However, for very short laser pulses for which the optical breakdown starts only at large irradiance values, the band gap energy has to be replaced by the effective ionization potential to account for the oscillation energy of the electron due to the electric laser field. The ionization potential is [Kel65]

$$\widetilde{\Delta} = \Delta + \frac{e^2\ E^2}{4\ m\ \omega^2}\ , \qquad (2.1)$$

where ω denotes the circular frequency, E is the amplitude of the electric laser field, e is the electron charge, and $1/m = 1/m_c + 1/m_v$ is the exciton reduced mass that is given by the effective masses m_c of the quasi-free electron in the conduction band and m_v of the hole in the valence band. The second term in equation (2.1) can be neglected in nanosecond optical breakdown but must be considered in femtosecond optical breakdown where E is orders of magnitude larger. For multiphoton ionization, the number of photons required to ionize is then

$$K = \left\langle \Delta + \frac{e^2\ E^2}{4\ m\ \omega^2} \right\rangle \qquad (2.2)$$

where the symbol <x> is the integer part of the number x.
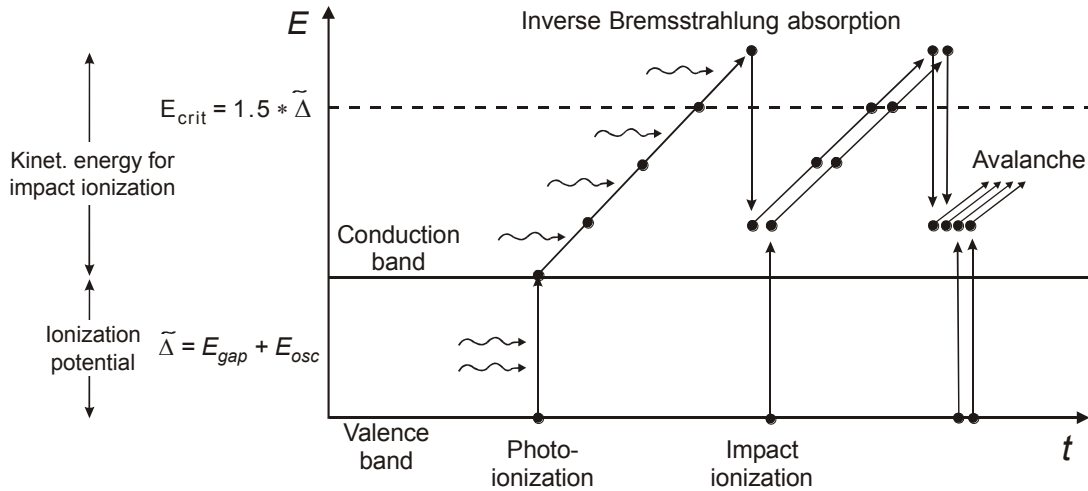
Figure 2.1 Interplay of photoionization, inverse Bremsstrahlung absorption and impact ionization in the process of plasma formation during optical breakdown in water. Recurring sequences of inverse Bremsstrahlung absorption events and impact ionization lead to an avalanche growth in the number of free electrons. The requirements to satisfy the conservation laws for energy and momentum in impact ionization, and their consequences for plasma formation are discussed in the text.

Photoionization

Multiphoton ionization (MPI) and tunneling are the mechanisms governing photoionization for different field strengths E and frequencies ω of the electromagnetic field. Keldysh introduced a parameter γ in his classical paper [Kel65] to distinguish between tunneling and MPI regime:

$$\gamma = \frac{\omega}{\omega_t} = \omega \frac{\sqrt{m\Delta}}{eE} . \qquad (2.3)$$

Here $1/\omega_t$ stands for the tunneling time through the atomic potential barrier which is inversely proportional to the strength of the electromagnetic field. For values $\gamma \ll 1$ as obtained with low frequencies and large field strengths tunneling is responsible for ionization, while for values $\gamma \gg 1$ typical for optical frequencies and moderate field strengths the probability of MPI is much higher than that of tunneling. With the parameter γ, the effective ionization potential in equation (2.1) can be written as

$$\widetilde{\Delta} = \Delta \left(1 + \frac{1}{4\gamma^2} \right) \qquad (2.4)$$

Femtosecond optical breakdown requires very high field strengths for which the tunneling time through the atomic potential barrier is extremely short, leading to values $\gamma < 1$ of the Keldysh parameter even for optical frequencies. Approximations of the Keldysh theory considering only multiphoton ionization that were used in previous breakdown models [Fen97, Ken95, Noa99] are thus inappropriate for the modeling of femtosecond breakdown, especially for pulse durations below 100 fs.

Impact ionization

Once a free electron is produced by photoionization in the focal volume of the medium, it can absorb photons in a non-resonant process called "inverse Bremsstrahlung" in the course of collisions with heavy charged particles (ions or atomic nuclei) [Rea71]. A third particle (ion/atom) is necessary for conservation of energy and momentum during the absorption process, as they cannot be both conserved if only an electron and a photon interact. The free electron in the conduction band gains kinetic energy during the absorption of the photon. After a sequence of several inverse Bremsstrahlung absorption events, the kinetic energy is sufficiently large to produce another free electron through impact ionization [Arn92, Kai00, Rid99, Tho91]. Two free electrons with low kinetic energies are now available which can gain energy through inverse Bremsstrahlung absorption. This process is shown in figure 2.1. The recurring sequence of inverse Bremsstrahlung absorption events and impact ionization leads to an avalanche growth in the number of free electrons if the irradiance is high enough to overcome the losses of free electrons through diffusion out of the focal volume and through recombination. The energy gain through inverse Bremsstrahlung must, moreover, be more rapid than the energy loss by collisions with heavy particles occurring without simultaneous absorption of a photon (the fraction of energy lost is proportional to the ratio of the electron and ion masses). The whole process is called "avalanche ionization", or "cascade ionization".

The basic requirement for impact ionization is that the kinetic energy of the impacting electron is larger than the effective ionization potential $\widetilde{\Delta}$ to satisfy the conservation laws for energy and momentum [Kel60, Rid99]. According to Ridley [Rid99], the critical energy for bands with parabolic energy dispersion is

$$E_{crit} = \left(\frac{1 + 2\mu}{1 + \mu} \right) \widetilde{\Delta}, \quad \text{with} \quad \mu = \frac{m_c}{m_v} . \qquad (2.5)$$

The value of μ depends on the band structure, it is 1 for a symmetric band structure with the Fermi level at the center of the band gap but smaller for semiconductors [Rid99]. Kaiser et. al. assumed $\mu = 1$ for α-SiO$_2$ [Kai00], and since we did not find information on the value of μ for water, we follow their assumption. This implies that a kinetic energy of $E_{crit} = 1.5 \, \widetilde{\Delta}$ is required for impact ionization [Kai00, Ret04]. The excess energy of $0.5 \, \widetilde{\Delta}$ that remains after impact ionization is distributed among the collision partners [Kai00, Rid99, Stu96]. Thus, each quasi-free electron produced by impact ionization has to gain less energy than $1.5 \, \widetilde{\Delta}$ to reach the critical energy. However, the average energy leading to an impact ionization event is larger than E_{crit} because the impact ionization rate increases with kinetic energy [Arn92, Kai00, Kel60, Ret04]. To consider both factors, we assume that the average energy gain required for a free electron to cause impact ionization is $1.5 \, \widetilde{\Delta}$, as illustrated in Fig. 2.1.

Since several consecutive inverse Bremsstrahlung absorption events are necessary for a free electron to pick up the critical energy for impact ionization, there are time constraints on cascade ionization. For a band gap of 6.5 eV in water and a Keldysh parameter $\gamma = 2$, the effective ionization potential is $\widetilde{\Delta} \approx 7.3$ eV, and the average gain in kinetic energy required to enable impact ionization is $1.5 \, \widetilde{\Delta} \approx 10.95$ eV. When laser irradiation of $\lambda = 1064$ nm wavelength with a photon energy of 1.17 eV is used to produce optical breakdown, an electron

must undergo at least 10 inverse Bremsstrahlung absorption events before impact ionization can occur. As mentioned above, inverse Bremsstrahlung absorption can only occur during collisions of the electrons with heavy particles. A recent comparison between experimental results for fused silica and modeling predictions yielded a time τ between these collisions of $\tau = 1.7$ fs [Sun05], and in our study we obtain a value of 1.6 fs for fs breakdown in water. Based on the latter value, the minimum time for one doubling sequence of the number of free electrons by cascade ionization is 16 fs even if every collision involves the absorption of one photon.

In our numerical model, we combine the Keldysh model for strong-field ionization (including both tunneling and multiphoton absorption) [Kel65] with Shen's, Kennedy's, and Stuart's description of avalanche ionization [Ken95, She84, Stu96] which is based on the Drude model. In theoretical investigations the breakdown threshold is usually defined by the irradiance required to produce a certain critical free electron density ρ_{cr} at the laser focus. Mostly, the electron density

$$\rho_{cr}^{'} = \omega^2 \frac{m_c \, \varepsilon_0}{e^2} \tag{2.6}$$

above which the plasma becomes both strongly reflective and absorbing is used as breakdown criterion [Kai00, Len98, Mao04, Stu96, Tie99]. Here ε_0 denotes the vacuum dielectric permittivity. The critical electron density ρ_{cr}' amounts to 0.984×10^{21} cm^{-3} for $\lambda = 1064$ nm, to 3.94×10^{21} cm^{-3} for $\lambda = 532$ nm, and to 8.86×10^{21} cm^{-3} for $\lambda = 355$ nm. As discussed by Vogel et al [Vog08], ρ_{cr} is an inappropriate criterion for comparison with measured threshold data because it relates to a change in laser-plasma coupling rather than to the phase transition underlying the experimental criterion of bubble formation. In the present study, based on our capability to track the temperature evolution in the focal volume, we will use the critical temperature for bubble formation as breakdown criterion (see 2.1.2).

Diffusion and recombination

A portion of the free electrons produced by multiphoton or cascade ionization will diffuse out of the focal volume during the laser pulse and no longer contribute to the ionization cascade. This loss mechanism will be most important for focusing at large numerical aperture and long pulse durations.

All electrons will, earlier or later, transit back from the conduction into the valance band, transferring their energy to the heavy particles. This process, together with collisions, contributes to the rise of the equilibrium (thermodynamic) temperature in the focal volume. If recombination occurs during the laser pulse, it constitutes another loss mechanism for the ionization avalanche besides the diffusion losses. Recombination losses become ever more severe with increasing free electron density ρ because the recombination rate is proportional to ρ^2 as two free carriers – electron and hole – are required for each recombination event. By contrast, avalanche ionization is just proportional to the free electron density ρ. Therefore, recombination can, under certain conditions, stop the avalanche before full ionization is reached.

Thermal ionization

In transparent dielectrics, laser energy can only be deposited by photo ionization and avalanche ionization. However, when the energy carried by the primary free electrons is thermalized by collision and recombination, thermal emission of free electrons can come into play as third process of generating free electrons, once the temperature in the focal volume is sufficiently high. For femtosecond pulses, this will occur only after the laser pulse because the thermalization time is in the order of several picoseconds. However, for nanosecond pulses that are 2 – 3 orders of magnitude longer than the thermalization time, considerable heating of the focal volume occurs during the laser pulse, and thermal ionization will support avalanche ionization in driving the breakdown process. For sufficiently high irradiance, this will overcome the inhibition of the avalanche by recombination, and breakdown will proceed to full ionization. To portray these features, modeling must include the energy transfer by collisions and recombination, as well as thermal ionization. We developed, to the best of our knowledge, the first approach for modeling the evolution of the focus temperature and the contribution of thermal ionization. This approach is presented in section 2.1.4.

Evolution of modeling approaches

In the first attempts to model optical breakdown in condensed matter, researchers concentrated on the modeling of avalanche ionization starting from a background free-electron density [Bas72, Bloe74]. Bloembergen mentioned the role of photo-ionization and of losses by recombination, trapping with exciton formation, and diffusion but ignored them because ".. in experiments with short laser pulses ($t_p < 10^{-8}$ s) losses are often negligible during the formation of the breakdown plasma (and) recombination is also negligible before the plasma reaches a high density." However, he did not consider what happens once a high density is reached. Photoionization across the band gap is also ignored because it is assumed that an initial carrier density of at least 10^8 cm^{-3} exists that will be sufficient to initiate avalanche ionization. Shen [She84] introduced the use of the

Drude model of the electric conductivity of the „free electron gas' in metals to describe both energy gain and loss by collisions, in a similar fashion as established earlier for gases [deM69, Smi76]. He derived a rate equation considering avalanche ionization, multiphoton ionization, and diffusion losses but assumed that multiphoton excitation of electrons to the conduction band is negligible besides for very short wavelengths. Other authors mention MPI as potential starting mechanism but then neglect it in their theoretical treatment of breakdown [Spa81]. The first comprehensive rate equation model including multiphoton and avalanche ionization was presented in the mid-nineties by Kennedy [Ken95], and Stuart et al. proved that results of the rate equation approach were similar to the predictions of more refined transport equations [Stu96]. A similar step from detailed transport equations [Kai00] to a rate equation approach was later made by Rethfeld [Ret04]. However, she refined this approach by following the non-stationary energy distribution of electrons on ultra-short time scales in order to consider the time constraints on avalanche ionization.

Many authors mention recombination in a qualitative discussion of the breakdown process but then neglect it in their quantitative treatment [Rea71, Smi76, Ken95, Stu96]. They all end up in describing the avalanche as exponential growth of free carriers, without any hindrance of growth besides the end of laser irradiation. In this concept, full ionization can be easily reached, and no steps in the growth of free-electron density with increasing irradiance are expected. Only Grey-Morgan acknowledged very early the existence of recombination-dominated regimes [Gre75]. Some researchers neglect recombination because they focus attention on breakdown induced by ultra-short laser pulses [Stu96, Ret04].

In our own modeling efforts, we considered photoionization, avalanche ionization, diffusion losses, and recombination from the very beginning [Noa99]. Initially, photoionization was treated in a multiphoton approximation, similar to Kennedy's approach [Ken95], but later we incorporated the full Keldysh theory of photoionization [Vog05]. In this study, we extend the modeling to include heating through linear absorption and via collision losses and recombination of the free electrons produced by nonlinear absorption, as well as its counteraction by heat diffusion out of the focal volume. Moreover, we consider that sufficiently high temperatures result in thermal ionization accelerating the ionization avalanche.

2.1.2 Breakdown criterion

In this study, bubble formation is used as criterion for optical breakdown in aqueous media. Because of the large volume change involved in a liquid-gas phase transition, this criterion is experimentally easily detectable. Moreover, it is well defined because the temperature threshold for bubble formation varies little with laser pulse duration, even though it is influenced by the degree of stress confinement upon energy deposition (see section 2.2). By contrast, the onset of plasma luminescence is not related to a well defined temperature because the brightness changes continuously with temperature. Furthermore, detection of the luminescence does not only depend on the plasma temperature but, at equal temperatures, also on the duration of the luminescence that is related to the laser pulse duration.

For consistency with the experimental criterion, we use the critical temperature T_{cr} required for bubble formation as threshold criterion in our breakdown model. The threshold for plasma luminescence is identified with a critical temperature of 6000 K. Historically; a certain critical free-electron density was usually employed for definition of the breakdown threshold. However, this approach is not suitable for comparison with experiments that detect a phase transition such as bubble formation, or plasma luminescence. Moreover, it is misleading because for different pulse durations the same free electron density will produce different plasma energy densities and temperature. In femtosecond breakdown, only one set of free electrons is produced the energy of which is subsequently thermalized. By contrast, during a nanosecond pulse that is much longer than the thermalization time, energy from free electrons is continuously transferred to the heavy particles, and the same free electron density can thus result in much larger energy density within the focal volume. A threshold criterion linked to a critical free-electron density is, therefore, not suitable to guide the selection of laser parameters for material processing that relies on the knowledge of the volumetric energy density ε and temperature T produced by the laser pulse.

2.1.3 Numerical simulations including the full Keldysh model

The time evolution of the electron density ρ_c in the conduction band under the influence of the laser light is calculated using a rate equation of the generic form [Noa99]

$$\frac{d\rho_c}{dt} = \eta_{\text{photo}} + \eta_{\text{casc}}\rho_c - \eta_{\text{diff}}\rho_c - \eta_{\text{rec}}\rho_c^2. \tag{2.7}$$

The first term represents the generation of free electrons mediated by the strong electric field in the laser focus (photoionization via multiphoton and tunneling ionization), the second term represents the contribution of cascade or avalanche ionization, and the last two terms describe the losses through diffusion of quasi free electrons out of the focal volume, and recombination of electrons and holes. The cascade ionization rate η_{casc} and the diffusion loss rate η_{diff} are proportional to the number of already produced free electrons, while the recombination rate η_{rec} is proportional to ρ_c^2, as it involves an interaction of both an electron and a hole. Diffusion and recombination are very important for plasma formation induced by nanosecond laser pulses and do not play a significant role for femtosecond laser pulses.

However, as described in section 3.1, for photon energies below the ionization potential, free electrons can only be generated by multiphoton or tunnel-ionization. At room temperature the initial steady-state „free' electron density in the conduction band ρ_c is negligible, and the electron density in the ground state corresponds to the total electron density $\rho_v = 6.68 \times 10^{22}$ cm^{-3} [Ken95, p.2246]. However, during the laser pulse it is reduced by ionization to $\rho_v - \rho_c$. The time averaged ionization rate for a field with angular frequency ω and intensity I acting on an electron density $\rho_v - \rho_c$ in the ground state was derived by Keldysh to be [Kel65]

$$\left(\frac{d\rho_c}{dt}\right)_{photo} = \frac{2\omega}{9\pi}\left(\frac{\sqrt{1+\gamma^2}}{\gamma}\frac{m\omega}{\hbar}\right)^{3/2} Q\left(\gamma,\frac{\tilde{\Delta}}{\hbar\omega}\right) \times (\rho_v - \rho_c)$$

$$\exp\left\{-\pi\left\langle\frac{\tilde{\Delta}}{\hbar\omega}+1\right\rangle \times \left[K\left(\frac{\gamma}{\sqrt{1+\gamma^2}}\right) - E\left(\frac{\gamma}{\sqrt{1+\gamma^2}}\right)\right]\middle/ E\left(\frac{1}{\sqrt{1+\gamma^2}}\right)\right\}$$

$$Q(\gamma,x) = \sqrt{\pi\middle/ 2K\left(\frac{1}{\sqrt{1+\gamma^2}}\right)} \times \sum_{l=0}^{\infty}\exp\left\{-\pi l\left[K\left(\frac{\gamma}{\sqrt{1+\gamma^2}}\right) - E\left(\frac{\gamma}{\sqrt{1+\gamma^2}}\right)\right]\middle/ E\left(\frac{1}{\sqrt{1+\gamma^2}}\right)\right\}$$

$$\times \Phi\left\{\left[\pi^2\left(2\langle x+1\rangle - 2x + l\right)\middle/ 2K\left(\frac{1}{\sqrt{1+\gamma^2}}\right)E\left(\frac{1}{\sqrt{1+\gamma^2}}\right)\right]^{1/2}\right\} \tag{2.8}$$

Here $\langle x \rangle$ represents the integer part of the number x, $K()$ and $E()$ denote the elliptic integrals of first and second kind, and $\Phi()$ denotes the Dawson probability integral

$$\Phi(z) = \int_0^z \exp\left(y^2 - z^2\right)dy \tag{2.9}$$

The Keldysh parameter γ and the effective ionization potential $\tilde{\Delta}$ for creating an electron-hole pair in condensed matter exhibiting a band structure are given by

$$\gamma = \frac{\omega}{e}\sqrt{\frac{c\,\varepsilon_0\,m\Delta\,n_0}{I}} \qquad and \qquad \tilde{\Delta} = \frac{2}{\pi}\Delta\frac{\sqrt{1+\gamma^2}}{\gamma}E\left(\frac{1}{\sqrt{1+\gamma^2}}\right). \tag{2.10}$$

For $\gamma \gg 1$ (for example nanosecond laser pulses), equation (2.8) reduces to the expression for multiphoton ionisation used in Refs. [Ken95, Noa99], and the ionization potential can be approximated by the band gap energy Δ. Under these circumstances the photoionization rate shows an intensity dependence proportional to I^k, k representing the number of photons required to cross the band gap.
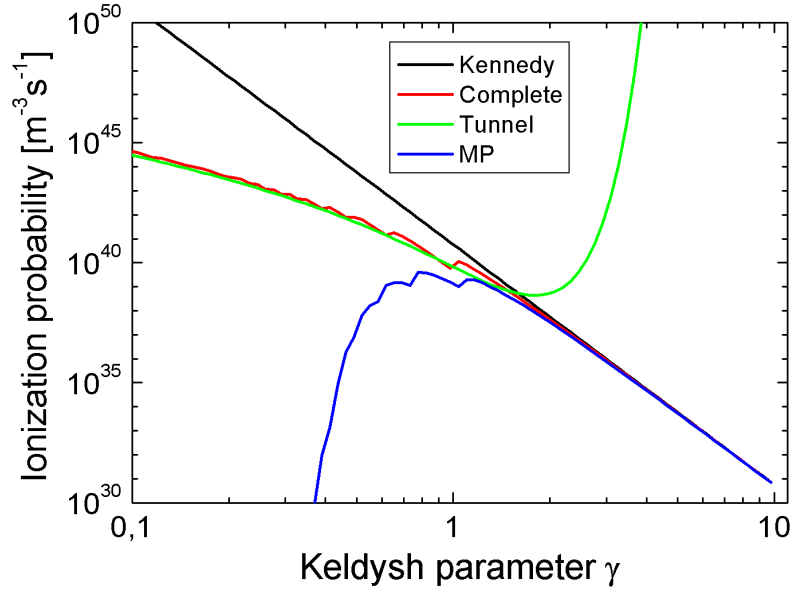
Figure 2.2 Nonlinear photoionization rate for water at λ = 780 nm calculated with the complete Keldysh model (red), Keldysh's approximations in the tunnel limit (green) and the multiphoton limit (blue), and with Kennedy's approximation in the multiphoton limit (black) [81, 110].

Figure 2.2 shows the calculated ionization rate for 780nm as a function of the Keldysh parameter γ calculated with the complete model in equation (2.8) and with various approximations. For values γ<<1, the Keldysh multiphoton approximation predicts photoionization rates that are too low by several orders of magnitude, while the predictions of Kennedy's multiphoton approximation [Ken95, Noa99] are by several orders of magnitude too large.

As soon as free electrons exists in the focal volume, they are able to gain kinetic energy through inverse Bremsstrahlung absorption of photons and can generate further free-electrons through impact ionization once their energy exceeds the critical energy described by equation (2.5). As explained above, we assume that the average gain of kinetic energy by each electron required to cause an impact ionization event is $E = 1.5 \widetilde{\Delta}$. The ionization rate per electron participating in the cascade is then, according to Kennedy [Ken95], given by

$$\eta_{casc} = \frac{1}{\omega^2 \tau^2 + 1} \left[\frac{e^2 \tau}{c \, n_0 \varepsilon_0 \, m_c \, (3/2) \widetilde{\Delta}} I - \frac{m_c \, \omega^2 \, \tau}{M} \right],$$ (2.11)

where τ is the time between collisions, c is the vacuum speed of light, and n_0 the refractive index of the medium at frequency ω. The masses of the electron and the water molecule are m_c and M, respectively. For large irradiances, the second term in (2.11) can be neglected and the cascade ionization rate is proportional to I.

Two aspects must still be considered to accurately determine the cascade contribution to the free electron density. First, a certain free "seed" electron density ρ_{ini} produced by photoionization is required for the start of the cascade. Second, it must be taken into account that inverse Bremsstrahlung absorption requires a finite time $t_{ion} = \tau \, n$ which is determined by the mean free time τ (1.6 fs) between electron/molecule collisions and the number n of photons that must be absorbed to gain sufficient energy.

Therefore, the contribution of cascade ionization at time t must be evaluated using the electron density created at the retarded time $t_{ret} = t - t_{ion}$. A first order approximation of this retardation of the cascade leads to the expression

$$\left(\frac{d\rho_c}{dt} \right)_{casc} = \begin{cases} \dfrac{\eta}{(1+\eta \, t_{ret})} \rho_c & \text{for} & \rho_c V \geq 0.5 \\ 0 & \text{for} & \rho_c V < 0.5 \end{cases}.$$ (2.12)

Free electrons are lost in the interaction volume by diffusion out of the volume V and through recombination. The focal volume is assumed to be ellipsoidal, which corresponds to illumination of the rear aperture of the microscope objective with a plane wave. The short axis d of the ellipsoid is identified with the diameter of the central maximum of the Airy pattern in the focal plane that is given by

$$d = 1.22 \frac{\lambda}{NA}. \tag{2.13}$$

The symbol λ refers to the vacuum wavelength of light. The refractive index of the medium is contained in the value of the numerical aperture (NA) of the microscope objective. The ratio l/d of the long and short axis can be obtained from the relation

$$\frac{l}{d} = \frac{(3 - 2\cos\alpha - \cos 2\alpha)^{1/2}}{1 - \cos\alpha} \tag{2.14}$$

that was derived by Grill and Stelzer for optical setups with a large solid angle [Gri99]. For example, a numerical aperture of NA = 1.3, which in water corresponds to a focusing angle of $\alpha = 77.8°$, we find $l/d = 2.4$. For smaller NAs, the focal shape is getting more elongated, the ratio l/d for NA = 0.9 is already 4.5.

Thus, the focal volume can be approximated by $V = (4/3)\,\pi\,a^2\,b$ where a and b are the short and long half-axis of the ellipsoidal irradiance distribution with $a = d/2$ and $b = l/2$ as described by equation (2.13) and (2.14). However, the source for electron diffusion is not the irradiance distribution but the free-electron distribution that scales with $d/\sqrt{k}$ and $l/\sqrt{k}$. The resulting (negative) ionization rate due to diffusion is [Car59, Ken95]

$$\left(\frac{d\rho_c}{dt}\right)_{diff} = -\frac{\tau\,E_{av}}{3\,m\,\Lambda^2} \times \rho_c = -\frac{\tau\,5\widetilde{\Delta}}{6\,m_c}\left[\frac{6}{a^2} + \frac{2}{b^2}\right] \times \frac{1}{k} \times \rho_c = -\frac{\tau\,5\widetilde{\Delta}}{6\,m_c}\left[\frac{24}{d^2} + \frac{8}{l^2}\right] \times \frac{1}{k} \times \rho_c, \tag{2.15}$$

where E_{av} is the average kinetic energy of the free electrons, and Λ is the characteristic diffusion length. Free electrons produced by impact ionization possess, on average, a start energy of $(1/2)\,\widetilde{\Delta}$ and produce another free electron through impact ionization when they reaches a kinetic energy of $2\,\widetilde{\Delta}$. Thus their mean kinetic energy is $(5/4)\,\widetilde{\Delta}$, leading to the expression on the right hand side of eq. (2.15).

For the recombination rate, we used an empirical value that was determined by Docchio through inspection of the decay of the plasma luminescence [Doc88c] and later confirmed independently by Sarpe-Tudoran et al. [Sar06]

$$\left(\frac{d\rho_c}{dt}\right)_{rec} = -2\times10^{-9}\,\mathrm{cm^3/s} \times \rho_c^2 = -2\times10^{-15}\,\mathrm{m^3/s} \times \rho_c^2 \tag{2.16}$$

In water of moderate temperature, recombination of free electrons is not a one-step process but consist in hydration of the electron within about 300 fs and subsequent decay of the hydrated state that has an average lifetime of ≈ 300 ns [Nik83]. However, this lifetime seems to be dramatically reduced at water temperatures in the range of the super critical heat limit, and at very high temperatures both the band structure and interband energy levels disappear.

To obtain the evolution of the free electron density during a Gaussian laser pulse

$$I(t) = I_0 \exp\left[-4\ln 2\left(\frac{t}{\tau_L}\right)^2\right], \tag{2.17}$$

the complete rate equation

$$\frac{d\rho_c}{dt} = \left(\frac{d\rho_c}{dt}\right)_{photo} + \left(\frac{d\rho_c}{dt}\right)_{casc} + \left(\frac{d\rho_c}{dt}\right)_{diff} + \left(\frac{d\rho_c}{dt}\right)_{rec} \tag{2.18}$$

was solved numerically for various laser pulse peak intensities I using a Runge-Kutta method with adaptive step size control. Separate book-keeping was used for the contribution of eq. (2.8) to evaluate the influence of multiphoton and cascade ionization. The breakdown threshold is here still defined as irradiance I_{rate} required to produce a maximum electron density ρ_{max} during the laser pulse that equals the critical density $\rho_{cr} = 10^{21}$ cm^{-3}. Besides the time evolution of the electron density, we also assess the dependence of the maximum electron density on irradiance, by calculating ρ_{max} as a function of I/I_{rate}. The numerical results for two different laser pulse durations and wavelengths in the IR are shown in **Fig. 2.3.** When heating of the focal volume and thermal ionization is included in the model (next section), we will be able to use a critical temperature representative for bubble formation of plasma luminescence as breakdown criterion.
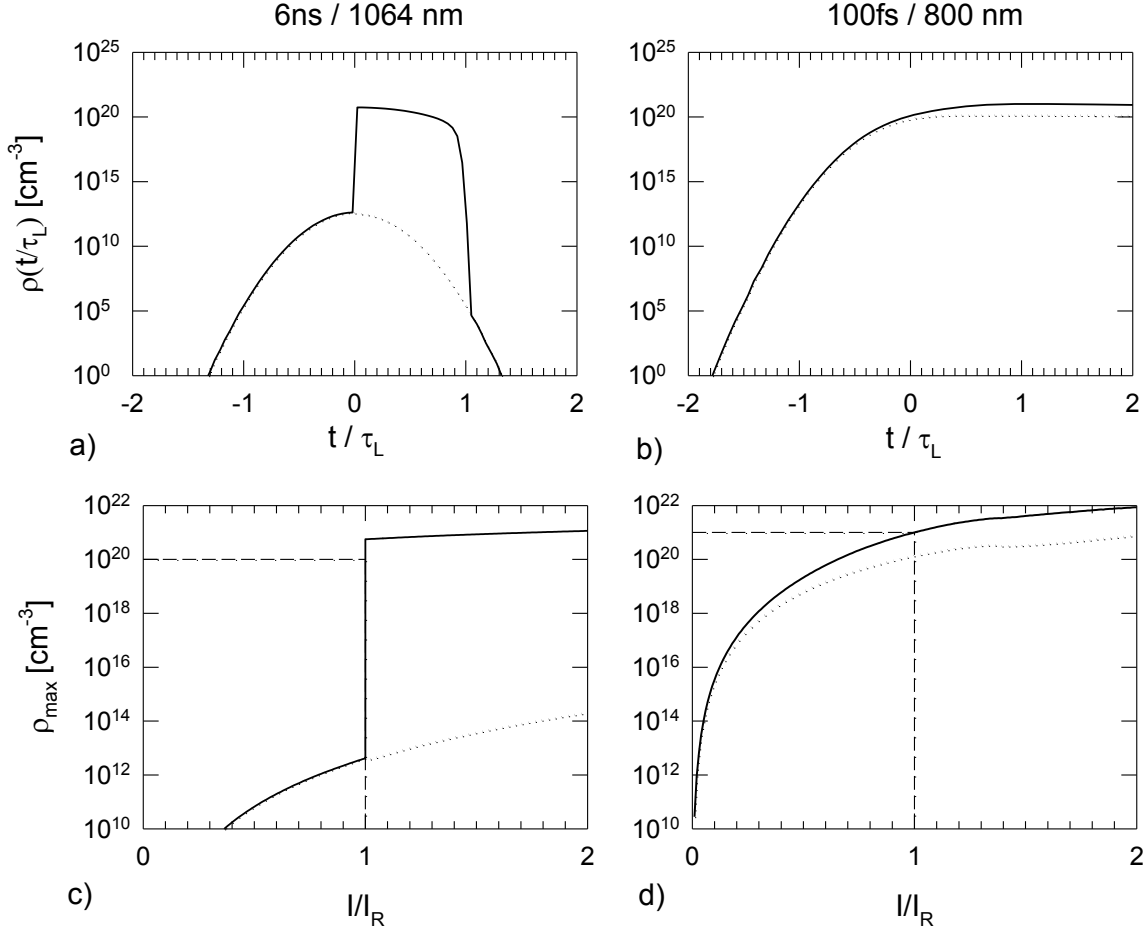
Figure 2.3 Top row: Evolution of the free-electron density during the laser pulse at the optical breakdown threshold for 6 ns, 1064 nm pulses and for 100 fs, 800 nm pulses. The time t is normalized with respect to the laser pulse duration τ_L. The contribution of multiphoton ionization to the total free-electron density is plotted as a dotted line. Bottom row: Maximum free electron density ρ_{max} achieved during the laser pulse as a function of irradiance, for the same laser parameters. The irradiance I is normalized with respect to the threshold irradiance I_{rate}. The threshold I_{rate} and the corresponding value of ρ_{max} are marked by dashed lines.

The top row of figure 2.3 presents the evolution of the free-electron density ρ_C during the laser pulse at the optical breakdown threshold for 6-ns, 1064-nm pulses, and for 100-fs, 800-nm pulses. To facilitate a comparison between the different pulse durations, the time t is normalized with the respective laser pulse duration τ_L. The contribution of photoionization to the total free-electron density is plotted as a dotted line. The bottom row of figure 2.3 shows how the maximum free electron density achieved during the laser pulse depends on irradiance.

It is obvious that the dynamics of plasma formation is extremely different for nanosecond and femtosecond pulses. With nanosecond pulses, no free electrons are formed for irradiance values below the optical breakdown threshold because the irradiance is too low to provide seed electrons by means of multiphoton ionization. Once the irradiance is high enough to provide a seed electron, the ionization cascade can start. It proceeds very rapidly owing to the high irradiance (Fig. 2.3c). The electron density shoots up by 9 orders of magnitude within a small fraction of the laser pulse duration until its rise is stopped by recombination which is proportional to ρ_c^2.

With femtosecond pulses, a much higher irradiance is necessary for optical breakdown to be completed during the shorter laser pulse duration than with nanosecond pulses. This favors the generation of free electrons through multiphoton ionization because of its stronger irradiance dependence $\propto I^k$ as opposed to $\propto I$ for the cascade ionization rate. While with nanosecond pulses at 1064 nm the total number of free electrons generated through avalanche ionization is 10^9 times larger than the number generated through multiphoton ionization (Fig. 2.3a), it is only 12 times larger with 100-fs pulses at 800 nm (Fig. 2.3b). As a consequence of the increasing importance of multiphoton ionization with shorter pulse durations, there is never a lack of seed electrons for avalanche ionization. An avalanche is initiated at irradiance values considerably lower than the breakdown threshold. The free-electron density reached at the end of the avalanche depends on irradiance in a much smoother way (Fig. 2.3d) than for ns pulses (Fig. 2.3c).

2.1.4 Numerical simulations including heating of focal volume and thermal ionization

2.1.4.1 Thermal ionization

In transparent dielectrics, free electrons can only be generated at high irradiances of the incident light by photo ionization (multiphoton and tunnel ionization), and cascade ionization. However, once the energy carried by the primary free electrons is thermalized, thermal emission of free electrons comes into play as third process of generating free electrons. In order to describe this process, we will again treat water as an amorphous semiconductor. The classical theory of semiconductors [Kit76] defines a state density $D(E)$ and an occupation probability $f(E,T)$ for a free electron gas with

$$D(E) = \frac{(2m_e)^{\frac{3}{2}}}{2\hbar^3\pi^2} E^{\frac{1}{2}}$$

(2.19)

and

$$f(E,T) = \frac{1}{\exp\left(\frac{E-E_F}{kT}\right)+1}$$

(2.20)

with m_e electron mass, $\hbar$ Dirac constant, k Boltzmann constant, and E_F Fermi energy. The state density $D(E)$ describes the "space" for free electrons with energy E in the conduction band whereas the function $f(E,T)$ specifies the probability that a free electron has the energy E at the temperature T of the semiconductor. The dependence of $D(E)$ and $f(E,T)$ on the energy E is illustrated in **Fig. 2.4**.
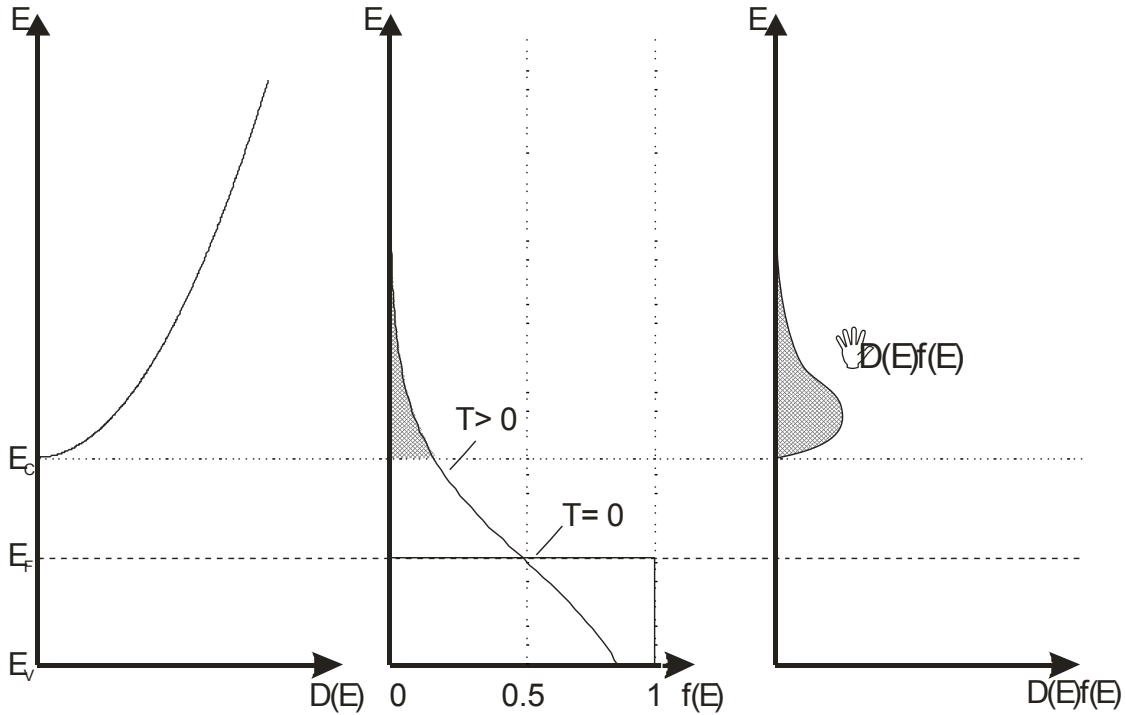

Figure 2.4 Dependence of $D(E)$ and $f(E,T)$ on laser pulse energy E. The integral over $D(E)f(E,T)$ yields the density of electrons in the conduction band for a given temperature T. E_F denotes the Fermi energy, and E_C and E_V are the energy levels of the lower edge of the conduction band and upper edge of valence band, respectively.

For low temperatures, the occupation probability $f(E,T)$ deviates strongly from the classical Maxwell-Boltzmann distribution. In the limit $T=0$, all states below the Fermi energy E_F are fully occupied, and all states with $E > E_F$ are empty. One can imagine that the electrons are filled into a quantum well with a specific space for each electron. The highest energy level of electrons in this quantum well at T = 0 K is defined as Fermi energy. For higher temperatures, electrons occupy higher energetic levels, and the energy distribution is smoothened in the range of $\pm kT$.

The Fermi energy E_F corresponds to an upper limit p_F of the momentum, i.e. $|\vec{p}| \le p_F$. This inequality describes a sphere in momentum space or, when momentum is expressed by wave number, in k-space: $|\vec{k}| \le k_F$. The number of different states in this sphere corresponds to the total number of electrons in the system. It can be obtained by dividing the value of the Fermi sphere $4/3\,\pi\,(k_F)^3$ by the space of an electron $(2\pi/L)$. Here k_F is the wave number at the Fermi surface, i.e. the surface of the Fermi sphere, and $2\pi/L$ is given by the periodic boundary conditions for constructive interference in a unit cube with edge length L and volume $V = L^3$. We obtain

$$N = 2 \cdot \frac{4\pi \frac{k_F^{\,3}}{3}}{\left(\frac{2\pi}{L}\right)^3} \cdot \qquad (2.21)$$

The factor 2 takes the electron spin (up and down) into account.

For an electron gas, Fermi energy and wave number are linked by [Kit76]

$$E_F = \frac{\hbar^2}{2m_e} k_F^2 \quad . \qquad (2.22)$$

Solving Eq (2.21) for k_F and substitution into Eq (2.22) yields:

$$\begin{aligned} E_F &= \frac{\hbar^2}{2m_e}\left(3\pi^2\,\frac{N}{V}\right)^{\frac{2}{3}} \\ &= \frac{\hbar^2}{2m_e}\left(3\pi^2 \rho_V^e\right)^{\frac{2}{3}} \end{aligned} \qquad (2.23)$$

where ρ_V^e is the electron density in the valence band.

As illustrated in figure 2.4, the free electron density in the conduction band can be expressed by

$$\rho_C^e(T) = \int_{E_C}^{\infty} D(E - E_C) f(E,T)\, dE \; . \qquad (2.24)$$

To describe the state density $D(E)$ of the free electron gas in the conduction band, we shift the "zero" energy to the lower edge of the conduction band, i.e. we replace E in equation (2.19) by $(E-E_C)$. For simplification, the upper limit of integration (2.24) has been extended from the upper boarder of the conduction band to infinity. This approximation is reasonable because of the very strong decrease of $f(E,T)$ with increasing energy E which leads to very small probability for pulse energies above the upper border of the conduction band. The extension of the integration allows an analytic solution of (2.24).

After inserting Eqs (2.19) and (2.20) into Eq (2.24), we obtain:

$$\rho_C^e(T) = \int_{E_C}^{\infty} \underbrace{\frac{(2m_e)^{\frac{3}{2}}}{2\hbar^3\pi^2}(E - E_C)^{\frac{1}{2}}}_{D(E-E_C)} \cdot \underbrace{\left(\exp\left(\frac{E - E_F}{kT}\right) + 1\right)^{-1}}_{f(E,T)} dE \; . \qquad (2.25)$$

For sufficiently large temperatures, the high energetic tail of the $f(E,T)$ distribution with $E-E_F > kT$, can be approximated by the Boltzmann distribution with

$$f(E,T) \approx \exp\left(-\frac{E - E_F}{kt}\right) . \qquad (2.26)$$

Then (2.25) reads

$$\rho_C^e(T) = \frac{(2m_e)^{\frac{3}{2}}}{2\hbar^3\pi^2} \int_{E_C}^{\infty} (E - E_C)^{\frac{1}{2}} \cdot \exp\left(-\frac{E - E_F}{kT}\right) dE \; . \qquad (2.27)$$

The substitution of $x = (E-E_C)/(kT)$, $dE = kT\,dx$ leads to new borders of the integral with $E = E_C \rightarrow x = 0$ and $E = \infty \rightarrow x = \infty$. Furthermore, when $E - E_F$ is expanded to $E - E_C - (E_F - E_C)$, Eq (2.27) can be written as:

$$\rho_C^e(T) = \frac{(2m_e)^{\frac{3}{2}}}{2\hbar^3\pi^2} \int\limits_{E_C}^{\infty} \left(\frac{E-E_C}{kT}\right)^{\frac{1}{2}} (kT)^{\frac{1}{2}} \cdot \exp\left(-\frac{E-E_C-(E_F-E_C)}{kT}\right) kT\,dx$$

$$= \frac{(2m_e)^{\frac{3}{2}}}{2\hbar^3\pi^2}(kT)^{\frac{3}{2}} \exp\left(-\frac{E_C-E_F}{kT}\right)\underbrace{\int\limits_{0}^{\infty} x^{\frac{1}{2}}e^{-x}\,dx}_{\frac{\sqrt{\pi}}{2}},$$

and the integral can be solved.

This way, we obtain a simple expression for the thermal free electron density in the conduction band:

$$\rho_C^e(T) = \left(\frac{m_e kT}{2^{\frac{1}{3}}\pi\hbar^2}\right)^{\frac{3}{2}} \cdot \exp\left(-\frac{E_C-E_F}{kT}\right). \tag{2.28}$$

To further simplify equation (2.27), we rearrange (2.23) to:

$$m_e = \frac{\hbar^2}{2E_F}\left(3\pi^2\rho_V\right)^{\frac{2}{3}}, \tag{2.29}$$

and insert m_e into equation (2.28):

$$\rho_C^e(T) = \frac{\hbar^3\left(3\pi^2\rho_V\right)\cdot(kT)^{\frac{3}{2}}}{2^{\frac{3}{2}}2^{\frac{1}{2}}\pi^{\frac{3}{2}}\hbar^3 E_F^{\frac{2}{3}}} \cdot \exp\left(-\frac{E_C-E_F}{kT}\right)$$

$$= \frac{3}{4}\pi^{\frac{1}{2}}\rho_V\left(\frac{kT}{E_F}\right)^{\frac{3}{2}} \cdot \exp\left(-\frac{E_C-E_F}{kT}\right). \tag{2.30}$$

If we assume a symmetric band structure, the Fermi energy level is located at the center of the bandgap, and $E_F = E_{gap}/2$ if $E_V = 0$. The thermal free electron density $\rho_c^e(T)$ can then be written as

$$\rho_C^e(T) = 3\sqrt{\frac{\pi}{2}}\rho_V\left(\frac{kT}{E_{gap}}\right)^{\frac{3}{2}} \cdot \exp\left(-\frac{E_{gap}}{2kT}\right) \tag{2.31}$$

In the following, we shall identify the thermal free electron density in the conduction band with thermal ionization, i.e. we write $\rho_{therm} \equiv \rho_c^e$. The electron density in the valence band can be calculated with $\rho_V = \rho_{bound} - \rho_{nl} - \rho_{therm}$ where ρ_{bound} is the electron density of the medium, and ρ_{nl} is the free electron density in the conduction band that was created by nonlinear absorption. With these substitutions, equation (2.31) becomes:

$$\rho_{therm} = 3\sqrt{\frac{\pi}{2}}(\rho_{bound} - \rho_{nl} - \rho_{therm})\left(\frac{kT}{\Delta E}\right)^{\frac{3}{2}} \cdot \exp\left(-\frac{\Delta E}{2kT}\right). \tag{2.32}$$

The electron density ρ_{bound} of water can be calculated with the Avogadro's constant $N_{Avo} = 6.022 \cdot 10^{23}$ mol^{-1}, the mol mass 1 mol = 18 g, and the mass density of 1000 kg/m³ assuming two donator electrons per water molecule (one from each O atom). We obtain $\rho_{bound} = 6.68 \cdot 10^{22}$ e$^-$/cm³.

Equation (2.32) solved for ρ_{therm} yields the final equation for the thermally ionized free electron density in the conduction band:

$$\rho_{therm} = (\rho_{bound} - \rho_{nl})\frac{3\sqrt{\frac{\pi}{2}}\left(\frac{kT}{E_{gap}}\right)^{\frac{3}{2}} \cdot \exp\left(-\frac{E_{gap}}{2kT}\right)}{1 + 3\sqrt{\frac{\pi}{2}}\left(\frac{kT}{E_{gap}}\right)^{\frac{3}{2}} \cdot \exp\left(-\frac{E_{gap}}{2kT}\right)} \tag{2.33}$$

Figure 2.5 shows the temperature dependence of the fraction of bound electrons (in %) that are thermally ionized.
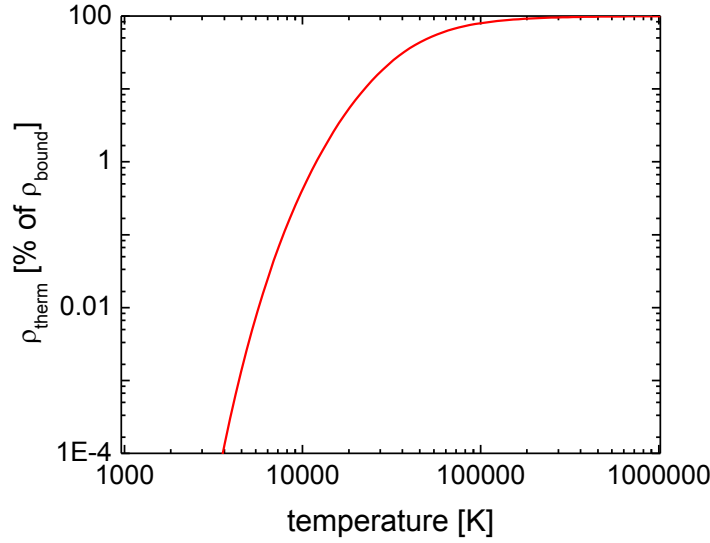

Figure 2.5 Temperature dependence of the fraction of bound electrons (in %) that are thermally ionized.

Figure 2.5 demonstrates that thermal ionization plays a significant role only for temperatures above ≈ 5000 K. However, the contribution of thermal ionization increases very rapidly with increasing temperature. Therefore, it is important to consider thermal ionization, especially for the numerical modeling of ns breakdown.

In deriving Eq. (2.33) we considered neither electron diffusion nor heat diffusion away from sub-volumes of the focal region, i.e. we implicitly assumed a spatially extended, homogeneous free electron sea. This assumption is problematic for the initial breakdown phase where many local avalanches start from individual seed electrons. However, the problem does not arise if the initial seed electron density produced by photoionization is sufficiently high such that thermal and free-electron diffusion is much faster than the laser pulse duration.

The above line of reasoning shows that it is inadequate to assume a constant *number* of start electrons per focal volume. This approach was introduced by Kennedy [Ken95] and later put to an extreme by Noack and Vogel [Noa99], and Vogel and coworkers [Vog05] who assumed that one free electron might suffice. Since the focal volume scales with NA^{-4}, the assumption implies that the seed electron density strongly decreases for lower NAs. This is not consistent with the experimental finding that hardly any dependence of I_{th} on the focusing angle Θ was observed in the range $1.8° \leq \Theta \leq 32°$ [Vog96]. Thus both experimental results and the above line of reasoning on thermal and free electron diffusion suggest that the initiation of avalanche ionization and of thermal emission of free electrons requires a minimum free seed electron *density ρ_0* created by photoionization.

Eq. (2.33) models temperature-related changes of the number density and energy distribution of electrons in the valence and conduction bands without any light irradiance. In addition, the temperature increase influences the electron-phonon collision rate, the energy distribution of the free electrons produced by nonlinear absorption, and the width of the band gap that needs to be overcome in nonlinear absorption processes. These changes will probably facilitate the ionization process, especially for long pulses during which the temperature increase via recombination and collision losses is most pronounced. On the other hand, for long pulses plasma expansion and hydrodynamic effects come into play that will lower the temperature. Consideration of the above mentioned factors goes far beyond the framework of the present study because 1) the collision cross sections and their temperature dependence are not yet known for water, 2) the numerical costs for computing would exceed our present capabilities.

Other effects that are not yet considered are energy losses by Bremsstrahlung, changes of the laser-plasma coupling efficiency at large free electron densities, and shielding effects by plasma formation in "upstream" regions.

2.1.4.2 Rate equation including thermal ionization

During optical breakdown, free electrons are generated by photoionization, cascade ionization and thermal ionization, while losses occur through recombination and diffusion of free electrons out of the focal volume. Consideration of all five mechanisms requires a complex model, and the individual elements of the model should thus be kept as simple as possible without sacrificing precision.

One important simplification is possible by considering the fact that the establishment of an equilibrium temperature in the focal volume lasts a few picoseconds, i.e. thermal ionization becomes important only in a regime where tunneling ionization can already be neglected. Therefore, we can use a multiphoton approximation of the Keldysh theory. Specifically, for the bubble formation thresholds with 1 ns laser pulses focused with NA = 0.8 and NA = 0.9 (see section 2), the Keldysh Parameter is $\gamma = 4.7$ for IR, $\gamma = 13.9$ for VIS, and $\gamma = 26.3$ for the UV wavelength. Figure 2.2 demonstrates that this is well inside the multiphoton regime. For our model, we employ Kennedy´s multiphoton approximation of photoionization [Ken95].

In the following, we first present the basic rate equation without thermal ionization (2.1.4.2.1). Then we describe the modeling of the temperature evolution in the focal volume that involves heating by linear absorption, thermalization of free electron energy, and heat diffusion (2.1.4.2.2). This modeling creates a basis for the implementation of thermal ionization into the rate equation which is described in section 2.1.4.2.3

2.1.4.2.1 Modification of the basic rate equation for consideration of thermal ionization

A generic form of the rate equation for the free electron density ρ is (see Eq. (2.7)) [Noa99, Ken95]

$$\frac{d\rho}{dt} = \left(\frac{d\rho}{dt}\right)_{photo} + \eta_{casc}\rho - \eta_{diff}\rho - \eta_{rec}\rho^2 \tag{2.34}$$

The rate equation consists of two terms for the generation of free electrons (photo- and cascade ionization) and two terms for the losses (diffusion and recombination).

Photoionization is described by equation (2.8) of section 2.1.3, the cascade ionization rate is given by equation (2.11), the diffusion rate by Eq. (2.15), and the recombination rate by Eq. (2.16).

The cascade term is only considered once a certain initial free electron density ρ_{ini} has been created by photoionization. Since at least on free "seed" electron is needed for the start of an ionization cascade ionization, we previously [Noa99, Vog05] assumed that ρ_{ini} equals the density for which the probability of having one start electron in the focal volume is 50%. However, as explained at the end of the previous section, this assumption implies that ρ_{ini} depends on *NA*, in contradiction to experimental results, and will in most cases strongly underestimate the actual start electron density required to launch an avalanche. Therefore, the code has now been changed to be able to freely select the start electron density. This enables us to use ρ_{ini} as a fit parameter in comparing experimental and numerical results. However, it must be ensured that the selected value is large enough to have at least one seed electron in the part $V = (4/3)\pi a^2 b (1/\sqrt{k})^3$ of the focal volume in which free electrons are produced. Here $a = d/2$, and $b = l/2$, with d and l being defined by Eqs. (2.13) and (2.14). If the selected ρ_{ini} value is too low, the cascade is not yet considered after the selected value is reached but only after the density corresponds to 50% probability of having one start electron per focal volume. Introduction of ρ_{ini} requires a reformulation of Eq. (1.12) for the time retardation $t_{ret} = t - t_{ion}$ in considering cascade ionization. The first order approximation of the retardation is now given by

$$\left(\frac{d\rho_c}{dt}\right)_{casc} = \begin{cases} \dfrac{\eta}{(1 + \eta\, t_{ret})}\rho_c & \text{for} & \rho_c \geq \rho_{ini} \\ 0 & \text{for} & \rho_c < \rho_{ini} \end{cases} . \tag{2.35}$$

To incorporate thermal ionization it does not suffice to simply add a term describing the rate of thermal ionization to the rate equation, but we also need to consider how the other terms of the rate equation (2.34) are affected by the thermal generation of free electrons. The following considerations apply:

• Thermal ionization becomes important when already large free electron densities are created via multiphoton and cascade ionization. Under these circumstances, the density of bound electrons in the valence band is reduced. This partial depletion reduces the multiphoton ionization rate and the cross section for impact ionization. Both multiphoton ionization (MPI) and impact ionization act on the density of bound electrons minus the total density of free electrons. The influence of the depletion on both multiphoton and impact ionization can be considered by multiplication of the two rates with a dimensionless depletion factor $(1-(\rho/\rho_{bound}))$.

• Once the cascade has started, the gain term acts on all free electrons. By contrast, the term describing collision losses in the avalanche acts merely on the difference between total free-electron density and electron density produced by thermal emission. Otherwise, the free-electron density would, towards the end of the laser pulse, drop below the density of thermally produced electrons which would correspond to a non-physical distortion of the Fermi-Dirac distribution of energetic states (2.20).

• The terms describing the losses by recombination and diffusion act also only on the difference between total electron density and electron density produced by thermal emission, because the thermally produced free-electron density reflects a dynamic equilibrium that is immediately restored after recombination, diffusion, or collision losses.

To implement the above considerations into the numerical solution of the differential equations, the electron density is normalized by the bound electron density of the medium

$$R = \frac{\rho}{\rho_{Bound}}, \tag{2.36}$$

which for water is $\rho_{bound} = 6.68 \cdot 10^{22}$ e$^-$/cm³, and the basic equations are modified to:

$$\frac{dR}{dt} = \left(\frac{dR}{dt}\right)_{photo} + \left(\frac{dR}{dt}\right)_{casc} - \eta_{diff} \cdot (R - R_{therm}) - \eta_{rec}\rho_{bound}(R - R_{therm})^2, \tag{2.37}$$

For the calculation of the photoionization rate $(dR/dt)_{photo}$, we use the full Keldysh model according to Eq. (2.8) when the Keldysh parameter γ is smaller than 10, but we use Kennedy's multiphoton approximation for $\gamma \geq 10$. This simplification is justified by the results in Fig. 2.2 showing excellent agreement of the multiphoton approximation with the full model solution for large γ values. The multiphoton approximation is [Ken95]:

$$\left(\frac{dR}{dt}\right)_{photo} \approx \left(\frac{dR}{dt}\right)_{mp} =$$

$$\frac{2\omega}{9\pi\rho_{bound}} \left(\frac{m'\omega}{\hbar}\right)^{3/2} \left[\frac{e^2}{16m'E_{gap}\omega^2 c\varepsilon_0 n} I\right]^K \times \exp(2k) \cdot \Phi\left(\sqrt{2K - \frac{2E_{gap}}{\hbar\omega}}\right) \times \left(1 - \frac{\rho}{\rho_{bound}}\right) \tag{2.38}$$

Where the last term describes the depletion of free electrons in the valance band during breakdown. The multi-photon ionization rate $(dR/dt)_{mp}$ shows an intensity dependence proportional to I^k, with k representing the number of photons required to cross the band gap:

$$\left(\frac{dR}{dt}\right)_{mp} = \alpha_{mp}\left(\frac{I}{I_{mp}}\right)^K, \tag{2.39}$$

where

$$\alpha_{mp} = \frac{2\omega}{9\pi\rho_{Bound}} \left(\frac{m'\omega}{\hbar}\right)^{3/2} \times \exp(2K) \cdot \Phi\left(\sqrt{2K - \frac{2E_{gap}}{\hbar\omega}}\right) \times \left(1 - \frac{\rho}{\rho_{bound}}\right),$$

and

$$I_{mp} = \frac{16m'E_{gap}\omega^2 c\varepsilon_0 n}{e^2}.$$

For the calculation of the cascade ionization rate in Eq. (2.37), we need to consider that the avalanche starts only after an initial free-electron density ρ_{ini} has been produced by photoionization (see Eq. 2.35), and this density must be normalized by the bound electron density. Furthermore, we need to consider that the gain term acts on all free electrons while the collision loss term only acts on free electrons produced by avalanche ionization and not on those created by thermal ionization, as discussed above.

The cascade ionization rate can then be expressed as:

$$\left(\frac{dR}{dt}\right)_{casc} = \begin{cases} \dfrac{\alpha_{casc}I}{1+\eta_{casc}t_{ret}} \times R - \dfrac{\beta_{casc}}{1+\eta_{casc}t_{ret}}(R-R_{therm}) & for \quad R \geq R_{ini} \\ \\ 0 & for \quad R < R_{ini} \end{cases} \tag{2.40}$$

where $R_{ini} = \dfrac{\rho_{ini}}{\rho_{bound}}$ represents the relative initial electron density,

$t_{ret} = \tau \left\langle 1 + \dfrac{1.5\,\widetilde{\Delta}}{\hbar\omega} \right\rangle$ is the cascade retardation time,

$\alpha_{casc} = \dfrac{1}{\omega^2\tau^2+1}\dfrac{e^2\tau}{cn\varepsilon_0 m_c(3/2)E_{gap}}\left(1-\dfrac{\rho}{\rho_{bound}}\right)$ is the gain in cascade ionization,

and $\beta_{casc} = \dfrac{m_c}{M}\dfrac{\omega^2\tau}{\omega^2\tau^2+1}\left(1-\dfrac{\rho}{\rho_{bound}}\right)$ is the collision loss term of cascade ionization.

The diffusion coefficient in Eq. (2.37) is

$$\eta_{diff} = -\frac{\tau 5\widetilde{\Delta}}{6m_c}\left[\frac{24}{d^2}+\frac{8}{l^2}\right]\times\frac{1}{k}, \tag{2.41}$$

where k is the number of required electrons to cross the band gap, and d and l are the short and long axis of the ellipsoid, respectively. The recombination rate is

$$\alpha_{rec} = \eta_{rec}\rho_{Bound}, \tag{2.42}$$

with $\eta_{rec} = 2\times10^{-15}\,\mathrm{m}^3/\mathrm{s}$ (see Eq. (2.16). We used separate book keeping for the contribution of equation (2.38) to be able to evaluate the influence of multiphoton ionization on the entire breakdown process. For this, the collision losses incorporated in the cascade ionization term as well as recombination and diffusion losses have to be considered also for the multiphoton-produced free electrons. Otherwise, the density of multiphoton-produced free electrons would, at the end of the pulse, exceed the total free electron density. As described above, the collision, recombination and diffusion losses act merely on the difference between total electron density and electron density produced by thermal emission.

2.1.4.2.2 Temperature evolution in the focal volume

To obtain a full numerical model of laser induced plasma formation in aqueous biological media, both thermal ionization and linear absorption is considered and implemented in the rate equation model. Although in water the linear absorption is almost zero, it should be considered for modeling of optical breakdown in aqueous media containing absorbing biomolecules. To assess the contribution of nonlinear absorption to the heating of the focal volume, we have to consider the temperature increase by thermalization of the energy carried by free electrons through recombination and collision losses, and the temperature decay by diffusion of heat out of the focal volume.

Heating by linear absorption

To account for the heating of the focal volume by linear absorption, the existing differential equations need to be extended by a further differential equation for the temperature of the focal volume. The temperature rise induced by linear absorption is given by

$$\left(\frac{dT}{dt}\right)_{absorb} = \frac{1}{lc_p\rho_0}\left[1-\exp\left(-\mu_a l\right)\right]I, \tag{2.43}$$

where l is the focal length given by equation (2.14), μ_a the absorption coefficient, c_p the specific heat capacity, and ρ_0 the density the medium. The absorption of photons by a molecule excites the molecule to a higher energetic state in which the electron is still bound to the molecule. We neglect fluorescence and assume that the entire excitation energy is transferred to the molecules in a non-radiative process. To describe this process in the framework of the rate equation model, we treat the excited electron in the same way as a free electron having a

kinetic energy equal to the excitation energy that was gained by absorbing a photon. The free electron can collide both with other electrons or with molecules and transfers with each impact a part ΔW of its energy W to the impact partner. Assuming an elastic impact process, the energy transfer amounts to

$$\frac{\Delta W}{W} = \frac{4m_1 m_2}{(m_1 + m_2)^2} \, , \tag{2.44}$$

with m_1 and m_2 being the masses of the collision partners.

It is obvious from equation (2.44) that an impact of electron onto a second electron with the same mass leads to a complete energy transfer, and the energy remains within the electronic system. By contrast, impacts between electrons and molecules are more relevant for an energy transfer and a temperature increase of the medium. The amount of transferred energy depends on the mass $m_2 = M$ of the molecule. Full thermalization is achieved when the average kinetic energy of all particles (electrons and molecules) is the same. The number of collisions after which an electron has lost half of its energy W, is, regardless of the initial value of W, given by

$$n = \frac{\ln(0.5)}{\ln\left(1 - \frac{4m_c M}{(m_c + M)^2}\right)} \, . \tag{2.45}$$

For water with $m_c = 9.1 \cdot 10^{-31}$ kg and $M = 3.0 \cdot 10^{-26}$ kg, more than 5700 collisions are necessary until the electron is in energy equilibrium with the molecule. The average time between the collision of a free electron and molecules is $\tau_{coll} = 1.6$ fs (section 4.3.2) and the temperature rise T of the medium is thus delayed by a time

$$\tau_{therm} = n \tau_{coll} \tag{2.46}$$

with regard to the energy deposition into the electronic system by the irradiance I. For water, the thermalization time is in the order of $\tau_{therm} = 10$ ps. It is thus obvious that thermal ionization will play a significant role only for laser pulse durations larger than a few picoseconds.

Temperature diffusion

When laser pulses are focused at large numerical aperture, the focal volume may be well below 1 μm³, and heat diffusion out of the volume plays a significant role on time scales as short as a few nanoseconds [Vog05]. Analog to the diffusion of free electrons out of the focal volume (Eq.(2.15)), we assume a characteristic diffusion length Λ for heat diffusion, with

$$\frac{1}{\Lambda^2} = \left(\frac{24}{d^2} + \frac{8}{l^2}\right)\frac{1}{k} \, . \tag{2.47}$$

Here d and l are the focus diameter and length given by equations (2.13) and (2.14), and $1/\sqrt{k}$ is the factor by which the free electron distribution is smaller than the focal irradiance distribution. Considering that the liquid surrounding the focus is not significantly heated during the laser pulse, we assume a constant temperature T_0 for the liquid in the vicinity of the focus which facilitates the calculation of heat diffusion. The temperature change by heat diffusion is then given by

$$\left(\frac{dT}{dt}\right)_{diff} = -\frac{\lambda_c}{\Lambda^2}\frac{1}{c_p \rho_0}(T - T_0) = -\frac{\lambda_c}{c_p \rho_0}(T - T_0) \times \left[\frac{24}{d^2} + \frac{8}{l^2}\right]\frac{1}{k} \, , \tag{2.48}$$

where T is the peak temperature in the focal volume, λ_c the heat conductivity, c_p the specific heat capacity and ρ_0 the density of water.

In cases of very strong linear absorption for which the optical penetration depth $1/\mu_a$ is smaller than the focal length l, we use $1/\mu_a$ instead of l for the calculation of heat diffusion.

Heating through collision losses during impact ionization

The temperature increase due to the collision losses during cascade ionization can be obtained by evaluating the second term in equation (2.11) [Noa99]. In the frame work of the present formalisms, the temperature increase is given by

$$\left(\frac{dT}{dt}\right)_{coll} = \frac{1}{c_p \rho_0}\frac{5}{4}E_{gap}\beta_{casc}(\rho - \rho_{therm}) = \frac{5}{4}E_{gap}\frac{\rho_{bound}}{c\rho_0}\beta_{casc}(R - R_{therm}) \, . \tag{2.49}$$

Heating through recombination

If the recombination is mostly a non radiative process, the released energy heats the focal volume and the temperature change is given by

$$\left(\frac{dT}{dt}\right)_{rec} = \frac{1}{c_p\rho_0}\frac{5}{4}E_{gap}\,\eta_{rec}\,(\rho - \rho_{therm})^2 = \frac{\rho^2_{bound}}{c_p\rho_0}\frac{5}{4}E_{gap}\,\eta_{rec}\,(R - R_{therm})^2 \qquad (2.50)$$

Temperature evolution

To describe the temperature evolution in the focal volume, we need to consider that the heating of the liquid by energy transfer from free or excited electrons is not an instantaneous process. The energy of the electrons is released stepwise through collisions with molecules. To model this process, we divide the release of electron energy in two steps. First, the energy is transferred to a virtual energy reservoir from which it is then, after a certain time given by its collision frequency, converted into an increase of the equilibrium temperature of the medium. The time delay is described by equation (2.46). The entire energy transfer process is modeled by two coupled differential equations:

$$\left(\frac{dT}{dt}\right) = \left(\frac{dT}{dt}\right)_{diff} + \left(\frac{dT}{dt}\right)_{delayed}, \qquad (2.51)$$

and

$$\left(\frac{dT}{dt}\right)_{delayed} = \left(\frac{dT}{dt}\right)_{absorb} + \left(\frac{dT}{dt}\right)_{coll} + \left(\frac{dT}{dt}\right)_{rec}. \qquad (2.52)$$

The terms in equations (2.51) and (2.52) can be reformulated and rearranged using equations (2.43), (2.48), (2.49), and (2.50). We obtain

$$\left(\frac{dT}{dt}\right) = B(T - T_0) + ET_{delayed}, \qquad (2.53)$$

and

$$\left(\frac{dT}{dt}\right)_{delayed} = AI + C(R - R_{therm}) + D(R - R_{therm})^2 - ET_{delayed}, \qquad (2.54)$$

with

$$A = \frac{2}{lc_p\rho_0}\left[1 - \exp\left(-\frac{\mu_a l}{2}\right)\right], \quad B = -\frac{\lambda_c}{c_p\rho_0}\times\left[\frac{24}{d^2} + \frac{8}{l^2}\right],$$

$$C = \frac{\rho_{bound}E_{gap}}{2c_p\rho_0}\beta_{casc}, \qquad D = \frac{\rho_{bound}E_{gap}}{2c_p\rho_0}\alpha_{rec},$$

and

$$E = \frac{\ln\left(1 - \frac{4m_c M}{(m_c + M)^2}\right)}{\ln(0.5)\cdot\tau_{coll}}, \quad \text{with } \tau_{coll} = 1.6 \text{ fs.}$$

2.1.4.2.3 Implementation of thermal ionization into the rate equation

The temperature increase described by (2.53) and (2.54) may result in thermal ionization. As derived in section 2.1.4.1, the total number of thermally ionized electrons at a certain temperature T is

$$\rho_{therm} = \rho_{bound} \frac{3 \cdot \sqrt{\frac{\pi}{2}} \left(\frac{kT}{E_{gap}}\right)^{\frac{3}{2}} \cdot \exp\left(-\frac{E_{gap}}{2kT}\right)}{1 + 3 \cdot \sqrt{\frac{\pi}{2}} \left(\frac{kT}{E_{gap}}\right)^{\frac{3}{2}} \cdot \exp\left(-\frac{E_{gap}}{2kT}\right)} . \tag{2.55}$$

To obtain the rate of thermal ionization, we have to calculate the temporal derivative of (2.55):

$$\frac{\partial}{\partial t}\left(\frac{\rho_{therm}}{\rho_{Bound}}\right) = \frac{\partial}{\partial T}\left(\frac{\rho_{therm}}{\rho_{Bound}}\right)\frac{\partial T}{\partial t} = \frac{\partial T}{\partial t} \frac{\left(\frac{3k}{E_{gap}} + \frac{1}{T}\right)\frac{3}{2}\sqrt{\frac{\pi}{2}}\left(\frac{kT}{E_{gap}}\right)^{\frac{1}{2}}\exp\left(-\frac{E_{gap}}{2kT}\right)}{\left[1 + 3 \cdot \sqrt{\frac{\pi}{2}}\left(\frac{kT}{E_{gap}}\right)^{\frac{3}{2}} \cdot \exp\left(-\frac{E_{gap}}{2kT}\right)\right]^2} . \tag{2.56}$$

By implementing this term into the rate equation (2.37) describing the entire breakdown process, we obtain

$$\frac{dR}{dt} = \left(\frac{dR}{dt}\right)_{photo} + \left(\frac{dR}{dt}\right)_{casc} - \eta_{diff}\left(R - R_{therm}\right) - \alpha_{rec}\left(R - R_{therm}\right)^2 + \left(\frac{\partial R}{\partial t}\right)_{therm}, \tag{2.57}$$

with

$$\left(\frac{\partial R}{\partial t}\right)_{therm} = \frac{\partial T}{\partial t} \frac{\left(\frac{3k}{E_{gap}} + \frac{1}{T}\right)\frac{3}{2}\sqrt{\frac{\pi}{2}}\left(\frac{kT}{E_{gap}}\right)^{\frac{1}{2}}\exp\left(-\frac{E_{gap}}{2kT}\right)}{\left[1 + 3 \cdot \sqrt{\frac{\pi}{2}}\left(\frac{kT}{E_{gap}}\right)^{\frac{3}{2}} \cdot \exp\left(-\frac{E_{gap}}{2kT}\right)\right]^2} . \tag{2.58}$$

As described above, $(dR/dt)_{photo}$ is calculated using the full Keldysh model according to Eq. (2.8) when the Keldysh parameter γ is smaller than 10, and using Kennedy's multiphoton approximation (Eqs. (2.38) and (2.39)) for $\gamma \geq 10$. The cascade ionization rate is calculated using Eq. (2.40), and the diffusion coefficient η_{diff} and recombination coefficient α_{rec} are described by Eqs. (2.41) and (2.42), respectively.

The heating rate $\partial T/\partial t$ is given by equations (2.53) and (2.54). Both thermally ionized electrons and multiphoton-ionized electrons can act as start electrons for the cascade.

Input parameters for the calculations that can be selected by the user are:

Optical parameters: laser pulse duration τ_L, wavelength λ, numerical aperture NA, linear absorption coefficient μ_a and refractive index n of the medium,

Material parameters: band gap ΔE, electron phonon collision time τ, bound electron density, mass density, heat capacity, heat conductivity, mass density, molecular mass.

Breakdown parameters: initial free electron density ρ_{ini} created by photoionization after which the avalanche term is considered, critical free electron density ρ_{cr} or temperature T_{cr} used as breakdown criterion.

To get more detail about the contributions of the different ionization mechanisms to the optical breakdown process, the contributions of multiphoton ionization, $\rho_{mp}(t)$, and thermal ionization, $\rho_{therm}(t)$, are calculated separately besides the total free electron density $\rho(t)$. To keep accurate trace of $\rho_{mp}(t)$, one has to consider that the losses by collision, recombination and electron diffusion do not only affect cascade ionization but also apply to free electrons that were created by multiphoton ionization.

2.2. Plasma growth and shielding above the breakdown threshold

At the breakdown threshold, plasma formation is restricted to the focal region of the laser beam. By contrast when the laser beam provides energy in excess of the breakdown threshold and is focused within a transparent medium, the plasma formation is characterized by a growth of the plasma from the beam waist towards the incoming laser beam as illustrated in **Fig. 2.6**. Almost no plasma develops behind the laser focus as most of the laser light is already absorbed prior to and in the beam waist. Thus the region behind the focus is 'shielded' by the plasma absorption [Doc88a, Doc88b, Vog96b, Nah96].
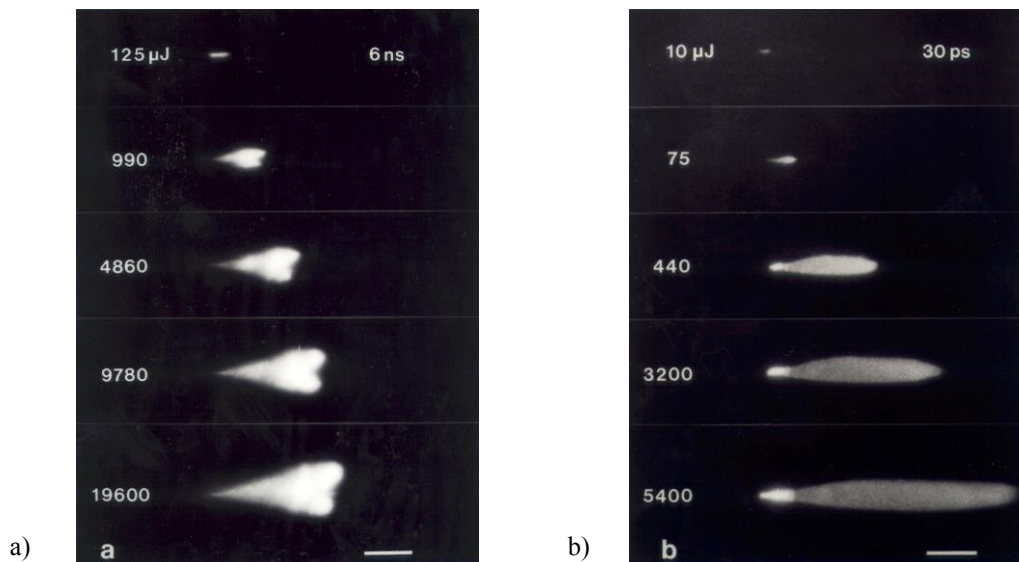
Figure 2.6 Plasma shape for different pulse energies above the optical breakdown threshold: (a) for 6 ns pulse duration, (b) for 30 ps pulse duration (from [Vog96b]). The plasmas were produced with Nd:YAG laser pulses at 1064 nm wavelength, using a focusing angle of 22°. The pulse energies are indicated in the frames. The laser light is incident from the right. The scale bar represents a length of 100 μm.

The expansion of plasmas in gases has been interpreted as a radiation driven detonation wave [Ram64, Dai67]. After plasma is first formed at the beam waist, a shock wave develops which compresses the surrounding medium and partially ionizes it within the shock front. The resulting free electrons cause increased absorption of the light and, thereby, the formation of more plasma. The advance of the plasma front, in turn, drives the shock front. This model can provide a correct description for plasma formation in gases by nanosecond pulses, where high shock speeds are attained, along with high temperatures in the shock front [Rai66], but it breaks down for short pulse durations, when the velocity of the plasma front exceeds the shock velocity. It is entirely unsuitable for describing the plasma growth in liquids. This failure can be illustrated by the example of plasma formation in water by a 10 mJ, 6 ns Nd:YAG laser pulse (Fig. 2.6a, 4th frame from top). Here, the plasma expansion creates a shock front in the water with a shock pressure at the plasma boundary of about 7000 MPa [Vog96a]. This corresponds to a temperature rise at the shock front of about 350 K [Duv63], which is far too low to cause significant ionization. In addition, the shock speed near the plasma is only 4.5 km/s [Vog96a]. This is much lower than the experimentally observed average plasma front velocities, which lay between 12 km/s and 76000 km/s, depending on the focusing angle and pulse duration [Vog96b].

A realistic explanation for the expansion of the plasma is provided by the 'moving breakdown' model originally proposed by Raizer [Rai65] and further refined by Docchio and coworkers [Doc88a]. In this model, it is assumed that optical breakdown is independent of the preceding plasma formation and occurs at all locations where the irradiation exceeds the breakdown threshold. As the power increases during the laser pulse, the plasma front moves along the optical axis at the same velocity as the location where the breakdown threshold is exceeded. This process is illustrated in **Fig. 2.7**. The model can explain the high plasma front velocities observed experimentally and, therefore, will serve as a basis for interpreting our following experimental results.

The original moving breakdown model was based on a conical shape of the laser beam and a triangular pulse shape with a linear rise in the laser power [Rai65]. This yielded a constant plasma front velocity during the rising portion of the laser pulse, contrary to experimental observations with a streak camera [Ram64, Dai67]. Docchio applied the concept of a moving breakdown front to pulses with a Gaussian time variation and took the shape of the beam waist of the laser focus into account, assuming a Gaussian beam cross section. In this way, he obtained substantially better agreement between predicted and measured motion of the plasma front [Doc88a].
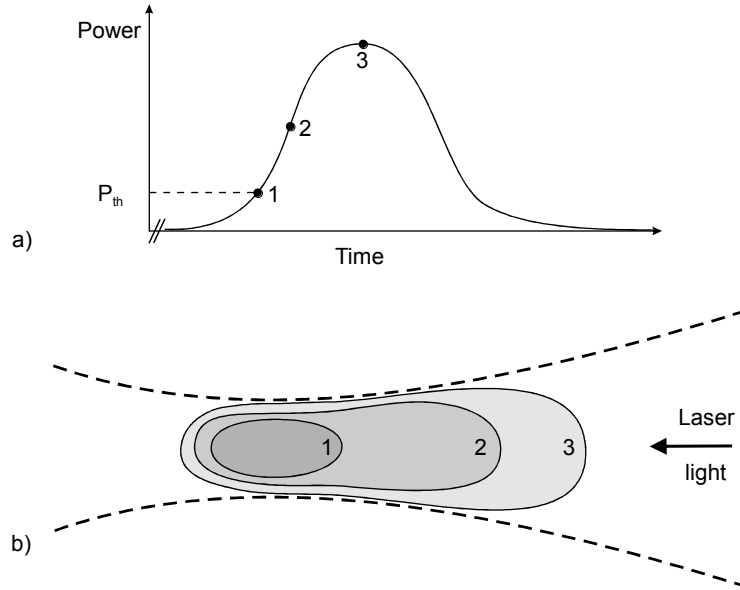
Figure 2.7 Temporal evolution of the laser power (a) and the plasma contours (b) during the optical breakdown process at superthreshold energies ("moving breakdown"). When the laser power exceeds the optical breakdown threshold P_{th}, plasma is formed in the beam waist (1). With increasing laser power, the threshold irradiance is exceeded further upstream in the incoming laser beam (2). The maximum plasma extension is reached when the laser power reaches its maximum (3). While upstream of the beam waist the plasma contours at times (1) to (3) correspond to iso-irradiance lines, this does not hold for the region behind the beam waist because of the light absorption within the plasma (plasma shielding).

The form of the moving breakdown model presented by Docchio et al. is based on a few simplifying assumptions: 1. The time for the completion of breakdown is negligibly short. 2. The breakdown threshold is independent of the laser beam diameter. 3. The breakdown threshold does not vary during the laser pulse, i.e., plasma formation during the pulse does not influence the breakdown threshold in the immediate neighborhood of the plasma. These assumptions yield the motion of the plasma front and the maximum extent of the plasma in the direction of the laser directly from the motion of the $I = I_{th}$ intensity contour during the pulse. The incident laser power is given by

$$P(t) = P_{\max} e^{-2(t/2A)^2} \tag{2.59}$$

for a Gaussian pulse with a maximum at $t = 0$, where $A = t_L / 2\sqrt{2\ln 2}$ is a measure of the laser pulse duration (FWHM) t_L. For diffraction limited focusing, where the beam cross section is also Gaussian, the intensity along the optical axis is

$$I(z,t) = \frac{P_{max}}{\pi \omega^2(z)} e^{-2 \ (t/2A)^2} \tag{2.60}$$

where

$$\omega(z) = \omega_0 \left[1 + (z/z_R)^2 \right]^{1/2}, \tag{2.61}$$

and $z_R = \pi \omega_0^2 / \lambda$ is the Rayleigh range. The peak intensity in the pulse compared to the threshold for optical breakdown is defined in terms of the dimensionless parameter $\beta = I_{max} / I_{th} = P_{max} / P_{th}$. P_{max} can thus be written in the form

$$P_{max} = \beta \pi \omega_0^2 I_{th}. \tag{2.62}$$

Setting $I(z,t) = I_{th}$ in Eq. (2.60), substituting Eqs. (2.61) and (2.62), and solving for t, we obtain the time for plasma formation as a function of position z along the optical axis,

$$t(z) = -A \sqrt{2 \ln \frac{\beta}{1 + (z/z_R)^2}}. \tag{2.63}$$

The time at which plasma formation begins in the beam waist is then given by $t_0 = t_{z=0} = -A\sqrt{2\ln \beta}$.

The inverse of Eq. (2.28) is

$$z(t) = z_R \sqrt{\beta e^{-2 \ (t/2A)^2} - 1} \ .$$
(2.64)

For *t = 0* this gives the *maximum plasma length* attained at the intensity maximum of the laser pulse,

$$z_{max} = z_R \sqrt{\beta - 1} \ .$$
(2.65)

The laser light incident on the plasma after the intensity peak of the laser pulse only heats the plasma and does not elongate it further.

Equation (2.65) also yields the *relationship between the length of the plasma and the focal angle* θ upon substituting $z_R = \pi \omega_0^2 / \lambda$ and $\omega_0 = \lambda / \pi \tan(\theta/2)$:

$$z_{max} = \frac{\lambda}{\pi \tan^2(\theta/2)} \sqrt{\beta - 1} \ .$$
(2.66)

The *dependence of the plasma length on the laser pulse duration* is only implicit in Eqs. (2.65) and (2.66). Evaluation of these dependencies requires knowledge of the threshold energy E_{th} for optical breakdown for the given pulse length. Since $\beta \equiv I_{max} / I_{th} = E / E_{th}$ for constant focal conditions, the value of β corresponding to each pulse energy can then be determined from E_{th} and, from that, z_{max} can be calculated.

Note that Eqs. (2.65) and (2.66) only give the length of the plasma from the beam waist in the direction of the laser. The actual plasma length is, as a rule, somewhat greater, for there is also some expansion of the plasma in the direction opposite the laser. Of course, this expansion is greatly limited by the high absorption of laser light in the plasma. Only when self-focusing and defocusing occur, plasma filaments develop in the region behind the laser focus.

The moving breakdown model is no longer applicable for long laser pulse durations and large focal angles, when the expansion velocity of the heated plasma volume becomes comparable to the propagation velocity of the breakdown front. For very short laser pulse durations and small focusing angles, where the spatial extent of the laser pulse is shorter than the observed plasma length, the assumptions of the model are, likewise, not satisfied. In that case, for pulse lengths under about 1 ps [Ham97, Ken97], the breakdown front moves in the propagation direction of the laser pulse. This movement will be affected in a complicated way by self-focusing and plasma defocusing, which will modify the focal region intensity distribution of Eq. (2.60) [Fen87, Vog99a, Arn05, Arn07]. However, in the present study the numerical apertures are sufficiently large to avoid nonlinear propagation effects even for femtosecond pulses. Due to the large focusing angles, the plasmas are short (see Eq. (2.66)). Therefore, the spatial extent of the laser pulse is always longer than the plasma length, and the moving breakdown model can be applied.

Based on very simple assumptions about the plasma absorption, Docchio and coworkers provided also a quantitative description of the temporal evolution and spatial distribution of the plasma shielding process, and of the resulting volumetric energy distribution [Doc88b]. It will be a challenge for future work to combine that kind of an approach with the advanced optical breakdown model of section 2.1.

We will, furthermore, see in section 5 of this report that the moving breakdown model provides reasonable predictions for $z_{\max}(\beta)$ only for femtosecond and picosecond breakdown. However, for nanosecond breakdown at large NA and pulse energies above the plasma luminescence threshold, the real plasma is an order of magnitude larger than the model prediction. Similar but not quite as extreme deviations have previously already been reported for nanosecond breakdown at moderate NAs [Vog96b]. The reason for this discrepancy is radiative energy transport from high-density plasma into regions surrounding the plasma and the laser cone angle, as will be discussed in section 5.4.

3. Experimental methods

In order to achieve reproducible laser effects and precise threshold values, we use femtosecond, picosecond and nanosecond laser pulses with smooth temporal shape and good transverse beam profile. The pulses are focused by UV-VI-IR corrected water-immersion microscope objectives built into the wall of the water cell providing a diffraction-limited focus.

Breakdown parameters determined for single-longitudinal mode (slm) nanosecond laser pulses with smooth shape are compared to the effects produced by pulses from regular laser sources exhibiting picosecond spikes due to longitudinal mode beating. All relevant laser parameters such as pulse duration, shape or spectrum, and energy are measured for each individual laser pulse, and the laser beam quality parameter M^2 is measured where appropriate.

Femtosecond- picosecond and nanosecond lasers emitting at fixed UV, visible (VIS), and IR wavelengths are used to examine R_{max} (E_L), $I_{th}(NA)$, and threshold sharpness at a grid of parameters in the (λ-τ_L) space. A femtosecond OPO and a slm nanosecond OPO are used to investigate $I_{th}(\lambda)$ for pulse durations of ≈ 265 fs in the range between 330 nm and 1100 nm at 50 individual wavelengths, and ≈ 2 ns in the range between 725 nm and 1030 nm at 21 wavelengths.

Acquisition of the large amount of data required to investigate the parameter dependencies listed above was made possible by a probe beam scattering technique for precise (10 nm accuracy) and rapid determination of the bubble size [Vog08]. The setup also enables photography of the plasma luminescence and cavitation bubbles with 1 μm spatial resolution. This capability is used to validate the probe beam scattering technique, and to investigate the plasma energy density.

The cavitation bubble energy R_{max} reflects the total amount of deposited energy but additional information is required to determine the corresponding plasma energy density and assess its temperature and pressure. We take photographs of the plasma luminescence to determine the plasma volume, and measure the plasma transmission to assess the energy absorbed in this volume. These data, together with structural details on the photographs, provide valuable information on the plasma size dependence on incident laser energy, the average plasma energy density, and hot regions within the plasma.

3.1. Laser systems

3.1.1. Femtosecond and picoseconds lasers with fixed wavelengths

Figure 1 shows the picosecon and femtosecond laser sources used for investigation of optical breakdown in aqueous media at three different fixed wavelengths (infrared, visible and ultraviolet). A Nd:YAG laser system YG 671-10 (Quantel International) is mounted on optical table 1 shown in **Fig. 3.1a**. This laser system is able to generate either nanosecond or picosecond laser pulses with a fundamental wavelength of 1064 nm and a repetition rate of 10 Hz. The nanosecond oscillator produces unseeded 8-ns laser pulses with 210 mJ pulse energy at 1064 nm (42 mJ after frequency doubling, and 26 mJ after frequency tripling). However, we soon noticed that unseeded ns pulses exhibit intensity spikes due to longitudinal mode beating. Since we later had a ns system available that could deliver single-longitudinal mode pulses as well as unseeded pulses, all nanosecond data quoted in this report were acquired with that system, which is described in section 3.1.2.

The picosecond oscillator/amplifier system produces 30-ps pulses (TEM00) with 4 mJ pulse energy at 1064 nm. Due to the nonlinearities in frequency conversion, the pulse duration is only ≈ 24 ps at 532 nm and ≈ 18 ps at 355 nm. The energies are 700μJ at 532nm, and 400 μJ at 355nm. It is possible to select single pulses out of the 10 Hz repetition rate signal by using a fast shutter (PRONTOR magnetic).

Femtosecond laser pulses are generated by the Yb:glass laser system IC-1045-30-fs Reg Amp/SHG/THG (High Q Laser Production) mounted on optical table 3 (**Fig. 3.1b**). This laser system delivers amplified pulses with a length of 350 fs, a center wavelength of 1040 nm, and 45 μJ pulse energy at 1 kHz repetition rate. Frequency doubling and tripling create pulses with 520 nm center wavelength, 306 fs duration, 21 μJ energy, and 347 nm center wavelength, 280 fs duration and 2,5 μJ energy, respectively. With a special combination of two fast shutters (Uniblitz electronics), single pulses can be selected out of the 1 kHz repetition rate signal. The oscillator leakage is suppressed by means of an external Pockels cell (Linos LM0202P).

For the measurements of the optical breakdown threshold, a precise energy adjustment of the pump beam is required. This goal is achieved by using combinations of λ/2 plates and thin film polarizers, the transmission of which depends on the polarization angle of the incident light. A rotation of the λ/2 plate causes an attenuation of

the transmitted laser beam. The λ/2 plates and thin film polarizers are wavelength-specific and for our experiments is a strong attenuation required (i.e. ps pulses from mJ down to several nJ). Therefore, we have integrated six different combinations of λ/2 plates and thin film polarizers in the experimental setup. The units are mounted on flip holders. This way they can be moved into the beam path without further adjustment whenever an attenuation of the laser irradiation is necessary. The energy of the laser pulses is measured by diverting a part of the pump beam onto an energy meter (Ophir PD10-pJ).

Laser pulses from table 1 and table 3 are combined on table 2 and directed into the setup for the investigation of the optical breakdown events. This setup is similar for all pulse durations and laser types investigated and will be described in section 3.2.
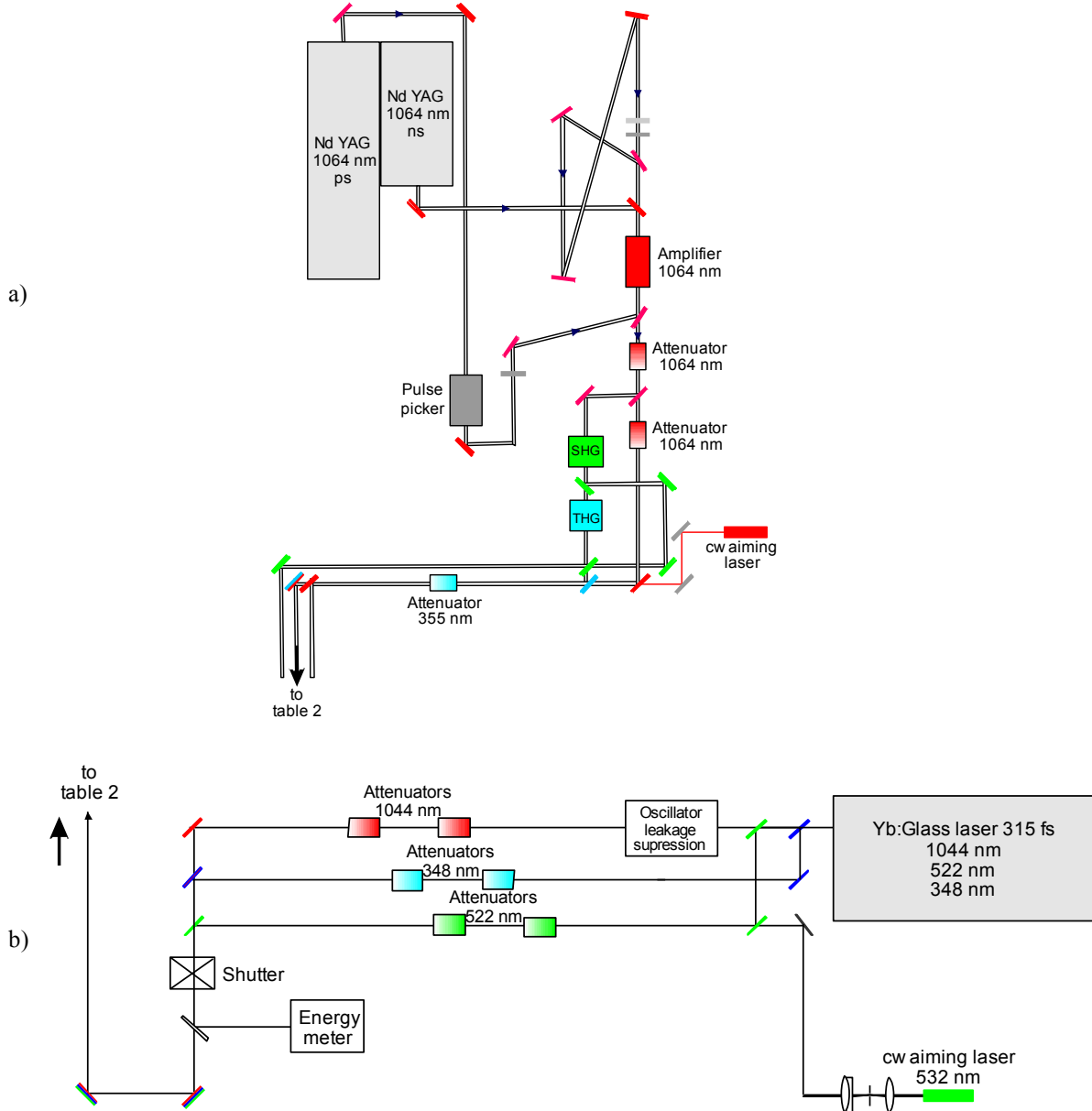
Figure 3.1 Experimental setup for the investigation of laser induced optical breakdown in water generated by laser pulses with wavelengths between 1064 nm and 348 nm and pulse durations of 8 ns, 30 ps, and 350 fs. (a) Table 1 with Nd:YAG ns- and ps- laser systems, frequency doubling, frequency tripling and controls for irradiation parameters. Table 2 (described in section 3.2) contains the setup for the investigation of breakdown thresholds, cavitation bubble size, and time-resolved photography of the laser-induced phenomena. (b) Table 3 with Yb:glass fs laser system including frequency doubling and frequency tripling, controls for irradiation parameters (attenuators, shutters, leakage suppression).

3.1.2. Seeded/non-seeded nanosecond laser

We acquired a Quanta-Ray Nd:YAG nanosecond laser system (Spectra Physics) with $\lambda = 1064$ nm wavelength that is switchable between seeded (single longitudinal mode) and unseeded (many longitudinal modes) operation, corresponding to either a Gaussian temporal laser pulse shape or a pulse exhibiting ps spikes. The beam from an instable resonator with "Gaussian" mirrors exhibited > 70% correlation between near-field profile and best fit to Gaussian profile, corresponding to $M^2 \approx 1.9$. This laser system was not financed by EOARD but became available through other funding sources. Beside fundamental mode operation, frequency doubling and frequency tripling was available for creating laser irradiation with $\lambda = 532$ nm and $\lambda = 355$ nm wavelength. The knowledge of the temporal pulse shape of the laser pulse (pulse duration, number and amplitude of the ps-spikes) is essential for the understanding of the physical effects underlying optical breakdown, and for a meaningful comparison between the results of experiments and numerical calculations.

We measured the pulse shapes of unseeded and seeded laser pulses in the IR, VIS and UV with high temporal resolution, using fast photodiodes (ANTEL AR-S1 and Newport 818-BB-35) and a 3 GHz oscilloscope (Tektronix TDS 694C). Later we acquired a 6 GHz oscilloscope (Tektronix DPO 70604). The Newport photodiode has a bandwidth of 12.5 GHz but, unfortunately, the detector material is InGaAs and it is only possible to detect the IR wavelength. The Antel photodiode has a rise time below 100 ps and is, thus, a little slower than the Newport photodiode. However, the detector material (silicon) allows to measure all three wavelengths. To compare the signals of both photodiodes, we measured an unseeded IR laser pulse simultaneously with the Newport and the Antel photodiode. The signals were almost identical, indicating that the temporal resolution in our setup is limited by the oscilloscope and not by the photodetectors. Therefore, we decided to record the pulse shapes for all wavelengths using the Antel photodiode. The temporal pulse shape of seeded and unseeded laser pulses with IR, VIS and UV wavelength is shown in **Fig. 3.2**.
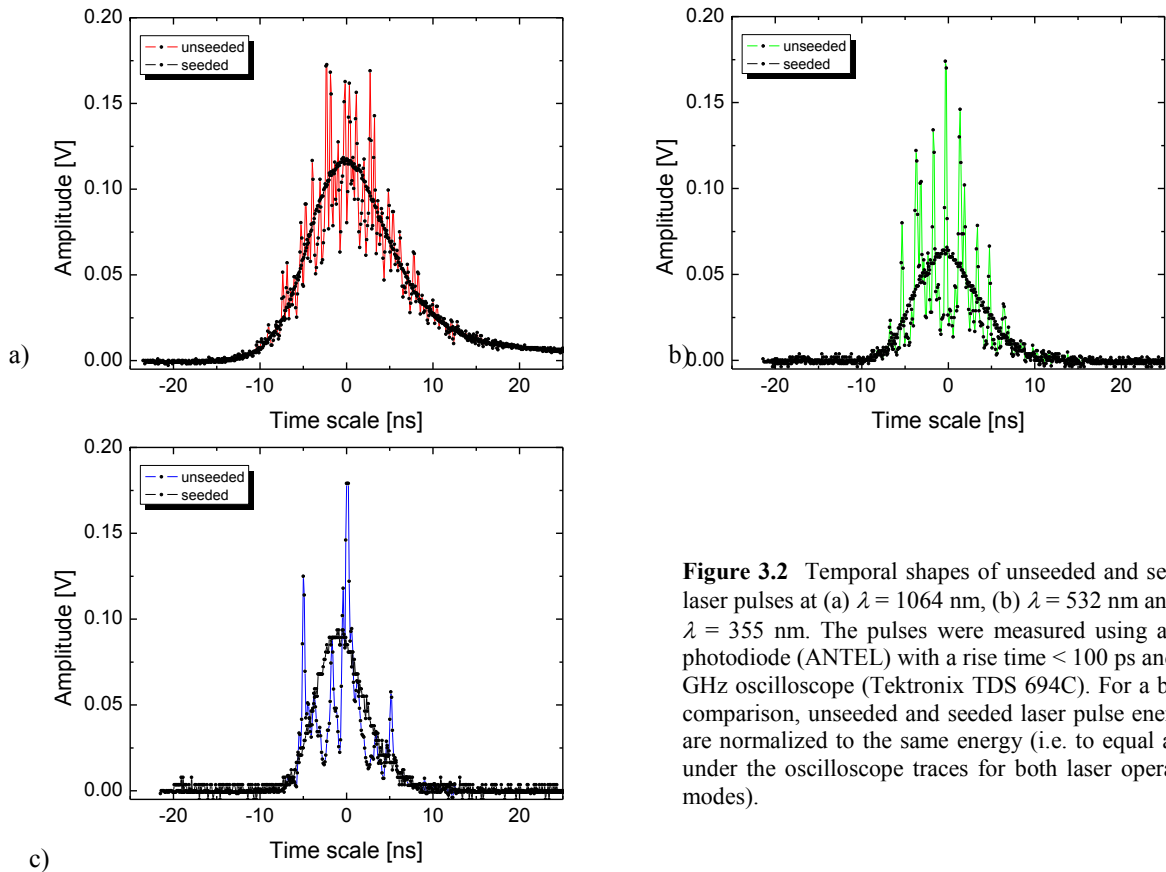
Figure 3.2 Temporal shapes of unseeded and seeded laser pulses at (a) $\lambda = 1064$ nm, (b) $\lambda = 532$ nm and (c) $\lambda = 355$ nm. The pulses were measured using a fast photodiode (ANTEL) with a rise time < 100 ps and a 3 GHz oscilloscope (Tektronix TDS 694C). For a better comparison, unseeded and seeded laser pulse energies are normalized to the same energy (i.e. to equal areas under the oscilloscope traces for both laser operation modes).

The temporal pulse shape of each seeded and unseeded laser pulse in Fig. 3.2 is an example out of a measurement series of six single shots for each wavelength and laser mode. We normalized the pulse energy of unseeded and seeded laser pulses to compare the ratio of the maximum amplitude in the unseeded mode to the maximum amplitude in the seeded mode. This ratio is a measure for the possible influence of the ps-spikes in the unseeded mode in comparison to the Gaussian pulse shape in the seeded mode. Furthermore, we fitted the experimental data with a Gaussian function to determine the FWHM pulse duration.

The results are shown in figure 3.3 and summarized in **Table 3.1**. In the unseeded laser mode, the number of ps-spikes decreases with decreasing wavelength and the relative amplitude is larger for UV and VIS than for IR. This is due to the nonlinearity of the frequency conversion process. This nonlinearity leads, furthermore, to a decrease of the pulse duration (FWHM) from 11.15 ns for IR, through 8.76 ns for VIS to 6.77 ns for UV. Interestingly, a Gaussian fit yielded the same pulse durations for the seeded and unseeded modes. Nevertheless, the UV unseeded laser pulse is more a sequence of ps pulses rather than one ns laser pulse.
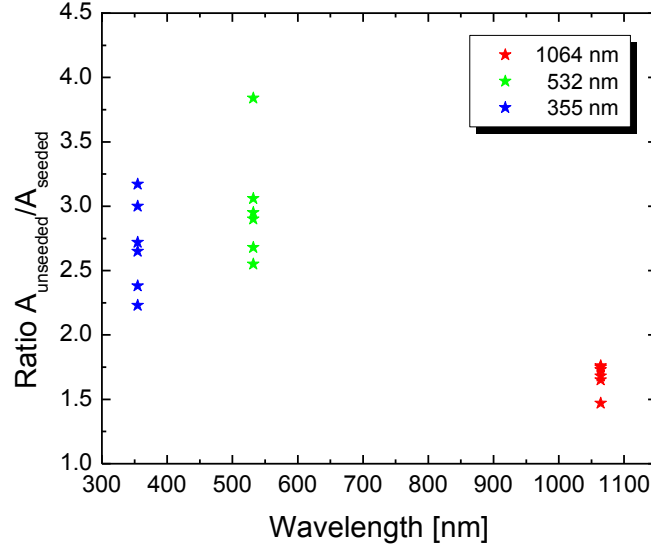
Figure 3.3 Ratio of the maximum amplitude of unseeded and seeded laser pulses evaluated from the measurements shown in figure 3.2. Both the magnitude and the scattering of the ratio are stronger for UV and VIS than for IR due to the nonlinear process of second harmonic and third harmonic generation.

λ [nm]	τ (FWHM) [ns]	$\Delta\tau$ [ns]	# spikes	Ratio A_{us}/A_s
1064	11.15	0.09	34	1.7
532	8.76	0.11	24	3.0
355	6.77	0.12	15	2.7

Table 3.1 Pulse duration, number of spikes in the unseeded laser mode, and ratio of the maximum amplitude of unseeded and seeded laser pulses evaluated from the measurements shown in figure 3.3 for the different wavelengths.

The temporal pulse shape of ns laser pulses has previously not been studied with similarly temporal resolution. The spikes that originate from longitudinal mode-beating in every unseeded laser system have influenced the results in almost all investigations of ns-laser induced breakdown performed in the past but were hardly ever considered. Even though authors were aware about the importance of the spatio-temporal structure of the laser irradiation (see, for example, the reviews by Bloembergen, 1974 [Blo74], and Smith & Meyerand, 1976 [Smi76]), attention was mainly focused on the transverse beam profile, and the temporal shape of the ns laser pulses was rarely discussed. One exception is the study by Glebov and coworkers [Gle84] who pointed out that the temporal pulse shape of ns laser pulses strongly influences the threshold sharpness. However, this study was performed only for the fundamental Nd:YAG laser wavelength, and the irregular laser pulse shape was not measured directly but deduced from measurements using a Fabry Perot interferometer.

The use of slm laser pulses involves the risk of another source of error if small focusing angles are used. Brewer and Rieckhoff showed in 1964 [Bre64] that focusing of a slm Q-switched ruby laser pulse in water results in stimulated Brillouin scattering (SBS). Glebov et al. [Gle84] reported that a considerable fraction of the incident laser light is reflected by SBS before it reaches the laser focus. This results in enormously large values for the optical breakdown threshold if the light reflection is not appropriately considered. A convenient way to circumvent this problem is the use of large focusing angles corresponding to a very short interaction length in which SBS could occur. In our study, large NAs are employed anyway to avoid disturbance of the optical breakdown process by nonlinear beam propagation effects and to match the conditions for cell surgery. Therefore, SBS is not a matter of concern.

3.1.3. Microchip lasers

Using temporally smooth laser pulses at VIS and UV wavelengths as emitted by the seeded ns laser system described in 3.1.2, we found two separate thresholds for the formation of minute bubbles and bright luminescent plasmas (BPL), as will be presented in section 4.2. The low-density plasma regime between bubble formation and BPL threshold enables to create fine laser effects that can be utilized for cell surgery, and nano-morphing of materials. Unfortunately, seeded Nd:YAG ns laser system are relatively complex and expensive devices. However, we discovered that cost-effective microchip lasers also emit smooth laser pulses because they can work in single mode operation. Therefore, we investigated the optical breakdown dynamics produced by microchip lasers with pulse durations between 0.5 and 1 ns for IR, VIS and UV wavelengths.

Pulses with ≈ 1 ns duration were produced by a Crylas microchip laser. The temporal pulse shape of the microchip laser pulses with IR, VIS and UV wavelength is shown in **Fig. 3.4**. The laser pulses have a smooth temporal shape with pulse durations of approximately 1 ns. The exact pulse durations are listed in **Table 3.2**.

The smooth temporal shape of the microchip laser pulses differs strongly from the spiking behavior exhibited by regular, unseeded Nd:YAG lasers (Fig. 3.3). The spikes originate from longitudinal mode-beating and can thus occur in every unseeded laser system. However, the spacing between the different longitudinal modes in a resonator is given by $c/(2L)$, where c is the speed of light and L the resonator length. A long resonator has many more modes under the gain curve of the laser medium than a short resonator. The resonator of regular actively Q-switched ns-laser is approximately 30 cm long whereas the Crylas microchip laser has a resonator length of only 7 mm. The shorter resonator alone does not yet provide single mode operation. However, when it is combined with passive Q-switching, the Q-switch is triggered by the strongest mode and thus acts as an additional filter that suppresses competing longitudinal modes. Hence, the large mode spacing of the microchip laser in combination with the mode selection by the passive Q-switch yields a single longitudinal mode operation without seeding. Therefore, the microchip laser is a very cheap and effective alternative to expensive, seeded single longitudinal mode laser systems, especially for industrial uses.

a)

b)

c)
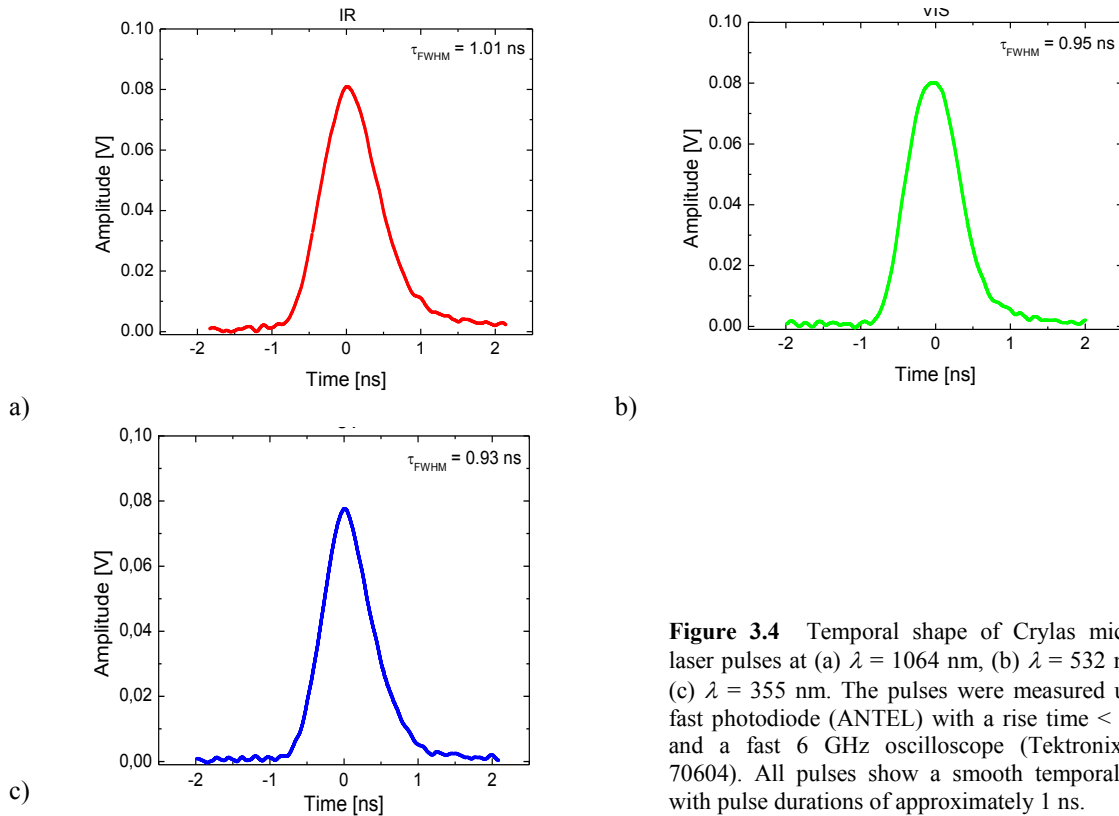
Figure 3.4 Temporal shape of Crylas microchip laser pulses at (a) λ = 1064 nm, (b) λ = 532 nm and (c) λ = 355 nm. The pulses were measured using a fast photodiode (ANTEL) with a rise time < 100 ps and a fast 6 GHz oscilloscope (Tektronix DPO 70604). All pulses show a smooth temporal shape with pulse durations of approximately 1 ns.

λ [nm]	τ (FWHM) [ns]	$\Delta\tau$ [ns]
1064	1.01	0.02
532	0.95	0.01
355	0.93	0.01

Table 3.2 Pulse duration of Crylas microchip ns laser pulses at different wavelengths.

UV laser pulses of ≈ 0.5 ns duration were generated by a Teem Photonics microchip laser (PNV-001525-140). This laser system delivers laser pulses with up to 30 µJ pulse energy at 355 nm wavelength and 10 Hz repetition rate. The laser pulses have a smooth temporal shape as shown in **Fig. 3.5**.
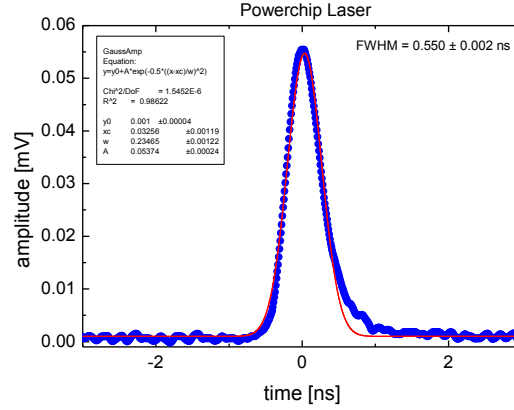

Figure 3.5 Temporal pulse shape of the UV microchip laser pulse, measured using a fast photodiode (ANTEL) with a rise time < 100 ps and a 6-GHz oscilloscope (Tektronix DPO 70604). A Gaussian function was fitted to the experimental data to obtain the exact value of the FWHM time (0.55 ns).

3.1.4. Nanosecond OPO system

The wavelength dependence $I_{th}(\lambda)$ of optical breakdown in aqueous media with ns laser pulses was investigated in the wavelength range between 725 nm and 1030 nm at 21 wavelengths. Initiation of the breakdown process by multiphoton ionization should result in a stepwise increase of the threshold irradiance, I_{th}, at wavelengths above which one more photon is required to overcome the band gap [Blo74], while extrinsic initiation should exhibit a smoother $I_{th}(\lambda)$ dependence. **Fig. 3.6** shows the single longitudinal mode optical parametric oscillator (slm OPO) employed for these measurements, and Table 3.3 summarizes it's specifications. Access to the OPO system was provided by Dr. Hannes Vogelmann and Dr. Thomas Trickl at the Institut für Meteorologie und Klimaforschung, Forschungszentrum Karlsruhe. This laboratory is located at Schneefernerhaus on top of Zugspitze, Germanys highest mountain. Measurements were performed in collaboration with Dr. Vogelmann.
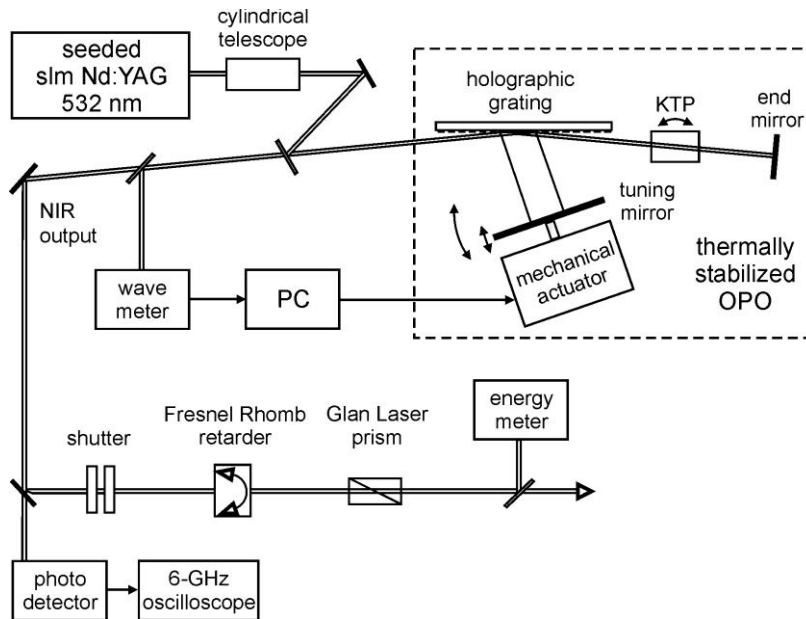
Figure 3.6 Schematic of the slm ns OPO laser system.

Pump laser	Frequency-doubled injection-seeded Nd:YAG laser
	Continuum Powerlite 8020, pulse length 7 ns, wavelength 532 nm, 20 Hz, 10 mJ
Laser oscillator	Littman OPO
Tuning range	720 nm - 1050 nm
Pulse length	1.5 ns - 3.0 ns
Pulse energy	150-500 μJ
Bandwidth	≈ 250 MHz
Long-term stability	± 5 MHz
Frequency noise	± 35 MHz
Spectral purity	> 99.9 %
Pointing stability	< 30 μrad
Beam divergence	< 0.4 mrad

Table 3.3 Specifications of the nanosecond single longitudinal-mode optical parametric oscillator (slm OPO).

The OPO is pumped by the second-harmonic output from a slm Nd:YAG laser. The thermally stabilized OPO is a modified version [Vog08] of a commercial instrument (Continuum Mirage) that is based on a short (≈ 5 cm) Littmann cavity and a KTP crystal for parametric frequency conversion [Bos93]. The vertical diameter of the 532-nm pump beam is compressed by a factor of two with a cylindrical telescope to suppress the out-of-plane modes in the OPO emission. The wavelength is actively stabilized to within ± 35 MHz by piezo-electrically adjusting the tilt angle of the tuning mirror according to the output of an interferometric wave meter (Cluster LM007). Depending on the wavelength, the OPO emits pulses of 1.5-3.0 ns duration and 0.1-0.5 mJ energy at 20 Hz repetition rate, with < 0.4 mrad beam divergence. The single-shot bandwidth of 2.0-ns-pulses is 250 MHz, which is almost Fourier-transform limited. The tuning range extends from 720 nm to 1050 nm. To achieve this broad wavelength range, two sets of optics are required, with a transition at ≈ 930 nm.

The trigger input of the Nd:YAG pump laser was used to also trigger a fast mechanical shutter controlled by a computer programmed in Labview. The shutter (Laser Imagineering, TTL shutter) was opened at a fixed time delay after the laser trigger for 40 ms to select a single pulse out of the 20 Hz pulse train. The pulse energy is adjusted by rotating a Fresnel-rhomb retarder in front of a Glan laser prism. Shape and duration of each laser pulse employed for the threshold determination are measured for each individual pulse using a fast photodiode (ANTEL AR-S1) with 100 ps rise time and an oscilloscope with 6 GHz bandwidth (Tektronix DPO 70604). **Fig. 3.7** shows examples of the temporal pulse shapes for different wavelengths.
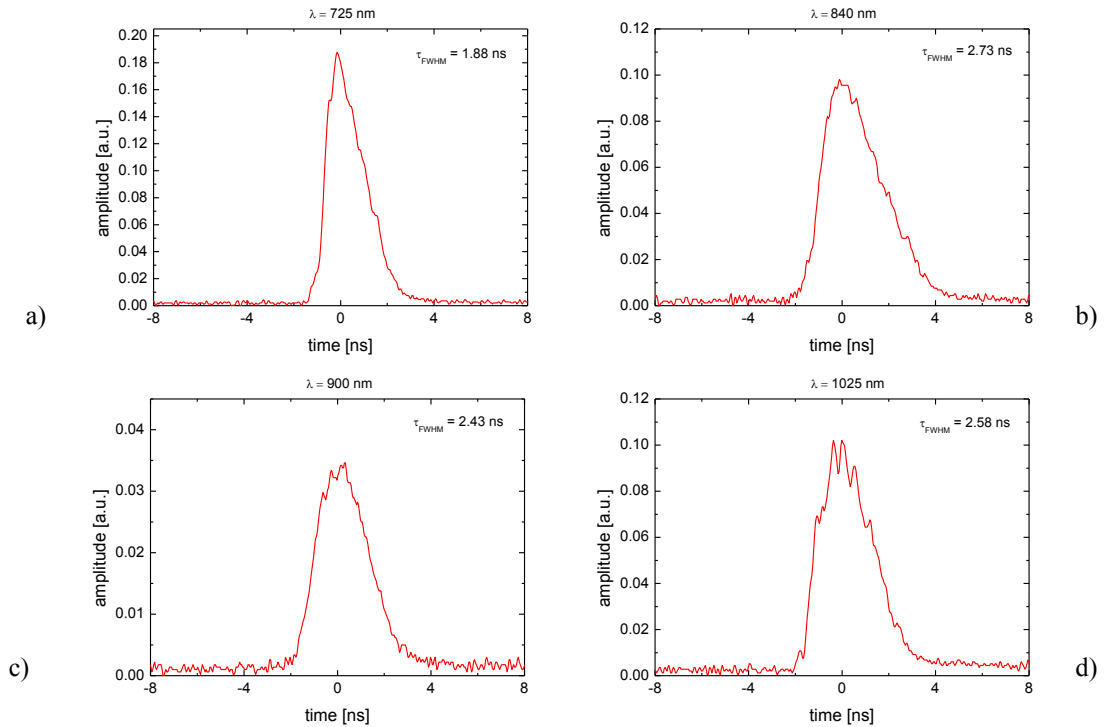
Figure 3.7 Temporal shape of single longitudinal mode OPO ns laser pulses at (a) λ = 725 nm, (b) λ = 840 nm, (c) λ = 900 nm, and (d) λ = 1025 nm.

Although the maximum pulse energy is 150 µJ, the system should be operated close to threshold if slm emission is desired. In this regime, the pulses show a nearly smooth shape with occasional small spikes on the pulse profile, as demonstrated in Fig. 3.7. The spikes are much smaller and significantly less frequent than in the case of an unseeded laser pulse exhibiting longitudinal mode beating (Fig. 3.2). Therefore, the existence of these small spikes should have only marginal influence on the optical breakdown threshold. The laser pulse duration ranged between 1.5 ns and 3.1 ns FWHM, depending on the wavelength, the quality of the alignment of the OPO, and the pump laser power. Because of these variations, we recorded the duration and shape for each pulse during the measurements for all objectives and wavelengths investigated. The averaged pulse duration for each individual measurement series with a specific wavelength and OPO adjustment was then used to calculate the respective irradiance threshold for breakdown.

Besides the temporal pulse shape, the transverse laser beam profile also influences the breakdown threshold because the beam quality influences the focal spot size. While all laser sources emitting at fixed wavelengths that were described in sections 3.1.1 – 3.1.3 have a good beam quality ($M^2 \leq 1.3$), this cannot be taken for granted for the OPO system, which has a very short resonator length to enable slm operation and must be tuned to achieve operation at different wavelengths. Therefore, we measured the beam quality factor M^2 as a function of wavelength over the entire tuning range of the OPO. The factor is defined as

$$M^2 = (\theta\, \pi\, \omega_0)/\lambda\,, \tag{3.1}$$

where θ is the half angle beam divergence, ω_0 is the beam radius at the beam waist, and λ the wavelength. A diffraction-limited beam has an M^2 factor of 1, and is a Gaussian beam.

We used a Hartman Shack Wavefront Analyzer provided by Laser-Laboratorium Göttingen e.V., Germany (www.llg.gwdg.de) that provides all beam parameters through single shot measurement. This feature is very important for pulsed laser operation with large shot-to shot fluctuations. The measurement results are presented in **Fig. 3.8**. As the beam is not circular symmetric, values in x and y direction are given together with a combined value $(M^2)^2 = M_x^2\, M_y^2$. The beam quality is optimal in the center region of the two sets of optics for the OPO and deteriorates at the borders of the range of each optics set.
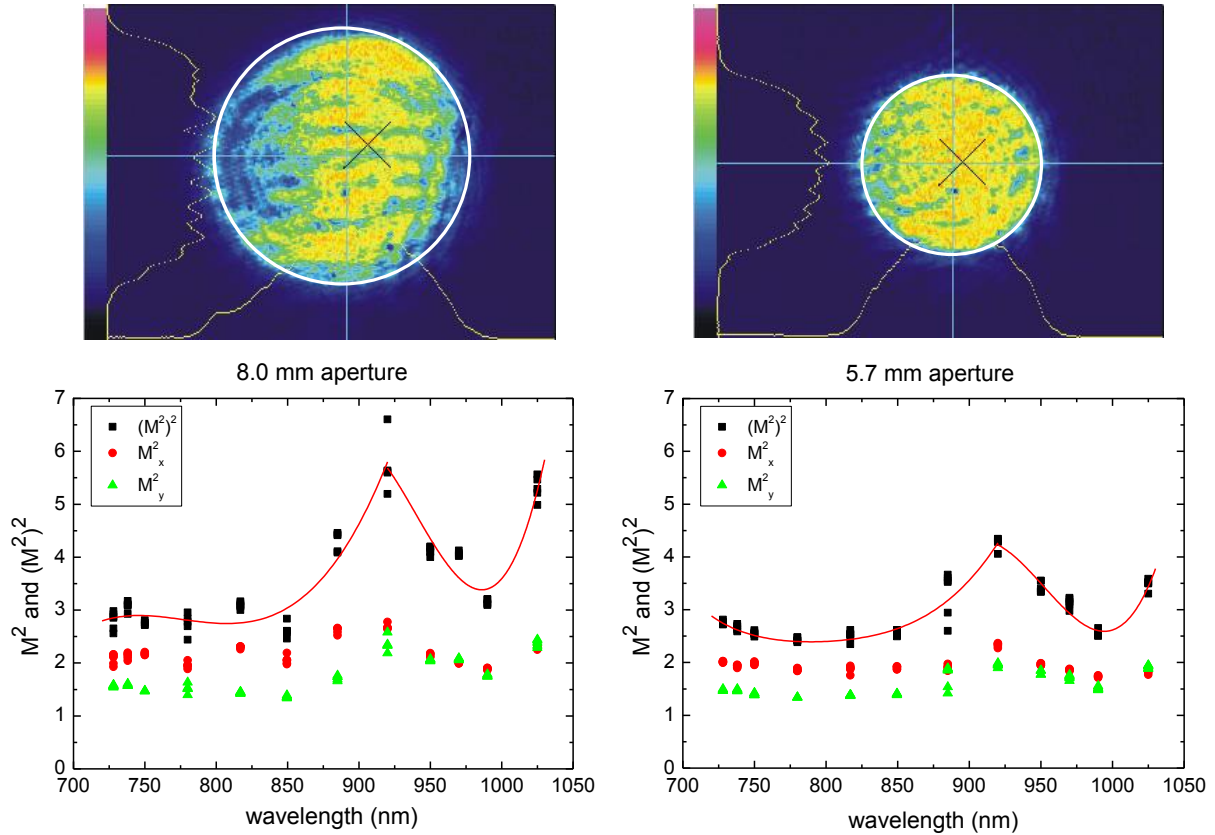
Figure 3.8 Top: CCD profiler images of the pump laser beam cross section within the effective objective aperture. Bottom: Measured beam quality parameter of the ns OPO system for various wavelengths. M^2 values in x and y direction are given together with a combined value $(M^2)^2$. Left column: results for the 40x objective (NA = 0.8) with 8 mm diameter, Right column: results for the 63x objective (NA = 0.9) with 5.7 mm diameter.

3.1.5. Femtosecond OPA system

The wavelength dependence of femtosecond optical breakdown was investigated for 50 wavelengths in the range between 330 nm to 1085 nm using a femtosecond **o**ptical **p**arametrical **a**mplifier (OPA) system. Fs laser pulses at tunable wavelength were created by a **t**raveling-wave **o**ptical **p**arametric **a**mplifier of **s**uperfluorescence (TOPAS 4/800, Light Conversion) that was pumped by a titanium sapphire fs laser (Spectra Physics Spitfire). A schematic drawing of the TOPAS system is shown in **Fig. 3.9**.
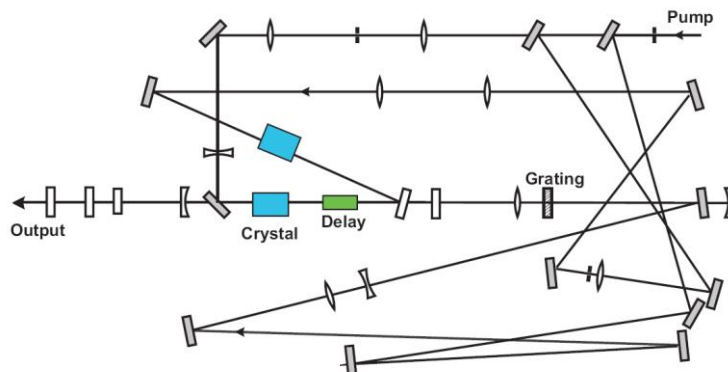
Figure 3.9 Schematic of the **t**raveling-wave **o**ptical **p**arametric **a**mplifier of super-fluorescence (TOPAS 4/800, Light Conversion) that is used to generate tunable fs laser pulses in the range from 300 nm to 1100 nm [Lig04].

The TOPAS system has to be pumped by an amplified fs laser in the wavelength range between 770 and 810 nm. Tunability is achieved by generating super-fluorescence in a BBO crystal and subsequent amplification of the signal (S) and idler (I) wave. The frequency selection is controlled by means of a grating between the amplifier stages. In the TOPAS system, super-fluorescence generation is followed by three preamplifier stages and a power amplifier. All these stages use only one nonlinear BBO crystal. A second crystal is employed to compensate the beam offset due to rotation of the nonlinear crystal that, together with the adjustment of the grating angle is used for wavelength tuning. The seed signal from the super-fluorescence generator is produced with low pump laser power, and the preamplifiers also work in a low-energy range to minimize the spectral line width and optimize the transverse beam quality. The power amplifier then uses approximately 85 % of the pump energy and is designed to achieve a high conversion efficiency in combination with a good beam quality and short duration of the generated pulses. To achieve a high pulse to pulse stability, the amplification stage is driven into saturation.

The generation of signal, idler, second-harmonic signal, second-harmonic idler, sum-frequency of pump and signal, sum-frequency of pump and idler, fourth-harmonic signal, and fourth-harmonic idler enables the TOPAS system to continuous tuning across the whole wavelength range from 300 nm to 1100 nm. Thereby, the operation of tuning the crystal and grating angle is completely computer controlled. Only the frequency mixers have to be rotated manually by the time.

The stability of the TOPAS system is largely determined by the stability of the pump laser. Because our institute owns only the TOPAS but no titanium sapphire femtosecond laser that is sufficiently powerful to pump it, we had to look for external collaboration partners. We found a powerful and stable titanium sapphire fs laser (Spectra Physics Spitfire) in the group of Kristian Werelius at the Laser Center Hannover. The Spectra Physics Spitfire system consists of a mode-locked, fs titan sapphire laser oscillator (MaiTai), a diode-pumped solid state pump laser (Empower), and a regenerative amplifier system. This laser system has a repetition rate of 1 kHz, 460 µJ pulse energy, 795 nm center wavelength, 120 fs pulse duration, and a high pulse-to-pulse stability (< 1% fluctuation). **Fig. 3.10** shows the complete fs laser OPA setup.
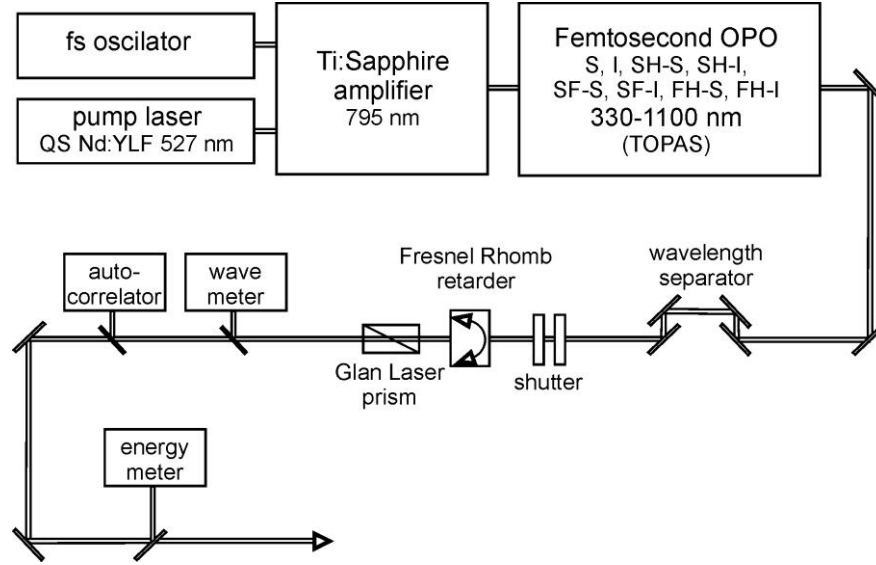
Figure 3.10 Schematic drawing of the fs laser OPA system consisting of Ti:sapphire pump laser and TOPAS.

The output of the TOPAS system is always a mixture of the target wavelength and different other wavelengths like, for example, the fundamental signal and idler wavelengths. Six different sets of four dichroic mirrors each were used to separate the target wavelength from other wavelengths over the entire tuning range. The trigger output of the Spitfire laser system was used to trigger two fast mechanical shutters (Uniblitz electronics) to select single pulses out of the 1 kHz repetition rate signal. Precise energy adjustment of the fs laser required for the measurements of the optical breakdown thresholds was achieved by a combination of a Fresnel rhomb retarder and a Glan laser prism (both Karl Lambrecht Corporation). The Fresnel rhomb retarder rotates the polarization angle of incident light regardless of wavelength, and the transmission through the Glan laser prism depends on the polarization angle of the incident light, also regardless of wavelength. A rotation of the Fresnel Rhomb retarder thus causes an attenuation of the transmitted laser beam. Additionally, spectrum and pulse duration were measured for each wavelength using a wavemeter (Ocean Optics, HR 2000), and an autocorrelator (APE pulse check).

Figure 3.11 shows the output power of the TOPAS system at 1 kHz repetition rate for all available wavelengths in the range from 285 nm to 2600 nm. In the wavelength range from 300 to 1100 nm used in our investigations, the available single pulse energies varied between 2.5 µJ and 50 µJ.
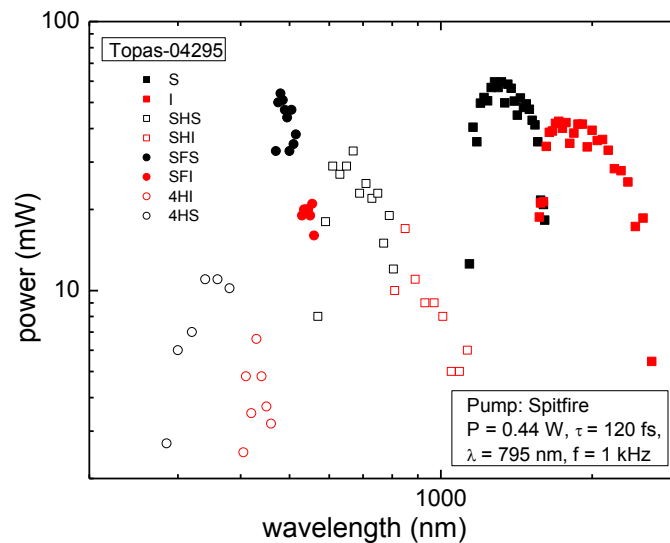
Figure 3.11 Measured output power of the TOPAS/Spitfire system at 1 kHz repetition rate for wavelengths in the range from 285 to 2600 nm.

In **Fig. 3.12** some examples of the measured autocorrelation and spectrum of the femtosecond laser pulses are presented for different wavelengths from VIS to IR. Unfortunately, we were not able to measure the auto-correlation in the UV range due to limitations in the sensitivity range of our autocorrelator.

λ= 544 nm
τ = 196 fs

λ= 799 nm
τ = 237 fs
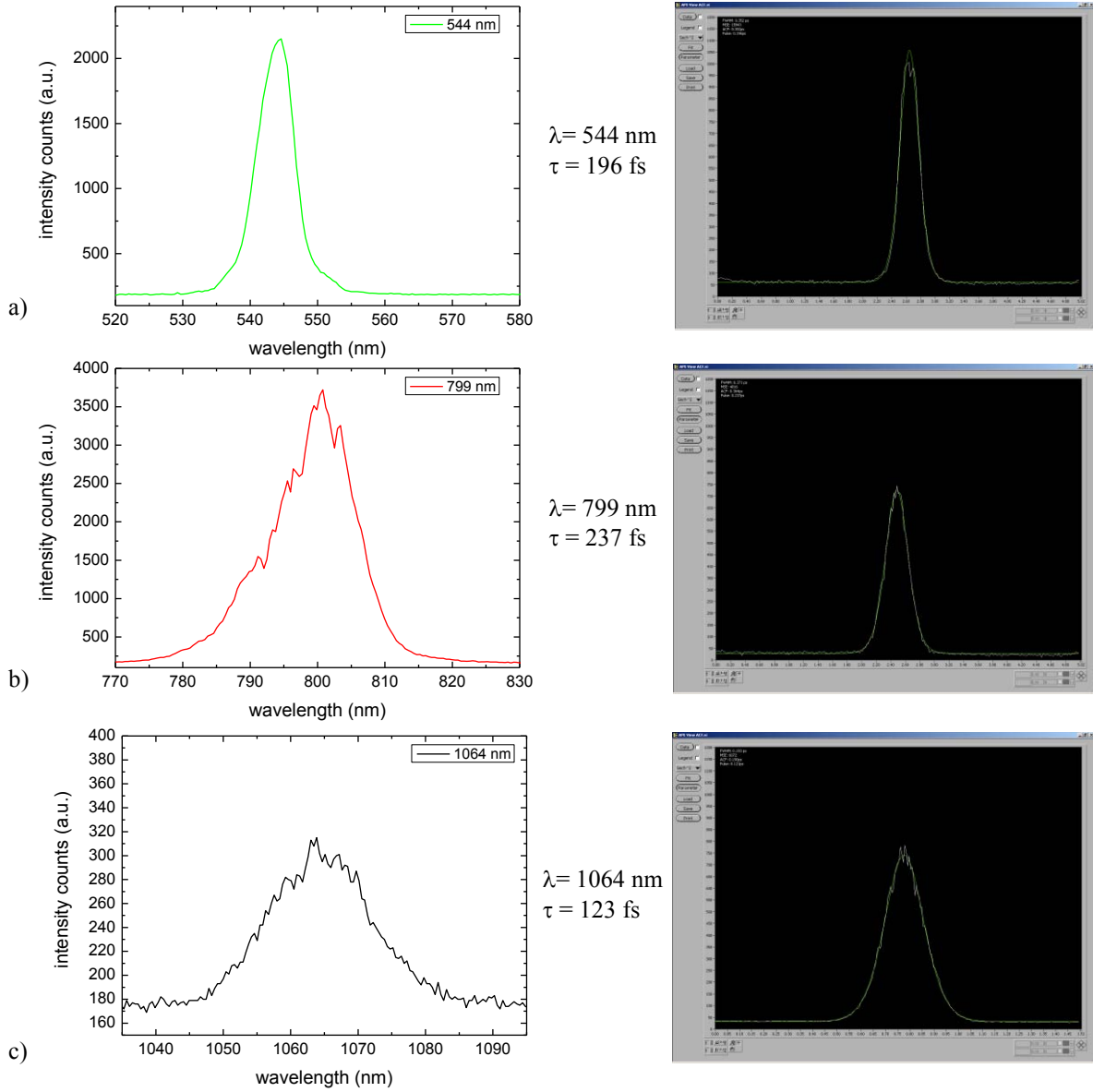
λ= 1064 nm
τ = 123 fs

Figure 3.12 Spectrum and autocorrelation of fs OPA laser pulses with center wavelengths of (a) λ = 544 nm, (b) λ = 799 nm, and (c) λ = 1064 nm.

For each individual wavelength, the output of the TOPAS system exhibited good stability with respect to pulse duration, wavelength, and beam divergence. However, the results in figure 3.12 indicate that the pulse duration strongly varies with wavelength. We attempted to avoid these fluctuations by changing the wavelength sepa-rators and the dichroic mirrors in the optical path between laser and measurement cell (see section 3.2), as well as by realignment of the TOPAS system but the fluctuations remained. It is thus unlikely that they are caused by wavelength-dependent group velocity dispersion in external optical elements but they rather seem to originate from the emission characteristics of the TOPAS itself. To account for the fluctuations, we measured spectrum and pulse duration for each wavelength and normalized the breakdown thresholds to the average value of the pulse duration for all wavelengths investigated, 265 fs, (see section 4.4.1).

3.2. Experimental setup and procedures for the investigation of optical breakdown

3.2.1. Overall description

Figure 3.13 shows the experimental setup for the measurement of the optical breakdown thresholds and the investigation of the breakdown-induced events.
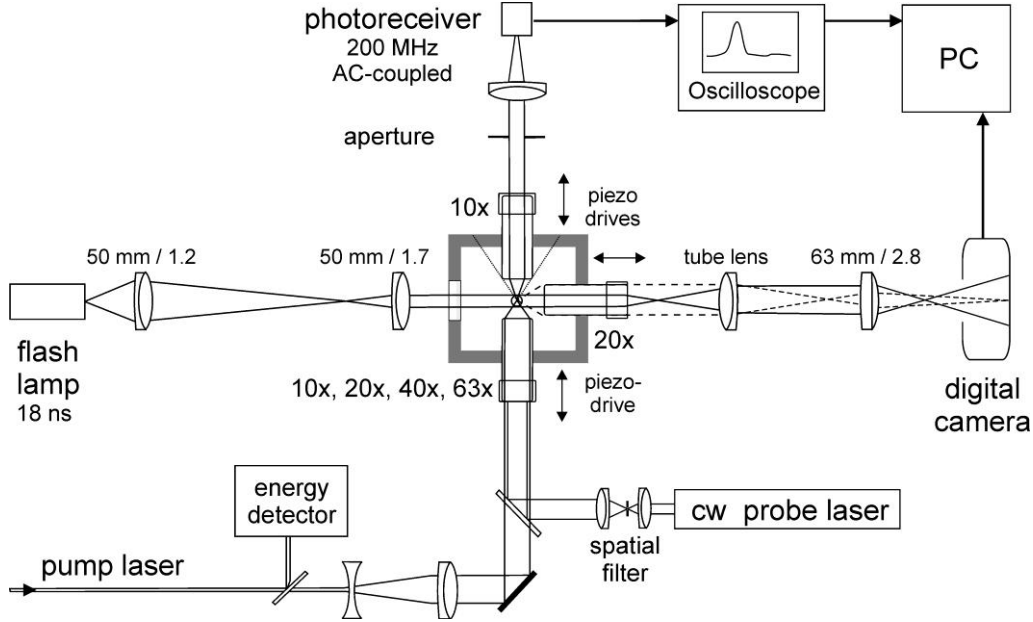
Figure 3.13 Experimental setup for the examination of laser-induced breakdown in water.

To determine femtosecond breakdown thresholds in transparent media, the laser pulses must be focused at a high NA (≥ 0.9) to avoid corruption of the results by nonlinear beam propagation altering the focal spot size [Sch01, Arn07]. For ns pulses, large NAs are important to avoid stimulated Brillouin scattering [Gle84]. Large focusing angles are difficult to realize without introducing spherical aberrations into the laser beam path that will lead to erroneous threshold values [Vog99b]. In the present study, we use water immersion microscope objectives built into the wall of a cuvette to provide diffraction-limited focusing conditions up to $NA = 0.9$.

As described in section 2.1.2, we use bubble formation as threshold criterion for optical breakdown. Close to threshold, femtosecond laser produced bubbles have a minute size below the diffraction limited resolution of the microscope objective used for bubble generation [Vog05]. To detect such small bubbles and determine their maximum radius R_{max}, we use the scattering of a continuous probe laser beam to determine the bubble oscillation time T_{osc} and deduce R_{max} from T_{osc}, which is the lifetime of the first cycle of the cavitating bubble [Vog96a, Noa98, Ven02, Hut07]. Previously, scattering techniques have been used for the analysis of single bubble sonoluminescence and the early expansion phase of fs-laser-produced bubbles [Sch02, Bar97]. The bubble dynamics was deduced from the temporal evolution of the *intensity* of the scattering signal which involved calibration problems. Since we are only interested in R_{max}, we can avoid such problems by resorting to the theoretically known relationship between R_{max} and T_{osc}. The present technique enables rapid measurements of both the bubble formation threshold and the dependence of bubble size from laser pulse energy [Vog08].

Breakdown in water is produced by focusing the laser pulses through long-distance water-immersion objectives (Leica HCX APO L U-V-I) built into the wall of a water-filled cell. We used 10x, 20x, 40x, or 63x objectives ($0.3 \leq NA \leq 0.9$) with free working distances between 3.6 mm and 2.2 mm. The rear entrance pupil of the objective is overfilled to create a uniform irradiance distribution corresponding to an Airy pattern in the focal plane [Bor70]. Single laser pulses are selected from the pulse train using a mechanical shutter. The energy of the laser pulses is measured by diverting a part of the incident laser pulse on an energy meter (Ophir PD10-pJ or Ophir PD 10, depending on energy). Precise energy adjustment of the laser pulses was for fixed laser wave-lengths achieved by combinations of λ/2 plates and thin film polarizers (see 3.1.1), or a combination of a Fresnel rhomb retarder and a Glan laser prism (see 3.1.5). As breakdown medium, we used aqua ad iniectabilia (Braun), additionally filtered with a 0,22 μm microfilter (Millipore) to avoid undesirable impurities in water.

To monitor bubble formation, a spatially filtered cw probe laser beam (CrystaLaser, 658 nm, 40 mW) is adjusted collinear and confocal with the fs beam. The transmitted probe light is collected by a 10x, $NA = 0.3$ water immersion objective and imaged onto an AC-coupled amplified photoreceiver (FEMTO, 25 kHz – 200 MHz bandwidth) that is protected from the fs laser irradiation by blocking filters. When the bubble is much smaller than the focal diameter, its scattering signal is considerably weaker than the total amount of transmitted light. The AC-coupling removes this bias and makes it possible to detect bubbles with only 15 ns oscillation time and 150 nm maximum radius with ± 10 nm accuracy.

To validate the scattering technique, larger bubbles are imaged with 1 μm optical resolution by a digital camera using a 20x, $NA = 0.5$ objective oriented perpendicular to the pump and probe beam axes. The object space is illuminated in Köhler technique using a plasma discharge lamp with 18 ns pulse duration (Nanolite KL-L, High Speed Photosystems). The image produced by the microscope objective and the tube lens was further magnified using a Nikkor objective (63mm/1:2.8) that is corrected for 8x magnification. This way, we achieved a total magnification factor of $M \approx 160$. Images were recorded by a digital camera connected to a PC (Fuji Film FinePix S1 Pro camera, or, at later stages of the project, Canon EOS 5D). The same imaging system can be readily modified into a Schlieren system for the visualization of laser-induced refractive index changes and shock wave emission [Vog06].

Simple open shutter photography in side view is used to record time-integrated images of the plasma luminescence (see section 3.2.6). For measurements of the plasma transmission, the photo receiver is replaced by an energy meter, and the 63x objective (NA = 0.9) is used to collect the transmitted laser light (section 3.2.7).

Initially, the ceramic coating of the objectives prohibited a confocal adjustment of objectives with a magnification larger than 20 x. Therefore, in cooperation with Leica, we removed the ceramic coatings from the objectives, sealed them to avoid intrusion of water and protected them with a self-built stainless steel cover to avoid mechanical damage during our measurements. Our mechanical workshop built a cuvette made of polyoxymethylene (POM) with openings fitted to the diameter of the Leica objectives (**Fig. 3.14**). This cuvette was water tight without any further sealing. Confocal adjustment of all objectives can now be achieved, when the 40x objective ($NA = 0.8$) is used to focus the fs-pulses but not with the 63x objective ($NA = 0.9$) because in the latter case the working distances of 2,2 mm is too short. Because the orthogonal confocal adjustment of the microscope objectives is critical for imaging in side view, the positions of the objectives can be controlled by piezo-driven devices.
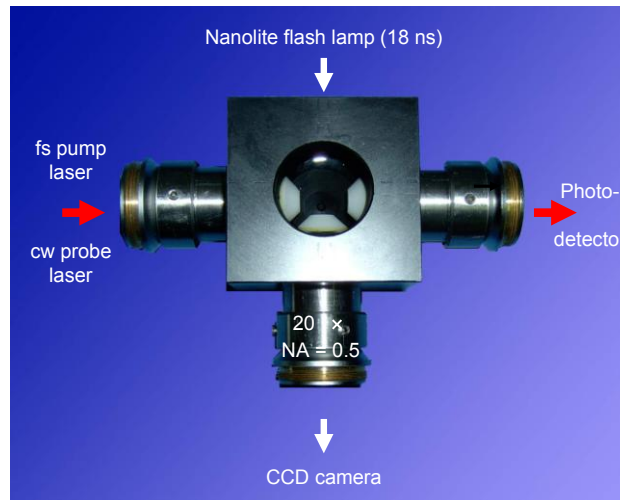
Figure 3.14 Photograph of the water immersion microscope objectives built into the wall of the measurement cell.

3.2.2. Energy calibration

For energy calibration, we performed reference measurements in front and behind the microscope objectives. That enabled us to calculate the laser pulse energy in the focus. In a previous study [Ven02], the laser energy contributing to breakdown was assessed from an energy measurement behind an iris aperture having the same diameter as the mechanical aperture on the rear side of the microscope objective. This approach did not only neglect transmission losses in the objectives and in water, but also assumed that the mechanical aperture is identical with the optical pupil of the objective. To avoid these sources of error, we adjusted the beam diameter to the pupil size and considered the wavelength dependent transmission of all objectives used.

When microscope objectives are used to focus parallel incoming laser light to create optical breakdown, their exit pupil serves as actual entrance pupil for the laser pulse. For a given *NA* and magnification *M* of the objective, the pupil diameter can be calculated assuming that a point source in the front focal plane results in a parallel output beam having a diameter [Lei05]

$$d = 2\,NA\,f \text{ , with } f = 200mm\,/\,M \,.$$ (3.2)

The mechanical aperture stop of the microscope objective is usually larger than the pupil diameter *d*, as summarized in **table 3.4** for the objectives used in our study.

Objective	NA	Mech. aperture [mm]	Pupil diameter [mm]
10x	0,3	12,4	12,0
20x	0,5	11,5	10,0
40x	0,8	9,3	8,0
63x	0,9	7,4	5,7

Table 3.4 Pupil diameters and mechanical apertures of the Leica water immersion objectives.

If the entire mechanical aperture of the microscope objective is illuminated, only part of the incident energy reaches the laser focus. To avoid this potential source of error in the energy calibration, we placed custom-built apertures with diameters equal to the respective pupil sizes directly in front of the objectives.

To assess the microscope transmission at UV, VIS and IR wavelengths, we compared specifications provided by the manufacturer with own measurements. Unfortunately, we were not able to measure the transmitted energy of the laser pulse through the microscope objectives directly at the location of the laser focus in the water cell, because our energy detector is too large to be immersed and not water resistant. Therefore, we measured the transmission in air. This approach may lead to an overestimation of transmission losses because the front lens of the microscope objective is antireflection-coated for water immersion and not for a glass-air interface. The measurement error will be largest for the peripheral rays that intersect the interface under a large angle. Therefore, we reduced the diameter of the incident laser beam by means of an iris diaphragm in front of the objective to 2 mm. In **table 3.5** the measured transmission values at three laser wavelengths are presented together with the specifications of Leica. Fig. 3.15 shows transmission data provided by the manufacturer over the entire wavelength range. Specified transmission values are usually at the lower limit of the actual transmission range. Therefore, it is understandable, that the measured values are larger than the specifications.

Objective	NA	λ [nm]	T_{meas} [%]	T_{leica} [%]
10x	0,3	355	88,3	80,0
20x	0,5	355	75,0	50,0
40x	0,8	355	68,4	60,0
63x	0,9	355	68,6	58,0
10x	0,3	532	95,0	92,0
20x	0,5	532	95,7	93,0
40x	0,8	532	92,2	87,0
63x	0,9	532	92,2	89,0
10x	0,3	1064	90,1	80,0
20x	0,5	1064	83,0	75,0
40x	0,8	1064	77,8	70,0
63x	0,9	1064	77,4	70,0

Table 3.5 Measured transmission values and Leica specifications for different water immersion objectives and wavelengths.
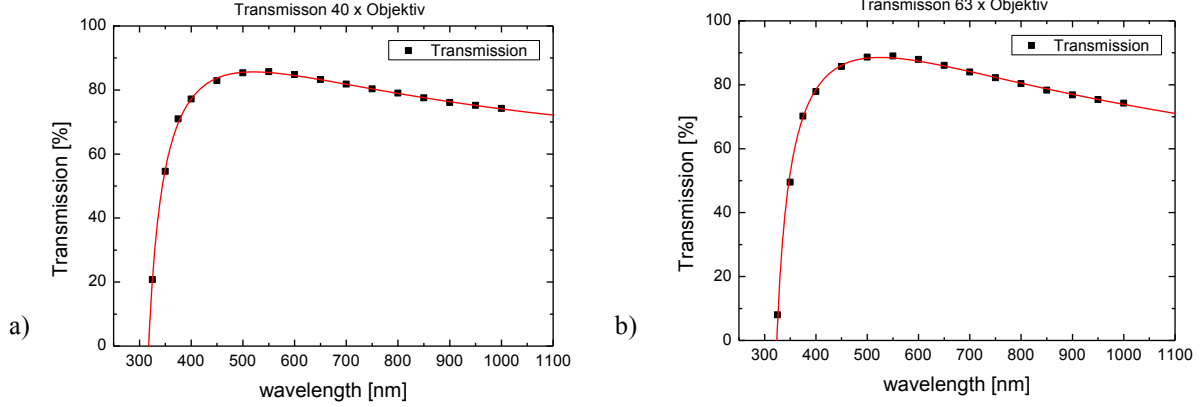
Figure 3.14 Transmission curves provided by Leica for the HCX APO L U-V-I water immersion microscope objectives.

The actual energy calibration was performed by comparing the readout of the energy detector with the energy value behind an aperture with diameter equal to the pupil size of the objective, considering the measured transmission losses in the objective and on the light path through water from objective to laser focus [Vog03]. Since the relation between energy in front of the objective and reference energy was not in all cases linear, we always determined a calibration curve for the entire energy range covered by each measurement for a given (τ_L, λ) parameter combination.

3.2.3. Measurement of energy reflected by stimulated Brillouin Scattering

Figure 3.16 shows the experimental setup for the measurement of the fraction of the pump laser light that is, especially at small numerical apertures, reflected by stimulated Brillouin scattering (SBS). For this measurement, a thin film polarizer (TFP) and a quarter wave plate are added to the setup of Fig. 3.13. The incident pump laser beam is fully transmitted through the TFP and becomes circular polarized after passing the $\lambda/4$ plate. Part of the laser beam is reflected by SBS in the focal region and passes the quarter wave plate a second time, after which its direction of polarization is turned by 90°. Therefore, the beam is reflected by the TFP onto energy meter 2. The fraction of the incident laser light reflected by SBS is obtained by comparing the readings of energy meters 1 and 2. Measurements were performed for *NA*s in the range of $0.075 < NA < 0.9$.

For calibration of the backscattered energy, we removed the microscope objective used for focusing the pump laser beam and placed a highly reflecting mirror at the focal plane. The reading of energy meter 2 under these circumstance, corrected by the transmission of the microscope objective and the water in the cuvette, was taken as standard for 100% reflection by SBS.
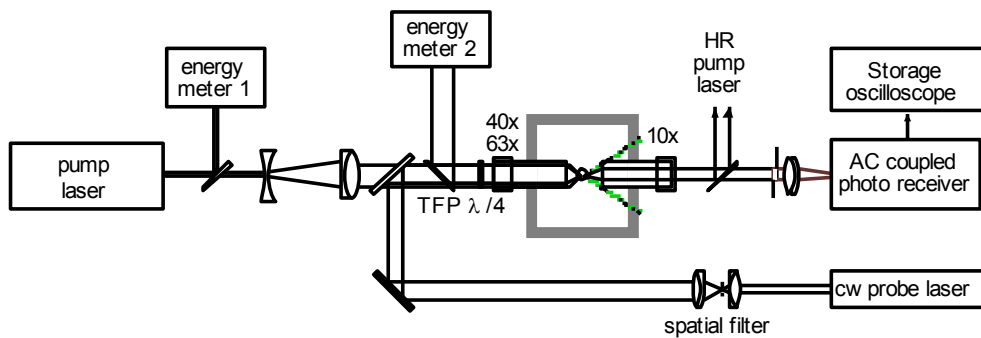
Figure 3.16 Experimental setup for the measurement of the energy reflected by stimulated Brillouin scattering. The probe laser beam path that is relevant for the SBS measurement is drawn in red.

Note that with the setup of Fig. 3.16, we can measure the light reflection by SBS only for circular polarized light while the breakdown thresholds were determined using linear polarized light.

3.2.4. Scattering technique for determination of bubble size

3.2.4.1. Shape and origin of the scattering signals

Figure 3.17 presents time-resolved signals from bubbles produced by 350-fs laser-induced optical breakdown in water using the setup of Fig. 3.13. A 1040-nm fs pump laser pulse and a 658-nm cw laser were focused with the 63x objective (NA = 0.9), and the probe laser light was collected with the 10x objective (NA = 0.3). An additional aperture with 4 mm diameter behind the 10x objective reduced the effective aperture to an NA of approximately 0.1, corresponding to α = 4,3°. We found empirically that the sensitivity of bubble detection is best at this NA. The reason for this finding is not yet completely understood but must be related to the Mie scattering characteristics [Mie08, Ker69] of the bubbles.

The signals are complex, due to the rapidly changing Rayleigh and Mie scattering characteristics during bubble expansion and collapse [Bar97] but T_{osc} can always be easily determined.
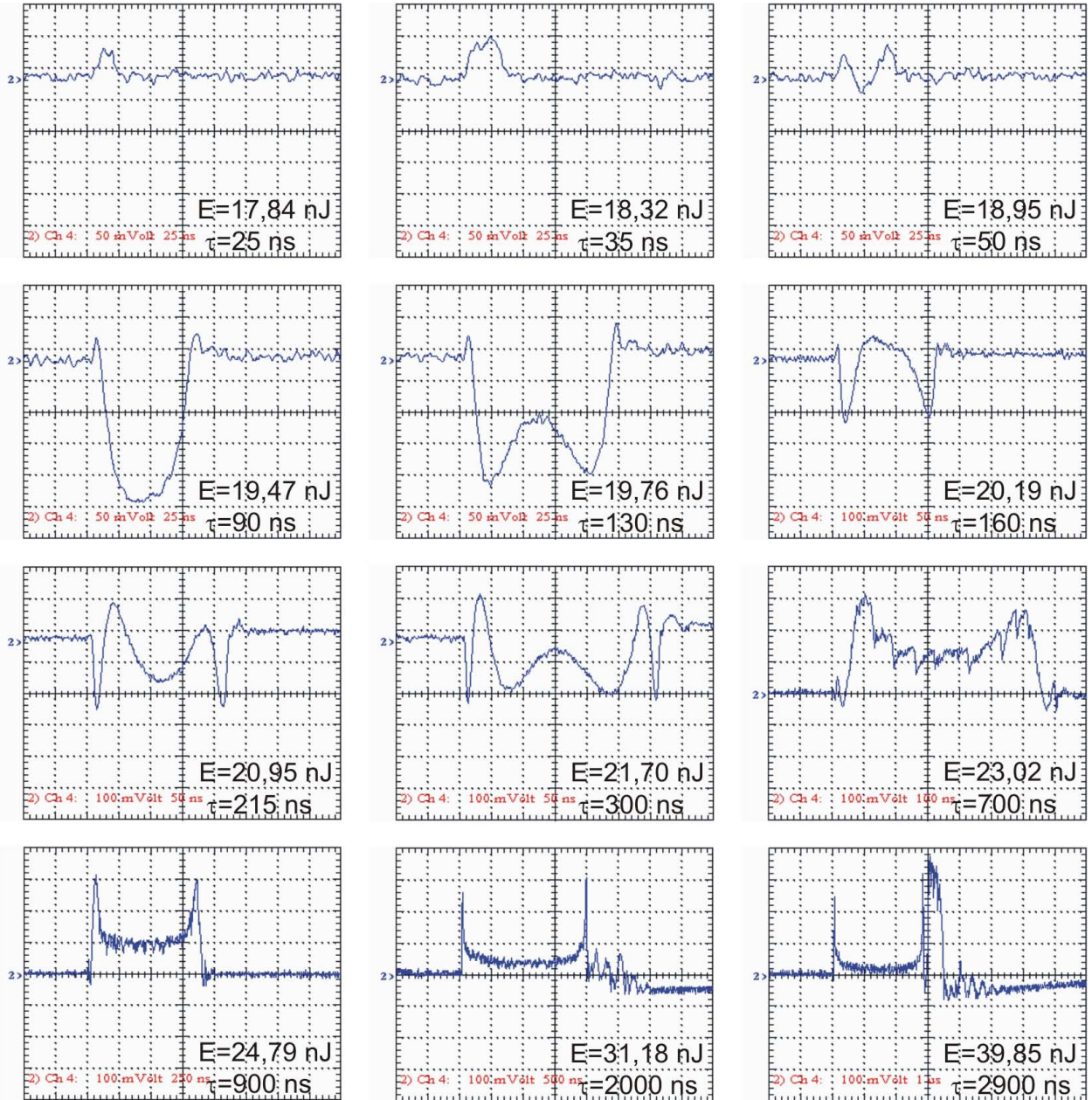
Figure 3.17 Time-resolved scattering signals of 350-fs laser pulses with 1040 nm wavelength induced bubbles in water. Pump- and probe laser are focused with the 63x objective (NA=0.9) and collected with the 10x objective (effective NA=0.1). The scattering signals provide information about the bubble oscillation time. Both pump laser pulse energy and the corresponding bubble oscillation time are given in each plot.

The scattering of probe laser light by bubbles larger and smaller than the beam waist is schematically depicted in **Fig. 3.18**.
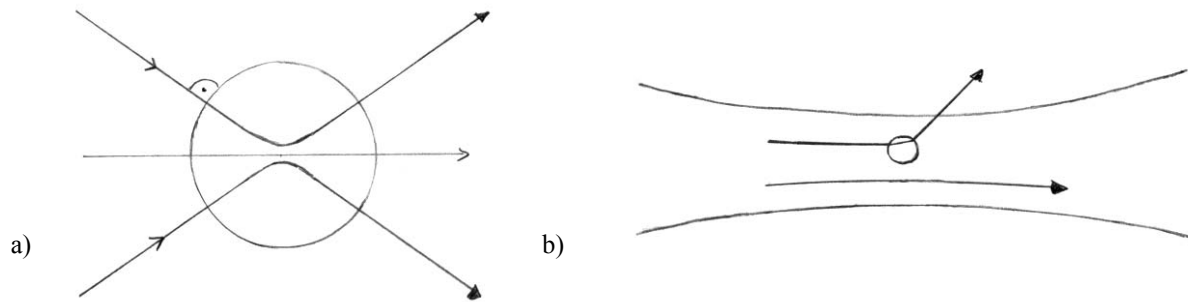
Figure 3.18 Schematic drawing of the interaction of probe laser light with bubbles that are a) much larger than the beam waist and b) much smaller than the beam waist. In a) geometrical optics can be applied. It predicts that the laser light passes the bubble with little disturbance because the light rays hit the bubble wall under 90°. In b), the light is scattered by the bubble [Mie08, Ker69].

While the probe laser is transmitted with little disturbance through bubbles that are considerably larger than the beam waist, it is scattered by bubbles smaller than the beam waist, as described by Mie theory [Mie08, Ker69]. The angular intensity distribution of Mie scattering on bubbles with different radii is shown in **Fig. 3.19,** and the dependence on the total scattering cross section on bubble radius is presented in **Fig. 3.20**. It should be noted, that the curves in figures 3.19 and 3.20 have been calculated for light incident as a plane wave with infinite extent. In reality, the light distribution in the beam waist is, however, given by an Airy pattern [Bor70]. Therefore, these figures can only serve as illustrations of the scattering phenomena and do not provide exact quantitative information.
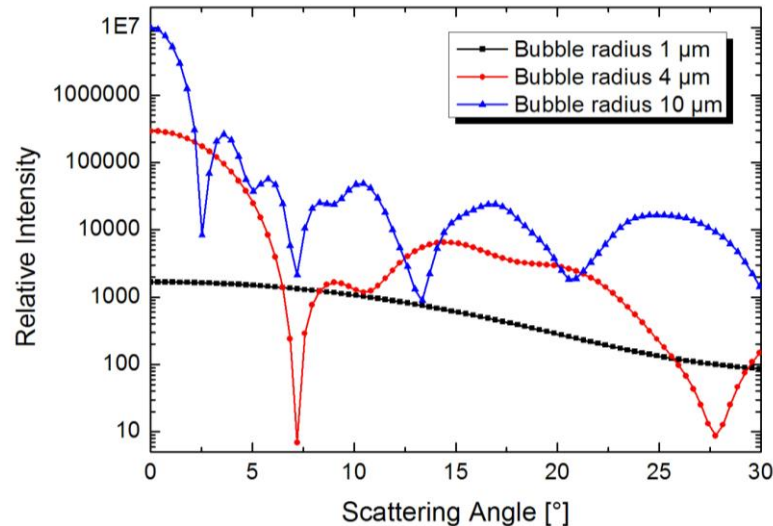
Figure 3.19 Angular intensity distribution of Mie scattering on bubbles (n=1.0) in water (n=1.33), for different bubble sizes and λ = 1040 nm. With increasing bubble size, scattering in forward direction becomes ever more important, and the angular distribution exhibits growing number of intensity peaks, or "scattering lobes" [Ore06].

Normalized Scattering Cross Section
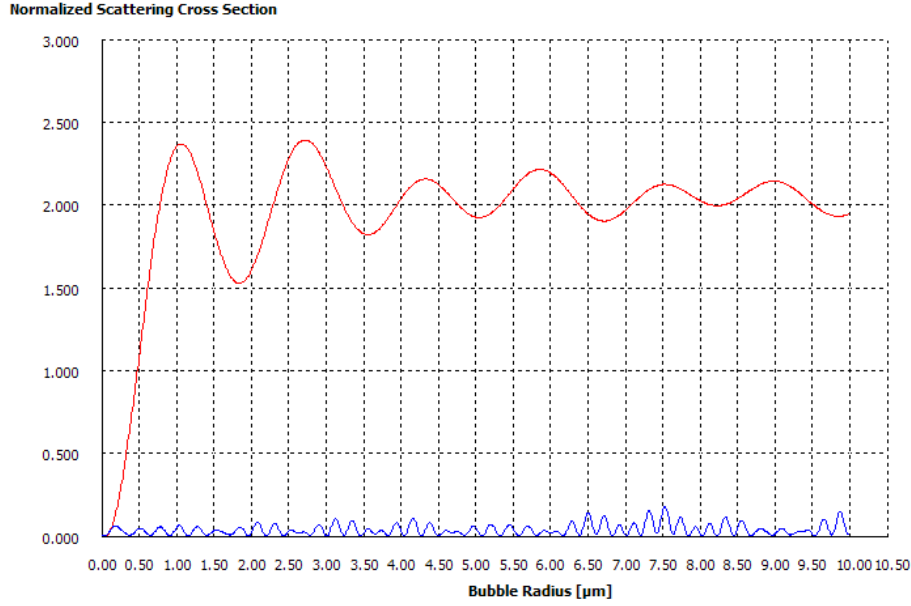
Figure 3.20 Scattering cross section (red line), normalized by the cross section πR^2 of the bubble, plotted as a function of bubble radius for $\lambda = 1040$nm calculated with scatlab 1.2. For $R \gg \lambda$, the scattering intensity is proportional to R^2, i.e. the normalized scattering cross section σ approaches a constant value. For $R \approx \lambda$, σ modulates with variations of R. For $R < \lambda$, the normalized scattering cross section decreases rapidly and monotonously with decreasing R. Additionally, the normalized backscattering cross section (blue line) is plotted. It contributes only a small fraction to the full scattering cross section. The regime of Rayleigh scattering (equal contributions of forward and backward scattering) reaches to about $R = 0.2\mu$m.

In our detection geometry (figure 3.13), the light collected by the photodetector is given by

$$I_{\text{det}} = I_0 \left(1 - \frac{\sigma(R)}{\pi R^2} \right) + I_{scat|\alpha < 4.3°} \; . \tag{3.3}$$

Here I_0 denotes the irradiance incident on the detector without the presence of a bubble in the probe laser beam, $\sigma(R)/\pi R^2$ is the normalized scattering cross section (figure 3.20), and represents all scattered light including the fraction scattered out of the collecting aperture. The last term in equation (3.3) describes the forward scattering into the effective aperture of the collecting microscope objective. It is evident from figure 3.20 that the term $I_0\sigma(R)/\pi R^2$ will undulate during bubble expansion and collapse. This applies also for the last term because the number of scattering lobes (Fig. 3.19) transmitted through the detection aperture will change with varying bubble radius. For very small bubbles, only light of the central lobe is detected. At a certain bubble radius, the central lobe plus the first minimum of the angular distribution pass through the detecting aperture. This demarcates a minimum of the detected light intensity. It increases again, when the next lobe also passes through the detection aperture, etc. The increase of light intensity can be quite pronounced because the decrease of light intensity with increasing scattering angle is compensated by an increase of the solid angle into which the respective light is scattered.

The entire variation of signal strength with bubble radius is thus given both by changes of the total amount of scattered light and by changes of the fraction scattered into the collecting aperture. This complex interplay can explain why for very small bubbles with a size well below the laser wavelength the light intensity at the photodetector increases rather than decreases as would be expected at first sight. For bubbles much larger than the beam waist, the probe laser passes perpendicular through the bubble walls and is thus hardly deflected by the bubble (figure 3.18a)). This explains the small signal strength for large radii.

Figure 3.17 shows that the measured scattering signal from the first bubble oscillation is symmetrical. The entire oscillation time can, therefore, be easily identified for all bubble sizes. For larger pulse energies, one or several rebounds of the oscillating bubble are observed after the first collapse.

The signal-to-noise ratio (SNR) of the method is mainly determined by the power of the probe laser beam. A fraction of only 100 μW passes through the detection aperture, which corresponds to a total energy of 2.5 pJ during a bubble oscillation time of 25 ns. The SNR of our measurement technique is very high because we

obtain R_{max} from the bubble oscillation time rather than from the scattering intensity. Therefore, we do not need to look from the side under an angle where the scattering intensity is proportional to the bubble cross section but can make use of the much stronger forward and back scattering signals. The SNR is further improved because of the heterodyne gain arising from coherent mixing with a strong reference wave (the directly transmitted light). Only for incoherent light (e.g. for fluorescence signals), detection under 90° with a dark background is usually the approach providing the best SNR. With a coherent probe beam, on-axis detection proved to be more advantageous because of the heterodyne gain.

3.2.4.2. Determination of bubbles size from the bubble oscillation period

How can we calculate the bubble radius from the bubble oscillation time? The simplest calculation is given by the well known Rayleigh formula [Ray17]:

$$R_{\text{max}} = \frac{T_{osc}}{1.83} \sqrt{\frac{p_\infty - p_v}{\rho_0}} \qquad (3.4)$$

where p_v is the vapor pressure inside the bubble (2330 Pa at 20° C). However, the Rayleigh formula was derived without consideration of surface tension, which exerts a pressure $p = 2\sigma/R$ in addition to the hydrostatic pressure. The pressure by surface tension can be neglected for large bubbles but becomes important for bubble radii of a few µm or below. In water at room temperature, the surface tension against air is 0.073 N/m, and the corresponding pressure acting on bubbles of for example 100 nm radius is 1.46 MPa. Since this value is much larger than the hydrostatic pressure of 0.1 MPa, surface tension will considerably alter the relationship between bubble oscillation time and maximum radius. Rough estimates of bubble size and bubble energy considering the surface tension can be obtained by the following approximations:

$$R_{\text{max}\,\sigma} = \frac{T_{osc}}{1.83} \sqrt{\frac{(p_\infty - p_v) + p_\sigma(R_{\text{max}})}{\rho_0}} \qquad (3.5)$$

$$E_{B\sigma} = \frac{4}{3}\pi \left[(p_\infty - p_v) + p_\sigma(R_{\text{max}\,\sigma})\right] R^3_{\text{max}\,\sigma} \quad, \qquad (3.6)$$

where $p_\infty = 0.1\,\text{MPa}$, $p_v = 2300\,\text{Pa}$, and $p_\sigma(R_{\text{max}\,\sigma}) = 2\sigma / R_{\text{max}}$, $\sigma = 0.073$ N/m.

Here, $R_{\text{max}\sigma}$ must be determined in an iterative fashion, starting with the p_σ-value based on R_{max} obtained with the Rayleigh equation (3.4). The correct R_{max}-value is then again inserted into equation (3.5) and after a few iterations of this kind, the found $R_{\text{max}\sigma}$ value is obtained.

Equation (3.5) is a simplification since it neglects the temperature dependence of surface tension that is important because the focal volume is heated during optical breakdown. Moreover, the pressure exerted by surface tension is not constant as suggested by the term $p_\sigma(R_{\text{max}})$ but is a function of time: $p_\sigma[R_{\text{max}}(t)]$. Note that the errors made by both simplifications will partly compensate each other because the first simplification leads to an overestimation of p_σ (σ decreases with increasing temperature), and the second simplification results in an underestimation of p_σ (it is larger than $p_\sigma(R_{\text{max}})$ during bubble growth and collapse). Therefore, equations (8) and (9) are useful as zero-order approximations for a determination of $R_{\text{max}\sigma}$ and $E_{B\sigma}$ under consideration of surface tension.

To increase the precision of the determination of R_{max}, we established a refined method based on our numerical model on stress-induced bubble formation in fs optical breakdown [Vog05] (see section 2.1). This model can shortly be summarized as follows:

In femtosecond optical breakdown, the heating of the focal volume occurs much faster than the acoustic transit time from the center of the focus to its periphery. Therefore, no acoustic relaxation is possible during the heating time, and large thermo-elastic stresses are produced because of this "stress confinement." Owing to conservation of momentum, stress wave emitted from the focal volume must contain both compressive and tensile components such that the integral of the stress over time vanishes. In water, the tensile stress wave causes the formation of a cavitation bubble when the rupture strength of the liquid is exceeded.

To determine the evolution of the thermo-elastic stress distribution in the vicinity of the laser focus, we solve the three-dimensional thermo-elastic wave equation arising from the temperature distribution at the end of the laser pulse. For large NAs, the focal volume is very small, and the presence of inhomogeneous nuclei that could facilitate bubble formation is unlikely. Therefore, we have to consider the tensile strength of pure water to estimate the bubble formation threshold. We use the crossing of the "kinetic spinodal" as defined by Kiselev

[Kis99] as threshold criterion for bubble formation. For superthreshold pulse energies, the size of the bubble nucleus is identified with the extent of the region in which the negative pressure exceeds the kinetic spinodal limit. The bubble dynamics is then calculated by means of the Gilmore model [Gil52, Kna71, Pal96], with the tensile stress around the bubble and the vapor pressure inside the bubble as driving forces for the bubble expansion. For the evolution of the vapor pressure, we consider two cases for the bubble content with respect to the surrounding liquid, namely case 1 of isothermal conditions, and case 2 of adiabatic conditions. Unlike the Rayleigh model, the Gilmore model takes the surface tension, viscosity and compressibility of the liquid into account. While in [Vog05] we still assumed a constant value of the surface tension (value at room temperature), we now consider the temperature-dependence of the surface tension at the bubble wall [NIS05].

Figure 3.21a shows the relationship between maximum bubble radius and oscillation time for the full model calculations (case 1 and case 2), the Gilmore model with constant σ, and the Rayleigh model. The bubble size in the Gilmore model was varied by using increasingly large equilibrium radii R_n with constant initial radius R_0. This leads to bubble oscillations with increasing amplitude. It turns out, that the Gilmore model yields a good approximation to the $R_{max} = f(T_{osc})$ relation obtained by our full numerical model, whereas the Rayleigh model leads to a marked underestimation of the bubble sizes, especially for short oscillation times. **Figure 3.21b** shows that the discrepancy between Gilmore and Rayleigh modeling becomes smaller with increasing bubble size and is negligible for bubble oscillation times $\geq 7\mu s$, corresponding to bubble radii $\geq 35 \mu m$.

For practical purposes, we simplify the determination of R_{max} from T_{osc} by using the Rayleigh equation (3.4) together with a correction factor $R_{Gilmore} / R_{Rayleigh}$ that is plotted in **Fig.3.22**. The correction factor can be approximated by the analytical equation:

$$f(T_{osc}) = 0,43238 * e^{\frac{-T_{osc}}{248,2074}} + 0,47292 * e^{\frac{-T_{osc}}{49,01347}} + 0,15773 * e^{\frac{-T_{osc}}{1589,40295}} + 1 . \tag{3.7}$$

Fig. 3.22 shows that for very small bubbles the actual radius corresponding to a given oscillation time is almost twice as large as predicted by the Rayleigh model. Surface tension acts as an elastic restoring force in addition to the hydrostatics pressure that accelerates the bubble oscillation. **Fig. 3.23** shows that the energy stored in the elastic deformation against surface tension is for R = 200 nm one order of magnitude larger than the potential energy $E_B = (4/3)\pi(p_\infty - p_v)R_{max}^3$. Thus Eq. (3.6) must be used for calculating the bubble energy

A last remark should be made on the fact that all above equations were developed for spherical bubbles while very close to the bubble formation thresholds the cavities formed around ellipsoidal plasmas may themselves have an ellipsoidal shape. Godwin et al. showed in an experimental and numerical study that the oscillation times of spherical and ellipsoidal or even cylindrical bubbles are very similar if their maximum volume is the same [God99]. Thus our method will yield the correct bubble size and energy.

(a)

(b)
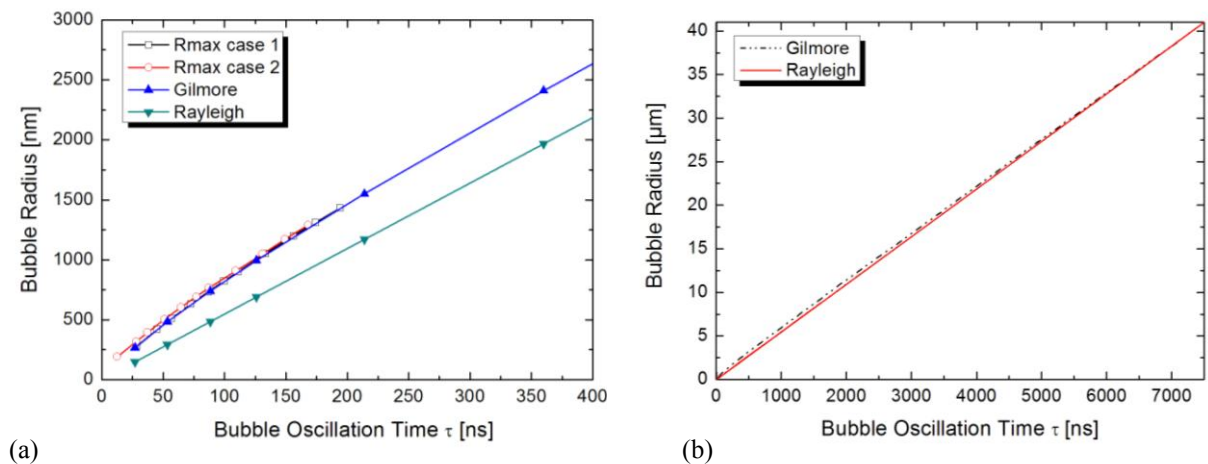
Figure 3.21 (a) Relationship between bubble oscillation time and maximum bubble radius predicted by our full model of thermoelastic bubble generation (case 1 and case 2) [Vog05], the Gilmore model of cavitation bubble dynamics [Gil52, Kna71, Pal96], and the Rayleigh equation (equation (3.4)). (b) Comparison between Gilmore and Rayleigh modeling for oscillation times up to 7 µs and bubble radii up to 40 µm. The discrepancy due to the neglect of surface tension in the Rayleigh equation diminishes with increasing bubble size.
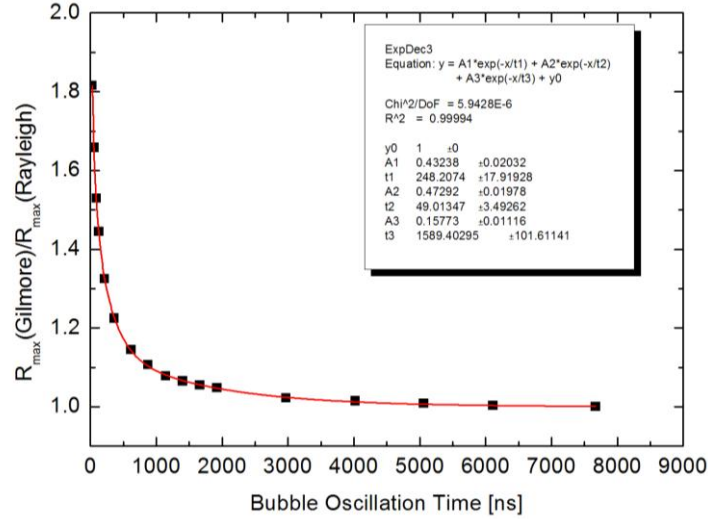
Figure 3.22 Ratio of the maximum bubble radius calculated with the Gilmore model to the maximum bubble radius calculated with the Rayleigh model for different bubble oscillation times. An analytic function was plotted to these values. This allows us, to calculate the maximum bubble radius of the Gilmore model by use of the simple Rayleigh model in combination with the correction factor for specific oscillation times. As expected from figure 3.21, the correction factor for bubble oscillation times $\geq 7\mu s$ is 1 and increases with decreasing bubble oscillation time. For the shortest oscillation times observed in our study, the actual bubble radius is almost twice as large as predicted by the Rayleigh model.
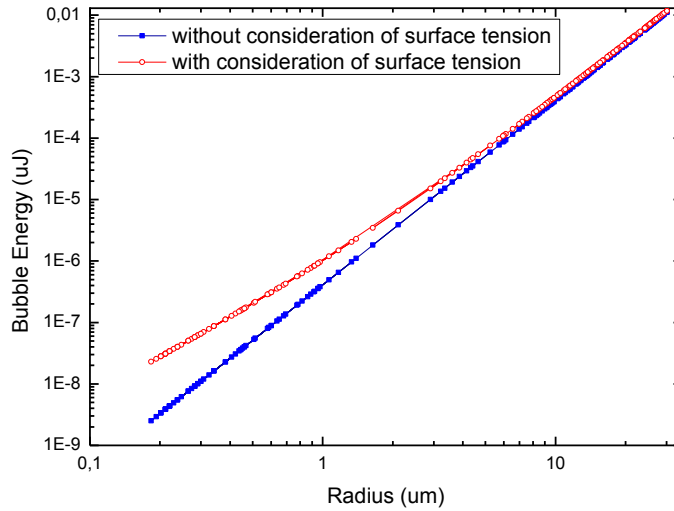
Figure 3.23 Cavitation bubble energy calculated using Eq. (3.6) with consideration of the term describing the additional pressure from surface tension (red) and without this term, considering only the potential energy arising from the work against the hydrostatic pressure.

3.2.4.3 Verification of scattering technique by comparison with flash photography

To verify our measurement, we compared the results obtained with the time-resolved light scattering technique to the results obtained by flash photography, as described in section 3.2.1. Since bubble expansion and collapse are symmetrical in time, one needs to take a photograph at time $t = T_{osc}/2$ to capture the maximum bubble radius R_{max}. The appropriate time can easily read from the scattering signals (see Fig. 3.17). Therefore, the first step in the measurement process for a certain laser pulse energy is the recording and analysis of the probe beam scattering signal. The Nanolite flash lamp was then triggered at $t = T_{osc}/2$ to take the photograph.

Two photographs of laser induced bubbles of different size are shown in **Fig. 3.24**. By means of aberration free imaging with the 20x water-immersion objective ($NA = 0.5$), we were able to measure the bubble size for bubbles with radii as small as 0.86 μm. Thus, the minimum photographed bubble diameter is 1.72 μm, very close to the optical resolution limit of 1.22 μm. Note that the images of the smallest bubbles photographed (Fig. 3.24a) are slightly blurred because the photographic exposure time (≈ 18 ns) is only about one fifth of the bubble oscillation time (≈ 100 ns).
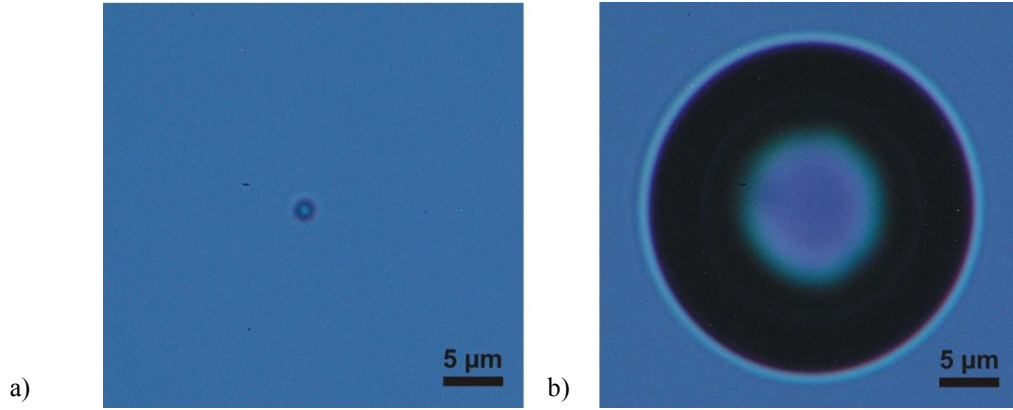
Figure 3.24 Photos of bubbles in water produced by 350-fs laser pulses with 1040 nm wavelength. The pump laser was focused by a 40x (*NA* = 0.8) water immersion objective. Images were taken in side view with 162x magnification

(a)	laser pulse energy: 23,9 nJ	(b)	laser pulse energy: 42,1 nJ
	laser-flashlamp delay: 50 ns		laser-flashlamp delay: 1260 ns
	bubble radius: 0,86 μm		bubble radius: 13,83 μm

Our findings obtained with the probe scattering technique are presented in **Fig. 3.25** and compared with the results of the photographic measurements. The oscillation times from the scattering signals were evaluated using both the Rayleigh equation (3.4) and the combination of equations (3.4) and (3.7) representative for the Gilmore model.
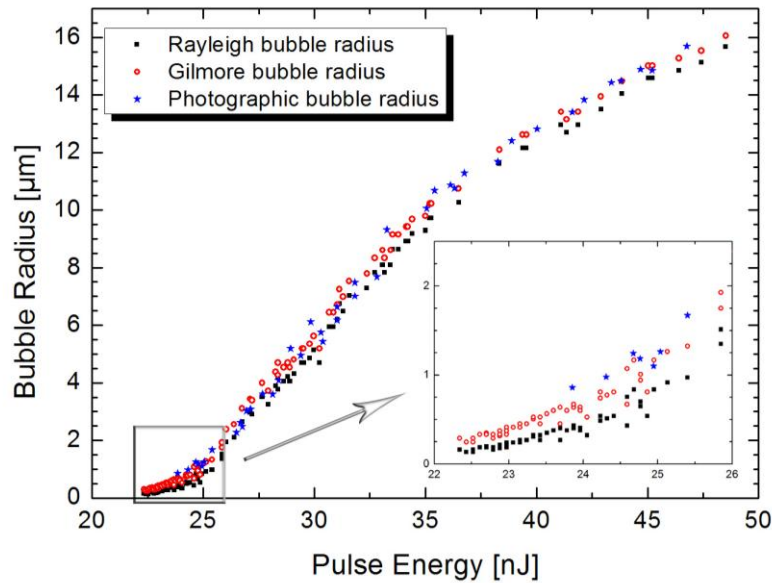
Figure 3.25 Comparison of the measured bubble radii with flash photography and the calculated bubble radii with the bubble oscillation time of the scattering signals. Both Rayleigh- and Gilmore model are used for the calculations, whereas the Gilmore radii better match the photo radii as expected.

We found a very good agreement between the results of both measurement techniques. For very small bubbles, the bubble radii determined by means of the Gilmore model agree better with the photographic results than the values calculated using the Rayleigh equation that neglects surface tension. This is a very good verification of our measurement method. The light scattering technique is much more sensitive than flash photography because it is not influenced by the optical resolution limit. We were able to detect bubbles with an oscillation time of 15 ns, corresponding to a radius as small as 150 nm. This made it possible to determine the breakdown threshold for IR-, VIS- and UV- wavelengths with unprecedented accuracy [Vog08].

3.2.5. Determination of the breakdown thresholds

We employed two criteria to determine experimental breakdown thresholds, as described in section 2.1.2. Bubble formation at the laser focus served as a general criterion for plasma formation, while the observation of bright plasma luminescence (BPL) served as criterion for the formation of high-energy density plasmas. For ns pulses, the onset of BPL either coincides with the bubble threshold (in the IR wavelength range), or is associated with a sudden increase in bubble size (for UV and VIS wavelengths). Therefore, the BPL threshold can also be determined by monitoring the bubble dynamics using the technique described in section 3.2.4. For breakdown by ultra-short laser pulses, the transition to the BPL regime is more gradual, and its detection requires direct detection of the plasma luminescence by means of a photodiode or plasma photography. We used the latter approach because it allows for simultaneous determination of the volume from which the luminescence is emitted.

Determination of the irradiance threshold for optical breakdown requires the use of pulses with smooth temporal and spatial profile, and knowledge of the pulse energy, pulse duration and focal spot size. Our efforts to optimize the temporal and spatial profile have been described in section 3.1. The pulse energy was measured for each individual pulse in each measurement series. The pulse duration was usually determined before and after each measurement series for a (pulse duration/wavelength) combination. If a drift in pulse duration had occurred during the series, it was discarded. The focal spot size is influenced by the quality of the laser beam and the focusing optics, as well as by nonlinear beam propagation effects. Nonlinear beam propagation effects and corruption of the results by stimulated Brillouin scattering were avoided by using large numerical apertures [Sch01, Arn07, Gle84]. Aberration-free focusing was achieved by using diffraction-limited water-immersion microscope objectives built into the wall of the measurement cell. A direct measurement of the laser spot size was not attempted because the diffraction-limited spot size for large numerical apertures and short wavelengths is well below 1 μm (for example, $d = 480$ nm for $NA = 0.9$ and $\lambda = 355$ nm) and thus hard to determine with sufficient accuracy. Therefore, we assumed diffraction-limited quality of the microscope objective and assessed the focus enlargement that may possibly originate from wave-front distortions in the laser beam. The laser beam quality was characterized either by direct measurement of the beam quality parameter M^2 (see section 3.1.4), or by data provided by the laser manufacturer. **Table 3.6** gives an overview of the M^2 data used for the evaluation of our measurement results.

Laser	Pulse duration	M^2	Source
High Q Laser Production Yb:glass IC-1045-30-fs	280 - 352 fs	1.2	measured (High Q) at delivery
Quantel International Nd:YAG YG 671-10	18 - 30 ps	1.3	Manual (spatially filtered beam)
TEEM Photonics PNV-001525-140	0.56 ns	1.3	Manual
Crylas microchip	0.93 - 1.01 ns	1.4	Manual
Spectra Physics Nd:YAG Quanta Ray	6.8 - 11.2 ns	1.9	Manual (instable resonator)
fs OPO Spectra Physics Spitfire & TOPAS 4/800	265 fs	1.4	Manual
ns OPO Continuum Powerlite 8020 & Littman OPO	2 ns	1.5 - 2.3	measured (Fig. 3.8)

Table 3.6 Summary of the M^2 values for the laser systems used in our investigations.

The breakdown thresholds were determined by counting how frequently bubble formation occurred as the energy was increased from sub-threshold to super-threshold values. For this purpose, data were binned into small energy intervals (about 15 for each threshold value), and more than 20 events per energy interval were evaluated. The laser pulses were released at time intervals of > 5 s to avoid plasma initiation at gas bubbles that remain for a short while in the vicinity of the laser focus after each laser pulse. To determine the energy threshold E_{th} for 50 % breakdown probability, the breakdown probability was plotted as a function of the incident energy, and the Gaussian error function was fitted to the measured data.

We calculated also the sharpness *S* of the breakdown threshold, which is defined as

$$S = E_{th}/\Delta E, \tag{3.8}$$

where ΔE is the energy interval between 10 % and 90 % breakdown probability [Vog96].

From the measured values for E_{th} and laser pulse duration τ_L, we calculated the threshold power P_{th}, threshold radiant exposure F_{th}, and threshold irradiance I_{th} using the equations

$$P_{th} = \frac{E_{th}}{\tau_L} \times 1.88 \;, \tag{3.9}$$

$$F_{th} = \frac{E_{th}}{\pi\,(M^2\omega_0)^2} \times 2.0 \;, \tag{3.10}$$

$$I_{th} = \frac{P_{th}}{\pi\,(M^2\omega_0)^2} \times 2.0 \;, \tag{3.11}$$

$$2\omega_0 = 1.22 \frac{\lambda}{NA} \;. \tag{3.12}$$

Here λ denotes the wavelength, w_0 the diffraction-limited beam waist in the focus, and *NA* the numerical aperture of the focusing objective. The factor 1.88 in Eq. (3.9) relates the peak power in a Gaussian pulse to the average power E_{th}/τ_L, and the factor 2.0 in Eqs. (3.10) and (3.11) relates the peak values for irradiance and radiant exposure in the focal plane to the respective average values across the laser spot. Calculation of the peak values is important because theoretical threshold values obtained by numerical modeling usually relate to the peak irradiance in the focal spot rather than to the average irradiance.

3.2.6 Plasma photography

Simple open shutter photography in side view is used to record time-integrated images of the plasma luminescence. The 20x objective was used for imaging when the pump pulses were focused through a 40x and 10x objective, and a 40x objective was employed when the pump pulses were focused through a 20x objective. The image produced by the 20x or 40x objective and the tube lens was further magnified using a Nikkor objective (63mm/1:2.8) that is corrected for 8x magnification. This way, we achieved a total magnification factor of 150 (20x) and 312 (40x), respectively, on the chip of the digital camera. To suppress block laser light scattered by the plasma, appropriate narrow band dielectric filters were placed in the imaging beam path. To minimize image distortions by the filter, we place it in the intermediate image plane between tube lens and 63/2.8 objective (Fig. 3.13).

In plasma photography, the Fuji-Film camera (and also the Nikon D100) exhibited interference phenomena on the chip originating from scattered pump laser light at 532 nm or 1064 nm. Similar phenomena were not observed with the Canon EOS 5D.

With total magnifications $M > 100$ used in our experiments, the image resolution is determined by the *NA* of the microscope objective. For $NA = 0.5$, the diameter of the Airy pattern is 1.2 µm, and the resolution (Rayleigh criterion) 0.6 µm. For $M = 100$ and a pixel size of 8.5 µm, the diameter of magnified image of the Airy pattern is 14 times larger than a pixel, and the camera chip does not impose any resolution limits.

3.2.7 Measurement of plasma transmission

For measurements of the plasma transmission, we used the 10x ($NA = 0.3$), 20x ($NA = 0.5$), and 40x objective ($NA = 0.8$) to produce the plasma, and the 63x objective ($NA = 0.9$) to collect all transmitted laser light. To measure the transmitted energy, the photo receiver was replaced by an energy meter (Ophir PE10 or PD10, depending on transmitted energy). The plasma radiation was blocked out by a filter (Schott RG 830) in front of the energy meter. To account for light losses by reflections at optical surfaces and by water absorption, the energy meter behind the cuvette was calibrated against a reference energy meter in front of the cuvette assuming that far below the optical breakdown threshold 100 % of the incident light is transmitted through the laser focus.

3.2.8. Determination of plasma volume and energy density

From the transmission data we calculated the plasma absorption assuming $A \approx 1 - T$, and, using the photographically determined values for the plasma volume, the plasma energy density.

Fig. 3.26 shows an example of a plasma photograph for explaining the technique used to determine the plasma volume. The border of the plasma luminescence is a little blurred. It is likely that, due to the rapid expansion of the luminescent plasma, the region exhibiting luminescence is larger than the volume within which the nonlinear energy deposition occurred. Plasma luminescence should disappear only after the expanding plasma has cooled down to a temperature at which free-electron recombination is not permanently counteracted by thermionic emission and at which the blackbody spectrum shifts into the IR (see section 2.1.4). Radiative energy transport is another possible reason that may extend the luminescent region beyond the volume into which the laser energy was originally deposited. In any case, it is not easy to deduce the ‚real' plasma size from the photographs. We decided to evaluate the inner part of the plasma with strong luminescence.

The volume of a frustrum with length l, and left and right diameters d_1 and d_2 is given by [Bro89]:

$$V = \frac{\pi}{12} l \left(d_1^2 + d_1 d_2 + d_2^2 \right) \tag{3.13}$$

Equation (3.13) allows to calculate cylindrical volumes, frustum volumes and a conical volumes by using the respective values for d_1 and d_2.
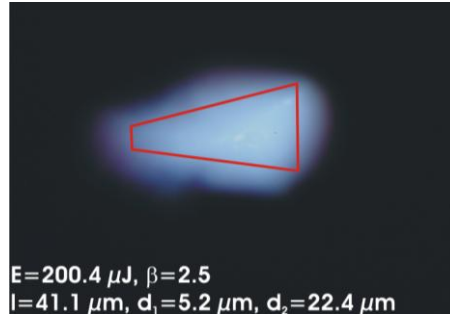
Figure 3.26 Plasma produced by a seeded 11-ns laser pulses with 1064 nm wavelength focused through a 40x water immersion objective (NA = 0.8) (laser light incident from the right). The plasma size was evaluated from the photos by measuring the size of the bright luminescence in the inner part of the plasma as indicated by the red line. The line delineates a frustrum-shaped volume with left diameter d_1 and right diameter d_2.

The average energy density $\varepsilon_{\mathrm{aver}}$ within the plasma volume V is given by

$$\varepsilon_{aver} = \frac{E_{abs}}{V} = \frac{A \cdot E_{inc}}{V}, \tag{3.14}$$

where E_{inc} and E_{abs} are the incident and absorbed energy, respectively. To determine the dependence of $\varepsilon_{\mathrm{aver}}$ on laser pulse energy, plasma volume, transmission and absoption data data are plotted as a function of the incident laser pulse energy and fitted using the TableCurve2D computer program that selects optimal fits out of a large number (≈ 4000) of analytic functions. Division of the fit functions for E_{abs} and V are then yields $\varepsilon_{\mathrm{aver}}(E_{\mathrm{inc}})$. The above approach for determining $\varepsilon_{\mathrm{aver}}$ is necessary because absorbed energy and plasma volume can experimentally be determined only in different measurement series. Therefore, one cannot calculate the energy values for individual laser exposures but has to use fit functions to obtain $\varepsilon_{\mathrm{aver}}(E_{\mathrm{inc}})$.

4. Breakdown threshold values and sharpness

The pulse duration, wavelength, and spot size dependence of both the absolute value of the breakdown threshold and the threshold sharpness bear information about the interplay of the various ionization mechanisms underlying the initiation and dynamics of plasma formation.

We first demonstrate how essential a good laser beam quality and, especially, a smooth temporal pulse shape are to obtain meaningful data that are suitable for comparison with modeling results (4.1). In (4.2) we then present experimental results at fixed UV-, VIS- and IR wavelengths for different pulse durations and interpret them through a comparison with the results of the advanced model of section 2.1. In sections (4.3) and (4.4) we present the wavelength dependence of nanosecond and femtosecond breakdown thresholds and the corresponding modeling predictions, and in (4.5) we look at the spot size dependence of IR nanosecond breakdown thresholds and threshold sharpness. In section (4.6.), all results are discussed to draw conclusions on the interplay of ionization mechanisms, and to extract the possible information on material properties such as the band gap, and collision time. In section 4.7, we finally draw conclusions for the control of nonlinear energy deposition and material processing in transparent dielectrics.

4.1 Influence of laser pulse shape and beam quality on threshold sharpness

To assess the influence of the temporal pulse shape of the breakdown statistics, we compared the threshold sharpness for longitudinal single- and multi-mode laser pulses using the fundamental wavelength (1064 nm). The single-longitudinal mode systems investigated were the Nd:YAG laser system, in which the seed laser could be switched on and off, that is described in (3.1.2) with pulse shapes in Fig. 3.4, and the ns slm OPO (3.1.4).

Figure 4.1 shows the pulse shapes of longitudinal single- and multimode Nd:YAG laser pulses (1064 nm) and of a typical pulse emitted by the slm OPO (900 nm), together with the respective results of the breakdown threshold measurements. Obviously, the threshold sharpness is strongly correlated with the smoothness of the laser pulse shapes. The sharpness is measured by $S = E_{th}/\Delta E$, with ΔE being the energy range between 10 % and 90 % breakdown probability. For slm Nd:YAG laser pulses focused at $NA = 0.8$, we obtain $S = 25.0$, which is close to the value 30.5 previously found for 350-fs pulses (1040 nm) focused at the same NA [Vog08]. For multimode Nd:YAG laser pulses exhibiting many intensity spikes of ≈ 300 ps duration, S drops to 2.7. The shape of the slm OPO pulse is not quite as smooth as that of the slm Nd:YAG laser pulse, resulting in an intermediate threshold sharpness $S = 8.8$.
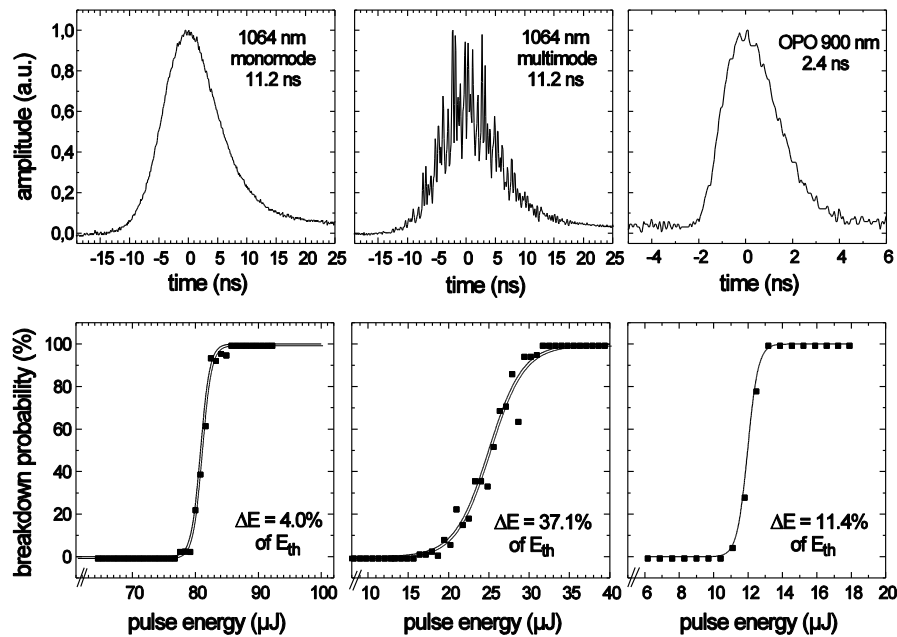
Figure 4.1 Top: Shapes of slm and multimode laser pulses at 1064 nm and a slm OPO pulse at 900 nm, all measured with 6 GHz bandwidth. Bottom: Corresponding breakdown probability curves. ΔE is the energy interval between 10% and 90% probability.

The correlation of threshold sharpness with the laser pulse shape is indicative for multiphoton initiation of the breakdown process that strongly depends on the peak power, especially for IR pulses for which multiphoton ionization in water implies a 5th or 6th order nonlinearity. Generation of seed electrons by thermal ionization from impurities would be less correlated to fluctuations of the peak power because it relies on deposited energy. These results suggest that fluctuations are mainly attributable to irregularities of the laser emission, while the breakdown process itself is inherently governed by a largely deterministic interplay between multiphoton and avalanche ionization.

In the early days of research on optical breakdown, scientists emphasized the importance of transverse and longitudinal mode control [Bloe74], and it was demonstrated that the mode composition of laser radiation influenced the statistics of optical breakdown of silicate glasses [Gle84]. However, later the spikes originating from longitudinal mode beating were mostly ignored because the temporal resolution of oscilloscopes was usually too poor to clearly display them (e.g. in [Vog96b]), and few scientists had access to streak cameras or high-quality Fabry Perot interferometers to monitor the mode structure.

4.2. Threshold values and sharpness at specific UV/VIS/IR wavelengths for various pulse durations

The bubble and plasma luminescence thresholds at fixed UV, VIS and IR wavelengths and the respective values of the threshold sharpness are summarized in **tables 4.1 – 4.5**. The corresponding breakdown probability curves for each threshold value are presented in the appendix, section 11.1.

All I_{th} values refer to the temporal and spatial peak irradiance in the pulse and laser focus, respectively, while the F_{th} values refer to the spatial peak of the radiant exposure (see 3.2.5).

4.2.1. Experimental results

Pulse duration 280-350 fs, wavelengths 347 nm, 520 nm, 1040 nm

λ [nm]	Pulse duration [fs]	NA	Diffraction limited $2\omega_0$ [µm]	Real focus $2\omega_0$ [µm]	E_{th} [nJ]	P_{th} [kW]	F_{th} [J/cm²]	I_{th} [10^{11} W/cm²]	S
1040	352	0.8	1.59	1.90	25.0	133.5	1.76	93.9	24.2
1040	352	0.9	1.41	1.69	22.3	119.2	1.99	106.1	14.9
520	306	0.8	0.79	0.95	4.76	29.2	1.34	82.1	34.3
520	306	0.9	0.70	0.85	3.95	24.2	1.41	86.3	50.8
347	280	0.8	0.53	0.64	3.64	24.4	2.30	154.3	66.4
347	280	0.9	0.47	0.56	4.13	27.7	3.30	221.6	64.2

Table 4.1 Threshold values for optical breakdown in water induced by ≈310-fs laser pulses with 1040nm, 520 nm, and 347 nm wavelength focused through two water immersion objectives with $NA = 0.8$ and $NA = 0.9$, respectively. $M^2 = 1.2$.

The absolute threshold values for femtosecond breakdown at VIS and IR wavelengths are in the same order of magnitude as previous results [Vog05]; results for UV wavelengths have previously not been available. However, note that previous threshold data usually refer to the irradiance averaged over the laser pulse duration and focal spot size. That is inadequate for a comparison with modeling results that usually refer to the peak irradiance.

For all wavelengths and NAs investigated, the threshold sharpness is very high, between $S = 15$ and $S = 66$, in accordance with previous results for femtosecond laser ablation of solids [Liu97]. These S values imply that an energy variation of $1.5 – 5.3$ % is sufficient to increase the breakdown probability from 10% to 90%. Considering that the pulse-to-pulse fluctuations of the laser energy are in the same order of magnitude, we do not attempt to draw conclusions about the dependence of S on laser parameters but merely emphasize that it is generally high for femtosecond breakdown, which creates the basis for a "deterministic" energy deposition and well predictable ablation behavior.

For λ = 1040 nm and λ = 520 nm, we observed little dependence of the optical breakdown threshold on *NA* (13% and 5% , respectively) but for λ = 347 nm, we observed a marked increase (43%) of the optical breakdown threshold with decreasing spot size. Similar observations were made for longer laser pulse durations (see tables 4.2 – 4.5). A possible explanation is that deviations from the diffraction-limited spot size in the deep UV range are larger for the 63x, *NA* = 0.9 objective than for the 40x, *NA* = 0.8 objective.

For femtosecond breakdown, plasma luminescence could not be observed with the naked eye. On photographs, plasma luminescence was visible only well above the bubble formation threshold (for example at E = 165 nJ, E/E_{th} = 7, *NA* = 0.8) and after integration over more than 150 laser pulses, even though the light emitted by the plasma was collected with a numerical aperture of NA = 0.5 (see 6.1.1).

Pulse duration 18-30 ps, 355 nm, 532 nm, 1064 nm

λ [nm]	Pulse duration [ps]	*NA*	Diffraction limited $2\omega_0$ [µm]	Real focus $2\omega_0$ [µm]	E_{th} [nJ]	P_{th} [kW]	F_{th} [J/cm²]	I_{th} [10^{11} W/cm²]	S
1064	30	0.3	4.33	6.06	3221.5	201.9	22.63	14.0	2.3
1064	30	0.5	2.60	3.63	1140.2	71.5	21.98	13.8	2.4
1064	30	0.8	1.62	2.27	452.6	28.4	22.34	14.0	1.7
1064	30	0.9	1.44	2.02	350.4	22.0	21.89	13.7	2.2
532	24	0.3	2.16	3.03	703.3	56.1	19.52	15.6	2.3
532	24	0.5	1.30	1.82	239.6	19.1	18.47	14.7	2.1
532	24	0.8	0.81	1.14	88.5	7.1	17.48	13.9	1.7
532	24	0.9	0.72	1.01	71.4	5.7	17.83	14.2	2.4
355	18	0.3	1.44	2.02	208.9	21.6	13.02	13.4	2.0
355	18	0.5	0.87	1.21	77.1	8.0	13.35	13.8	2.2
355	18	0.8	0.54	0.76	34.9	3.6	15.48	16.0	2.6
355	18	0.9	0.48	0.67	32.4	3.3	18.17	18.8	3.1

Table 4.2 Threshold values for optical breakdown in water induced by ≈24-ps laser pulses with 1064 nm, 532 nm, and 355 nm wavelength focused through four water immersion objectives with different numerical aperture in the range $0.3 \leq NA \leq 0.9$. The beam quality parameter was M^2 = 1.4. The pulse duration was measured upon installation for 1064 nm; the durations for 532 nm and 355 nm are assumed to be shorter by the same ratio as the measured values for ns pulses in table 4.3 (i.e. 78.6% for 532 nm, 60.7% for 355 nm).

As for femtosecond breakdown, we observed no significant dependence of the optical breakdown threshold on spot size for IR and VIS wavelengths but for λ = 355 nm, the threshold increases with decreasing spot size.

The breakdown threshold is generally not very sharp ($1.7 \leq S \leq 3.1$). However, we are not sure whether this can be interpreted as a general physical feature of picosecond breakdown. First, the pulse-to-pulse energy fluctuations of the passively Q-switched and mode-locked laser pulses were large, in the order of $\pm$ 10%. Second, the measurements were performed in the initial project phase when the sensitive probe beam scattering method for bubble detection had not yet been developed. Instead, we detected bubble formation by taking photographs of the breakdown region. This technique is less precise because exact focusing on the bubble is hard to achieve, the time of maximum bubble expansion can only be guessed if the probe beam scattering signal is not available, and the spatial resolution is, even under optimum conditions, not as good as with the scattering technique (see 3.2.4).

The ratio of the irradiance thresholds at 1064 nm and 532 nm wavelength is 1.21. Nearly the same value (1,20) was obtained in previous investigations using 30 ps pulses by Vogel and coworkers [Vog96b].

Pulse duration 7-11 ns, seeded & unseeded, 355 nm, 532 nm, 1064 nm

λ [nm]	Pulse duration [ns]	mode	NA	Diffraction limited $2\omega_0$ [µm]	Real focus $2\omega_0$ [µm]	Break-down criterion	E_{th} [µJ]	P_{th} [kW]	F_{th} [J/cm²]	I_{th} [10^{11} W/cm²]	S
1064	11.2	m	0.8	1.62	3.08	Bubble	25.0	4.2	669	1.13	2.7
1064	11.2	s	0.8	1.62	3.08	Bubble	80.8	13.6	2165	3.65	24.9
1064	11.2	m	0.9	1.44	2.74	Bubble	18.3	3.1	622	1.05	2.6
1064	11.2	s	0.9	1.44	2.74	Bubble	55.3	9.3	1877	3.16	13.5
532	8.8	m	0.8	0.81	1.54	Bubble	2.0	0.4	213	0.46	1.1
532	8.8	s	0.8	0.81	1.54	Bubble	7.5	1.6	804	1.72	4.8
532	8.8	s	0.8	0.81	1.54	BPL	84.4	18.1	9040	(19.40)	7.4
532	8.8	m	0.9	0.72	1.37	Bubble	1.7	0.4	228	0.49	1.2
532	8.8	s	0.9	0.72	1.37	Bubble	5.5	1.2	750	1.61	9.1
532	8.8	s	0.9	0.72	1.37	BPL	62.6	13.4	8485	(18.21)	8.1
355	6.8	m	0.8	0.54	1.03	Bubble	0.6	0.2	145	0.40	0.7
355	6.8	s	0.8	0.54	1.03	Bubble	1.4	0.4	335	0.93	2.1
355	6.8	s	0.8	0.54	1.03	BPL	42.4	11.8	10212	(28.36)	9.1
355	6.8	m	0.9	0.48	0.91	Bubble	0.5	0.1	151	0.42	0.7
355	6.8	s	0.9	0.48	0.91	Bubble	1.5	0.4	453	1.26	4.5
355	6.8	s	0.9	0.48	0.91	BPL	25.4	7.1	7735	(21.48)	12.1

Table 4.3 Bubble formation and bright plasma luminescence (BPL) threshold values for optical breakdown in water induced by unseeded and seeded nanosecond laser pulses with 1064 nm, 532 nm, and 355 nm wavelength. Pulse durations were 11.2 ns for λ = 1064 nm, 8.8-ns for λ = 532 nm, and 6.8-ns for λ = 355 nm. The pulses were focused through water immersion objectives with NA = 0.8 and NA = 0.9, respectively. BPL threshold values for seeded ns pulses must be interpreted with care (see text). M^2 = 1.9 (instable resonator). The operation modes are "s" for seeded operation (longitudinal single mode), and "m" for unseeded operation (longitudinal multimode).

As already discussed in 4.1, the thresholds are generally much sharper when seeded slm pulses are used than for unseeded longitudinal multimode pulses exhibiting intensity spikes.

For seeded pulses, we observe a significant decrease of threshold sharpness with decreasing wavelengths: The value relevant for bubble formation drops from S = 24.9 at 1064 nm (NA = 0.8) to S = 2.1 at 355 nm (NA = 0.8). The explanation of this phenomenon requires utilization of modeling results and will, therefore, be presented in a later section (4.2.2.2.).

A comparison with previous measurements [Vog96b] can only be made for unseeded pulses at IR and VIS wavelengths because slm pulses and UV wavelengths were previously not available. The ratio of the irradiance thresholds for unseeded pulses at 1064 nm and 532 nm is 2.3, compared to 2.6 in the previous investigations using 6-ns pulses. Other researchers found lower thresholds for visible than for IR wavelengths also for ns and ps breakdown in solids [Blo74, Soi89].

For λ = 1064 nm, optical breakdown was always associated with the generation of luminescent plasmas and large bubbles (detailed information on the bubble sizes will be presented in 5.1). By contrast, we observed for UV and VIS wavelengths that nanosecond optical breakdown with *seeded* laser pulses is a two-step process. In the first step, very small bubbles with radii between 500 nm and 20 μm are generated in a low-density plasma regime and no visible plasma luminescence can be observed (6.1.1). The conversion efficiency of laser energy into bubble energy is, at threshold, as small as 0.00003%, as will be shown in section 5.2. The second step occurs abruptly at energies 10 to 30 times larger than the bubble formation threshold. Here the plasma suddenly assumes a much larger size (1600× the focal volume), bright luminescence is observed, large bubbles are produced ($R \geq 200$ μm), and the conversion efficiency of laser energy into bubble energy exceeds 10%. By contrast, *unseeded* laser pulses exhibit only one threshold for both bubble formation and plasma luminescence. Here, the threshold values are lower than both bubble and BPL thresholds for seeded slm pulses because the intensity spikes facilitate multiphoton ionization. However, at the same time, the bubble size at threshold is larger than at the bubble formation threshold for seeded pulses.

Both bubble formation and the onset of bright plasma luminescence are characterized by sharp thresholds. Interestingly, the BPL threshold is, for UV pulses, even sharper than the bubble formation threshold. This observation will be explained in section 4.2.2.2. Note that the absolute values quoted for the irradiance threshold for BPL must be interpreted with care because they refer to the cross section in the laser beam waist. In reality, low-density plasma has already grown relatively far upstream into the cone angle of the laser beam when plasma luminescence sets in, and the focal region is partially shielded (see section 6.1.1). Therefore, the BPL irradiance values given in tables 4.3 – 4.5 are actually too high and are, therefore, put into brackets.

Our discovery of the possibility of producing nano-effects by means of nanosecond laser pulses more than 40 years after optical breakdown in water was first described [Bre64] opens new avenues for cost-effective cell and tissue surgery, and for nanomorphing of solid transparent dielectrics. Prerequisites for the discovery of the two steps in ns breakdown were i) the use of a single longitudinal mode laser (Gaussian pulses), ii) the investigation of UV and VIS wavelengths (not just IR as done in many previous studies), iii) aberration free focusing even at large *NA,* iv) the use of bubble formation as breakdown criterion instead of plasma luminescence, v) the capability to detect very small bubbles with sub-micrometer radius, and vi) the investigation of breakdown events up to energies far above bubble threshold, which revealed the jump from low- to high-density plasmas. Previous studies were far away from meeting all these demands.

The existence of two separate thresholds for the formation of bubbles and bright luminescent plasmas is consistent with a stepwise increase of the free-electron density and volumetric energy density in the plasma. An explanation for this behavior will be given in section 4.2.2, based on our extended rate equation model that includes the heating of the focal volume and thermal ionization during the breakdown process (2.1). We will show that first a non-luminescent low-density plasma is formed in which electron hole recombination balances the ionization avalanche thus limiting the free-electron density to values $\leq 10^{20}$ cm^{-3}. For laser pulse energies exceeding a critical value well above the bubble formation threshold, thermal ionization overcomes recombination and full-density plasmas are produced in a runaway process.

The potential of the nanosecond low-density plasma regime for cost-effective cell-surgery would be largest if the complex, expensive, seeded Nd:YAG laser system that has been used to obtain the results in table 4.3 could be replaced by a simpler and cheaper laser that also produces pulses with a smooth temporal profile. We found that microchip lasers also emit smooth laser pulses because they can work in single mode operation (3.1.3.). Therefore, we studied the optical breakdown dynamics produced by microchip lasers with pulse durations between 0.5 and 1 ns. The results of these investigations are presented in the next section.

Pulse duration 1 ns, Gaussian, 355 nm, 532 nm, 1064 nm

λ [nm]	Pulse duration [ns]	NA	Diffraction limited $2\omega_0$ [μm]	Real focus $2\omega_0$ [μm]	Break-down criterion	E_{th} [μJ]	P_{th} [kW]	F_{th} [J/cm²]	I_{th} [10^{11} W/cm²]	S
1064	1.02	0.8	1.62	2.27	Bubble	4.21	7.8	208	3.83	23.2
1064	1.02	0.9	1.44	2.02	Bubble	3.58	6.6	224	4.12	15.2
532	0.95	0.8	0.81	1.14	Bubble	0.84	1.7	166	3.30	49.5
532	0.95	0.8	0.81	1.14	BPL	1.20	2.4	237	(4.72)	48.5
532	0.95	0.9	0.72	1.01	Bubble	0.65	1.3	162	3.23	66.4
532	0.95	0.9	0.72	1.01	BPL	0.91	1.8	228	(4.53)	66.1
355	0.93	0.8	0.54	0.76	Bubble	0.27	0.6	121	2.45	63.1
355	0.93	0.8	0.54	0.76	BPL	0.77	1.6	341	(6.90)	66.5
355	0.93	0.9	0.48	0.67	Bubble	0.23	0.5	130	2.62	53.7
355	0.93	0.9	0.48	0.67	BPL	0.66	1.3	370	(7.47)	41.0

Table 4.4 Bubble formation and bright plasma luminescence (BPL) threshold values for optical breakdown in water induced by Gaussian nanosecond laser pulses from a microchip laser with 1064 nm, 532 nm, and 355 nm wavelength. Pulse durations were 1.01 ns for λ = 1064 nm, 0.95 ns for λ = 532 nm, and 0.93 ns for λ = 355 nm. The pulses were focused through water immersion objectives with NA = 0.8 and NA = 0.9, respectively. M^2 = 1.4.

In agreement with the results for longer ns pulses, we found for VIS and UV wavelengths a two-step process exhibiting separate well-defined thresholds for minute bubble formation and plasma luminescence accompanied by large bubble formation. The second step occurs at energies 1.5 times (VIS) and 3 times (UV) above bubble formation threshold. For the IR wavelength, both thresholds coincided.

Although the energy range suitable for producing nano-effects is smaller with microchip lasers than with longer ns pulses, it is still sufficiently large for practical purposes, considering the good pulse-to-pulse energy stability of these lasers.

For VIS and UV wavelengths, both bubble and BPL thresholds are extremely sharp, with $S \approx 60$. Thus, the breakdown probability increased from 10 % to 90 % when the pulse energy is raised by only 1.7 %. To resolve this rapid increase, the energy had to be varied in even smaller steps which was done by means of a motorized stage for a rotation of the Fresnel rhomb retarder in front of the Glan laser polarizer.

The optical breakdown threshold at the IR wavelength was less sharp than with VIS and UV pulses; it was in the order of $S \approx 20$. This feature is remarkable since both thresholds coincide for IR wavelengths, for which breakdown is governed by a higher-order nonlinearity. Thus, at first sight, it should be linked with a sharper threshold than for each of the two separate thresholds of VIS and UV. However, for equal stability of the laser emission, the threshold sharpness is primarily related to the statistics of the process initiating breakdown rather than to the nonlinearity of the subsequent dynamics. Since multiphoton ionization occurs more easily at shorter wavelengths, the seed electron density is higher for these wavelengths, and breakdown initiation can be more deterministic (see also 4.2.2.2.).

The radiant exposure thresholds for bubble formation and bright plasma luminescence exhibit no clear dependence on NA. For the different wavelengths, the irradiance threshold for bright plasma luminescence increases with decreasing wavelength, whereas the threshold for bubble formation decreases with decreasing wavelength. This leads to the increasing gap between bubble formation threshold and bright plasma formation threshold for decreasing wavelength.

Pulse duration 0.56 ns, Gaussian, 355 nm

λ [nm]	Pulse duration [ns]	NA	Diffraction limited $2\omega_0$ [µm]	Real focus $2\omega_0$ [µm]	Break-down criterion	E_{th} [µJ]	P_{th} [kW]	F_{th} [J/cm²]	I_{th} [10^{11} W/cm²]	S
355	0.55	0.3	1.44	1.73	Bubble	0.83	2.8	70	2.40	63.1
355	0.55	0.3	1.44	1.73	BPL	2.95	10.1	250	8.56	66.5
355	0.55	0.5	0.87	1.04	Bubble	0.33	1.1	77	2.62	63.1
355	0.55	0.5	0.87	1.04	BPL	1.05	3.6	248	8.47	66.5
355	0.55	0.8	0.54	0.65	Bubble	0.14	0.5	83	2.83	63.1
355	0.55	0.8	0.54	0.65	BPL	0.38	1.3	228	7.80	66.5
355	0.55	0.9	0.48	0.58	Bubble	0.16	0.5	121	4.12	53.7
355	0.55	0.9	0.48	0.58	BPL	0.44	1.5	333	11.38	41.0

Table 4.5 Bubble formation and bright plasma luminescence (BPL) threshold values for optical breakdown in water induced by 0.55-ns laser pulses with 355 nm wavelength. The pulses were focused through four objectives with different numerical apertures in the range $0.3 \leq NA \leq 0.9$. $M^2 = 1.2$.

The results obtained with UV laser pulses of 0.55 ns duration are similar to those in table 4.4 for $\tau \approx 1$ ns. However, both bubble and BPL thresholds are even sharper, with values reaching up to $S > 150$. This corresponds to an increase of the breakdown probability from 10 % to 90 % when the pulse energy is raised by only 0.7 %.

In this measurement series, we demonstrated that the separation of the breakdown dynamics in two distinct regimes of low and high plasma density holds also for smaller numerical apertures down to $NA = 0.3$. The width of the low-density plasma regime in which small bubbles are produced is characterized by the ratio E_{BPL}/E_{Bubble}. This width is, in fact, even slightly larger for smaller NA than for larger focusing angles (**Fig. 4.2**). The increase of E_{BPL}/E_{Bubble} from 2.8 for $NA = 0.9$ to 3.6 for $NA = 0.3$ may be explainable by an increasing plasma shielding with decreasing NA, for which the plasma length at equal values of E/E_{th} rapidly increases [Doc88, Vog96]. Due to the increased shielding, it is harder to reach the critical temperature for thermal runaway with small NAs. This leads to a larger BPL threshold and thus to a broader energy range for the small bubble generation. Otherwise, the threshold irradiance for bubble formation and bright plasma luminescence shows little variation with NA.
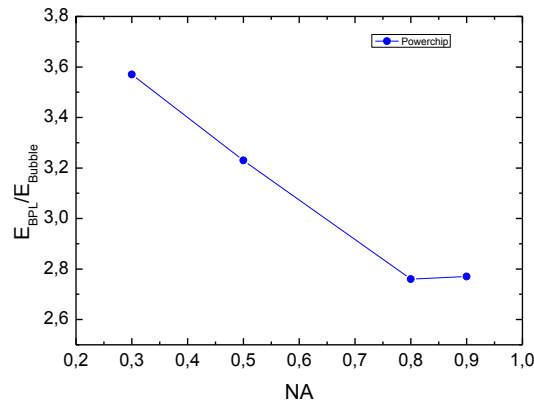
Figure 4.2 Increase of the regime of minute bubble formation (E_{BPL}/E_{Bubble}) with decreasing NA.

The threshold irradiance measured with the 63x objective is almost 50% larger than the values obtained with the other objectives, both for bubble formation and BPL threshold. Similar observations were made for the other laser pulse durations, but the difference is largest in the present measurement series. As already mentioned, a possible explanation is that the objectives are not perfectly corrected for 355 nm (Leica specifies correction down to 400 nm), and that the degree of aberrations increases with increasing NA.

Pulse duration dependence at fixed UV, VIS, and IR wavelengths

Table 4.6 shows a summary of the threshold data for fixed UV, VIS, and IR wavelengths at different pulse durations. In **Fig. 4.3** these data are plotted as a function of wavelength, and **Fig. 4.4** shows the same data plotted as a function of pulse duration. We present the data for $NA = 0.8$ or, where data for $0.3 \leq NA \leq 0.9$ are available, the averaged values for $0.3 \leq NA \leq 0.8$. The data for the 63x, $NA = 0.9$ objective are not included because of the above mentioned indication that this objective may not be diffraction limited at $\lambda = 355$ nm.

		UV	VIS	IR
≈300 fs	Bubble	154.3	82.1	93.9
≈30 ps	Bubble	14.4	14.7	13.9
≈1 ns	Bubble	2.45	3.3	3.83
	BPL	(6.9)	(4.72)	
≈10 ns	Bubble/BPL unseeded	0.40	0.46	1.13
	Bubble seeded	0.93	1.72	3.65
	BPL seeded	(28.3)	(19.4)	

Table 4.6 Summary of bubble formation and bright plasma luminescence (BPL) threshold values for fixed UV, VIS, and IR wavelengths at different pulse durations. The UV wavelength is 347 nm for the fs pulses and 355 nm otherwise; the VIS wavelength is 520 nm for the fs pulses and 532 nm otherwise, and the IR wavelength is 1040 nm for the fs pulses and 1064 nm otherwise. All threshold values are given in units of 10^{11} W/cm^2. BPL threshold values for seeded ns pulses must be interpreted with care (see text).
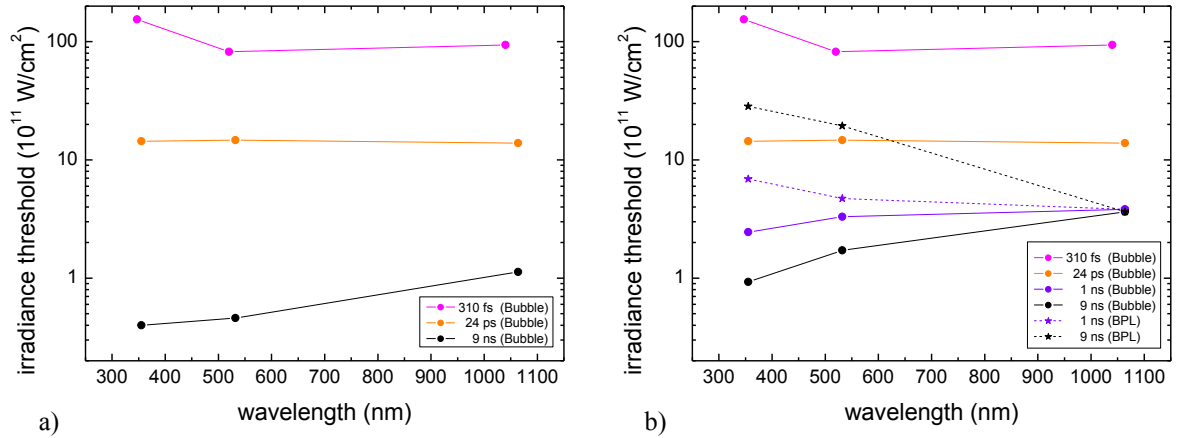
Figure 4.3 Wavelength dependence of optical breakdown thresholds at fixed UV, VIS, and IR wavelengths, (a) for fs and ps pulses, and for unseeded nanosecond pulses of 7-11 ns duration, (b) for fs and ps pulses as well as for seeded (Gaussian) pulses of 0.5 ns – 11 ns duration. The graph in (b) includes the thresholds for both bubble formation and bright plasma luminescence.
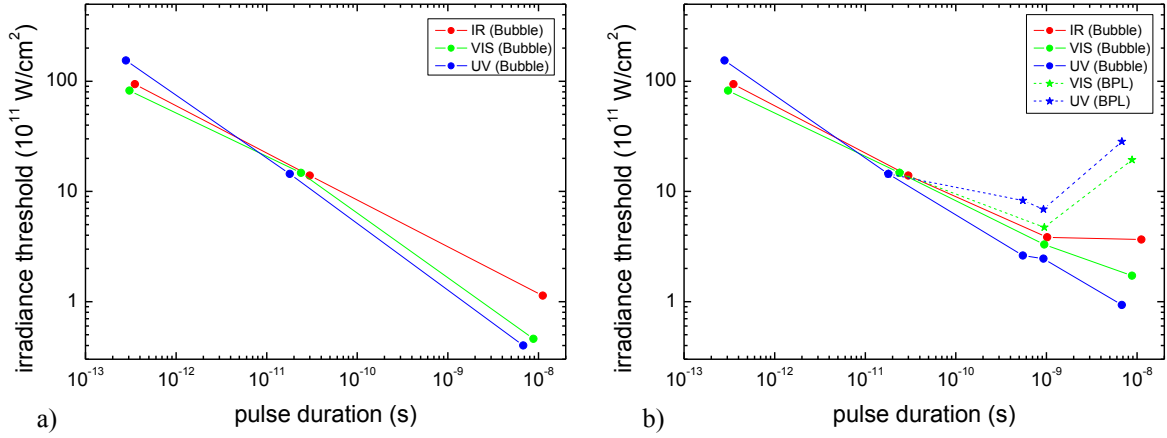
Figure 4.4 Pulse duration dependence of optical breakdown thresholds at fixed UV, VIS, and IR wavelengths, (a) for fs and ps pulses, and for unseeded nanosecond pulses of 7-11 ns duration, (b) for fs and ps pulses as well as for seeded (Gaussian) pulses of 0.5 ns – 11 ns duration. The graph in (b) includes the thresholds for both bubble formation and bright plasma luminescence.

Table 4.6 and Figs. 4.3 and 4.4 show the importance of a smooth laser pulse shape and a consistent, well-defined threshold criterion (bubble formation) for the analysis of the wavelength and pulse duration dependence of breakdown thresholds, especially for the UV and VIS nanosecond data. The $I_{th}(\tau)$ and $I_{th}(\lambda)$ trends differ strongly in the ns regime when unseeded pulses exhibiting intensity spikes are used instead of temporally smooth pulses, and when the breakdown criterion is changed from bubble formation for ultra-short pulses to BPL for ns pulses. As already discussed above, the quotation of an irradiance threshold for BPL that refers to the cross section in the laser beam waist is actually misleading because at the BPL threshold low-density plasma has already grown relatively far upstream into the cone angle of the laser beam, and the focal region is partially shielded (see section 6.1.1). Therefore, these values are put into brackets.

The bubble threshold exhibits a monotonous decrease with increasing pulse duration for UV and VIS wavelengths but levels out in the ns range for IR pulses. The BPL threshold for UV and VIS wavelengths even increases for longer pulse durations in the ns range. Thus we find no „universal' laws for the pulse duration and wavelength dependences. This is because the interplay between the various ionization and loss mechanism varies strongly with pulse duration and wavelength. For IR ns pulses the initiation of seed electrons by photoionization becomes a critical hurdle for the onset of avalanche ionization, while seed electrons are readily available for shorter pulse durations and wavelengths. A detailed analysis of the observed $I_{th}(\tau)$ and $I_{th}(\lambda)$ trends will be presented below in conjunction with the numerical model predictions.

Our results showing different $I_{th}(\tau)$ trends for different wavelengths and ranges of pulse duration differs from previous findings that the radiant exposure threshold for plasma-induced ablation at material surfaces scales approximately proportional to $(\tau)^{1/2}$ for pulse durations larger than a few picoseconds [Stu95, Stu96, Liu97]. In surface ablation, the energy density distribution evolving on a picoseconds to nanosecond time scale is not just influenced by nonlinear energy deposition but also by heat conduction from the thin (< 50 nm) plasma skin layer at the target surface. In the present study, the focal dimensions are larger and the role of heat diffusion is, therefore, much less pronounced. Thus, the parameter dependence of nonlinear energy deposition shows up more clearly, providing more direct information about the interplay of the ionization and loss mechanisms.

4.2.2. Modeling results

4.2.2.1. Parameter selection

In this section, we interpret the experimental results of 4.2.1 through a comparison with the predictions of the advanced model of section 2.1. The calculations were performed for pulse durations of 300 fs, 30 ps, 1 ns, and 10 ns for the UV, VIS and IR wavelengths used in the experiments. The actual pulse durations slightly varied with pulse duration around the values assumed in the calculations. To match the data in table 4.6, the calculations were carried out for NA = 0.8.

The start temperature was 293 K in all calculations. For pulse durations $\tau_L \geq 200$ ps, the critical temperature T_{cr} identified with the bubble formation threshold was assumed to be 300°C, i.e. 573 K. This value for T_{cr} corresponds to the kinetic spinodal temperature, i.e. the superheat limit at which a phase explosion leading to bubble formation will occur even in the absence of any vaporization nuclei [Vog03, Kis99]. For ultra-short laser pulses, energy deposition is stress confined, and the kinetic spinodal limit will, therefore be reduced to a value as low as 151.5°C at $\lambda = 800$ nm, $NA = 1.3$ [Vog05], and 167.7°C at $\lambda = 1040$ nm, $NA = 0.8$ [Vog08]. The acoustic transit time from the center to the periphery of a plasma produced by 800-nm pulses is ≈ 160 ps for NA = 0.9. It is longer for smaller NAs and shorter for VIS and UV wavelengths. Full stress confinement is reached for pulse durations much shorter than the acoustic transit time. Therefore, we set here $T_{cr} = 168°C = 441$ K for $\tau_L \leq 50$ ps, and an intermediate value of $T_{cr} = 500$ K for the transition regime $50 < \tau_L < 200$ ps. The heat capacity was assumed to be constant, regardless of the peak temperature reached. Linear absorption was assumed to be zero such that the first seed electron(s) in the focal volume can only be produced by multiphoton ionization.

In order to obtain the breakdown dynamics under conditions where bright plasma luminescence sets in, we set $T_{cr} = 6000$ K for all pulse durations. This choice is supported by the observation that luminescent fs plasmas have a whitish appearance (see section 6.1.1), corresponding to a blackbody temperature of ≈ 6000 K, and by spectroscopic measurements yielding blackbody temperatures of 7000 - 10000 K for 5-ns pulses and ≈ 6000 K for ps pulses [Sto96]. The above choice is somewhat arbitrary because plasma radiation reflects the average plasma temperature only after an approximate thermodynamic equilibrium is reached, and the electron temperature as well as the peak temperature in specific regions may be considerably hotter than the average temperature at the end of the laser pulse (see sections 6.3 and 6.4). However, it is not supposed to be representative for all kinds of plasma radiation but for the *onset* of bright luminescence.

As described in section 2.1.1, we treat water as an amorphous semiconductor and identify the excitation energy (energy required for a transition from the molecular $1b_1$ orbital into the excitation band) with the band gap energy E_{gap}. Results of earlier physico-chemical measurements of E_{gap} reported in the physico-chemical literature range from 6.5 eV to 7.2 eV [Wil76, Gra79, Nik83]. Following Sacchi [Sac91], we used the value of $E_{gap} = 6.5$ eV in our previous publications [Noa99, Vog05, Vog08]. This value is very close to the result provided by our $I_{th}(\lambda)$ measurements of in the present study that provide an independent method of determining E_{gap}. Initiation of the breakdown process by multiphoton ionization should result in a stepwise increase of the breakdown threshold at wavelengths above which one more photon is required to overcome the electronic band gap between valence and conduction band. The measured distance between the steps then yields the band-gap energy. The best fit between model predictions and experimental data is, below in section 4.3.2, obtained for $E_{gap} = 6.55$ eV. For the sake of consistency, this value is used in all model calculations.

We assume a minimum seed electron *density*, ρ_{ini}, required to start the ionization avalanche, deviating from earlier studies in which a constant *number* of seed electrons, N_{0min}, was assumed [Ken95, Noa99, Vog05]. The assumption of a constant number of free electrons per focal volume was introduced by Kennedy [Ken95] and later put to an extreme by Noack and Vogel [Noa99], and Vogel and coworkers [Vog05] who assumed that the start electron density corresponded to the value for which one free electron was present in the focal volume with 50 % probability. However, since the focal volume scales with NA^{-4}, this assumption implies that the seed electron density strongly decreases for lower NAs. This is not consistent with earlier experimental findings that hardly any dependence of I_{th} on the focusing angle Θ was observed in the range $1.8° \leq \Theta \leq 32°$ [Vog96], and with the findings in the present study also showing little dependence of I_{th} on NA (4.2.1 & 4.4.). Vogel et al [Vog96] showed that the number of seed electrons for which the calculated threshold equals the measured breakdown threshold increased by a factor of 12500 when the focusing angle was reduced from $\Theta = 32°$ to $\Theta = 1.8°$. Therefore, we now find it essential to be able to freely select the start electron density ρ_0 to obtain the optimum fit between experimental and numerically calculated $I_{th}(\lambda)$ dependence.

Physical considerations show that, besides perhaps for very large NA, one start electron per focal volume cannot suffice to produce a homogeneous plasma in the entire focal volume. The spatial extent of the avalanche

originating from one free electron is limited by the diffusion length of the electrons during the cascade. Moreover, heat diffusion will impair the onset of thermal runaway leading to bright plasma luminescence if the avalanches originating from individual start electrons are too far separated in space. It is hard to theoretically assess the distance between individual start electrons that still allows for homogeneous plasma formation because collision cross sections for water are, to the best of our knowledge, not known, and they will change during breakdown due to the associated temperature increase. Therefore, we derive ρ_{ini} from the best fit between model predictions and experimental I_{th} (λ) data on nanosecond breakdown (see section 4.3.2). We obtained $\rho_{ini} = 2 \times 10^{13}$ cm^{-3}, corresponding to an average distance of 368 nm between the seed electrons.

Another material parameter required for modeling is the collision time τ between free electrons and heavy particles. This aspect of the modeling has been much discussed in the past for optical breakdown in condensed matter [Blo74, Spa81, Arn92, Stu96, Tzo01, Sud02, Kai05, Sun05, Jia06, Oli08] but no conclusive picture is available: Values as short as 0.2 fs have been quoted in a theoretical study of electron-phonon interaction in SiO$_2$ [Arn92], while values of 1 - 5 fs (depending on electron energy) have been derived for NaCl [Spa81], and a considerably larger value of 23,3 fs has been obtained in a study of nonlinear beam propagation in fused silica [Sud02]. Bloembergen [Bloe74] emphasiszes that short collision times are essential to explain the similarity of DC and AC breakdown thresholds. It is intuitively clear that at least one collision during a light cycle must occur to reverse the electron momentum in phase with the reversal of the electric field.

Theoretical or experimental data for water are not at all available to date. Therefore, the value used in our calculations was obtained by fitting the model predictions to our experimental $I_{th}(\lambda)$ and $I_{th}(\tau_L)$ data. From the fs OPO measurements, we obtained $\tau = 1.6$ fs, as described in section 4.3.2. By contrast, a value of 3.0 fs provided the best fit for ps and ns breakdown when the model results were fitted to the $I_{th}(\tau_L)$ data (4.2.2.4). This discrepancy looks surprising at first sight but can be explained by the fact that the electron scattering rate depends strongly on the energy of the free electrons, especially for low kinetic energies of a few eV [Arn92]. The average energy of free electrons depends on the band gap and the oscillation energy (see Eq. 2.1 and 2.5). It is larger for fs breakdown than for ps and ns breakdown because for fs breakdown the oscillation energy amounts to a considerable fraction of the band gap energy while it is almost negligible for $\tau_L \geq 20$ ps.

The values used in our calculations are close to the estimate of 1.0 fs by Bloembergen [Bloe74], the value of 1.7 fs for fused silica obtained by Sun [Sun05] through fitting experimental threshold values to model predictions, and to the values of 1.0 and 2.0 fs selected by Jia and coworkers [Jia06] for modeling of breakdown in fused silica and CaF$_2$, respectively. In a recent publication, Olivié et al [Oli08] investigated the wavelength dependence of IR fs breakdown at the corneal surface and deduced a collision time of 0.11 fs through a comparison with model calculations. However, their data exhibit an extreme scatter, and the comparison to model calculations is partly based on assumptions on UV breakdown thresholds that are not supported by experimental data, but were simply adopted from other measurements performed in SiO$_2$ [Jia06].

We assume an *average* value for the collision frequency, i.e. we do neither attempt to include the dependence of collision times on energy distribution of the free electrons, nor do we consider the dependence of this distribution on the temperature increase during the laser pulse. Consideration of these factors would go far beyond the framework of the present study because 1) the collision cross sections required for a more detailed modeling are not yet known for water, and 2) the numerical costs for computing would exceed our present capabilities. Note, however, that the temperature change from room temperature to the bubble formation threshold is only moderate, and the associated changes in collision frequencies are probably not very large. The neglect of these changes in our model will, therefore, probably have little influence of the accuracy of its predictions for the threshold values. However, it will more strongly affect the predictions of maximum free electron densities and temperatures reached at superthreshold irradiance values.

4.2.2.2 Time evolution and irradiance dependence of the breakdown dynamics

Figures 4.5 to 4.8 show the time evolution and irradiance dependence of the breakdown dynamics for pulse durations of 300 fs, 30 ps, 1 ns, and 10 ns and the UV, VIS and IR wavelengths used in the experiments. They each contain a combination of four graphs showing a) the time evolution of the degree of ionization $R = \rho / \rho_{bound}$ b) the temperature evolution, c) the maximum degree of ionization as a function of normalized irradiance I/I_{th}, and d) the peak temperature as a function of normalized irradiance. For each (τ_L, λ) combination, a set of these graphs is plotted at the bubble formation threshold (T_{cr} = 573 K for ns pules, T_{cr} = 441°C for 30 ps and 300 fs), and for T_{cr} = 6000 K. Note that, although the range of normalized irradiance in the $R_{max}(I/I_{th})$ and $T_{max}(I/I_{th})$ plots is the same in both cases, the real irradiance range is larger for the BPL threshold than for the bubble threshold because I_{th} is larger at the BPL threshold.

300 fs, 347 nm, T_{cr} = 424.5 K

a) b) c) d)
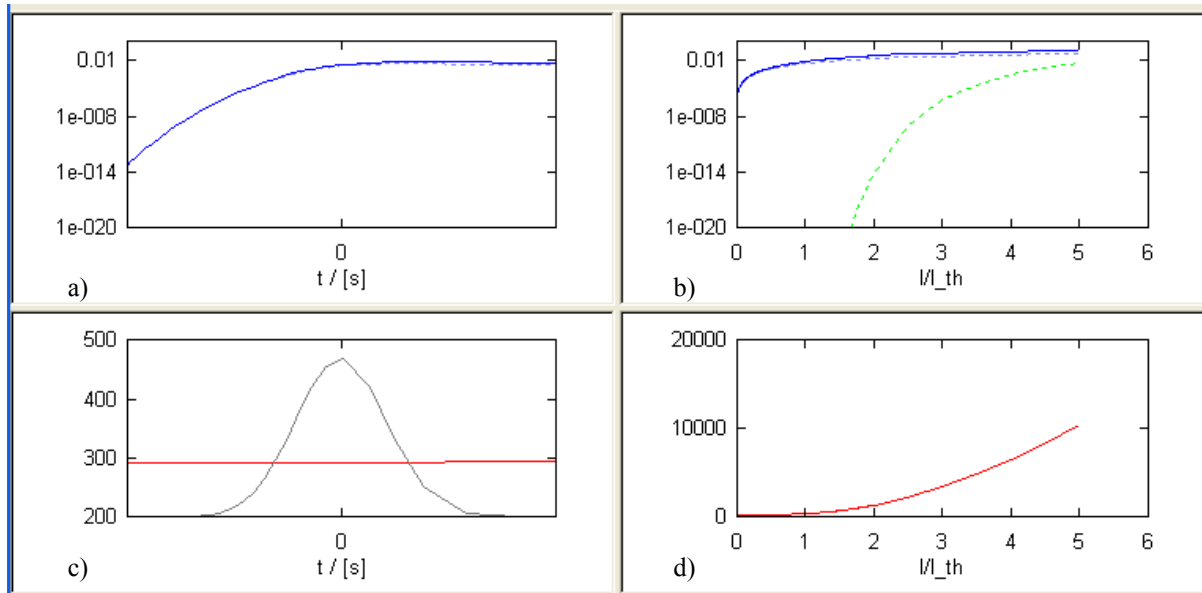
300 fs, 347 nm, T_{cr} = 6000 K

a) b) c) d)
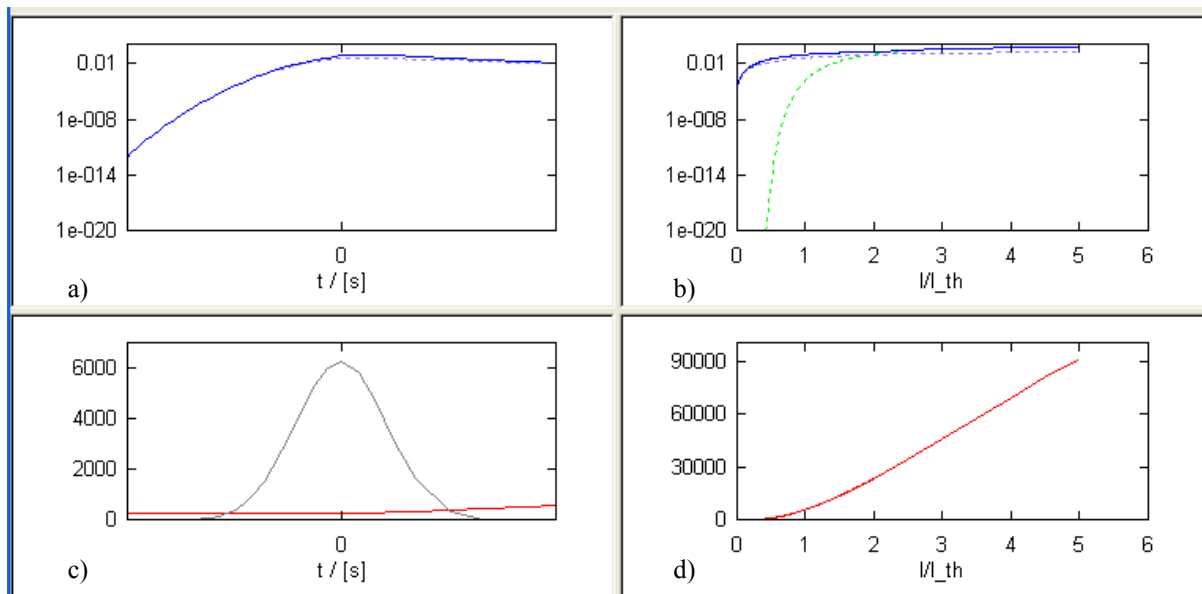
300 fs, 520 nm, T_{cr} = 424.5 K
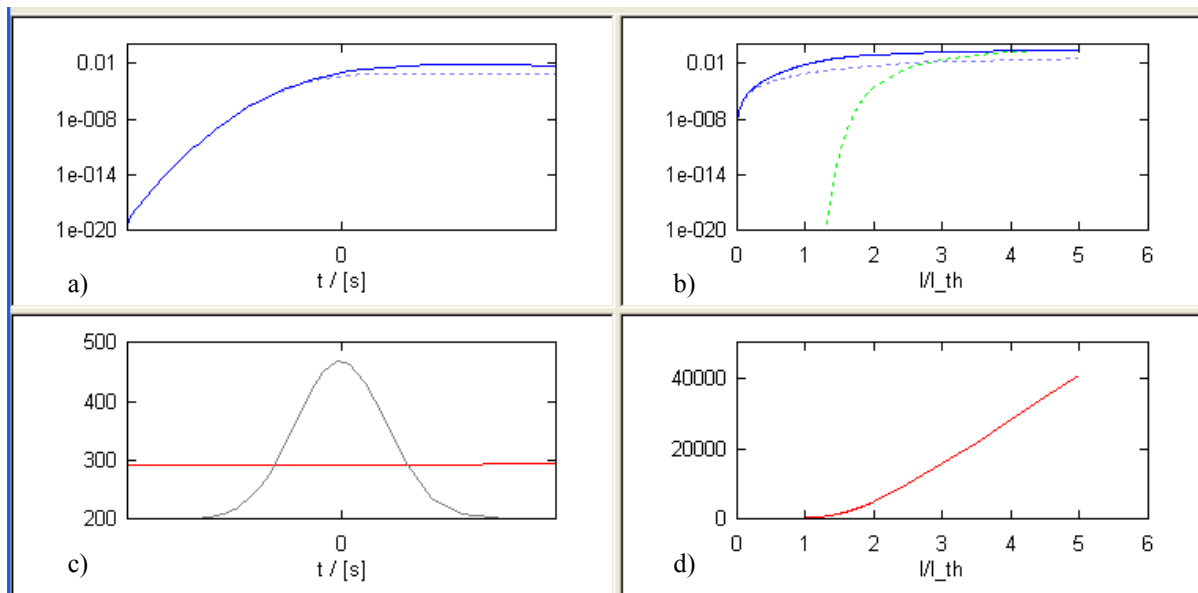
300 fs, 520 nm, T_{cr} = 6000 K
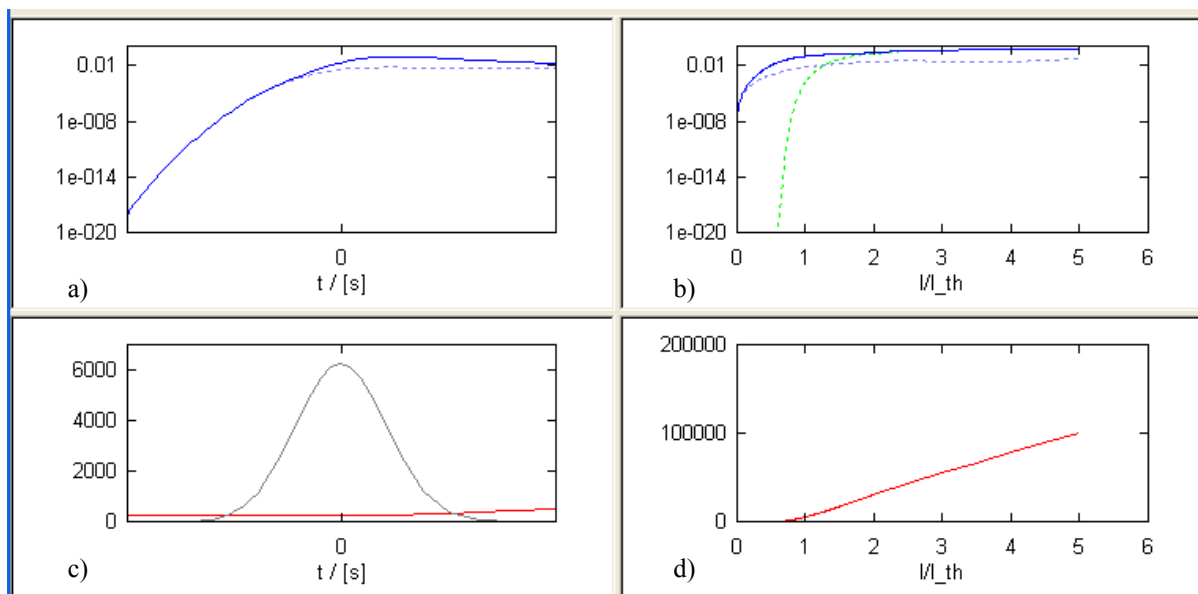
300 fs, 1040 nm, T_{cr} = 424.5 K
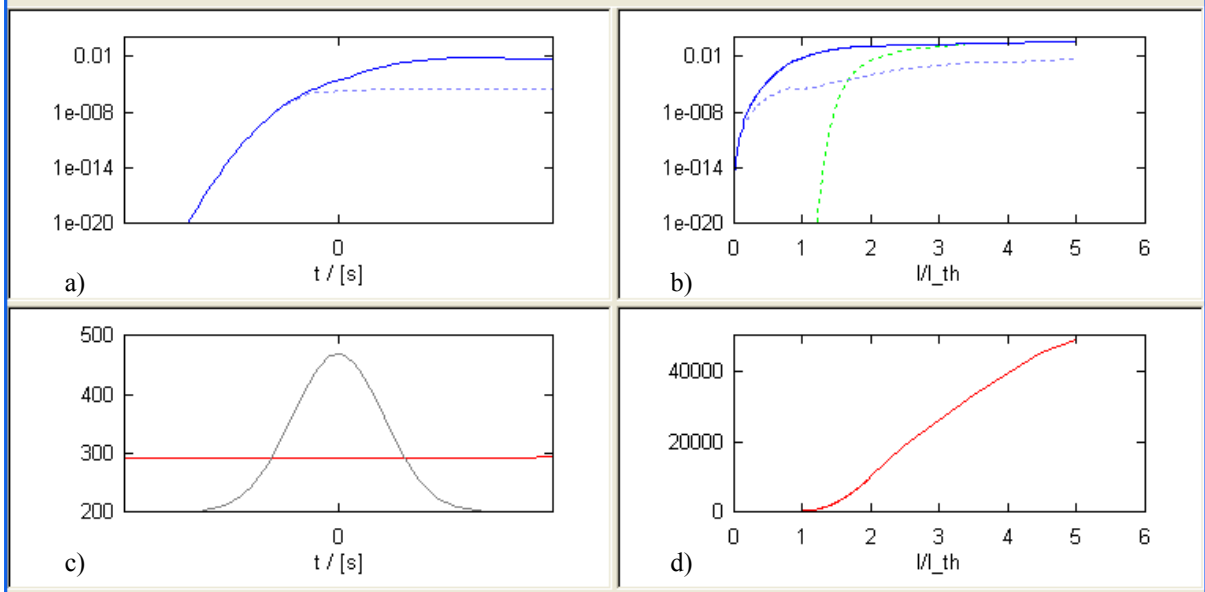
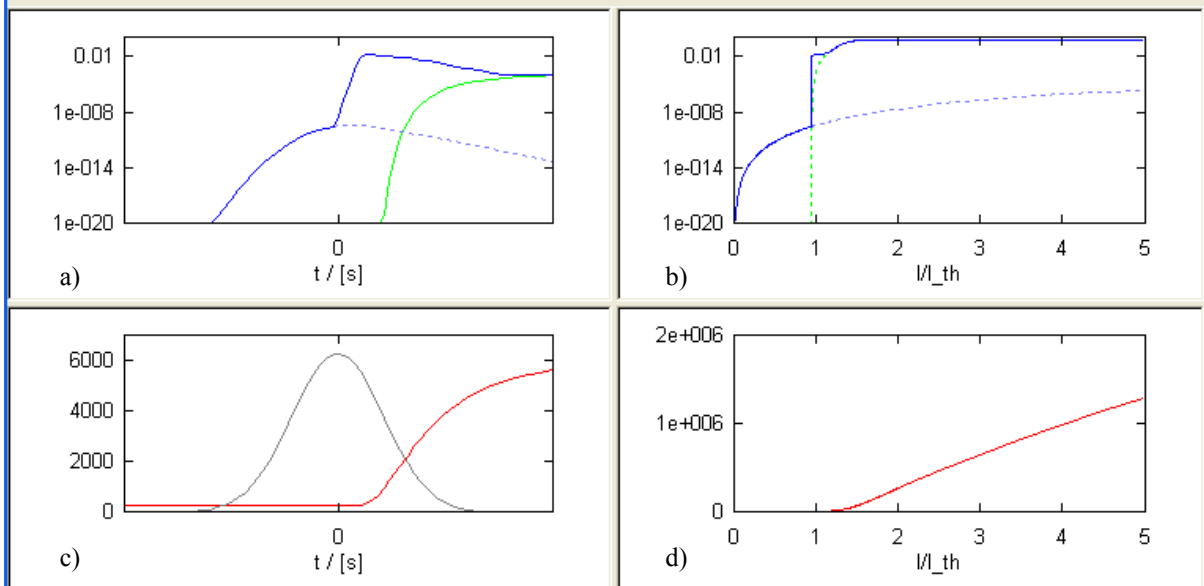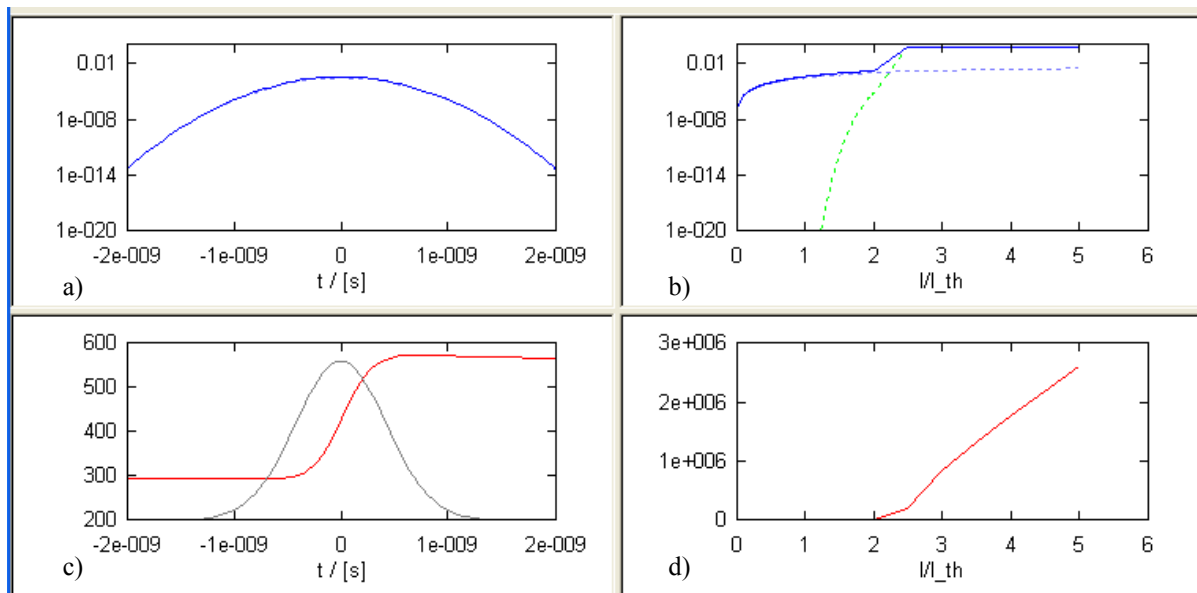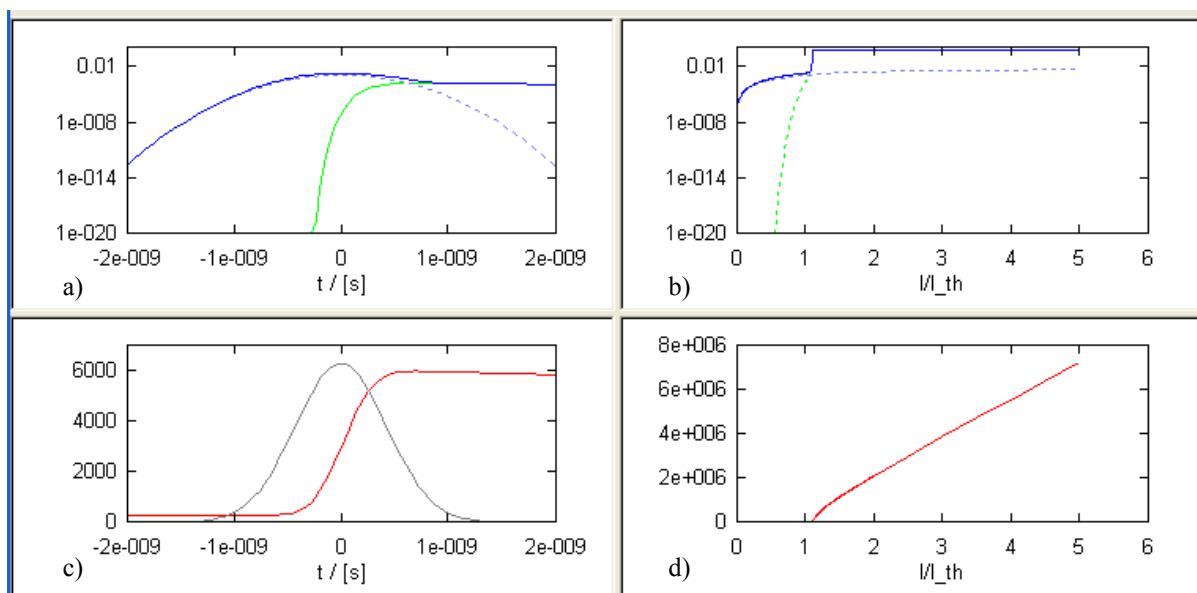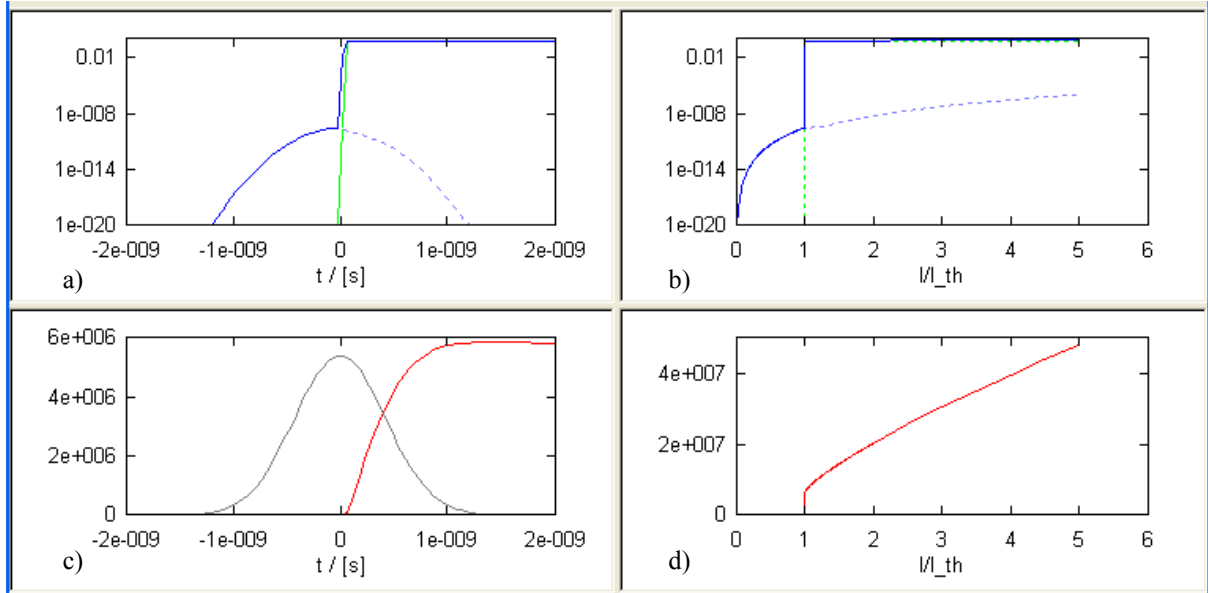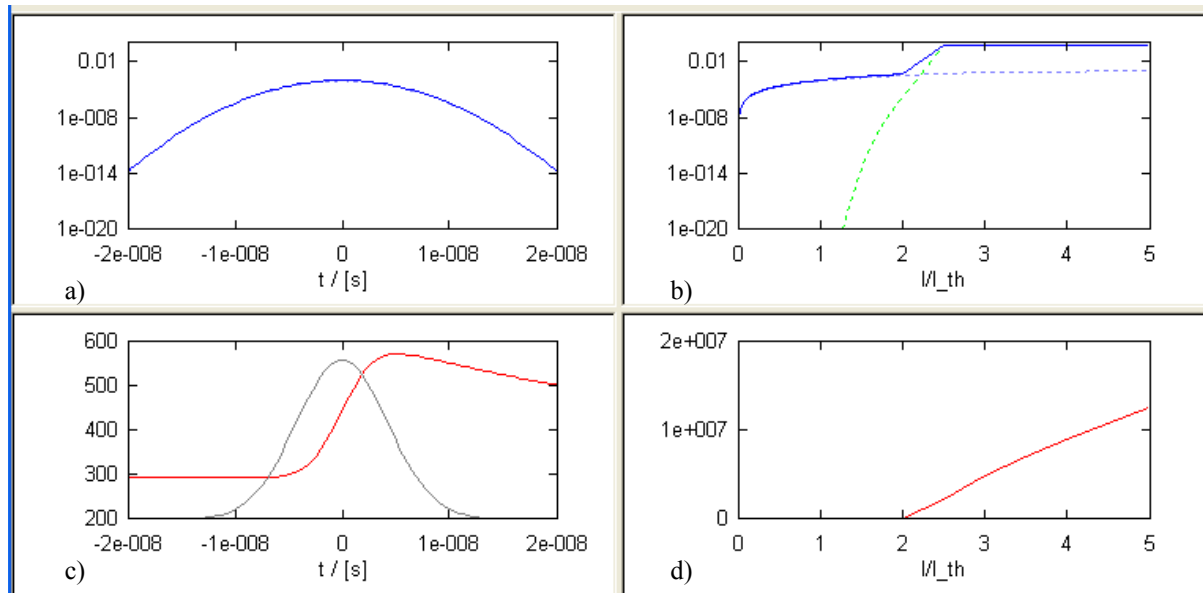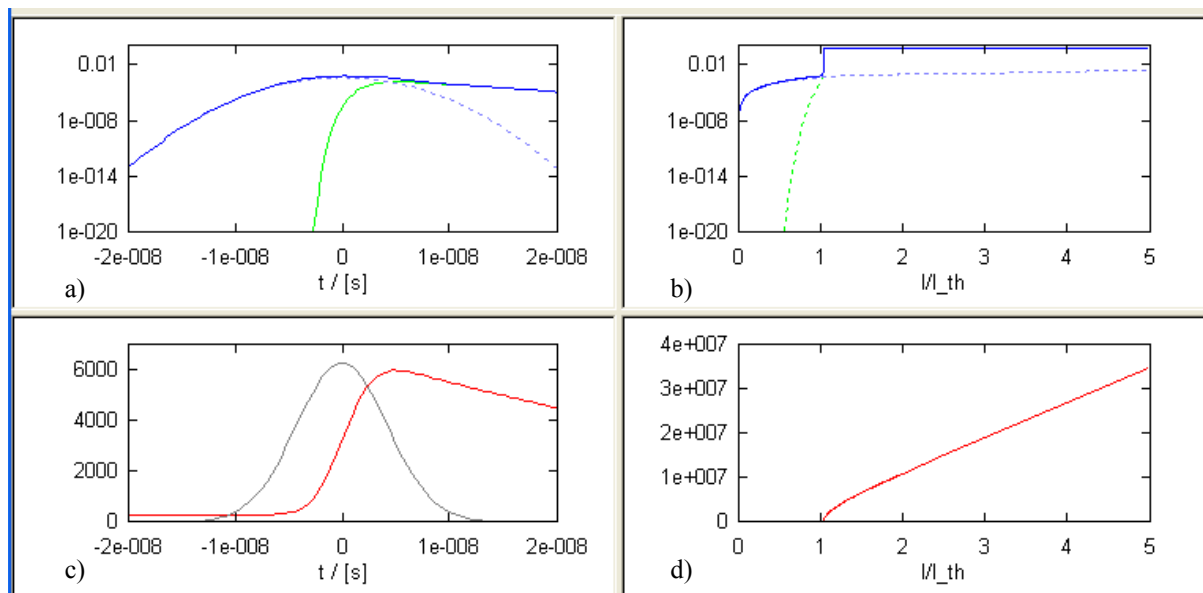**300 fs, 1040 nm, T_{cr} = 6000 K**
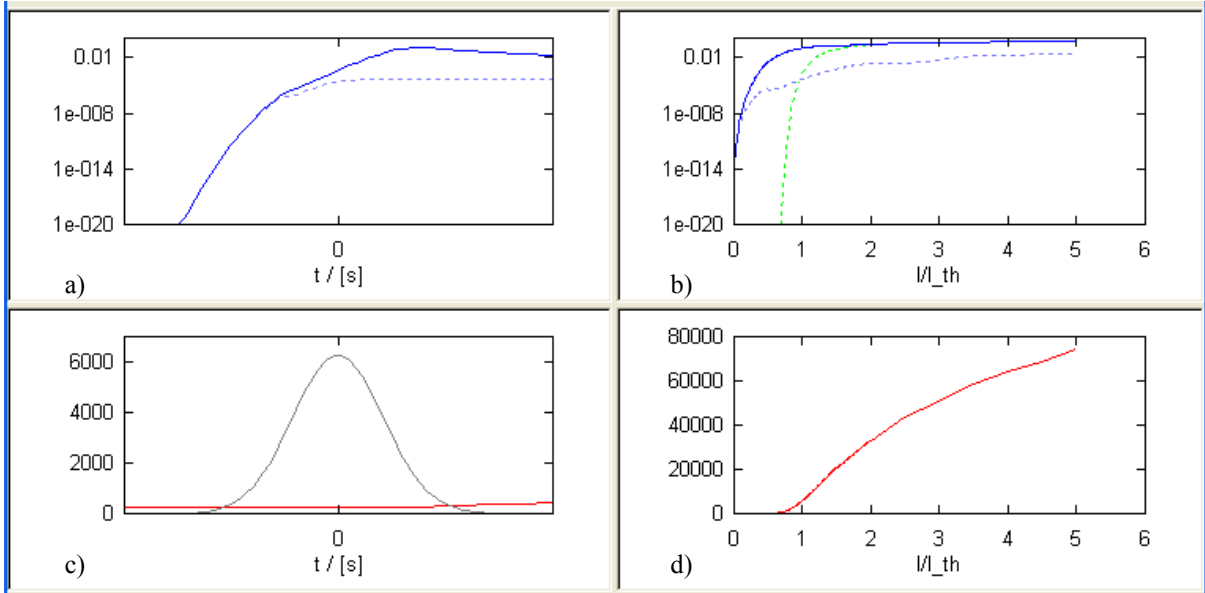
Figure 4.5 Numerical simulations of plasma formation by 300-fs pulses at wavelengths of 347 nm, 520 nm, and 1040 nm. In each plate, graph a) portrays the evolution of the ionization degree R as a function of time. Full ionization (i.e. a degree of 1.0) corresponds to a free-electron density of 6.64×10^{22} cm^{-3}. The dark blue line represents the total degree of ionization, the bright blue line the part produced by multiphoton ionization, and the green line the part arising from thermal ionization. Graph b) presents the maximum ionization degree produced during a laser pulse as a function of irradiance, normalized by the irradiance I_{th} at the threshold for bubble formation. Besides the total ionization degree, the parts arising from MPI (dotted blue line) and thermal emission (dotted green line) are also plotted. Graph c) shows the temporal evolution of the plasma temperature (red) in relation to the temporal shape of the laser pulse (grey). Graph d) shows the peak temperature reached during breakdown as a function of normalized irradiance.

30 ps, 355 nm, T_{cr} = 424.5 K
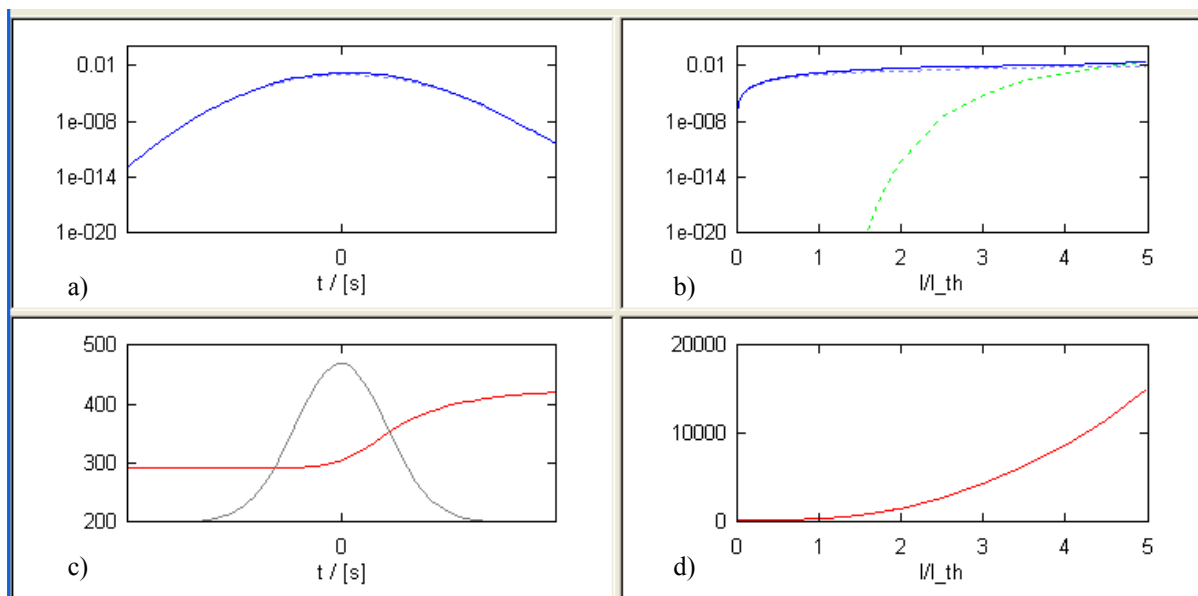
30 ps, 355 nm, T_{cr} = 6000 K
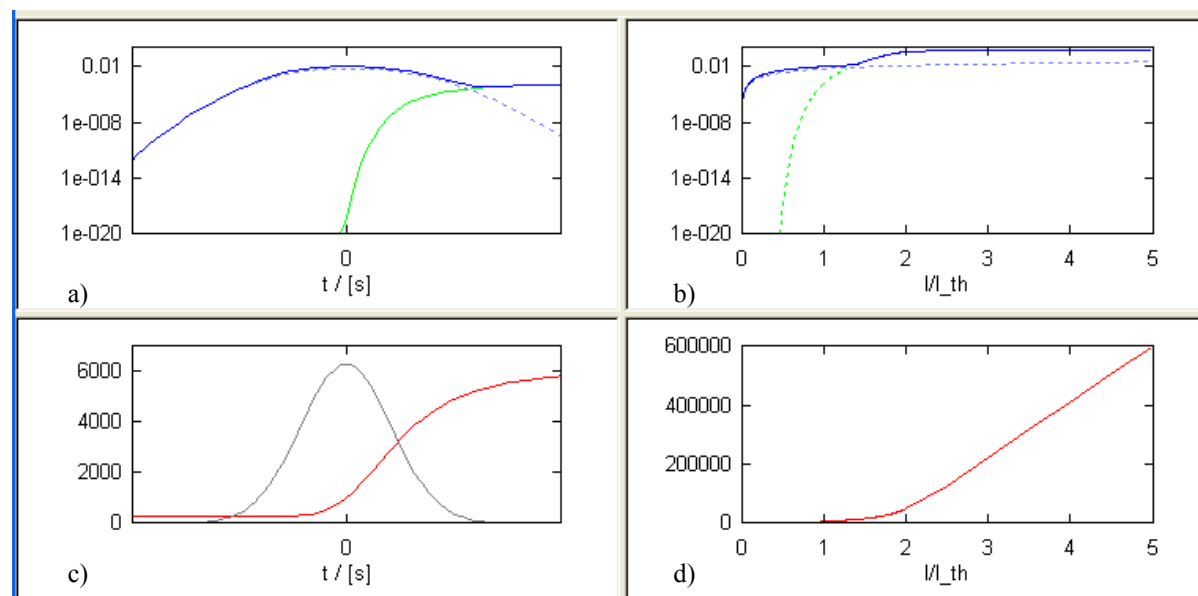
30 ps, 532 nm, T_{cr} = 424.5 K
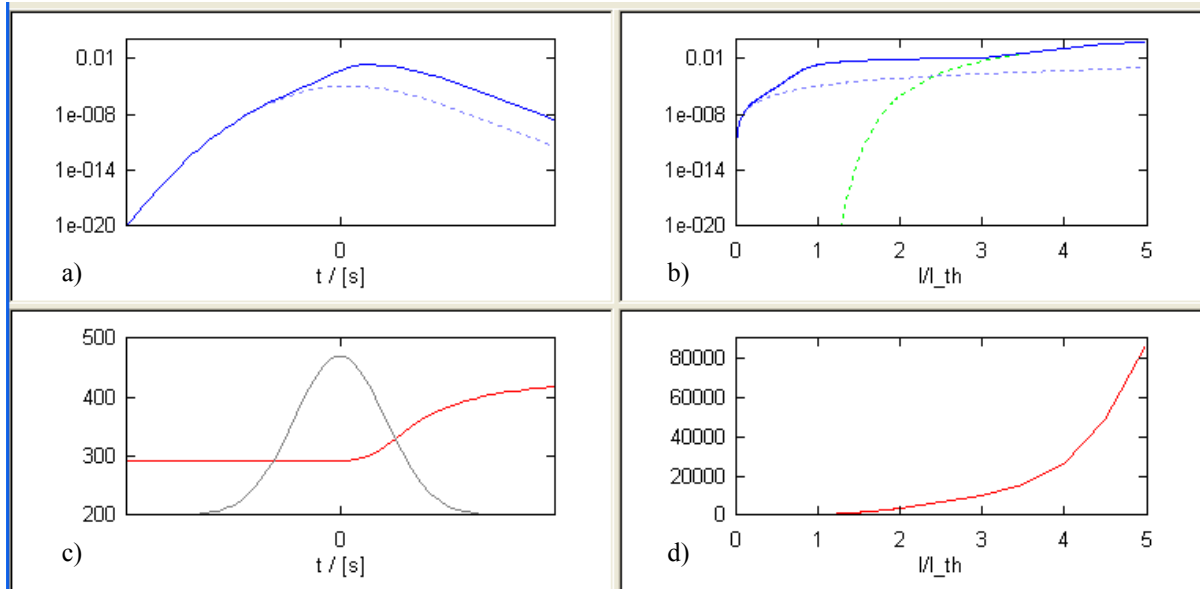
30 ps, 532 nm, T_{cr} = 6000 K
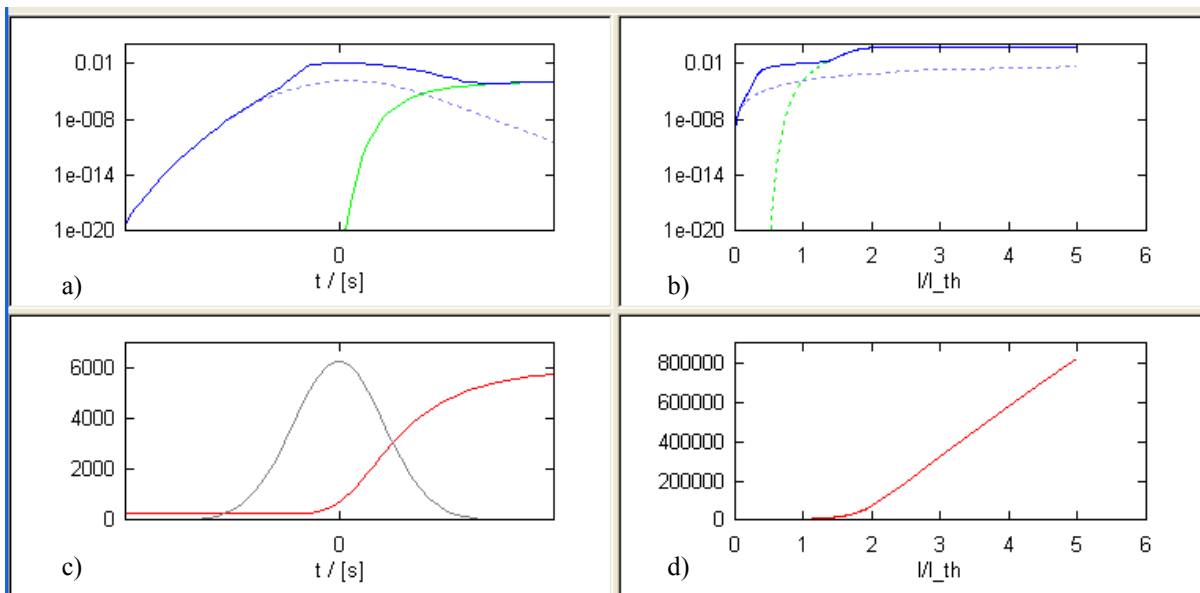
30 ps, 1064 nm, T_{cr} = 424.5 K
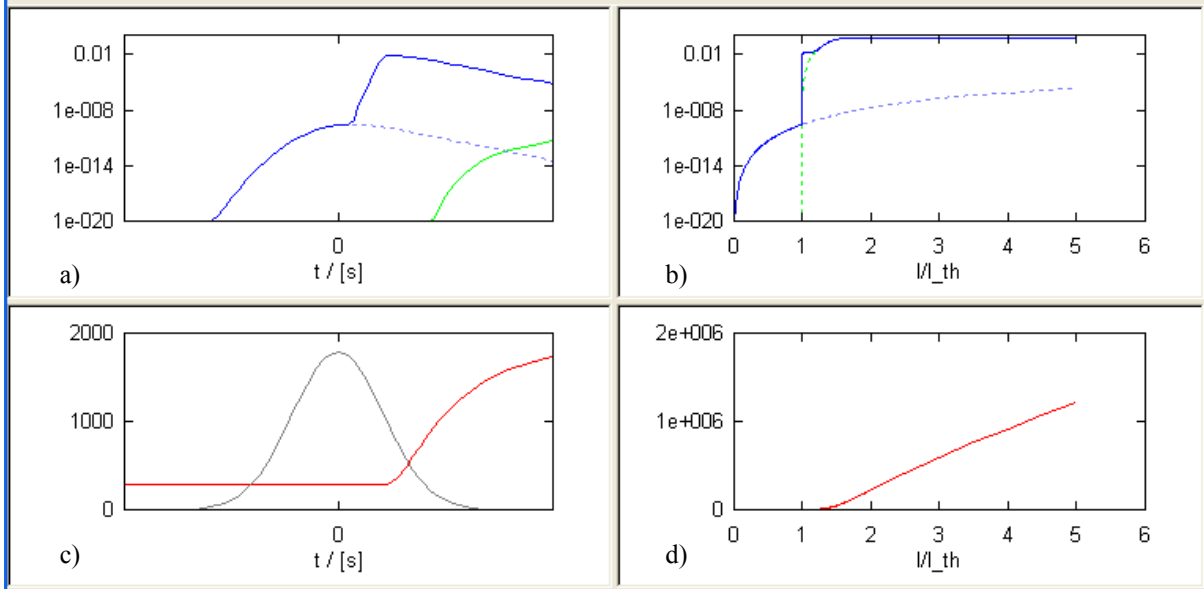
30 ps, 1064 nm, T_{cr} = 6000 K

Figure 4.6 Numerical simulations of plasma formation by 30-ps pulses at wavelengths of 355 nm, 532 nm, and 1064 nm. In each plate, graph a) portrays the evolution of the ionization degree R as a function of time, b) presents the maximum ionization degree produced during a laser pulse as a function of normalized irradiance, c) shows the temporal evolution of the plasma temperature T (red) in relation to the temporal shape of the laser pulse (grey), and d) shows the peak temperature reached during breakdown as a function of normalized irradiance.

1 ns, 355 nm, T_{cr} = 573 K

1 ns, 355 nm, T_{cr} = 6000 K

1 ns, 532 nm, T_{cr} = 573 K
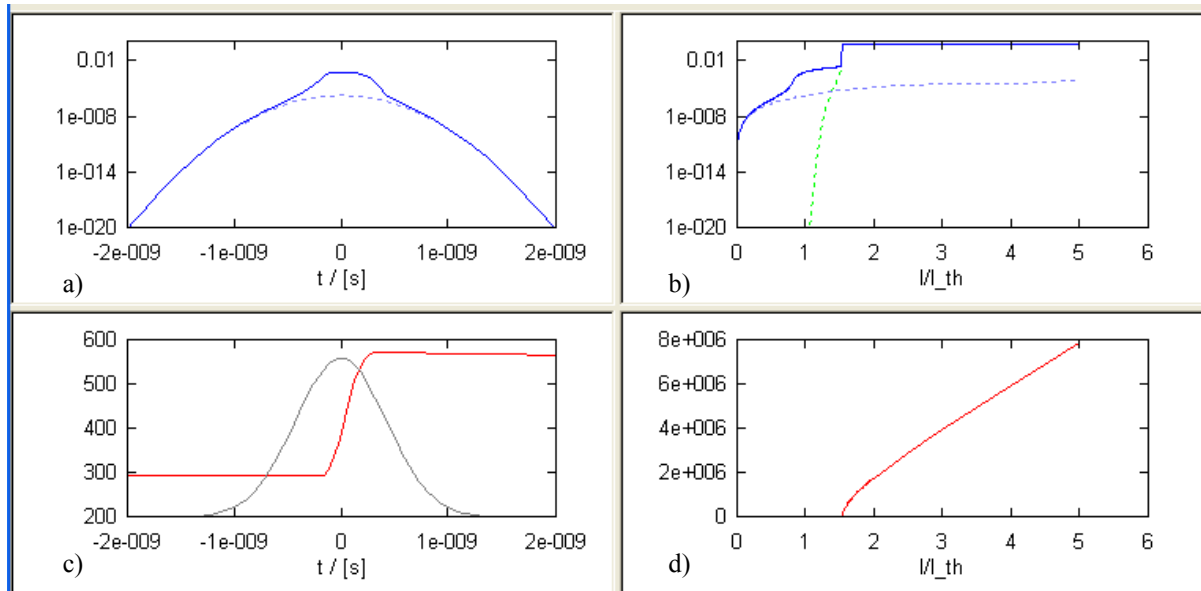
1 ns, 532 nm, T_{cr} = 6000 K
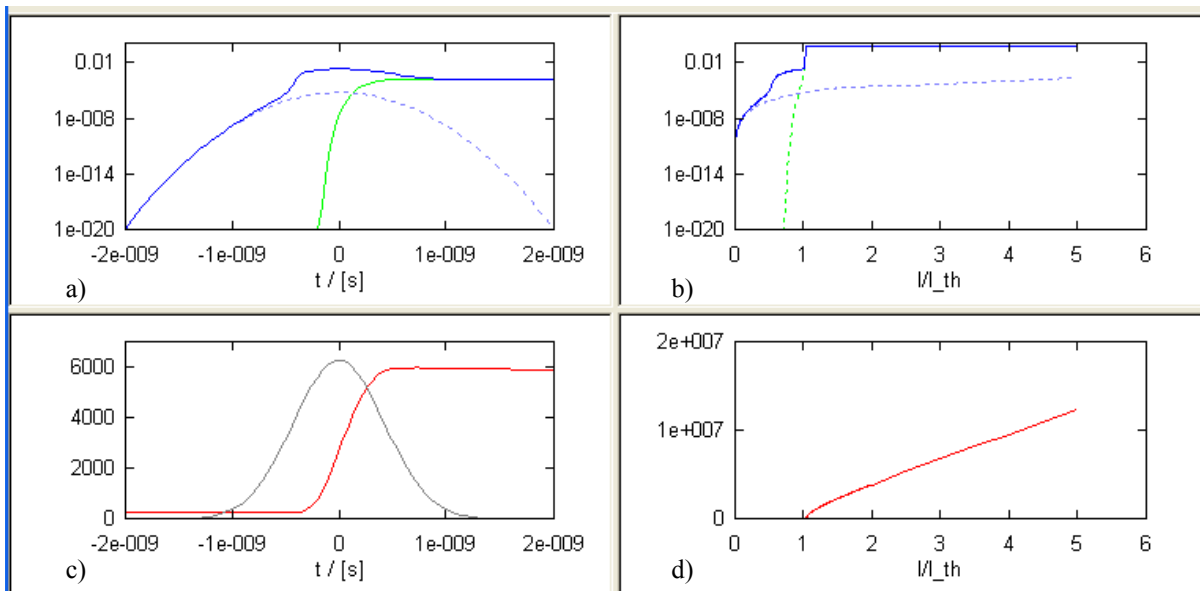
1 ns, 1064 nm, T_{cr} = 573 K
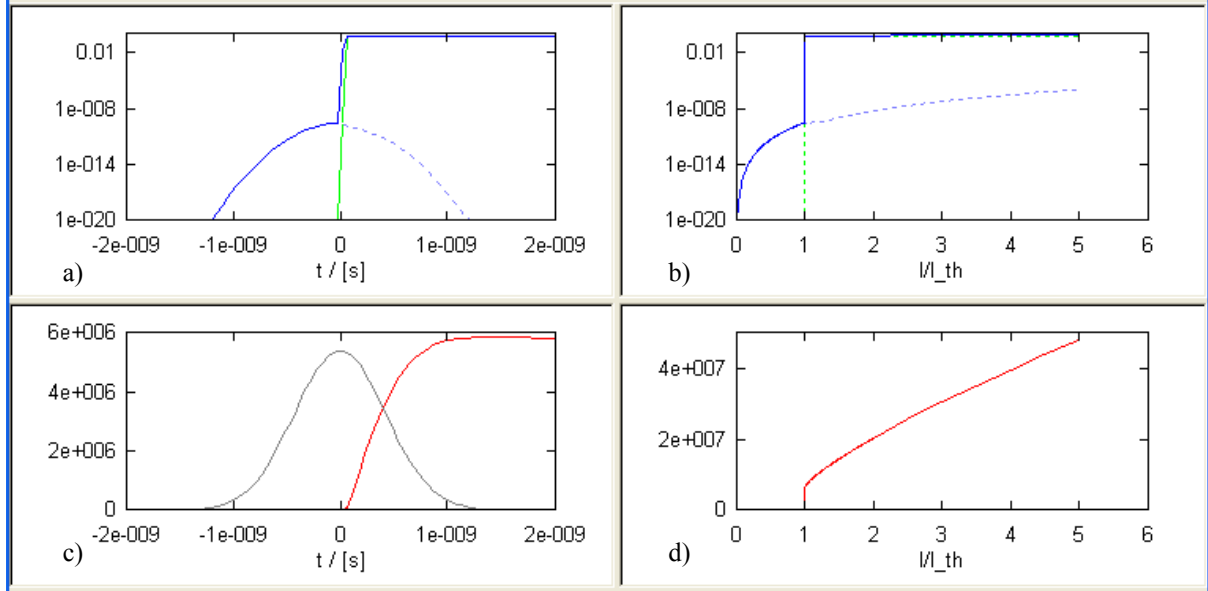
1 ns, 1064 nm, T_{cr} = 6000 K

Figure 4.7 Numerical simulations of plasma formation by 1-ns pulses at wavelengths of 355 nm, 532 nm, and 1064 nm. In each plate, a) portrays the evolution of the ionization degree R as a function of time, b) presents the maximum ionization degree produced during a laser pulse as a function of normalized irradiance, c) shows the temporal evolution of the plasma temperature (red) in relation to the temporal shape of the laser pulse (grey), and d) shows the peak temperature reached during breakdown as a function of normalized irradiance.

10 ns, 355 nm, T_{cr} = 573 K

10 ns, 355 nm, T_{cr} = 6000 K

10 ns, 532 nm, T_{cr} = 573 K

a) b) c) d)
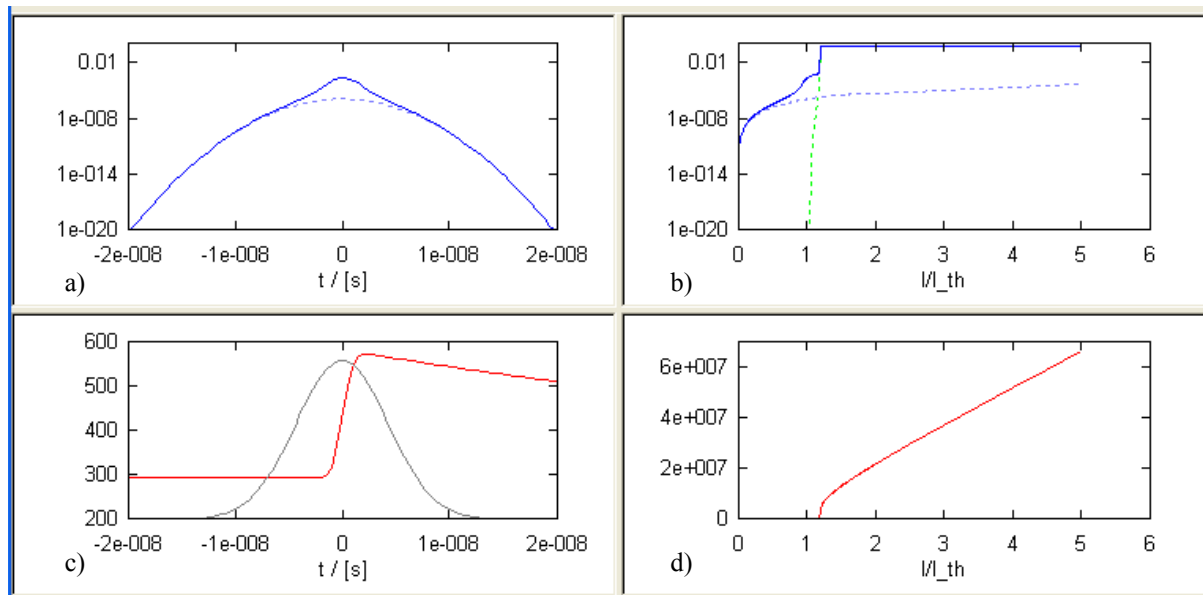
10ns, 532 nm, T_{cr} = 6000 K

a) b) c) d)
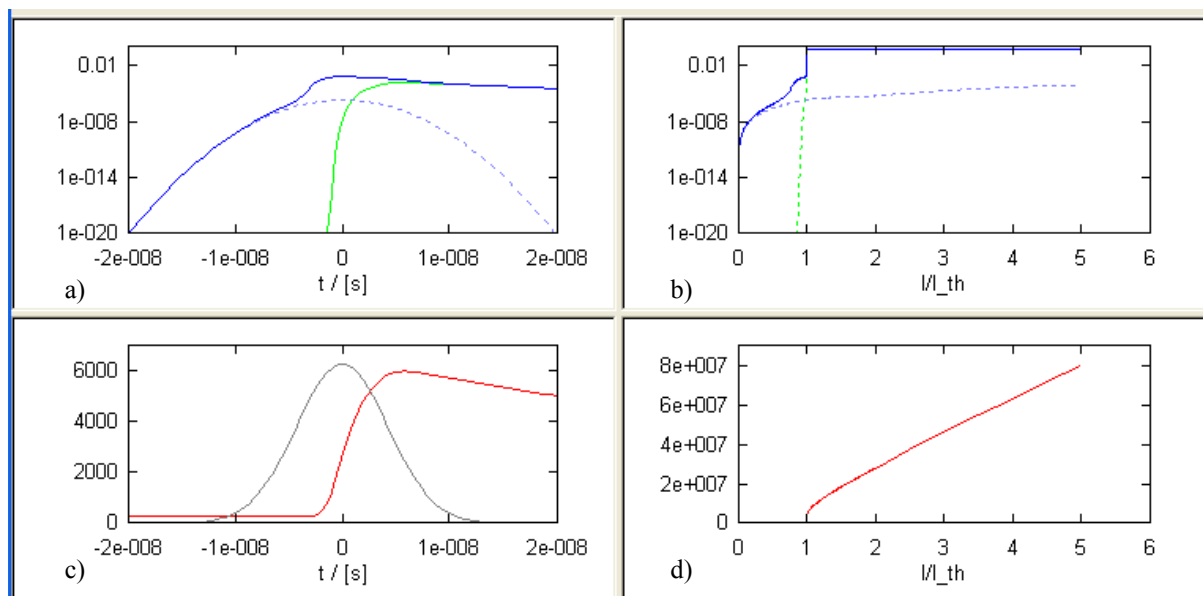
10 ns, 1064 nm, T_{cr} = 573 K
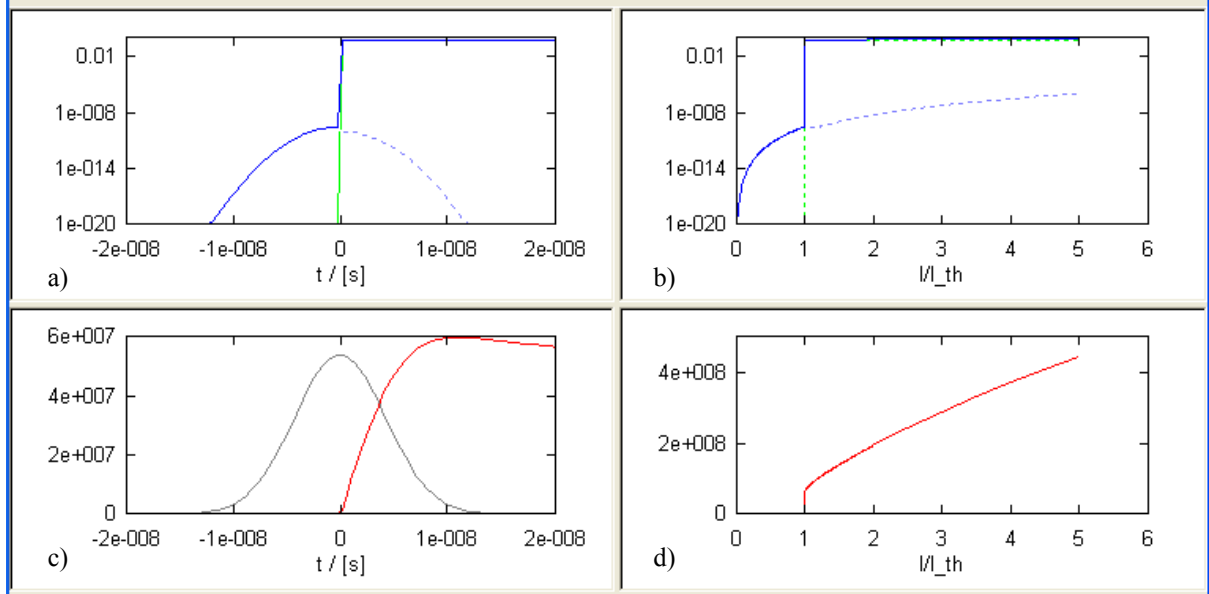
10 ns, 1064 nm, T_{cr} = 6000 K
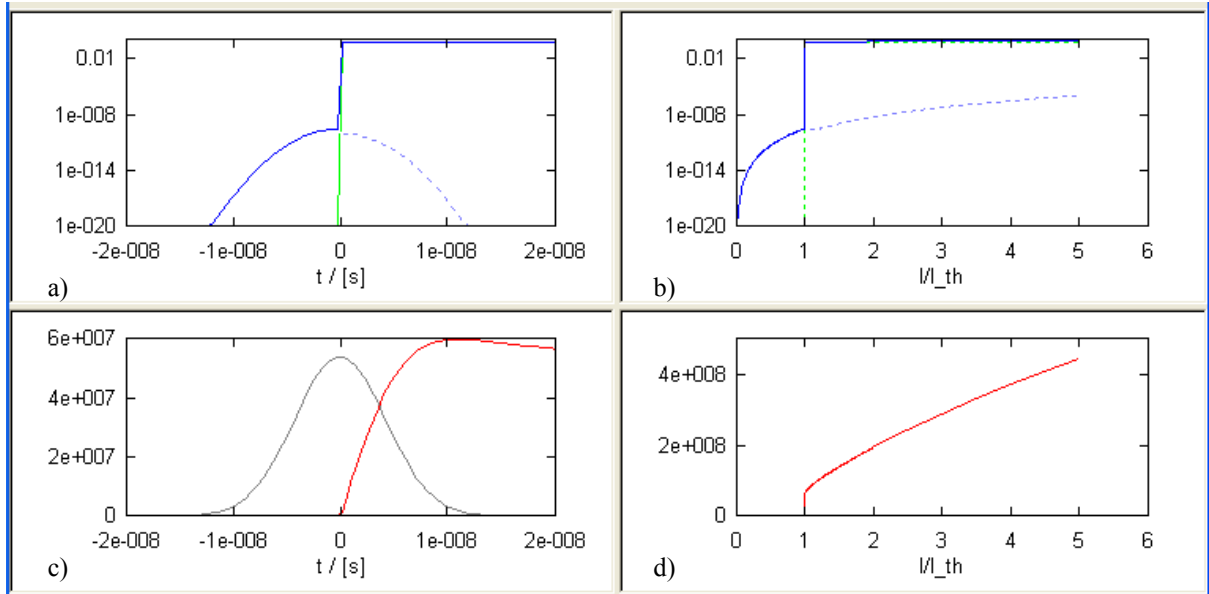
Figure 4.8 Numerical simulations of plasma formation by 10-ns pulses at wavelengths of 355 nm, 532 nm, and 1064 nm. In each plate, a) portrays the evolution of the ionization degree R as a function of time, b) presents the maximum ionization degree produced during a laser pulse as a function of normalized irradiance, c) shows the temporal evolution of the plasma temperature (red) in relation to the temporal shape of the laser pulse (grey), and d) shows the peak temperature reached during breakdown as a function of normalized irradiance.

In the following, we first give a qualitative interpretation of the breakdown dynamics for the different pulse durations and wavelengths as revealed by the numerical simulations. In section 4.2.2.3. and 4.2.2.4., we then compare the predicted threshold values for bubble formation with our measurement results for seeded and non-seeded pulses, respectively. To facilitate the comparison between different pulse durations and wavelengths, all plots for the time evolution of the ionization degree at the bubble and BPL thresholds are combined in one tableau in **Figs. 4.9 and 4.10**, respectively, and all plots for the irradiance dependence of the maximum ionization degree are composed into one tableau in **Fig. 4.11**.
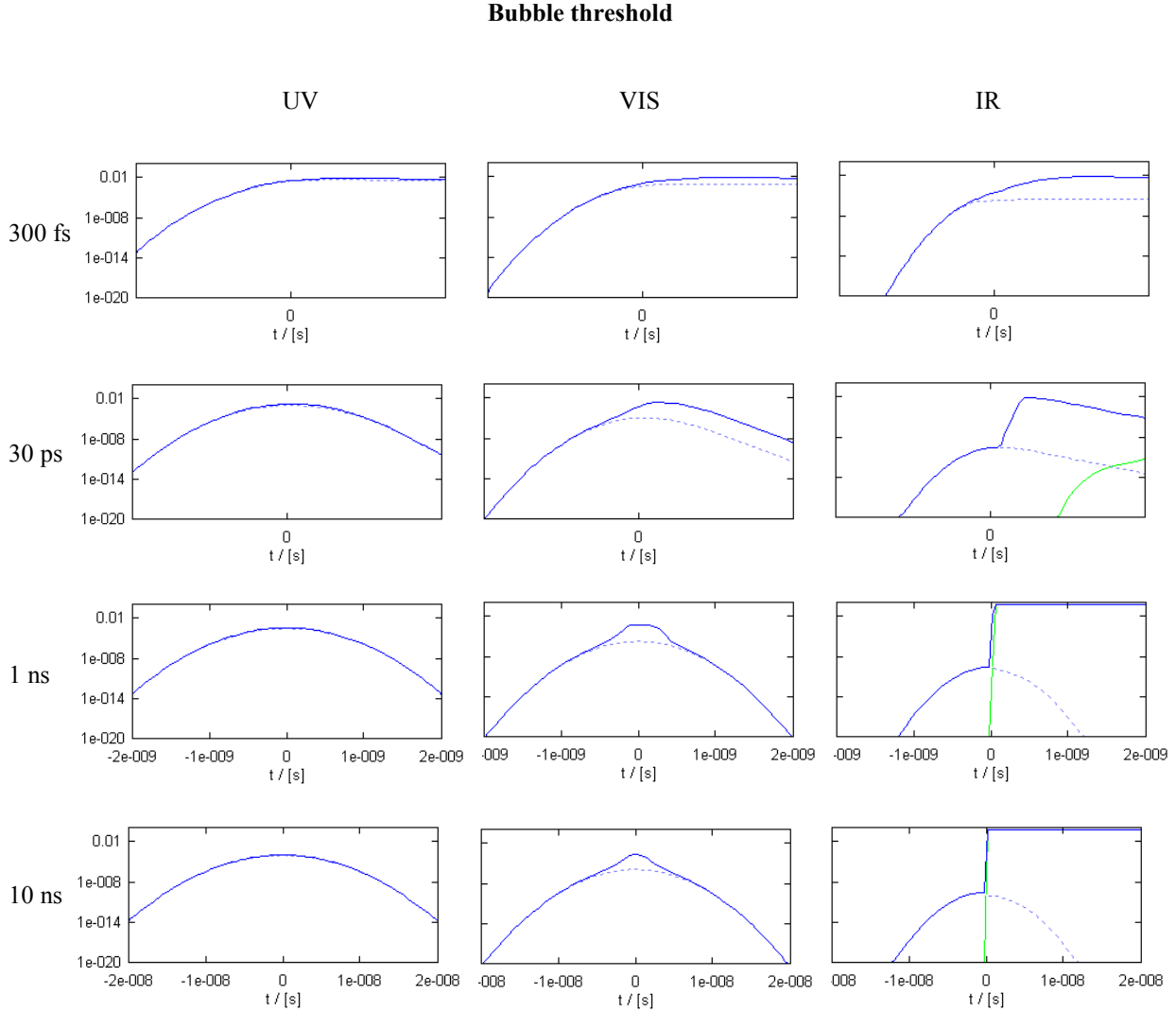
Bubble threshold

Figure 4.9 Time evolution of the ionization degree R at the bubble formation threshold (T_{cr} = 4441 K for 300 fs and 30 ps, T_{cr} = 573 K for 1 ns and 10 ns) for UV, VIS and IR wavelengths and pulse durations of 300 fs, 30 ps, 1 ns, and 10 ns.

BPL threshold

UV   VIS   IR
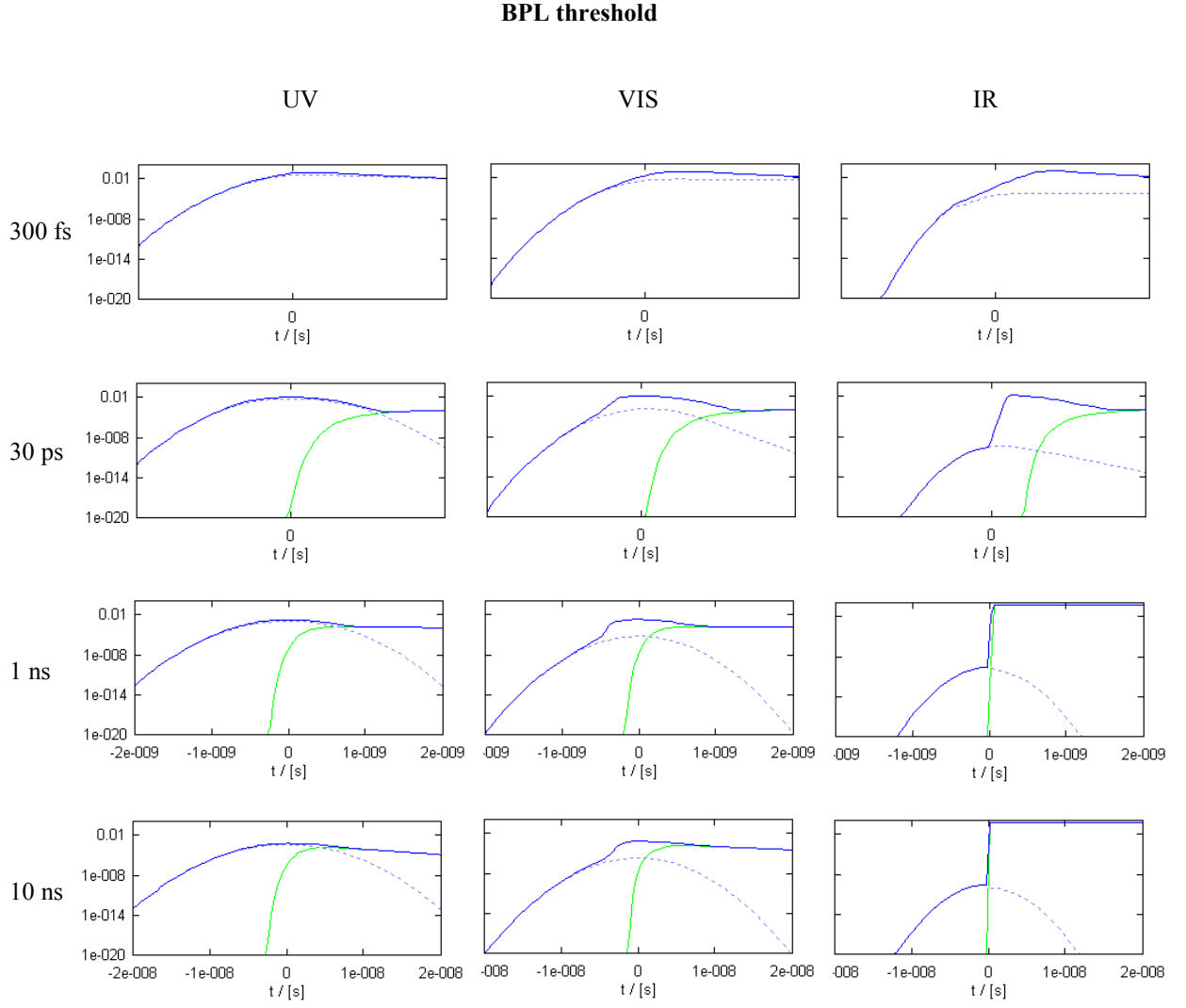
Figure 4.10 Time evolution of the ionization degree, $R(t)$, at the BPL threshold ($T_{cr} = 6000$ K) for UV, VIS and IR wavelengths and pulse durations of 300 fs, 30 ps, 1 ns, and 10 ns.
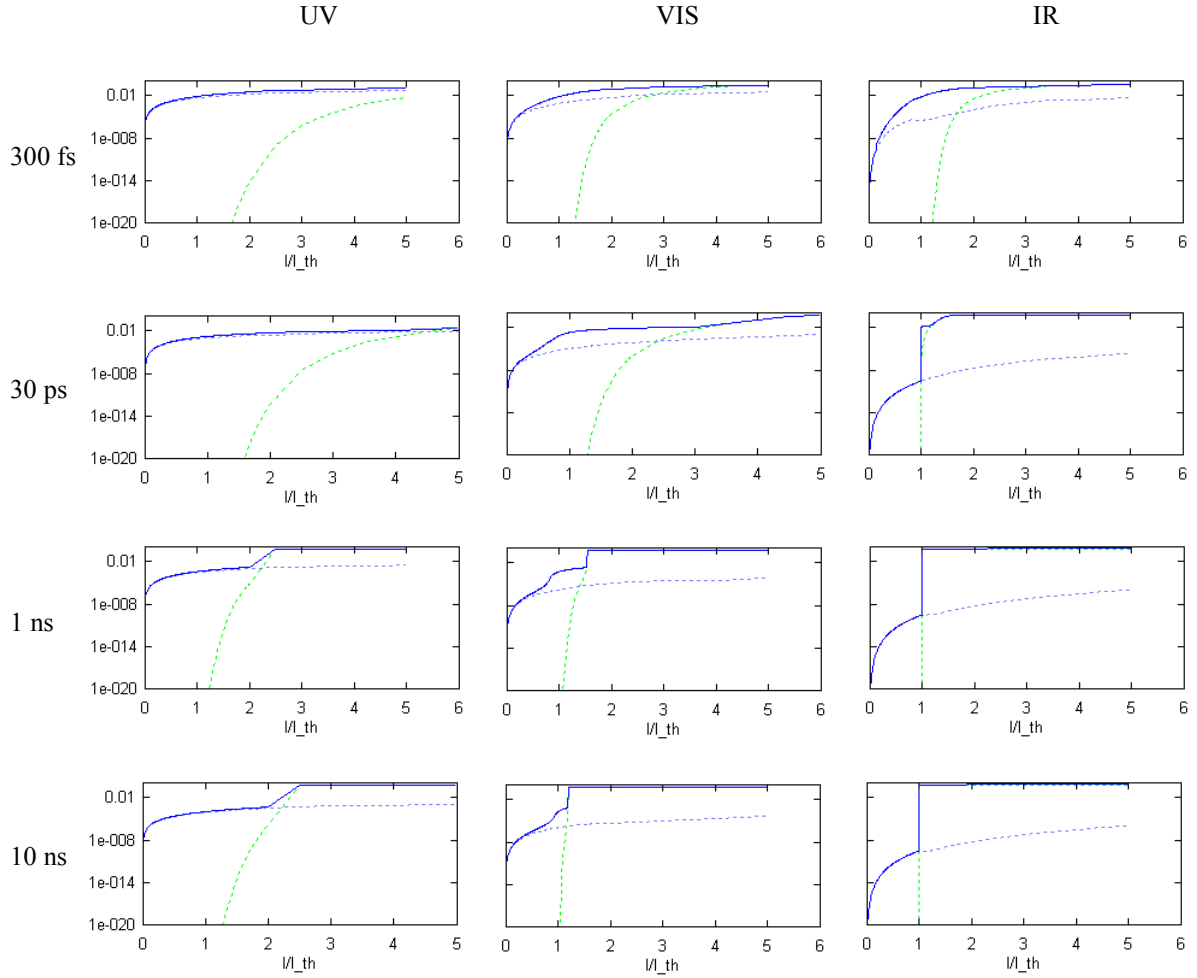
Figure 4.11 Irradiance dependence of the maximum ionization degree, $R(I/I_{th})$, for UV, VIS and IR wavelengths and pulse durations of 300 fs, 30 ps, 1 ns, and 10 ns.

Time evolution of the degree of ionization, R(t) at the bubble threshold. For UV pulses, ionization at the bubble formation threshold gradually increases during the pulse and is mainly driven by photoionization (PI). Even for nanosecond UV-pulses with no time constraints for avalanche ionization (AI), it produces only 20 % of the free electrons in comparison to PI. By contrast, for IR pulses, PI provides merely seed electrons, and by far the largest contribution to ionization arises from AI. This applies even for 300-fs pulses where 160 times more electrons are ionized by AI than by PI and the contribution of AI rises rapidly for super-threshold energies. Because AI is very efficient at IR wavelengths, a gradual increase of ionization is observed only for 300 fs. For IR pulses $\geq$ 30 ps the ionization avalanche progresses in a fraction of the pulse duration, and for pulses $\geq$ 1 ns, the avalanche does not stop at a value corresponding to the target temperature but, once initiated, immediately progresses to almost full ionization, altogether by more than 10 orders of magnitude. While for τ_L < 1 ns electron-hole recombination ($\propto \rho^2$) limits the free-electron density, thermal ionization (TI) overcomes recombination for $\tau_L \geq$ 1 ns, and full-density plasmas are produced in a runaway process. Therefore, bubble and BPL threshold coincide. For VIS wavelengths, an intermediate behavior is observed: when AI sets in, it leads to a rapid increase of the ionization degree by several orders of magnitude but at the trailing edge of the laser pulse ionization is rapidly diminished by recombination, especially for $\tau_L \geq$ 1 ns.

Time evolution of the degree of ionization, R(t) at the BPL threshold. At the BPL threshold, PI remains the dominant ionization mechanism for UV wavelengths during the initial part of the laser pulse but finally, after the peak of the pulse, TI becomes the dominant ionization mechanism. While in ns breakdown TI takes over the leading role already during the laser pulse, this occurs well after the laser pulse in fs breakdown because the thermalization time is in the order of 10-20 ps.

Figure 4.12 shows this process on an extended time scale. For T_{cr} = 6000 K, R drops initially faster than for T_{cr} = 424.5 K because recombination is proportional to ρ^2 but then levels out due to TI.
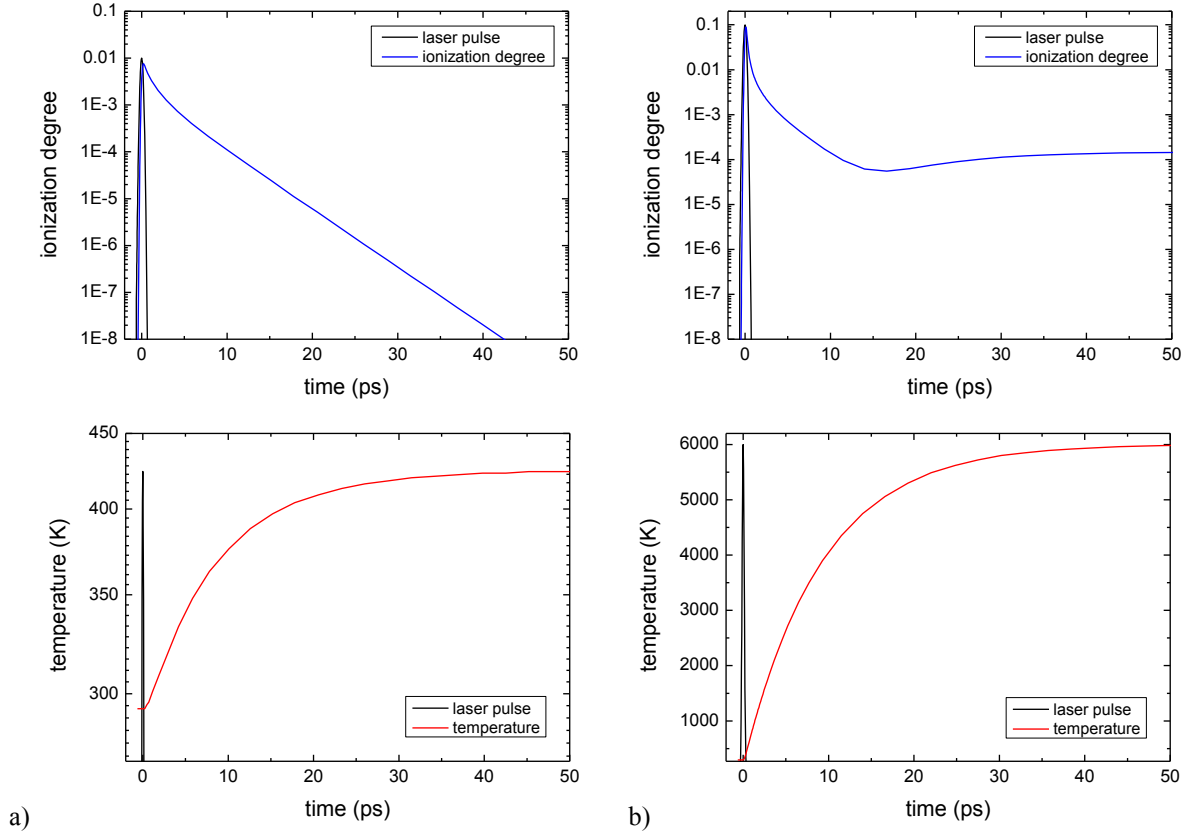
Figure 4.12 Evolution of the ionization degree (top row) and plasma temperature (bottom row) in relation to the temporal shape of a UV 300-fs laser pulse, a) for T_{cr} = 424.5 K, and b) for T_{cr} = 6000 K. The time scale is extended far beyond the laser pulse duration to include the thermalization time and the onset of heat diffusion.

For IR pulses, the breakdown dynamics at the BPL threshold differs from that at the bubble threshold only for $\tau_L \leq 30$ ps but is identical for nanosecond pulses where bubble and BPL thresholds coincide. For ns pulses, AI+TI immediately progress to full ionization in a runaway process. For VIS pulses, Fig. 4.11 suggests that a very small irradiance range exists around the BPL threshold in which recombination is capable of balancing AI+TI. This is the case shown in Fig. 4.10 where for VIS ns breakdown full ionization is not reached

In those cases, in which AI+TI balance or overcome recombination, the model predicts a very slow decrease of the ionization degree after the end of the laser pulse (no decrease at all is visible for IR pulses and $\tau_L \geq 1$ ns). This model prediction is physically not correct because the rapid plasma expansion leads to adiabatic cooling which allows for recombination to occur once the temperature has dropped below the critical temperature for AI+TI runaway. However, as the model considers only thermal diffusion but neglects hydrodynamic processes, it does not incorporate the consequences of plasma expansion.

Irradiance dependence of the maximum ionization degree, $R_{max}(I/I_{th})$, and temperature, $T_{max}(I/I_{th})$ for UV breakdown. For UV femtosecond pulses, the maximum degree of ionization and the peak temperature gradually increase with increasing irradiance. For small irradiances, in the initial part of the $R_{max}(I/I_{th})$ curve, PI dominates but TI in conjunction with AI become more important when the irradiance is increased and finally begin to dominate for $I/I_{th} > 5$. For longer UV pulses, a stepwise behavior develops. PI still dominates in the initial part of the $R_{max}(I/I_{th})$ curve but then a relatively fast changeover to a dominance of TI+AI occurs. This changeover becomes faster with increasing pulse duration (Figs. 4.7 and 4.11). The irradiance corresponding to the bubble formation threshold lies within the initial part of the $R_{max}(I/I_{th})$ curve, while the irradiance corresponding to the onset of plasma luminescence is located where R_{max} abruptly rises. Thus the model predicts that for UV femtosecond breakdown we should observe a gradual increase of plasma luminescence when the irradiance is raised above the bubble formation threshold while for UV nanosecond breakdown we should

observe a distinct BPL threshold. This prediction is in excellent agreement with our experimental finding of two separate, sharp thresholds for bubble formation and BPL in UV ns breakdown.

At short wavelengths, the cascade ionization rate is relatively small (it is proportional to $(1/\omega^2)$, see Eq. 2.11, and the cascade is slowed down by recombination processes once a large free electron density is reached. For pulse durations longer than the recombination time, this establishes a dynamic equilibrium in which the energy input into the electronic system by the laser irradiation is balanced by thermalization of the energy of the free electrons through collisions and recombination. The equilibrium is reached in a low density plasma regime with an ionization degree R of about 10^{-3} (i.e. 0.1%,) with R increasing with irradiance. The dynamic equilibrium is associated with heating of the focal volume, and since the thermal ionization rate depends exponentially on temperature (see Eq. 2.33), thermal ionization will overcome recombination once a critical temperature is exceeded. When this has happened, the runaway process starts in which the accelerated ionization process leads to a faster heating that accelerates ionization even further, and a full density plasma is produced. Note that both avalanche ionization and thermal ionization contribute to this runaway process. As the energy input from laser irradiation occurs mainly via inverse Bremsstrahlung absorption (at large free electron densities this process dominates compared to multiphoton ionization), the runaway process cannot just be described as ‚thermal runaway,' even though it is triggered and partially mediated by thermal ionization. The sharp increase of R_{max} results in a sharp BPL threshold.

For UV ns pulses, the BPL threshold is close to the irradiance at which thermal ionization can overcome recombination and full-density plasmas start to be produced in a runaway process. For τ_L = 30 ps, runaway to full ionization occurs only at slightly larger irradiance than BPL, and for τ_L = 300 fs no runaway occurs but the R_{max} increase is smooth. The sharp BPL threshold for ns pulses is associated with an abrupt increase in T_{max}. Nevertheless, T_{max} continues to increase with irradiance even above the BPL threshold because the runaway process occurs at an ever earlier time during the laser pulse.

It must be emphasized that the T_{max} values above the BPL threshold are unrealistically high because our model does not consider the plasma growth with increasing irradiance that shields the focal region but assumes that the entire laser energy reaches the beam waist even at energies well above the BPL threshold. Moreover, the model does not consider the enlargement of the plasma volume beyond the laser cone angle by radiative energy transport (see section 5.4) and the rapid hydrodynamic plasma expansion that leads to a rapid adiabatic cooling. Experimental and theoretical investigations of plasma-induced cavitation bubble generation suggest that the hydrodynamic expansion sets in after a few nanoseconds [Vog96a]. It is thus relevant for the temperatures reached in nanosecond optical breakdown but plays no role for picosecond or femtosecond pulses. For irradiance values up to the bubble threshold, the model predictions of T_{max} are realistic. For $I_{bubble} < I < I_{BPL}$, the predicted T_{max} value rises faster with irradiance than in reality because the model neglects plasma growth and shielding. This leads to an underestimate of the energy gap between bubble and BPL threshold. This underestimate becomes ever more important the larger the energy gap is, i.e. with increasing laser pulse duration. For example, the measured energy of the BPL threshold at $\approx$ 10 ns pulse duration is 10-30$\times$ larger than the bubble formation threshold (depending on wavelength), while the energy ratio predicted by the model lies between 1.2 (VIS) and 2.0 (UV).

Irradiance dependence of the maximum ionization degree, $R_{max}(I/I_{th})$, and temperature, T_{max} (I/I_{th}) for IR breakdown. For IR fs breakdown, the $R_{max}(I/I_{th})$ curve increases gradually but with a steeper slope than for UV fs breakdown. However, for IR ns breakdown, the threshold scenario is very different from UV ns breakdown: luminescent plasmas are produced in one step already at the bubble formation threshold. The avalanche progresses faster than for UV and visible wavelengths because of the high irradiance required to produce seed electrons by MPI, which is a 6-photon process for 1064 nm, and due to the larger cross section for inverse bremsstrahlung absorption. The degree of ionization increases by 10 orders of magnitude within a fraction of the laser pulse, and reaches a level of 5-10 % of maximum ionization before it can be shortly slowed down by recombination $\propto \rho^2$. At this high free-electron density, the focal volume is heated very rapidly within a fraction of the laser pulse duration, and runaway driven by TI+AI thus occurs already at the irradiance level where seed electrons by PI have just become available. This is the classical scenario of vigorous ns optical breakdown that is confirmed also by our present experimental results.

For IR breakdown at 30 ps, a two-step behavior is predicted, with a fairly high ionization degree in the plateau before full ionization is reached in the second step. This behavior can explain the two levels of plasma luminescence in the photographs of ps plasmas Fig. 2.6b. The plateau corresponds to weak luminescence, and bright luminescence is observed after the second step.

Irradiance dependence of the maximum ionization degree, $R_{max}(I/I_{th})$, and temperature, T_{max} (I/I_{th}) for VIS breakdown. For ns breakdown at visible wavelengths, we experimentally observed two separate thresholds for bubble formation and BPL, like for UV breakdown. This behavior is well reproduced by the model predictions. The general scenario for VIS breakdown at different pulse durations is intermediate between those for UV and IR wavelengths: AI plays a much larger role than in UV breakdown but can, in an intermediate range above the bubble threshold, still be balanced by recombination. Only for larger irradiance values, the temperature exceeds the critical value for runaway and BPL sets in. Due to the larger AI rate, the energy range between bubble and BPL threshold is narrower than for UV breakdown.

The model calculations explain, why IR breakdown is always a very vigorous process in which already at threshold the energy densities required for a phase transition are far exceeded. By contrast, with UV and VIS wavelengths the energy density in the low-density plasmas produced by the first breakdown step just exceeds the threshold for a phase transition, and the vigorous runaway process associated with the formation of brightly luminescent plasmas occurs only in the second step, at larger irradiance.

From the above results obtained with fixed wavelengths, we can conclude that the transition from ns breakdown with two separate thresholds for bubble formation and BPL to the vigorous behavior with only one threshold at which immediately full ionization occurs at a wavelength between 532 nm and 1064 nm. The results of the OPO measurements presented in section 4.3.1.1 demonstrate that already at 730 nm only one threshold is observed. Thus the transition occurs between 532 nm and 730 nm. It will be described in more detail in section 4.3.2.

Our discovery of the two steps in UV and VIS ns breakdown, the explanation of the second step by thermal ionization runaway, and the excellent agreement between experimental data and numerical predictions represent a milestone towards a better understanding of laser-induced breakdown. The two-step behavior can be correctly reproduced only by a model that considers both recombination *and thermal ionization* besides the usual terms of PI and AI. **Figure 4.13** demonstrates that our old rate equation model does predict the existence of a low-density plasma regime for UV and VIS laser pulses (hence, it could explain the formation of minute bubbles) because it considers recombination that limits the plasma density achievable by AI. However, it does not predict the abrupt increase of free electron density that corresponds to the experimentally observed distinct threshold for the formation of bright luminescent plasmas. Moreover, the maximum free electron densities predicted by the old model are much lower than with the new model where they reach full ionization, corresponding to $\rho = 6.64 \times 10^{22}$ cm^{-3}. Both shortcomings are due to the neglect of thermal ionization in the old model.
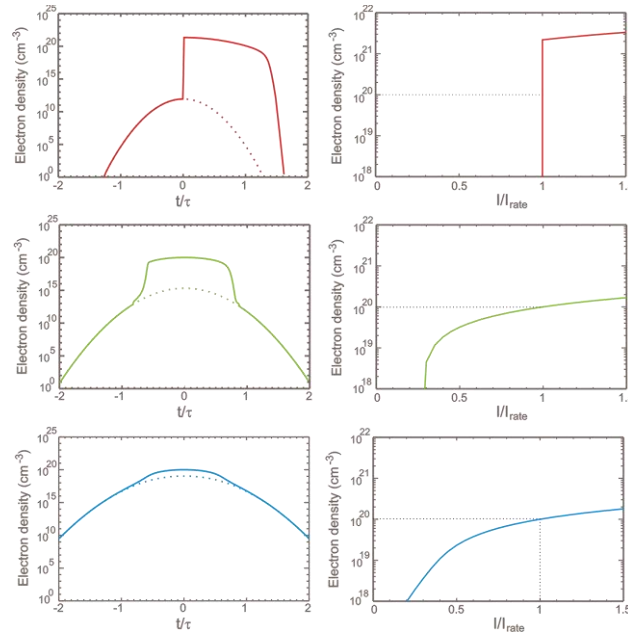
Figure 4.13 Numerical simulations of plasma formation by 6-ns pulses at wavelengths of a) 1064 nm, b) 532 nm, and c) 355 nm without consideration of thermal ionization, taken from [Vog01]. The left column shows the evolution of the free electron density as a function of the normalized laser pulse time. The free electron density produced by MPI is plotted as dotted line. The right column presents the maximum free electron density produced during a laser pulse as a function of irradiance. The old model does not reproduce the experimentally observed breakdown dynamics in two steps at UV and VIS wavelengths.

The discovery of separate thresholds for bubble formation and BPL in ns breakdown implies the existence of an irradiance range in which the energy deposition can be precisely tuned, similar to fs breakdown. No tunability at all is only observed in parameter regions in which the creation of seed electrons is the critical hurdle for breakdown, i.e. for IR ns pulses. The tunability range is wide whenever AI is slowed down, either by time constraints such as in fs bd, or by a small AI rate such as in UV ns breakdown (or by a combination of both such as in UV fs breakdown). A map of the tunability range in the (τ_L, λ) parameter space is presented in section 4.5.

4.2.2.3. Pulse duration dependence at different wavelengths

Figure 4.14 presents a comparison of the experimental bubble threshold data of Fig. 4.4b with the predictions of our numerical model. The BPL threshold data are not included in the comparison because plasma growth and shielding, which influence the experimental BPL threshold, are not considered in the model.

As already mentioned in 4.2.2.1, the time between collisions of electrons with heavy particles, τ, and the seed electron density, ρ_{ini}, are not known for water. Therefore, they are used as fit parameters for the model calculations, and the fitting process is used as information source for the determination of these parameters.
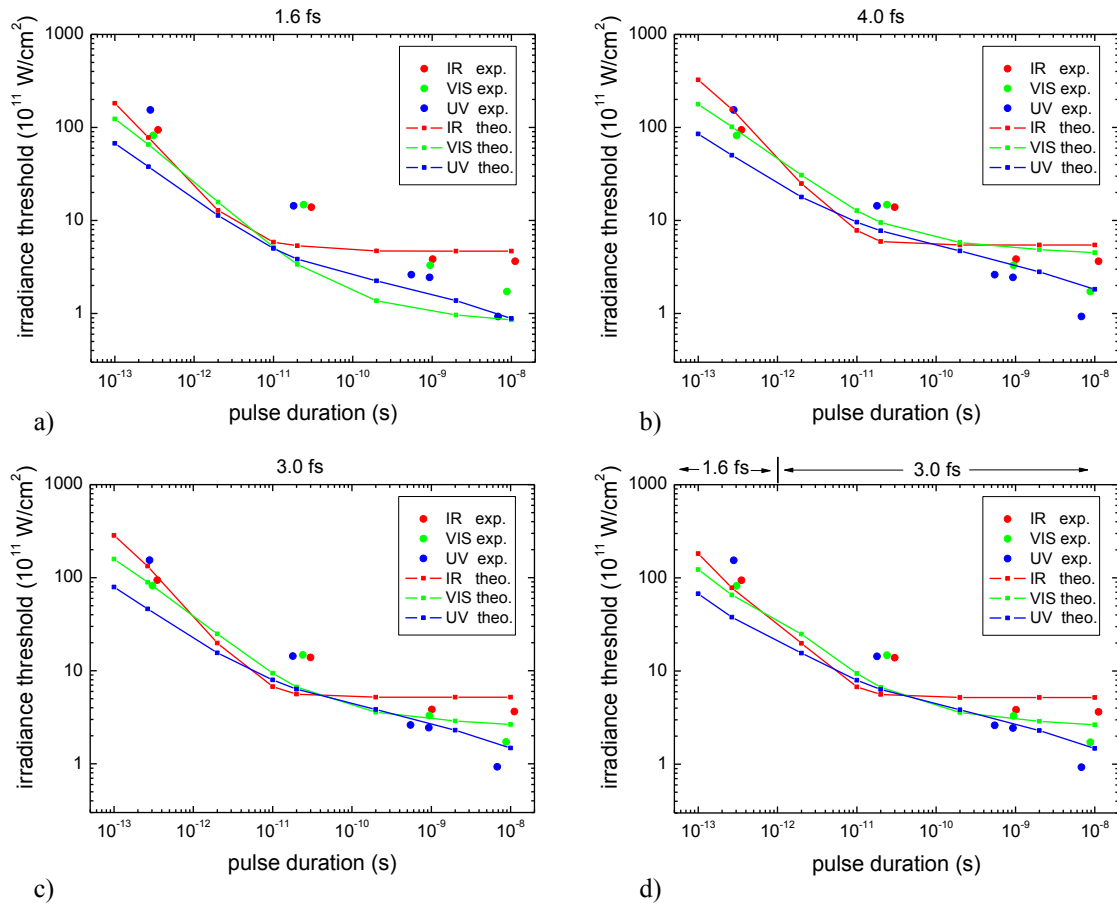
Figure 4.14 Comparison of numerical simulations and experimental results for the pulse duration dependence of the bubble threshold at fixed UV, VIS, and IR wavelengths for Gaussian pulses. The experimental values are taken from Fig. 4.4b. The seed electron density in all calculations is $\rho_{ini} = 2 \times 10^{13}$ cm^{-3}. The collision time is a) $\tau = 1.6$ fs, b) $\tau = 4.0$ fs, c) $\tau = 3.0$ fs, and d) $\tau = 1.6$ fs for pulse durations below 1 ps, and $\tau = 3.0$ fs for pulse durations above 1 ps.

Both experimentally and in the model calculations, the bubble threshold exhibits a monotonous decrease with increasing pulse duration for UV and VIS wavelengths but levels out in the ns range for IR pulses. For long IR pulses, the generation of seed electrons by photoionization (PI) becomes a critical hurdle for the onset of avalanche ionization. Here the breakdown threshold is determined by the peak irradiance of the laser pulse, and neither the time span available for avalanche ionization nor the AI rate play a decisive role. The observed similarity of the threshold values for IR pulses of $\approx$ 1 ns and $\approx$ 10 ns duration indicates intrinsic generation of seed electrons by PI. If linearly absorbing impurities provided seed electrons by thermionic emission, the threshold would be lower for the longer pulses that, at constant irradiance, contain much more energy.

In the regime in which generation of seed electrons by photoionization (PI) is the critical hurdle for the occurrence of breakdown, the threshold value remains constant when the collision time is varied but depends on ρ_{ini}. The value of $\rho_{ini} = 2\times10^{13}$ cm^{-3} that is obtained from fitting model predictions to the IR ns OPO data in section 4.3.2, provides a fair compromise in fitting the IR ps and ns data in Fig. 4.1.4.

The experimental 30-ps data are, for all wavelengths, larger than the model results. This may, at least partially, be due to the fact that we determined the ps data early in the research project by means of photographic detection of bubble formation. This technique is less sensitive than the probe beam scattering technique ([Vog08] and (3.2.4)) developed later, which will lead to an enlargement of the experimental threshold values.

The calculated $I_{th}(\tau_L)$ curves in Fig. 4.14 exhibit a strong dependence on the collision time τ, especially for durations $\tau_L \geq 10$ ps. Here not only the the absolute I_{th} values but also the ratio of these values for the different values are strongly affected by the choice of τ. Quite obviously, the collision time of 1.6 fs in Fig. 4.14a that yields the best match of model predictions with our fs OPA data (see section 4.3.2) does not provide the best fit for the ps and ns data at fixed UV and VIS wavelengths. The best agreement for the longer pulse durations was obtained with $\tau = 3$ fs in Fig. 4.14c. We explain this discrepancy by the dependence of the electron scattering rate on the energy of the free electrons [Arn92, Kai00] that was already mentioned in (4.2.2.1). The average energy of free electrons depends on the band gap and the oscillation energy of the free electrons in the electric field (see Eq. 2.1 and 2.15, respectively). It is larger for fs breakdown than for ps and ns breakdown because for fs breakdown the oscillation energy amounts to a considerable fraction of the band gap energy. Since, close to threshold, the electron scattering rate increases with free electron energy [Arn92], the theoretically expected collision rate is larger for fs breakdown than for ps and ns breakdown, in good agreement with our fitting results. Fig. 4.14d shows the calculated $I_{th}(\tau_L)$ curve with $\tau = 1.6$ fs for pulse durations below 1 ps, and $\tau = 3.0$ fs for pulse durations above 1 ps that leads to the best agreement between numerical calculations and experimental results.

4.2.2.4. Factors determining the intrinsic threshold sharpness for smooth pulses

A compilation of threshold sharpness values for smooth pulses (average values over all *NA*s investigated) is presented in **Table 4.7**. An analysis of the variation of these values with pulse duration and wavelength may provide some insight in the underlying breakdown dynamics. Values for 30-ps pulses are put into brackets because the measurements were performed in the initial project phase when the sensitive probe beam scattering method for bubble detection had not yet been developed. Moreover, the pulse-to-pulse energy fluctuations of the passively Q-switched and mode-locked laser pulses were large, in the order of $\pm$ 10%. Therefore, we are not sure how representative the low *S* value are for the physics of the breakdown process itself.

		UV	VIS	IR
≈300 fs	Bubble	65.3	42.6	19.6
≈30 ps	Bubble	(2.5)	(2.1)	(2.2)
≈1 ns	Bubble	58.4	60.0	19.2
	BPL	53.8	57.3	
≈10 ns	Bubble	3.3	7.0	19.2
	BPL	10.6	7.8	

Table 4.7 Summary of threshold sharpness values for bubble and bright plasma luminescence thresholds for fixed UV, VIS, and IR wavelengths at different pulse durations. The UV wavelength is 347 nm for the fs pulses and 355 nm otherwise; the VIS wavelength is 520 nm for the fs pulses and 532 nm otherwise, and the IR wavelength is 1040 nm for the fs pulses and 1064 nm otherwise. The *S* values are averaged from data at all investigated *NA*s.

The threshold sharpness for a phase transition induced by linear absorption and for plasma formation mediated by nonlinear absorption mainly depends on the statistics of the initiation process. Homogeneous nucleation at the spinodal limit will be associated with a sharp and well defined vaporization threshold, as much as inhomogeneous nucleation involving a large number density of bubble nuclei of similar size will result in a well-defined boiling point [Kis99, vog03]. In the same way, a large number density of intrinsically produced seed electrons as much as a large number of impurities with similar properties will be associated with a sharp breakdown threshold – provided that the laser pulse shape and energy is highly reproducible. By contrast, small number densities of seed electrons or impurities, and strong variations among the properties of individual impurities will lead to statistical variations of the breakdown process.

In the following, we restrict our discussion to intrinsic breakdown produced by smooth pulses; the role of intensity spikes in the pulse will be discussed in section 4.2.2.5, and the role of impurities in section 4.4. It is known that during fs breakdown seed electrons produced by PI are abundant. Therefore, it is not surprising that the threshold sharpness at $\tau_L \approx 300$ fs was found to be very high for all investigated wavelengths. However, it is remarkable that the IR breakdown threshold exhibits high sharpness ($S = 19.2$) even for 1 ns and 10 ns pulse duration where the generation of seed electrons constitutes the critical hurdle for breakdown. This finding implies that the seed electron density produced by PI must be sufficiently high to limit statistical variations to a relatively low degree. The average number of electrons per focal volume for a seed electron density of $\rho_{ini} = 2\times10^{13}$ cm^{-3} and $\lambda = 1064$ nm is 148 at NA = 0.9. This implies that even around the intensity peak at the focus center sufficiently many seed electrons are located to reliably initiate breakdown.

Another remarkable observation is the low sharpness of the bubble formation threshold for UV breakdown at ≈ 10 ns duration ($S = 3.3$). Sharpness values are higher the BPL thresholds, and all thresholds relating to the microchip laser pulses. Likely, the sharpness depends on the local slope of $\rho_{max}(I)$ curve or $T(I)$ curve, respectively at the bubble and BPL thresholds (see Figs. 4.5 – 4.8). If the slope is low, large energy variations are required to induce small temperature variations, corresponding to low threshold sharpness. Close to the BPL threshold, the ionization degree varies always very strongly with pulse energy, and the BPL thresholds are sharp. However, at the bubble formation threshold for UV pulses of ≈ 10 ns duration, the local slope of the $\rho_{max}(I)$ curve is very small

For microchip laser pulses of VIS and UV wavelengths, both bubble and BPL thresholds are extremely sharp, with $S \approx 60$. Thus, the breakdown probability increased from 10 % to 90 % when the pulse energy is raised by only 1.7 %. This rapid increase could be resolved because of i) the high pulse-to-pulse stability of the laser, and ii) the possibility of precise energy variation in small steps by means of a motorized stage for a rotation of the Fresnel rhomb retarder in front of the Glan laser polarizer, which has been established in the course or our research project (Figs. 3.6 and 3.10). However, in the light of the low S value for UV breakdown at ≈ 10 ns duration, which cannot be just related to measurement uncertainties, we must also relate this observation to the local slope of the $\rho_{max}(I)$ curve.

4.2.2.5. Comparison of thresholds for seeded and unseeded pulses

We implemented in our model the possibilities to calculate the breakdown threshold and dynamics for arbitrary pulse shapes, either measured or described by an analytic function. We now use this feature to compare the threshold predictions for seeded (slm) pulses and unseeded (mm) pulses to the experimental values. The threshold was calculated for a Gaussian pulse and for 6 measured unseeded pulse shapes of equal energy. We used $\rho_{ini} = 2\times10^{13}$ cm^{-3} for the seed electron density, and a collision time $\tau = 3$ fs, as determined in 4.2.2.3. We first determined the irradiance threshold for a given measured pulse shape and then calculated the energy by integration over the temporal pulse shape and the radiant exposure distribution in the focal spot.

To calculate the energy of a Gaussian pulse $I(t) = I_0 \exp[-4\ln2\,(t/\tau)^2]$ focused to a spot with diameter D, we first convert the irradiance to radiant exposure:

$$\Phi(t) = \int I(t)\,dt = \int I_0 \exp[-4\ln2\left(\frac{t}{\tau}\right)^2]\,dt = I_0\int \exp[-\left(2\sqrt{\ln2}\left(\frac{t}{\tau}\right)\right)^2]\,dt$$

$$= \frac{\tau}{2\sqrt{\ln2}} I_0 \int \exp[-\left(2\sqrt{\ln2}\left(\frac{t}{\tau}\right)\right)^2]\, d\left(2\sqrt{\ln2}\left(\frac{t}{\tau}\right)\right) = \frac{\sqrt{\pi}}{2\sqrt{\ln2}} I_0\,\tau = 1.0645 \times I_0\,\tau \tag{4.1}$$

Assuming a top-hat irradiance distribution, this radiant exposure corresponds to the energy

$$E = \Phi \times A = \Phi \times \pi\left(\frac{D}{2}\right)^2. \tag{4.2}$$

In order to consider the real spatial distribution of the radiant exposure in the focal area, a factor of (1/2) needs to be added, which yields the result

$$E = \frac{\Phi}{2}\,\pi\left(\frac{D}{2}\right)^2 = \frac{\Phi}{2}\,\pi\left(\frac{1}{2}\times\frac{1.22\,\lambda}{NA}\right)^2 = \frac{\Phi}{2}\,\pi\left(\frac{0.61\lambda}{NA}\right)^2 \quad \text{and, after inserting } \Phi \text{ from (4.1)}$$

$$E = \frac{1}{2}\times1.0645\times I_0\,\tau\,\pi\left(\frac{\lambda}{NA}\right)^2 \times 0.61^2 = 0.6222 \times I_0\,\tau\left(\frac{\lambda}{NA}\right)^2 \tag{4.3}$$

The results are summarized in **Table 4.8** and **Fig 4.15**.

		UV	VIS	IR
Pulse duration [ns]	measured	6.8	8.8	11.2
E_{th} **Gaussian** [µJ]	measured	1.40	7.50	80.8
	calculated	3.56	9.38	64.0
E_{th} **unseeded** [µJ]	measured	0.60	1.99	25.0
	calculated	2.53	7.36	39.6
E_{th} **Gaussian/** E_{th} **unseeded**	measured	2.33	3.77	3.23
	calculated	1.41	1.28	1.62
S (unseeded)	measured	0.7	1.1	2.7
	calculated	5.6	3.5	4.8

Table 4.8 Measured and calculated values of the bubble formation thresholds for seeded and non-seeded nanosecond pulses at different wavelengths. The calculated threshold value for the unseeded pulses is an average value based on 6 measured pulse shapes. The experimental threshold sharpness is $S = E_{th}/\Delta E$, where ΔE refers to the 10% and 90% values of the breakdown probability curve. For the calculated threshold sharpness, ΔE refers to the highest and lowest threshold value.
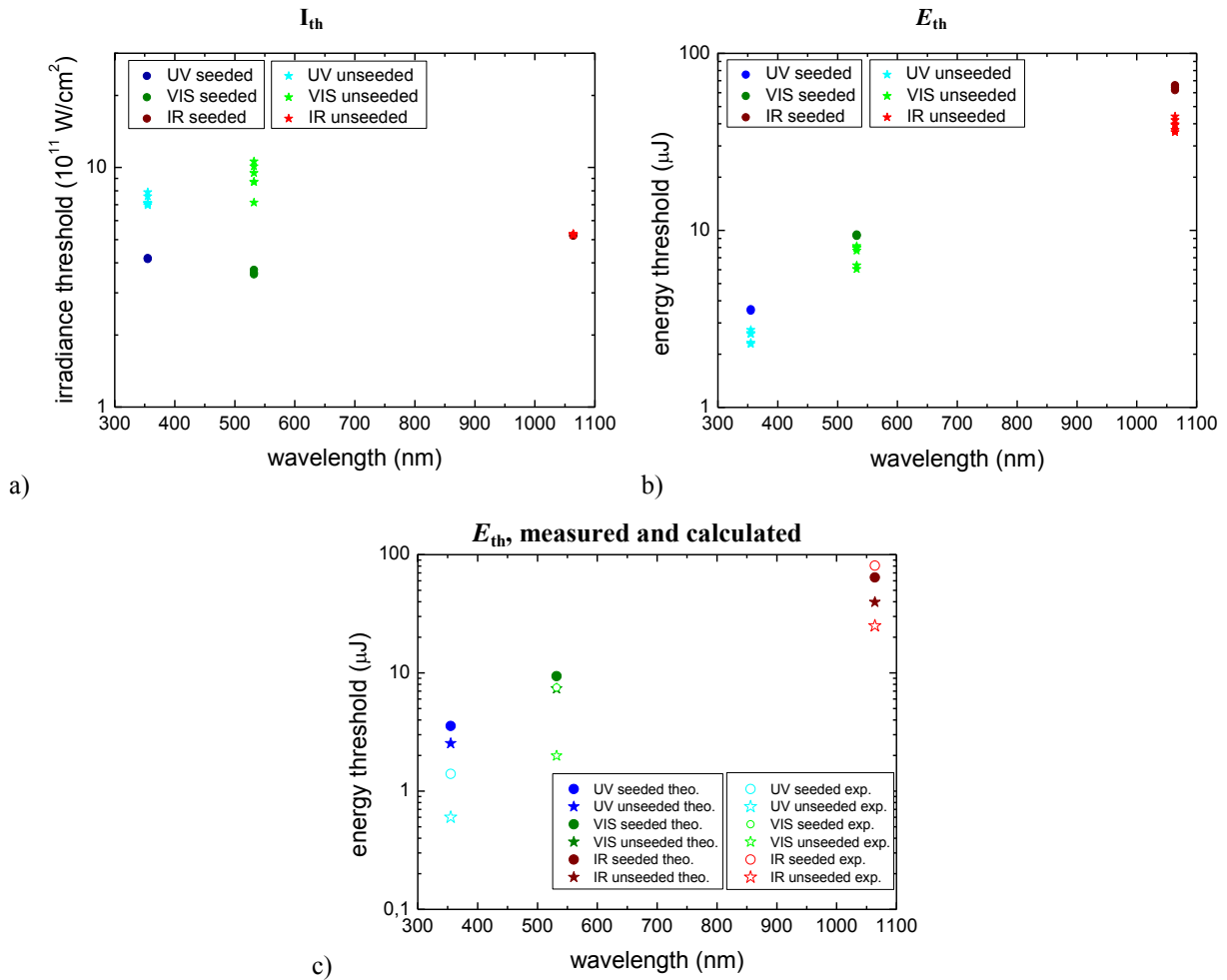
Figure 4.15 Numerical simulations for the bubble thresholds of seeded and unseeded pulses at different wavelengths. UV: 355 nm, 6.8 ns, VIS 532 nm, 8.8 ns, IR 1064 nm, 11.2 ns. a) irradiance thresholds based on 6 different measured pulse shapes, b) corresponding energy thresholds, c) comparison of numerical simulations and experimental results.

For IR breakdown, the irradiance threshold I_{th} is the same for all pulse shapes (Fig. 4.15a) because the creation of seed electrons by PI is the critical hurdle for breakdown. However, the corresponding energy thresholds E_{th} for unseeded pulses vary (Fig. 4.15b) because the same peak irradiance can be associated with different pulse energies due to the statistical variations in the distribution of intensity spikes. For UV and VIS pulses, not only the energy threshold varies but also the irradiance threshold because PI provides a considerable contribution to the total free electron density which critically depends on the amplitudes of the spikes. The degree of statistical variations determine the value of the threshold sharpness S.

While the absolute values of calculated and experimental bubble thresholds agree fairly well in Fig. 4.15c, the difference between thresholds for seeded and unseeded operation is, for all wavelengths, considerably larger in the experimental observations than in the numerical predictions. The model does also not yet portray the full degree of statistical threshold variations (S values are too large). Moreover, for UV and VIS breakdown the model predicts a two-step behavior with increasing irradiance, similar to that for Gaussian pulses in Fig. 4.8. In reality, for non-seeded, spiky laser pulses, no stable low-density plasma regime was observed at any laser wavelength but breakdown was always associated with BPL. We must conclude that some important aspects are not yet considered in our breakdown model. One important aspect not considered in the model is the interplay between local avalanches starting around individual seed electrons and global avalanche that finally arises from the merging of the many local avalanches by electron and heat diffusion. This interplay might be different in smooth and spiky pulses due to the different ratio of the contributions of PI and AI. Spikes in UV and VIS pulses correspond to a larger seed electron density created by MPI early in the laser pulse and thus to an earlier merging of local avalanches to one global avalanche. However, it is not yet clear how this should push the breakdown process into the runaway regime and prevent the formation of minute bubbles.

4.3. Wavelength dependence of nanosecond and femtosecond breakdown

4.3.1. Experimental results

4.3.1.1. OPO measurements of nanosecond breakdown

We measured the bubble formation thresholds in water produced by slm OPO ns laser pulses of ≈ 2 ns duration for 21 wavelengths ranging from 725 nm to 1025 nm. The pulses were focused through water immersion objectives with $NA = 0.8$ and $NA = 0.9$, respectively. The probability curves are presented in Fig. 11.14 of the Appendix. The energy thresholds derived from the probability curves are summarized in **table 4.9**, together with P_{th}, F_{th} and the irradiance threshold I_{th}. The M^2 values of Fig. 3.8 that are listed also in table 4.9 were used to calculate F_{th} and I_{th}. All I_{th} values refer to the temporal and spatial peak irradiance in the pulse and laser focus, respectively, while the F_{th} values refer to the spatial peak of the radiant exposure.

The sharpness of the thresholds ranges between 2.0 and 19.4. The average value is $S = 6.0$, which is between the sharpness values of the thresholds for unseeded ($S = 2.7$) and seeded ($S = 24.9$) laser pulses with fixed IR wavelength (Table 4.3). Reasons for the reduced sharpness of the slm OPO laser pulses as compared to slm pulses at fixed wavelength are the small, statistical spikes on the temporal profile (Fig. 3.7), and shot-to-shot fluctuations of the OPO laser output in terms of beam divergence and beam profile. The relatively strong shot-to-shot fluctuations arise from the need to operate the system close to threshold to achieve single longitudinal mode operation.

For all wavelengths investigated, large bubbles of about 80 – 100 μm radius were produced already at threshold, as will be demonstrated in (5.1). Small bubbles with < 2 μm radius were generated with less than 2 % probability. This indicates that optical breakdown is a one-step process for IR wavelengths down to 725 nm. Thus, the transition to a two-step process with separate bubble and BPL thresholds must occur somewhere between 725 nm and 532 nm. The vigorous character of the breakdown process in the entire wavelength range between 725 nm and 1025 nm indicates that the breakdown threshold is here defined by the irradiance threshold for producing seed electrons by photoionization. The necessary irradiance is large due to the high order of the multiphoton process ($k = 4 - 6$) and, at the same time, the rate of avalanche ionization is high because it scales with λ^2. Therefore, once initiated, the avalanche cannot be counterbalanced by recombination as for UV and VIS pulses but progresses already at threshold to the BPL regime associated with the formation of large bubbles.

The I_{th} data from table 4.9 are plotted in **Fig. 4.16** to show the wavelength dependence of the optical breakdown threshold between 725 nm and 1025 nm. It strikes attention that the irradiance values obtained from the measurements with the 40x objective are, for 725 nm < λ < 900 nm, considerably higher than those obtained with the 63x objective. An explanation is offered by figure 3.8, which reveals that the effective aperture of the 63x objective is completely filled by the laser beam whereas the aperture of the 40x objective is only partially filled. This means that the *effective* numerical aperture used in the experiments with the 40x objective is smaller than the nominal aperture of 0.8. Consequently, the values of I_{th} calculated using the diffraction limited spot size for NA = 0.8, which is smaller than the real spot size, will be too large.
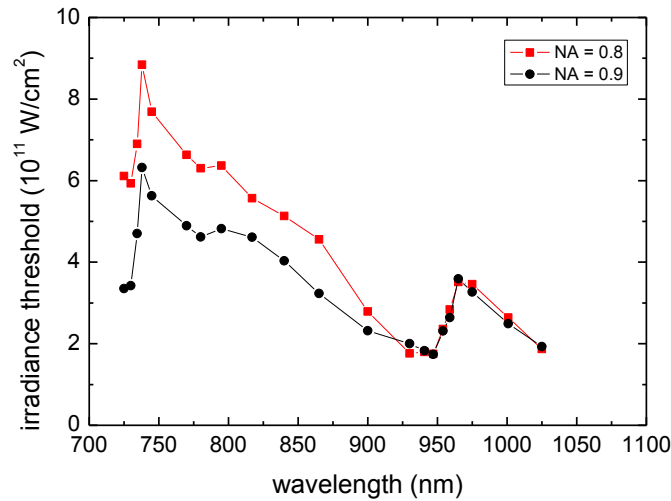
Figure 4.16 Raw data for the wavelength dependence of optical breakdown threshold for ns slm OPO laser pulses ranging from 725 nm to 1025 nm at NA = 0.8, and NA = 0.9. The data for the 40x objective are not yet corrected for inhomogeneous illumination of the objective aperture.

λ [nm]	Pulse duration [ns]	NA	M^2	Diffraction limited $2\omega_0$ [μm]	Real focus $2\omega_0$ [μm]	E_{th} [μJ]	P_{th} [kW]	F_{th} [J/cm²]	I_{th} [10^{11} W/cm²]	S
725	1.71	0.8	1.68	1.11	1.86	7.3	8.0	539	6.11 (3.94)	19.4
725	1.89	0.9	1.67	0.98	1.64	3.5	3.4	326	3.35	8.5
730	2.17	0.8	1.69	1.11	1.88	9.2	8.0	663	5.93 (3.81)	6.0
730	2.17	0.9	1.65	0.99	1.63	4.0	3.5	382	3.42	3.2
735	2.06	0.8	1.70	1.12	1.90	10.4	9.5	733	6.90 (4.45)	9.9
735	1.88	0.9	1.63	1.00	1.62	4.7	4.7	455	4.70	7.9
738	2.25	0.8	1.70	1.13	1.91	14.7	12.3	1025	8.84 (5.67)	5.3
738	2.25	0.9	1.62	1.00	1.62	7.6	6.3	733	6.32	5.8
745	1.90	0.8	1.70	1.14	1.93	11.0	10.9	754	7.69 (4.91)	16.3
745	1.90	0.9	1.60	1.01	1.62	5.7	5.6	551	5.63	2.3
770	2.18	0.8	1.69	1.17	1.98	11.5	9.9	746	6.63 (4.21)	3.0
770	2.18	0.9	1.56	1.04	1.63	5.7	4.9	549	4.89	2.0
780	1.93	0.8	1.68	1.19	2.00	9.8	9.6	627	6.30 (4.00)	11.3
780	1.93	0.9	1.55	1.06	1.64	4.9	4.7	460	4.62	5.9
795	2.51	0.8	1.66	1.21	2.01	13.1	9.8	824	6.37 (3.97)	3.5
795	2.51	0.9	1.55	1.08	1.67	6.8	5.1	623	4.82	4.2
817	2.49	0.8	1.66	1.25	2.07	12.0	9.1	714	5.57 (3.44)	9.6
817	2.49	0.9	1.56	1.11	1.73	6.9	5.2	591	4.61	6.2
840	2.73	0.8	1.71	1.28	2.19	13.6	9.4	721	5.13 (3.16)	3.3
840	2.73	0.9	1.60	1.14	1.82	7.4	5.1	568	4.03	3.5
865	1.98	0.8	1.83	1.32	2.41	10.6	10.1	465	4.56 (2.76)	3.5
865	1.98	0.9	1.68	1.17	1.97	5.0	4.8	329	3.23	3.4
900	2.43	0.8	2.15	1.37	2.95	12.0	9.3	350	2.79 (1.67)	8.9
900	2.43	0.9	1.89	1.22	2.31	6.1	4.7	290	2.32	3.2
930	1.63	0.8	2.30	1.42	3.26	6.2	7.1	148	1.76 (1.49)	3.2
930	1.96	0.9	2.01	1.26	2.53	5.1	4.9	202	2.00	15.2
941	1.84	0.8	2.18	1.43	3.13	6.6	6.7	171	1.80 (1.51)	3.7
941	1.74	0.9	1.94	1.28	2.47	3.9	4.3	164	1.83	6.9
947	1.78	0.8	2.12	1.44	3.06	5.9	6.2	160	1.75 (1.47)	5.5
947	2.19	0.9	1.89	1.28	2.43	4.5	3.9	196	1.74	5.0
954	2.61	0.8	2.04	1.45	2.97	11.0	7.9	317	2.36 (1.96)	5.2
954	2.61	0.9	1.84	1.29	2.38	6.9	5.0	311	2.31	4.9
959	1.51	0.8	1.99	1.46	2.91	7.4	9.2	221	2.84 (2.37)	7.7
959	1.52	0.9	1.80	1.30	2.34	4.5	5.5	207	2.64	2.7
965	1.44	0.8	1.94	1.47	2.85	8.3	10.9	260	3.51 (2.91)	2.9
965	1.76	0.9	1.75	1.31	2.29	6.7	7.2	326	3.59	6.8
975	2.42	0.8	1.87	1.49	2.78	13.1	10.2	431	3.46 (2.85)	6.4
975	2.20	0.9	1.68	1.32	2.22	7.2	6.1	371	3.27	3.8
1001	2.18	0.8	1.90	1.53	2.90	9.8	8.5	297	2.64 (2.16)	3.9
1001	2.42	0.9	1.62	1.36	2.20	5.9	4.6	311	2.49	4.4
1025	2.59	0.8	2.29	1.56	3.58	12.6	9.1	250	1.87 (1.50)	3.4
1025	3.07	0.9	1.86	1.39	2.58	8.0	4.9	305	1.93	3.3

Table 4.9 Threshold values for optical breakdown in water induced by single longitudinal mode ns OPO pulses. We measured the pulse duration τ for each wavelength and calculated the threshold values from τ and E_{th}, using the M^2 values of Fig. 3.8. The I_{th} values for the 40x objective had to be corrected for incomplete illumination of the rear entrance pupil (I_{th}-values in brackets, see text). For all wavelengths investigated, bubble and BPL threshold coincided.

Unfortunately, it was not possible to avoid this complication by expanding the laser beam to a diameter that overfilled the aperture of both the 63x and 40x objectives because for some wavelengths the available pulse energy just sufficed to induce breakdown. Stronger beam expansion would have reduced the energy transmitted through the 63x objective and thus impaired the threshold measurement. Therefore, we need to correct the I_{th}-values for the 40x objective retrospectively by considering the incomplete filling of the objective aperture.

A correction is possible using the data of the energy reference measurements described in section 2.1. A homogeneous pump laser light illumination of both objective apertures would yield a ratio of the transmitted energy for the 40x and 63x objectives of V = (8 mm)²/(5.7 mm)² = 1.97. In reality, however, the ratio is only 1.59, for example, for λ = 865 nm. If we assume that the 63x objective is homogeneously illuminated (this assumption is supported by figure 3.8), we can conclude that 1.59/1.97 = 80.7 % of the aperture of the 40x objective is used. If only 80.7 % of the NA is effective, this corresponds to a correction factor C = 0.65 for the 40x I_{th}-value. **Figure 4.17** shows the correction factor for all investigated wavelengths.
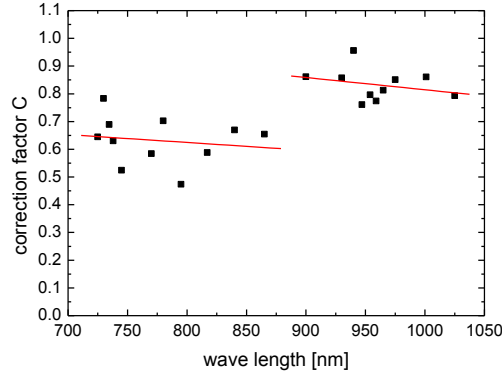
Figure 4.17 Correction factors for the calculation of the irradiance threshold for the 40x objective (see text). The data were linearly fitted in two different regions using the computer program Origin.

The correction factor has two regions that can each be fitted by a linear function. The transition between the two regions occurs at approximately 900 nm, where we had to change the OPO crystal and optics in the pump laser. This could explain the different laser beam diameter at the focusing objective. The linear fit functions for the correction factor C were used to calculate the irradiance threshold for the 40x objective. Figure 4.18a shows the corrected wavelength dependence of optical breakdown threshold for the 40x and 63x objectives, and Fig 4.18b shows the average of the threshold values for both objectives.

The $I_{th}(\lambda)$ curve exhibits two steps at ≈735 nm and ≈955 nm where the threshold abruptly increases. These steps occur at wavelengths where the number of photons required for overcoming the band gap energy increases. At the same time, I_{th} exhibits an overall decrease with increasing wavelength. This decrease is partially related to the fact that the MPI probability increases with wavelength in each interval for which a certain photon number is needed to overcome the band gap (Fig. 4.22). Other reasons related to an increasing role of background free electrons for larger wavelengths will be discussed in section 4.4.
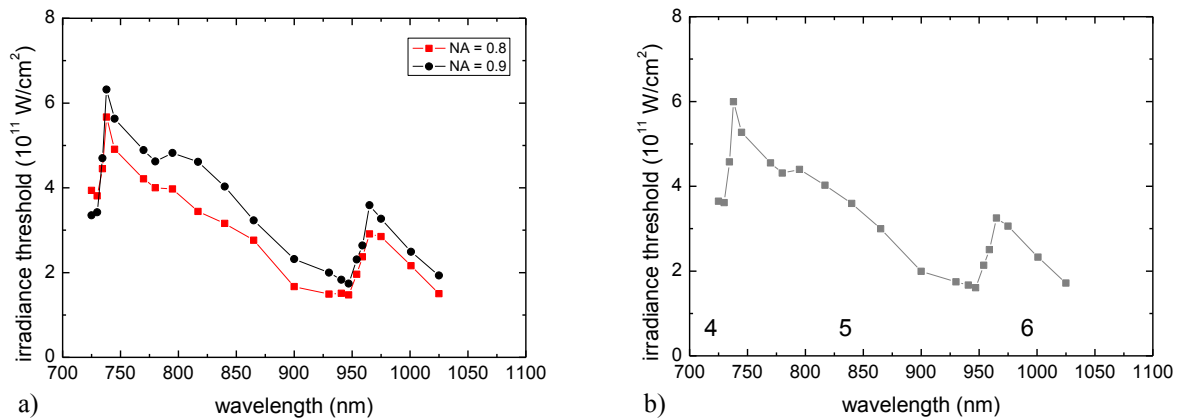
Figure 4.18: Wavelength dependence of optical breakdown threshold for ns slm OPO laser pulses from 725 nm to 1025 nm. The laser pulses were focused through a 40x water immersion objective (NA = 0.8, red line in a)), and a 63x water immersion objective (NA = 0.9, black line in a)). The data for the 40x objective are corrected for the incomplete filling of the objective aperture by the laser beam. Figure b) shows the average of the threshold values for both objectives. The numbers indicate the respective order of the multiphoton process required to overcome the band gap.

Bloembergen mentioned already in 1974 that multiphoton initiation of the breakdown threshold should be reflected in a stepwise increase of I_{th} at those wavelengths for which one additional photon is required to overcome the band gap [Bloe74]. He took the lack of experimental evidence for such $I_{th}(\lambda)$ dependence at that time as support for his view of an exclusive role of avalanche ionization. In our study, the hypothesis about the $I_{th}(\lambda)$ dependence associated with multiphoton generation of seed electrons has, for the first time, been tested by means of lasers with widely tunable wavelength delivering pulses with smooth temporal shape. The result contradicts Bloembergen's original conclusion and corroborate our view that IR ns breakdown in the investigated wavelength range is initiated by photoionization.

The distance between the peaks in the $I_{th}(\lambda)$ curve can be used to determine the band gap energy E_{gap}. Previous results for E_{gap} in the physico-chemical literature range from $E_{gap} = 6.5$ eV to $E_{gap} = 7.2$ eV [Wil76, Gra79, Nik83]. We obtain a band gap energy within this range if we assume that the steps in Fig. 4.18 correspond to an increase of the order of the multiphoton process from 4 to 5 and 5 to 6, respectively. **Table 4.10** shows the results obtained by evaluating the distance between the maxima and minima in the $I_{th}(\lambda)$ curve using the above assumption. The assumption of a transition from 3 to 4 photons at $\lambda \approx 735$ nm and 4 to 5 photons at $\lambda \approx 955$nm would lead to $E_{gap} = 5.13$ eV, while the assumption of a transition from 5 to 6 and 6 to 7 photons at the respective wavelengths would correspond to $E_{gap} = 8.13$ eV. Both values are outside the range of previous measurement results.

	Max		Min	
	λ [nm]	λ [nm]	λ [nm]	λ [nm]
	738	965	729.85	947
photon energy [eV]	1.683	1.287	1.702	1.312
# photons	4	5	4	5
band gap [eV]	**6.73**	**6.44**	**6.81**	**6.56**

Table 4.10 Band gap energy calculated from the position of the steps in the of $I_{th}(\lambda)$ dependence in figure 4.18.

The average value for the band gap energy obtained from table 4.10 is $E_{gap} = 6.63$ eV ± 0.15 eV. The best fit to model predictions in section 4.3.2 below yield 6.55 eV. These values corroborate the value of 6.5 eV used in previous theoretical models and numerical calculations [Sac91, Ken95b, Noa99, Fan02, Vog05, Arn07, Vog08, Oli08]. For the calculations in this study, we use the value of 6.55 eV.

The steps in the $I_{th}(\lambda)$ curve are not abrupt but have a finite width. This suggests that the zones with distinct order of multiphoton process are separated by transition zones in which excitation of electrons to the lower edge of the conduction band requires one photon less than excitation to slightly higher energy levels that can accommodate a larger population density $D(E)$ (see section 2.1.4 and Fig. 2.4).

4.3.1.2. OPA measurements of femtosecond breakdown

We measured the bubble formation thresholds in water produced by fs OPA laser pulses of ≈ 265 fs duration for 50 wavelengths ranging from 334 nm to 1085 nm. The pulses were focused through water immersion objectives with $NA = 0.8$ and $NA = 0.9$, respectively. The probability curves are presented in Fig. 11.15 of the Appendix. The energy thresholds derived from the probability curves are summarized in **table 4.11**, together with P_{th}, F_{th} and the irradiance threshold I_{th}. We determined the pulse duration τ_L for each wavelength >450 nm by measuring the autocorrelation function. The average pulse duration was 265 fs. For the range $\lambda < 450$ nm, in which the autocorrelator was not sensitive, we assumed the pulse duration to equal the average duration of 265 fs. The spectrum was also measured for each laser pulse, and the respective center wavelengths are listed in table 4.11. We used a value of $M^2 = 1.4$ to calculate F_{th} and I_{th} from E_{th} and τ_L. All I_{th} values refer to the temporal and spatial peak irradiance in the pulse and laser focus, respectively, while the F_{th} values refer to the spatial peak of the radiant exposure.

The sharpness of the thresholds ranges between 0.8 and 126.6, with an average of $S = 10.2$. These fluctuations do not seem to be associated with transitions between mirror sets, and it is remarkable that S strongly differs even for measurements with same wavelength but different NA (for example, for $\lambda = 1021$ nm, $S = 126.6$ for the 63x objective, $NA = 0.9$, but only 8.7 for the 40x objective, $NA = 0.8$). In the latter case, the pupil diameter of the objective is larger (Fig. 3.8), and shot-to-shot fluctuations of the laser beam profile will thus play a larger role. Shot-to-shot fluctuations of the beam profile may also differ from wavelength to wavelength. However, the origin of the fluctuations is not yet completely understood.

λ [nm]	Pulse duration [fs]	NA	Diffraction limited $2\omega_0$ [µm]	Real focus $2\omega_0$ [µm]	E_{th} [nJ]	P_{th} [kW]	F_{th} [J/cm²]	I_{th} [10^{11} W/cm²]	S
334	265	0.8	0.51	0.71	3.37	23.9	1.69	123.7	1.3
334	265	0.9	0.45	0.63	3.60	25.5	2.28	167.0	1.5
347	265	0.8	0.53	0.74	3.31	23.5	1.53	112.3	14.5
347	265	0.9	0.47	0.66	3.46	24.6	2.03	148.8	6.1
360	265	0.8	0.55	0.77	3.47	24.6	1.50	109.7	4.8
360	265	0.9	0.49	0.68	2.70	19.1	1.48	108.0	11.3
373	265	0.8	0.57	0.80	2.84	20.2	1.14	83.5	5.5
373	265	0.9	0.51	0.71	2.51	17.8	1.28	93.5	5.0
389	265	0.8	0.59	0.83	2.95	20.9	1.09	79.7	4.3
389	265	0.9	0.53	0.74	2.46	17.5	1.15	84.3	8.4
410	265	0.8	0.63	0.88	4.17	29.6	1.39	101.4	2.4
410	265	0.9	0.56	0.78	2.83	20.1	1.19	87.0	2.1
425	265	0.8	0.65	0.91	4.09	29.0	1.26	92.6	3.3
425	265	0.9	0.58	0.81	3.60	25.6	1.41	103.2	4.9
441	265	0.8	0.67	0.94	4.76	33.7	1.37	100.0	7.8
441	265	0.9	0.60	0.84	4.03	28.6	1.47	107.3	8.2
456	380	0.8	0.70	0.97	4.82	23.8	1.29	66.1	2.1
456	380	0.9	0.62	0.87	4.56	22.5	1.55	79.1	3.7
471	274	0.8	0.72	1.01	4.49	30.8	1.13	80.1	3.7
471	274	0.9	0.64	0.89	3.83	26.3	1.22	86.4	2.4
485	380	0.8	0.74	1.04	6.44	31.8	1.53	78.0	6.0
485	380	0.9	0.66	0.92	5.05	25.0	1.52	77.4	2.9
498	265	0.8	0.76	1.06	5.16	36.6	1.16	85.0	5.0
498	265	0.9	0.68	0.95	4.12	29.2	1.17	85.9	9.2
513	262	0.8	0.78	1.10	7.02	50.4	1.49	110.4	7.8
513	262	0.9	0.70	0.97	4.95	35.5	1.33	98.4	4.7
529	244	0.8	0.81	1.13	8.20	63.1	1.64	130.1	3.0
529	244	0.9	0.72	1.00	7.07	54.4	1.79	141.9	2.2
544	199	0.8	0.83	1.16	6.35	60.0	1.20	116.9	2.8
544	199	0.9	0.74	1.03	4.77	45.1	1.14	111.2	7.2
560	245	0.8	0.85	1.20	8.03	61.6	1.43	113.3	10.7
560	245	0.9	0.76	1.06	5.75	44.1	1.30	102.6	5.4
580	598	0.8	0.88	1.24	9.17	28.8	1.52	49.4	5.6
580	598	0.9	0.79	1.10	7.63	24.0	1.60	52.0	11.1
595	215	0.8	0.91	1.27	8.69	75.9	1.37	123.7	4.9
595	215	0.9	0.81	1.13	6.50	56.8	1.30	117.1	4.8
610	620	0.8	0.93	1.30	7.91	24.0	1.19	37.1	6.7
610	620	0.9	0.83	1.16	6.41	19.4	1.22	38.1	7.1
627	228	0.8	0.96	1.34	7.48	61.7	1.06	90.5	6.1
627	228	0.9	0.85	1.19	6.07	50.0	1.09	92.8	4.7
644	238	0.8	0.98	1.37	7.38	58.3	0.99	81.0	6.7
644	238	0.9	0.87	1.22	6.52	51.5	1.11	90.6	5.1
660	271	0.8	1.01	1.41	9.60	66.6	1.23	88.1	12.1
660	271	0.9	0.89	1.25	8.04	55.8	1.30	93.4	9.5
677	225	0.8	1.03	1.45	7.85	65.6	0.96	82.5	14.2
677	225	0.9	0.92	1.28	6.44	53.8	0.99	85.7	16.4
709	190	0.8	1.08	1.51	8.68	85.9	0.97	98.5	30.1
709	190	0.9	0.96	1.35	7.23	71.5	1.02	103.8	7.5
725	204	0.8	1.11	1.55	9.42	86.8	1.00	95.2	86.3
725	204	0.9	0.98	1.38	7.74	71.3	1.04	99.0	5.8

λ [nm]	Pulse duration [fs]	NA	Diffraction limited $2\omega_0$ [μm]	Real focus $2\omega_0$ [μm]	E_{th} [nJ]	P_{th} [kW]	F_{th} [J/cm²]	I_{th} [10^{11} W/cm²]	S
740	300	0.8	1.13	1.58	8.51	53.3	0.87	56.1	23.5
740	300	0.9	1.00	1.40	7.56	47.4	0.98	63.1	12.3
755	279	0.8	1.15	1.61	10.32	69.6	1.01	70.4	31.8
755	279	0.9	1.02	1.43	8.53	57.5	1.06	73.5	61.8
770	265	0.8	1.17	1.64	10.39	73.7	0.98	71.6	15.7
770	265	0.9	1.04	1.46	8.98	63.7	1.07	78.4	14.4
785	250	0.8	1.20	1.68	10.82	81.3	0.98	76.1	7.3
785	250	0.9	1.06	1.49	9.09	68.3	1.04	80.9	7.3
799	240	0.8	1.22	1.71	9.18	71.8	0.80	64.8	7.5
799	240	0.9	1.08	1.52	7.67	60.0	0.85	68.6	6.4
814	375	0.8	1.24	1.74	11.35	56.9	0.96	49.5	2.1
814	375	0.9	1.10	1.54	11.26	56.5	1.20	62.2	1.9
835	211	0.8	1.27	1.78	14.68	130.9	1.18	108.3	0.8
835	211	0.9	1.13	1.58	12.08	107.7	1.23	112.8	3.3
845	166	0.8	1.29	1.80	15.55	176.1	1.22	142.1	3.5
845	166	0.9	1.15	1.60	12.26	138.9	1.21	141.9	2.1
865	310	0.8	1.32	1.85	12.63	76.6	0.94	59.0	5.1
865	310	0.9	1.17	1.64	12.71	77.1	1.20	75.1	3.9
883	220	0.8	1.35	1.88	14.91	127.4	1.07	94.2	3.0
883	220	0.9	1.20	1.68	13.92	119.0	1.26	111.3	6.8
903	210	0.8	1.38	1.93	11.62	104.0	0.80	73.6	6.1
903	210	0.9	1.22	1.71	8.28	74.1	0.72	66.3	7.6
924	151	0.8	1.41	1.97	13.53	168.9	0.89	114.1	12.6
924	151	0.9	1.25	1.75	10.72	133.9	0.89	114.4	10.8
942	280	0.8	1.44	2.01	17.14	115.1	1.08	74.8	4.0
942	280	0.9	1.28	1.79	13.54	90.9	1.08	74.8	5.9
957	167	0.8	1.46	2.04	16.62	187.0	1.01	117.8	12.1
957	167	0.9	1.30	1.82	12.37	139.2	0.96	111.0	17.3
973	109	0.8	1.48	2.08	15.89	273.1	0.94	166.3	6.8
973	109	0.9	1.32	1.85	14.13	242.8	1.06	187.1	8.1
993	96	0.8	1.51	2.12	12.48	243.4	0.71	142.3	35.8
993	96	0.9	1.35	1.88	9.74	190.0	0.70	140.6	4.6
1005	131	0.8	1.53	2.15	18.29	262.8	1.01	150.0	12.1
1005	131	0.9	1.36	1.91	12.80	183.9	0.90	132.9	14.3
1021	185	0.8	1.56	2.18	13.94	141.6	0.75	78.4	8.7
1021	185	0.9	1.38	1.94	14.38	146.2	0.98	102.4	126.6
1036	243	0.8	1.58	2.21	21.76	168.4	1.13	90.5	8.9
1036	243	0.9	1.40	1.97	16.29	126.0	1.07	85.7	6.4
1051	98	0.8	1.60	2.24	14.24	273.1	0.72	142.5	3.5
1051	98	0.9	1.42	1.99	10.67	204.8	0.68	135.2	4.7
1063	123	0.8	1.62	2.27	12.77	195.2	0.63	99.5	4.3
1063	123	0.9	1.44	2.02	9.25	141.3	0.58	91.2	7.0
1073	116	0.8	1.64	2.29	12.26	198.7	0.60	99.6	3.9
1073	116	0.9	1.45	2.04	8.71	141.2	0.54	89.6	5.9
1085	162	0.8	1.65	2.32	14.62	170.2	0.69	83.3	5.7
1085	162	0.9	1.47	2.06	11.77	137.1	0.71	84.9	2.4

Table 4.11 Threshold values for optical breakdown in water induced by fs OPA pulses in the wavelength range from 334 nm to 1085 nm. We determined the pulse duration τ_L for each wavelength > 450 nm by measuring the autocorrelation function The average pulse duration was 265 fs. For λ < 450 nm, where the autocorrelator was not sensitive, we assumed the pulse duration to equal the average duration of 265 fs. The threshold values were calculated from τ_L and E_{th}, using $M^2 = 1.4$.

The I_{th} data from table 4.11 are plotted in **Fig. 4.19a** to show the wavelength dependence of the optical breakdown threshold between 334 nm and 1085 nm. Strong fluctuations are observed along the $I_{th}(\lambda)$ curve but for each wavelength, the reproducibility for the measurements at different *NA*s is good.

The measured pulse durations are shown in figure **Fig. 4.19b.** The pulse duration exhibits strong fluctuations with wavelengths (see section 3.1.5), and a trend of shorter pulse durations for longer wavelengths. These features will distort the shape of the $I_{th}(\lambda)$ curve because for fs breakdown I_{th} depends strongly on τ_L. **Figure 4.20** shows calculated $I_{th}(\tau_L)$ curves for different wavelengths to illustrate this point. Therefore, the threshold values must be corrected for the fluctuations of pulse duration to obtain meaningful results on the wavelength dependence of the fs breakdown thresholds. Note that a similar correction is not necessary for the wavelength dependence data on IR ns breakdown in Fig. 4.18 because in this regime I_{th} hardly varies with τ_L.
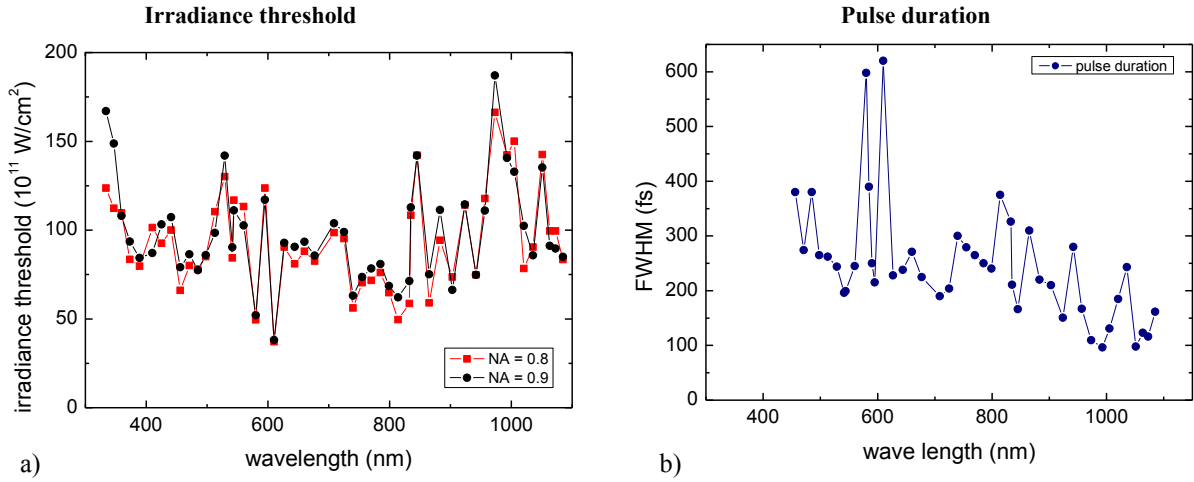
Figure 4.19 a) Wavelength dependence of the optical breakdown threshold for fs OPO laser pulses ranging from UV to IR at NA = 0.8, and NA = 0.9. b) Wavelength dependence of the pulse duration with strong fluctuations.
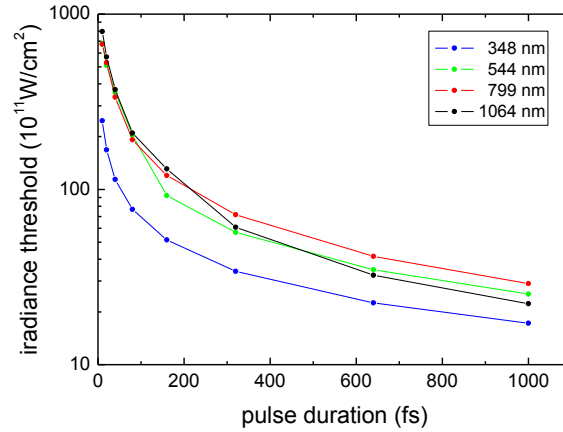
Figure 4.20 Numerical calculation of the $I_{th}(\tau_L)$ dependence assuming T_{cr} = 441 K, τ = 1.6 fs, and $\rho_0 = 2\cdot10^{13}$ e$^-$/cm³ for UV, VIS and IR wavelengths.

With the help of our numerical model, we normalized the experimental threshold values to the average pulse duration of 265 fs. For this purpose, we calculated the irradiance threshold for a given wavelength both for the measured pulse duration and for 265 fs. The ratio of these values is then used to normalize the measured threshold value to 265 fs for any given wavelength. The result of this normalization is shown in **Fig. 4.21** for the averaged data from both objectives.
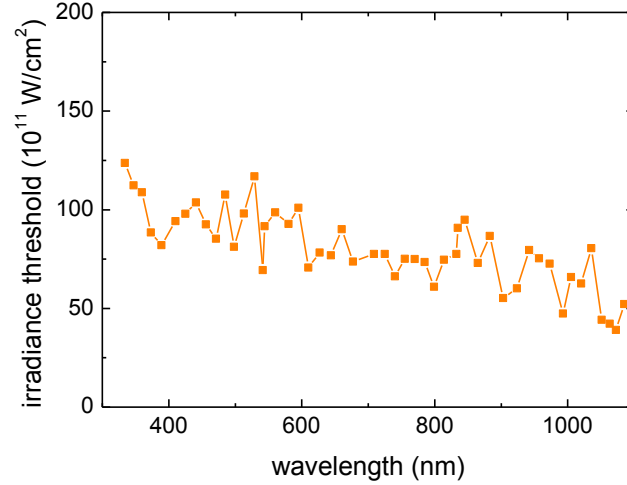
Figure 4.21 Experimentally determined wavelength dependence of the optical breakdown threshold for 265-fs laser pulses in the wavelength range between 334 nm and 1085 nm. The figure shows the average of the threshold values obtained at $NA = 0.8$ and $NA = 0.9$.

The optical breakdown threshold slightly decreases with increasing wavelength. This is indicative of a significant contribution of avalanche ionization even for femtosecond breakdown because the rate of avalanche ionization increases with increasing wavelength while the photoionization rate decreases.

For $\lambda < 360$ nm, the optical breakdown threshold in Fig. 4.19a increases strongly with decreasing wavelength for the measurements with the 63x, $NA = 0.9$ objective. The values obtained with this objective deviate here strongly from the results obtained with the 40x, $NA = 0.8$ objective, while for all other wavelengths similar values were obtained with both objectives. Analogous observations of larger threshold values at UV wavelengths obtained with the 63x, $NA = 0.9$ objective were also made at fixed wavelengths (see tables 4.2 – 4.5). Most likely, the focus quality of this objective is not diffraction-limited for deep UV range wavelengths (it is specified by the manufacturer for use at $\lambda > 380$ nm). Therefore, we used in Fig. 4.21 for the data points at $\lambda = 334$ nm and $\lambda = 347$ nm only the values measured with 40x, $NA = 0.8$ objective.

The measured $I_{th}(\lambda)$ curve exhibits fluctuations but, unlike for IR nanosecond breakdown, no pronounced steps that could be attributed to wavelengths at which one additional photon is necessary to overcome the band gap via multiphoton ionization. Multiphoton ionization is not the only photoionization process relevant for femtosecond breakdown, and tunnel ionization featuring no $I_{th}(\lambda)$ dependence becomes ever more with decreasing pulse duration. However, it seems premature at this point to conclude from the lack of clear steps in the $I_{th}(\lambda)$ curve that MPI plays no role at the investigated pulse duration of 265 fs. In the next section, we will compare the experimental $I_{th}(\lambda)$ data to the predictions of our model that considers both MPI and tunnel ionization and continue the discussion on that basis.

4.3.2. Modeling results

In this section, we will first present the wavelength dependence of avalanche ionization, multiphoton ionization and tunnel ionization alone to create a basis for interpreting the predictions of our model that includes all these ionization mechanisms, together with thermal ionization. We will then fit the model predictions for fs and ns breakdown to our experimental $I_{th}(\lambda)$ data to obtain estimates for the electron collision time τ and the seed electron density ρ_{ini}. On this basis, we will then compare all experimental results with model predictions in one comprehensive plot covering the $I_{th}(\lambda)$ dependence for pulse durations from 10 fs to 10 ns. From this comparison we will deduce information with regard to the relative importance and the interplay of the different ionization mechanisms at the various pulse durations.

Figure 4.22 shows the ionization probabilities by avalanche, multiphoton, and tunnel ionization as a function of wavelength. For the avalanche ionization rate, we used the formulation of the Drude-Shen model given by Kennedy [Ken95a], which is also part of our model (Eq. 2.7)

$$\eta_{casc} = \frac{1}{\omega^2\tau^2 + 1}\left[\frac{e^2\tau}{c\,n_0\varepsilon_0\,m_c\,(3/2)\tilde{\Delta}}I - \frac{m_c\,\omega^2\,\tau}{M}\right], \quad \text{with} \quad \tilde{\Delta} = \Delta + \frac{e^2\,E^2}{4\,m\,\omega^2} \tag{4.4}$$

To describe the ionization probability by pure multiphoton ionization, we used Keldysh's approximation for MPI [Kel65, Eq. 41] together with an irradiance value of 10^{12} W/cm^2 for which this approximation is known to be valid and a good approximation to the results of the full Keldysh model [Vog05]

$$\omega = \frac{2}{9\pi}\omega\left(\frac{m\omega}{\hbar}\right)^{3/2}\Phi\left[\left(2\left\langle\frac{\tilde{\Delta}}{\hbar\omega}+1\right\rangle - \frac{2\tilde{\Delta}}{\hbar\omega}\right)^{1/2}\right] \times \exp\left\{2\left\langle\frac{\tilde{\Delta}}{\hbar\omega}+1\right\rangle\left(1-\frac{e^2F^2}{4m\omega^2\Delta}\right)\right\}\left(\frac{e^2F^2}{16m\omega^2\Delta}\right)^{\left\langle\frac{\tilde{\Delta}}{\hbar\omega}+1\right\rangle}, \tag{4.5}$$

with
$$\Phi(z) = \int_0^z \exp\left(y^2 - z^2\right)dy.$$

In a similar way, we used Keldysh's approximation for tunnel ionization [Kel65, Eq. 40] to describe the ionization probability by pure tunnel ionization, together with an irradiance value of 10^{16} W/cm^2 for which this approximation is known to be a good approximation to the results of the full Keldysh model [Vog05]

$$\omega = \frac{2}{9\pi^2}\frac{\Delta}{\hbar}\left(\frac{m\Delta}{\hbar^2}\right)^{3/2}\left(\frac{e\hbar F}{m^{1/2}\Delta^{3/2}}\right)^{5/2} \times \exp\left\{-\frac{\pi}{2}\frac{m^{1/2}\Delta^{3/2}}{e\hbar F}\left(1-\frac{1}{8}\frac{m\omega^2\Delta}{e^2F^2}\right)\right\}. \tag{4.6}$$
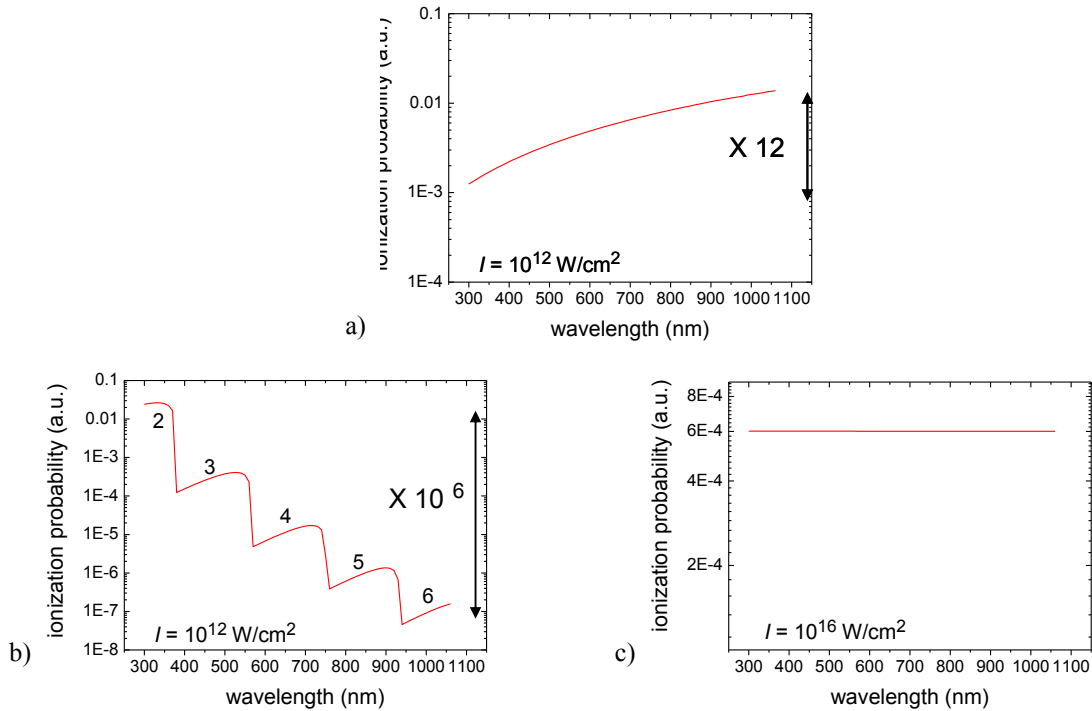
Figure 4.22 Wavelength dependence of ionization probabilities by a) avalanche, b) multiphoton, and c) tunneling ionization.

The ionization probabilities by avalanche ionization is 12 times larger for IR breakdown than for UV breakdown, which would correspond to a 12 times lower threshold for IR wavelengths than for UV wavelengths if the entire breakdown process was driven only by avalanche ionization. By contrast, the multiphoton ionization rate is 6 orders of magnitude lower for IR breakdown than for UV wavelengths, which would correspond to a much higher threshold for IR wavelengths if the entire breakdown process was driven only by MPI. Tunnel ionization exhibits hardly any wavelength dependence, in spite of the complex mathematical form of Eq. (4.6). This prediction of the Keldysh model for condensed matter is in good agreement with the ADK model for noble gases that predicts no wavelength dependence at al. [Amm86].

In **Fig. 4.23**, the experimental $I_{th}(\lambda)$ data for femtosecond breakdown are plotted together with the model predictions for different collision times. The seed electron density ρ_{ini} does not matter for femtosecond breakdown as long as it stays below 5×10^{15} cm^{-3} for $\lambda = 1040$ nm and 10^{19} cm^{-3} for $\lambda = 347$ nm ($\tau_L = 265$ fs, $\tau = 1.6$ fs, $T_{cr} = 441$ K). Thus we can focus on the determination of the collision time. For the calculations in Fig. 4.23, the seed electron density is set to $\rho_{ini} = 2\times10^{13}$ cm^{-3} which will below be shown to provide the best fit for the $I_{th}(\lambda)$ data in the nanosecond range. For fs breakdown, the best fit is obtained for $\tau = 1.6$ fs (Fig. 4.23b).

a)   b)
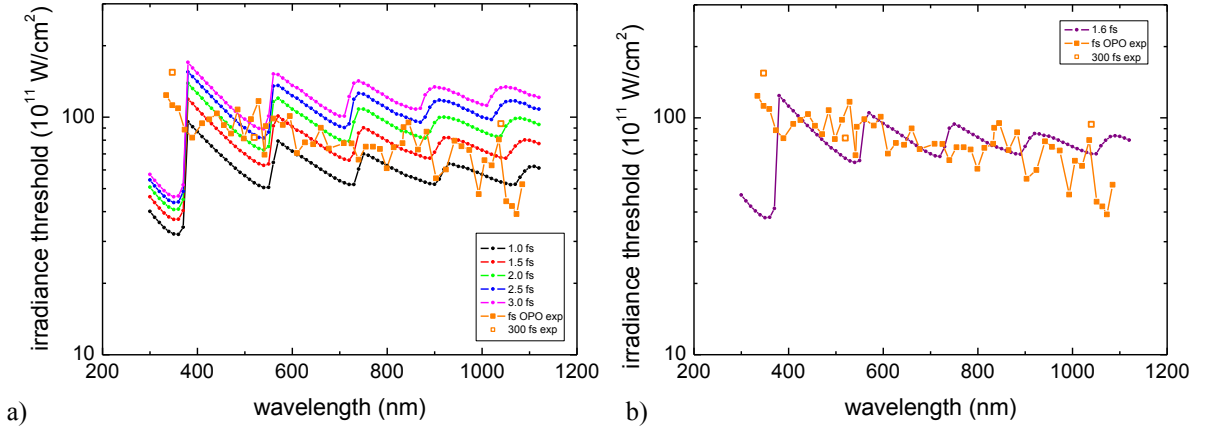
Figure 4.23 Fit of model predictions to the experimental $I_{th}(\lambda)$ data of Fig. 4.21 for femtosecond breakdown at $\tau_L = 265$ fs. Additionally, the threshold values of fs breakdown at fixed wavelengths (section 4.2.1) are included to obtain the best overall fit. The threshold criterion used for the bubble threshold is $T_{cr} = 424.5$ K (see 4.2.2.1); $NA = 0.8$. The graph in a) shows model predictions for different collision times, and b) shows calculated and experimental $I_{th}(\lambda)$ data for the best fit of $\tau = 1.6$ fs.

We showed in section 4.3.1.1 that for IR nanosecond breakdown, the generation of seed electrons by photoionization is the critical hurdle for the occurrence of breakdown. In the entire investigated wavelength range between 725 nm and 1025 nm, the avalanche progresses already at threshold to the BPL regime associated with the formation of large bubbles. Therefore, the choice of the collision time used for modeling avalanche ionization should have only little influence of the prediction of the bubble formation threshold. Indeed, an increase of the collision time by 200 % from 1 fs to 3fs changes the threshold value by no more than 56 % for $\lambda = 725$ nm, and by 20% for $\lambda = 1025$ nm. Hence, the prediction of $I_{th}(\lambda)$ depends mainly on the choice of the seed electron density ρ_{ini}. in the wavelength range between 725 nm and 1025 nm.

In **Fig. 4.24**, we fit model results both to the experimental $I_{th}(\lambda)$ data for nanosecond breakdown and the experimental data of ns breakdown at fixed wavelengths (section 4.2.1) by varying ρ_{ini}, and at the same time we adjust the value of the band gap energy E_{gap} such as to provide the best fit between the location of the peaks in the measured and calculated $I_{th}(\lambda)$ curves. The value for the collision time was set to $\tau = 3$ fs, which was obtained in section 4.2.2.3 by fitting model predictions to experimental $I_{th}(\tau_L)$ data in the UV and VIS wavelength range (Fig. 4.14).The best fit of the experimentally observed $I_{th}(\lambda)$ values is obtained for $\rho_{ini} = 2\times10^{13}$ cm^{-3} and $E_{gap} = 6.55$ eV.

Besides influencing amplitude and slope of the $I_{th}(\lambda)$ curve, the choice of ρ_{ini} determines also at which wavelength the breakdown dynamics changes from a two-step behavior with separate bubble and BPL thresholds to a one-step behavior. Experimentally, a one-step behavior was observed at 725 nm. The $R(t)$ plots in **Fig. 4.25** demonstrate that this behavior is reproduced by the model only for a seed electron density $\rho_{ini} \geq 2\times10^{14}$ cm^{-3} but not for $\rho_{ini} = 2\times10^{13}$, which provided the best fit in Fig. 4.24. For $\rho_{ini} = 2\times10^{13}$ the transition from a two-step behavior to a one-step behavior occurs at $\lambda = 758$ nm. Both fitting approaches thus yield results for the seed electron density that lie within the range $2\times10^{13} < \rho_{ini} < 2\times10^{14}$ cm^{-3}. It should be emphasized that the experimentally observed 2-step behavior at $\lambda = 532$ nm is well portrayed with all ρ_{ini} values in this range.
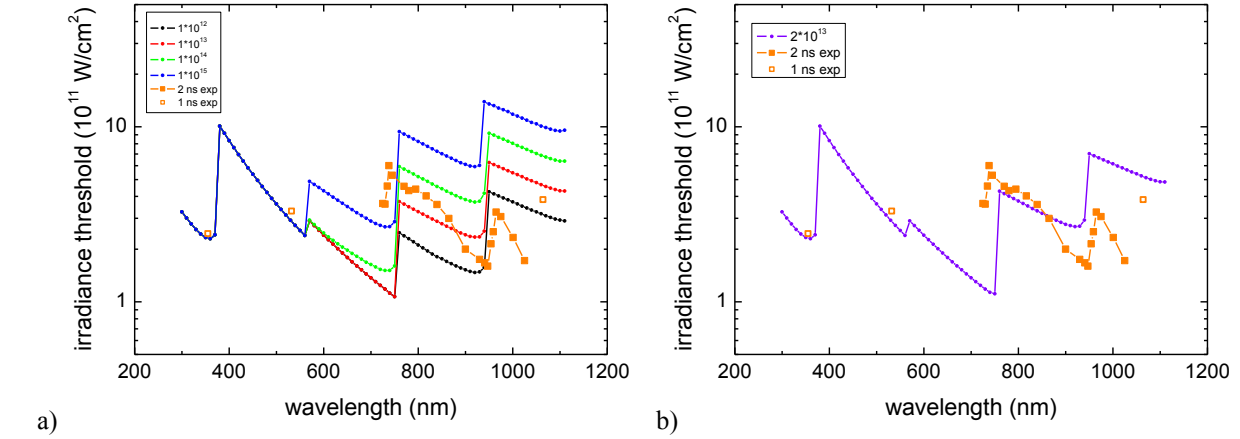
Figure 4.24 Fit of model predictions to the experimental $I_{th}(\lambda)$ data of Fig. 4.18b for IR nanosecond breakdown at $\tau_L = 2$ ns together with the experimental data of 1-ns breakdown at fixed wavelengths (section 4.2.1). The threshold criterion used for the bubble threshold is $T_{cr} = 573$ K (see 4.2.2.1); $NA = 0.8$, $\tau = 3$ fs. The graph in a) shows model predictions for different seed electron densities, and b) shows calculated and experimental $I_{th}(\lambda)$ data for the best fit of $\rho_{ini} = 2\times10^{13}$ cm^{-3}
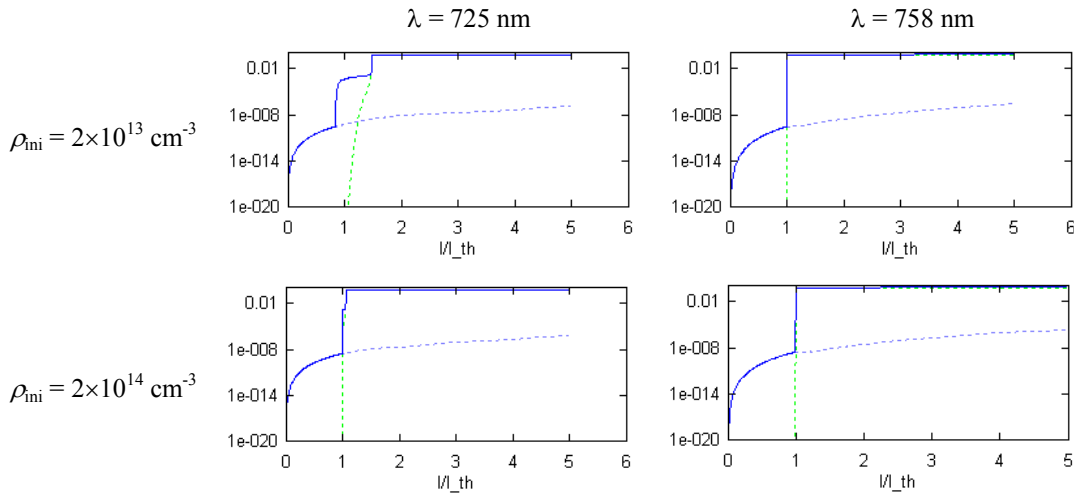
Figure 4.25 Time evolution of the ionization degree, $R(t)$, for wavelengths of 725 nm (left column) and 758 nm (right column) for $\rho_{ini} = 2\times10^{13}$ cm^{-3} (top) and $\rho_{ini} = 2\times10^{13}$ cm^{-3}(bottom). The calculations were performed for a collision time of 3 fs. Experimentally, a one-step behavior was observed at 725 nm. This is reproduced by the model only for a seed electron density $\rho_{ini} \geq 2\times10^{14}$ cm^{-3} but not for $\rho_{ini} = 2\times10^{13}$, which provided the best fit in Fig. 4.24.

Table 4.12 summarizes the model parameters obtained by fitting procedures to experimental data and the threshold criteria employed in different pulse duration ranges.

Pulse duration	< 1 ps	1 ps – 50 ps	50 ps - 200 ps	>200 ps
T_{cr} at bubble threshold [K]	441		500	573
Collision time τ [fs]	1.6	3		
Seed electron density ρ_{ini}	2×10^{13} cm^{-3}			
Band gap [eV]	6.55			

Table 4.12 Threshold criteria and model parameters employed in different pulse duration ranges.

The parameters of table 4.12 were used to calculate $I_{th}(\lambda)$ curves from UV to IR wavelengths over a range of pulse durations from 10 fs to 10 ns, as shown in **Fig. 4.26.** The calculated curves are plotted together with the experimental $I_{th}(\lambda)$ data for $\tau_L \approx 265$ fs (OPA measurements), $\tau_L \approx 300$ fs (fixed wavelengths), $\tau_L \approx 2$ ns (OPO measurements), and $\tau_L \approx 1$ ns (fixed wavelengths).
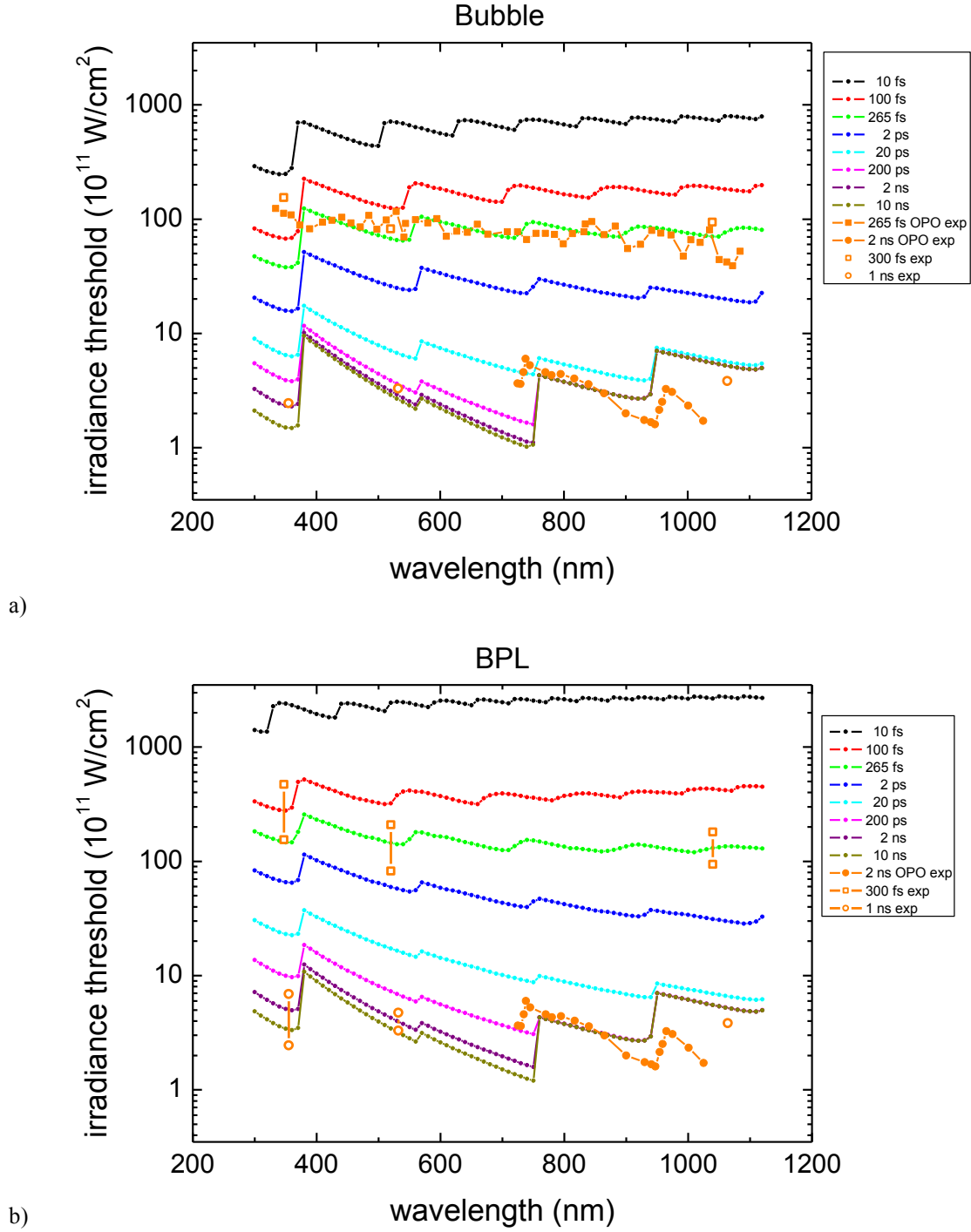
Figure 4.26 Comparison of model predictions to experimental $I_{th}(\lambda)$ data for femtosecond and nanosecond laser pulses. The calculated $I_{th}(\lambda)$ curves were obtained using the parameters of table 4.12., assuming NA = 0.8. a) Calculated and experimental values for the bubble formation threshold, b) Calculated and experimental values for the BPL threshold (T_{cr} = 6000 K). In b) the experimental values (orange square) for fs breakdown mark the irradiance range from the bubble formation threshold to the minimum irradiance at which brightly luminescent plasmas have been observed photographically (see 5.1.1 and 11.2). The experimental nanosecond IR data in b) are the same as in a) because bubble and BPL threshold coincide in this parameter range.

The results in Fig. 4.26 together with the $R(t)$ and $R_{max}(I/I_{th})$ plots in section 4.2.2.2 suggest that the breakdown dynamics is governed by an *interplay* between photoionization (PI) and avalanche ionization (AI) or AI in conjunction with thermal ionization (TI) in a very large part of the (τ_L, λ) parameter space.

For IR nanosecond breakdown, the $I_{th}(\lambda)$ curve exhibits steps occurring at wavelengths where the number of photons required for overcoming the band gap energy increases. These steps are indicative for initiation of the breakdown process by multiphoton ionization (MPI), refuting earlier views by Bloembergen [Blo74] and Shen [She84]. If AI would start from background free electrons or be initiated by thermal emission of free electrons via heating of linearly absorbing impurities, the $I_{th}(\lambda)$ curve would be more continuous. The distance between the peaks in the $I_{th}(\lambda)$ corresponds to a band gap energy E_{gap} = 6.55 eV, which is within the range between 6.5 eV and 7.2 eV that has been reported previously [Wil76, Gra79, Nik83].

For shorter wavelengths the MPI probability increases by several orders of magnitude (Fig. 4.22b). Here MPI does not just provide seed electrons for AI but contributes significantly to the entire breakdown process. For nanosecond breakdown at 355 nm, AI produces only 20 % of the free electrons in comparison to MPI. With decreasing pulse durations, for which a larger irradiance is required to complete breakdown within an ever shorter time span, the contribution of PI also increases because the PI rate exhibits a much stronger dependence on irradiance than the AI rate. However, AI does not at all become insignificant for short wavelengths and pulse durations because besides being proportional to irradiance, it is proportional to the free electron density. PI contributes most free electrons during the initial part of the laser pulse but later AI takes over. Therefore, the AI rate determines the breakdown threshold in a large part of the (τ_L, λ) parameter space. Exceptions are the ns IR region, where the main hurdle for breakdown is the creation of seed electrons by MPI, and ultrashort pulse durations <<100 fs where PI dominates because of the time constraints on AI that relies not only on irradiance but requires a large number of successive collisions to proceed. If the pulse duration is not much longer than the collision time, only few inverse bremsstrahlung absorption events can occur and even less impact ionization events, and AI thus becomes insignificant. Note, however, that for IR 300-fs pulses, AI still produces 160 times more free electrons than PI at the bubble threshold, and even more above I_{th}. The experimentally observed decrease of the optical breakdown threshold with increasing wavelength for $\tau_L \approx 265$ fs is also indicative of a significant contribution of avalanche ionization. Since the AI rate increases with increasing wavelength while the PI rate decreases (Fig. 4.22), an overall decrease of I_{th} can only arise if AI plays an important role.

The interplay of AI and PI explains the relatively flat wavelength dependence of the breakdown threshold. With MPI alone, thresholds would drastically increase with wavelength (Fig. 4.22b) but this trend is balanced by the opposite wavelength dependence of AI (Fig. 4.22a). A change of the AI rate by a factor of 12 from UV to IR wavelengths can balance a change of MPI probability by 10^6 because the proportionality between AI and free electron density adds to the vigor of the ionization avalanche. For pulse durations in the fs range, the flat spectrum of the tunnel ionization probability (Fig. 4.22c) also contributes to the flatness of the $I_{th}(\lambda)$ curve.

Although the overall wavelength dependence of I_{th} is weak, the calculated $I_{th}(\lambda)$ curves exhibits undulations over the entire range of pulse durations down to 10 fs. The undulations are due to the stepwise changes of the MPI probability with λ. For large irradiances, the location of the steps shifts towards shorter wavelengths because of the increasing oscillation energy of the free electrons in the electric field that increases the effective ionization energy and lowers the wavelength at which an additional photon is required to provide this energy. The steps disappear only for IR breakdown at 10 fs, where the Keldysh parameter is only $\gamma \approx 0.5$. A value of the Keldysh parameter of $\gamma \approx 1$ marks the transition from the multiphoton ionization regime ($\gamma > 1$) to the tunneling regime [Kel65, Vog05]. For $\lambda = 355$ nm and $\tau_L \approx 265$ fs, $\gamma = 2.7$. The large γ - values in most of the (τ_L, λ) parameter space explain the omnipresence of the undulations in the $I_{th}(\lambda)$ curves.

The omnipresence of the undulations makes it difficult to experimentally discriminate between regions governed by MPI and by tunnel ionization. We had hoped that we could identify regions with an important contribution of MPI to the entire breakdown process by the appearance of steps in the measured $I_{th}(\lambda)$ curve. However, the height of the steps varies less with pulse duration than originally expected. While for ultrashort pulses <<100 fs the steps are smoothened by tunnel ionization, they are for longer pulses smoothened by the continuous wavelength dependence of AI. For $\tau_L \approx 265$ fs, only the calculated step around 380 nm is larger than the experimental fluctuations in the $I_{th}(\lambda)$ curve, and all other steps predicted by the model are considerably smaller. Therefore, the fluctuations observed in the measured $I_{th}(\lambda)$ curve could not be attributed to wavelengths at which one additional photon is necessary to overcome the band gap via multiphoton ionization. By contrast, for IR ns breakdown, the steps originate from the need to create seed electrons by PI that largely determines I_{th} and are, therefore, hardly smoothened by the continuous wavelength dependence of AI. Thus, the steps are larger and more easily detectable.

On the whole, our model that combines the full Keldysh model of photoionization with a Drude model for avalanche ionization and recombination, and incorporates thermal ionization provides very good agreement with experimental $I_{th}(\lambda)$ data over a large range of pulse durations, with reasonable assumptions for the collision time ($1.6 < \tau < 3$ fs) and seed electron density (2×10^{14} cm^{-3} $\leq \rho_{ini} \leq 2 \times 10^{14}$ cm^{-3}). The Keldysh model [Kel65] yields fairly accurate predictions even for short UV wavelengths down to the UV region of the optical spectrum even though it was originally developed to describe breakdown at longer wavelengths. Further improvements could likely be achieved by introducing a rigorous energy dependence of the reduced effective electron–hole mass as recently suggested by Gruzdev and coworkers [Gru07a, Gru07b]. However Gruzdev's analysis was performed for wide band-gap solids, and cannot easily be transferred to water.

In our model, the AI rate is somewhat larger than predicted in Kaiser's and Rethfeld's models for fused silica [Kai00, Ret04] but significantly smaller than in the approach followed by University of Michigan group [Tie99, Jog03, Jog04] that is based on the avalanche ionization model by Thornber [Tho81]. The latter group dispute that multiphoton ionization plays a significant role because of quenching by collisions, especially for IR breakdown, [Du96]. As a consequence, tunnel ionization is regarded to be the only significant photoionization mechanism, even for pulse durations of hundreds of femtoseconds for which the Keldish parameter is much larger than one [Jog03, Jog04]. Following Bloembergen [Bloe74], initiation of nanosecond breakdown by multiphoton ionization is neglected, and it is assumed that breakdown starts from free background electrons [Tie99] or, for ultrashort pulses, from a small number of seed electrons produced by tunnel ionization. Time constraints in avalanche ionization, which are considered in detail by Kaiser and Rethfeld [Kai00, Ret04] and in a simpler way also in the present model, are neglected by Mourou and coworkers. Due to these assumptions and to the adoption of Thornber's theory in which the avalanche progresses faster than in the Drude model (????), breakdown is not regarded as an interplay of PI and AI but even femtosecond breakdown is considered to be dominated by AI.

As a consequence, the experimentally well established deterministic character of femtosecond breakdown can be explained only by hypothesizing that the target material is fully ionized even at the breakdown threshold. A small number of seed electrons cannot explain the deterministic character of breakdown, and if the ionization avalanche is assumed to be responsible for the regular outcome of the breakdown process, it must have a clearly defined endpoint. For a very rapidly advancing avalanche, "full ionization" is the only well reproducible end-point [Jog04]. By contrast, the present study and its predecessors [Ken95, Noa99, Vog05] explain the deterministic character of breakdown in a large part of the (τ_L, λ) parameter space by assuming that seed electrons produced by direct photoionization are always readily available – either because large irradiances are required for the completion of the breakdown process within a short laser pulse duration, or because of the low order of the multiphoton process for short wavelengths. Due to the time constraints for the ionization avalanche in femtosecond breakdown and the limiting role of recombination in picosecond and nanosecond breakdown, the AI progresses at a moderate rate and the endpoint can thus vary with irradiance. The deterministic character of breakdown emerges as a genuine consequence of the continuous interplay between photoionization, AI, and recombination. Thus, the theoretical framework put forward by the University of Michigan group has strong implications for practical femtosecond laser applications. It denies the existence of a low-density plasma regime that could be used for cellular surgery below the threshold for bubble formation. Implicitly, it also questions established theories for nonlinear imaging that explain image formation by multiphoton effects ("multiphoton microscopy").

By detecting steps in the $I_{th}(\lambda)$ data for IR ns breakdown, we demonstrated MPI initiation of ns breakdown in pure media. The observed steps are not as high as predicted by our model that is based on the Keldysh theory of photoionization may be attributable to a partial quenching of MPI [Du96] – but certainly MPI is not fully quenched. The importance of MPI is corroborated also by the slow decrease of I_{th} with λ for 265-fs pulses (Fig. 4.26) that should be much steeper if AI was the dominant mechanism governing femtosecond breakdown. It is confirmed also by the experimentally observed tunability of plasma-mediated laser effects in a large part (τ_L, λ) parameter space that will be demonstrated in sections 5 and 6 of this report. Thus, our theoretical approach considering the interplay of PI (including MPI), AI, recombination and TI, has proven to be a powerful tool for modeling controlled nonlinear energy deposition. Moreover, it provides a theoretical basis for the explanation of our discovery of nanosecond laser-produced nanoeffects that rely on the existence of separate thresholds for bubble formation and BPL in the UV and VIS wavelength range.

4.4 Conclusions for the control of nonlinear energy deposition

The good agreement between the predictions of our advanced breakdown model and experimental results together with the ability to portray the origin of different thresholds for bubble and luminescent plasma formation encouraged creating a map of the (λ, τ_L) parameter space in which the dependence of target temperature on laser energy is calculated for each (λ, τ_L) value and both thresholds are marked. The relative distance between these thresholds defines the "tunability" of nonlinear energy deposition. If the thresholds coincide, such as for IR nanosecond breakdown, there is no tunability at all. If the thresholds are far apart on the energy scale, the tunability is very good. We define the tunability parameter ξ as

$$\xi = \frac{I_{BPL} - I_{Bubble}}{I_{Bubble}} = \frac{I_{6000\,K} - I_{573\,K}}{I_{573\,K}}. \tag{4.7}$$

For the sake of consistency we use the same critical temperature $T_{cr} = 573$ K in the entire (λ, τ_L) parameter space. If BPL and bubble threshold coincide, $\xi = 0$. If the BPL threshold is twice as high as the bubble threshold, $\xi = 1$, i.e. the irradiance must be increased by 100% to tune the effect from bubble formation to BPL. A "tunability map" is presented in **Fig. 4.27**.
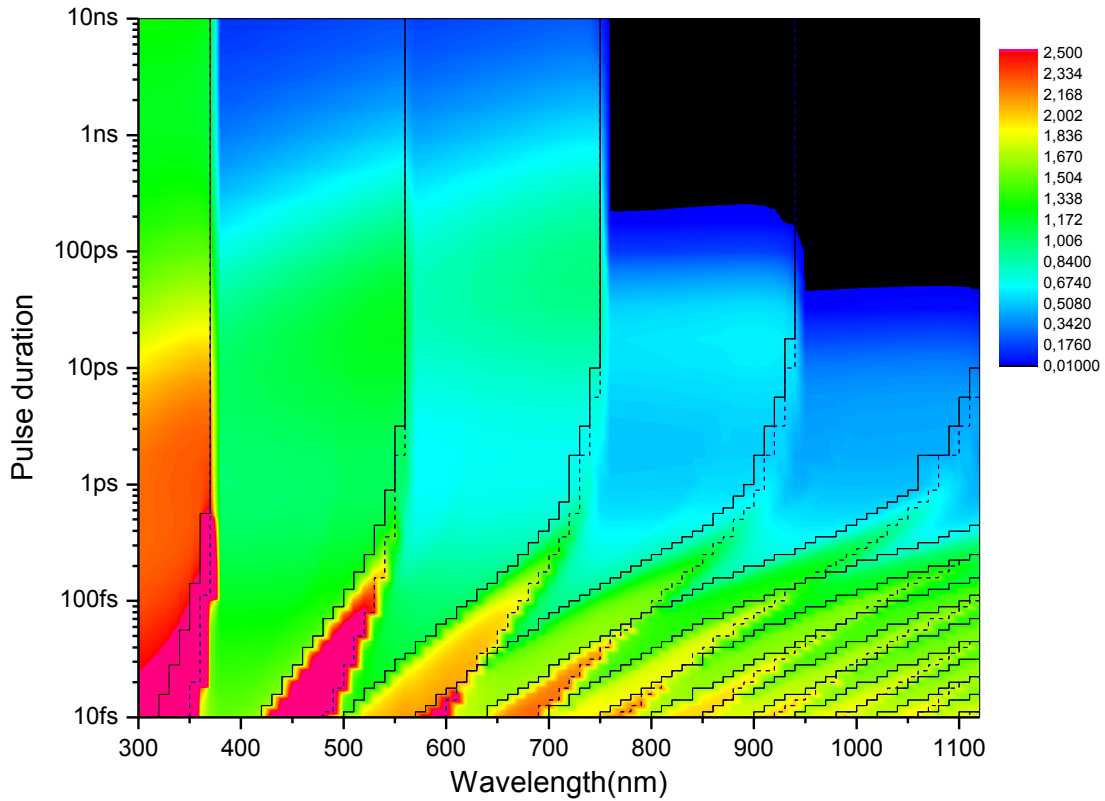
Figure 4.27 "Tunability" map in which the normalized difference between BPL and bubble threshold is plotted in the (λ, τ_L) parameter space. The map has been calculated for $T_{cr} = 573$ K, $NA = 0.8$, $\tau = 3$ fs, $\rho_{ini} = 2 \times 10^{13}$ cm^{-3}, $E_{gap} = 6.55$ eV.

Borders between regions with different tunability arise wherever an additional photon is required to overcome the band gap. The wavelengths at which these borders are located change with decreasing pulse duration because the threshold irradiance increases for shorter pulses, which results in an increase of the oscillation energy of the free electrons in the electric field and, thus, in an increase of the effective ionization potential (2.1). The solid lines indicate the borders of the regions relevant for the bubble threshold, and the dashed lines demarcate the borders relevant for the BPL threshold. Since ξ depends on the normalized difference between both thresholds, it varies with λ and τ_L in a complicated fashion, especially for very short pulse durations. The shift between black lines and color change is due to the finite width of the steps in the $I_{th}(\lambda)$ curves (Fig. 4.26).

For any specific wavelength, tunablity increases with decreasing pulse duration. For a given pulse duration, tunability increases with decreasing wavelength. Tunability is zero for IR wavelength and nanosecond pulse durations (reaching into the picoseconds range) and best for UV femtosecond pulses. The map is useful in guiding the choice of laser parameters for a large variety of applications. Its utility could be further improved by incorporating plasma growth and shielding into the breakdown model that influence the tuning range.

5. Plasma size, structure, and energy density at energies above the breakdown threshold

While the cavitation bubble energy (section 6) reflects the total amount of deposited energy, additional information is required to determine the corresponding plasma energy density and assess its temperature and pressure. We take photographs of the plasma luminescence to determine the plasma volume, and measure the plasma transmission to assess the energy absorbed in this volume. These data, together with structural details on the photographs, provide valuable information on the plasma size dependence on incident laser energy, the average plasma energy density and pressure, and hot regions within the plasma.

A complete compilation of plasma photographs at different pulse durations, wavelengths and pulse energies is presented in the appendix, together with measurement results for plasma volume, transmission and energy density as a function of laser pulse energy. In this section, we present an overview with emphasis on results that highlight characteristic features of the breakdown dynamics.

5.1. Plasma structure, size, and emission characteristics

5.1.1. Photographs of nanosecond breakdown

Figure 5.1 shows photographs of plasmas produced by slm 355-nm, 6.8-ns pulses for which we first observed separate thresholds for bubble formation and bright plasma luminescence (BPL). In the small-bubble regime, no plasma luminescence was observed. However, we observed that residual green laser light from the SHG/THG process was scattered from the optical breakdown region. We assume that in this breakdown regime a low-density plasma is produced, that does not emit the typical bluish plasma radiation but produces a refractive index change that is strong enough to scatter the incident laser light. The light scattering region grows with increasing laser energy towards the incoming laser beam. The green scattering was very weak such that the photographs had to be integrated over 100 laser pulses. At $E_\mathrm{L} = 45$ µJ, more than 20 times above the bubble formation threshold, bright plasma luminescence appears abruptly in a much larger volume than that from which the light scattering originates at lower energies. The bright luminescence was photographed with single exposures.
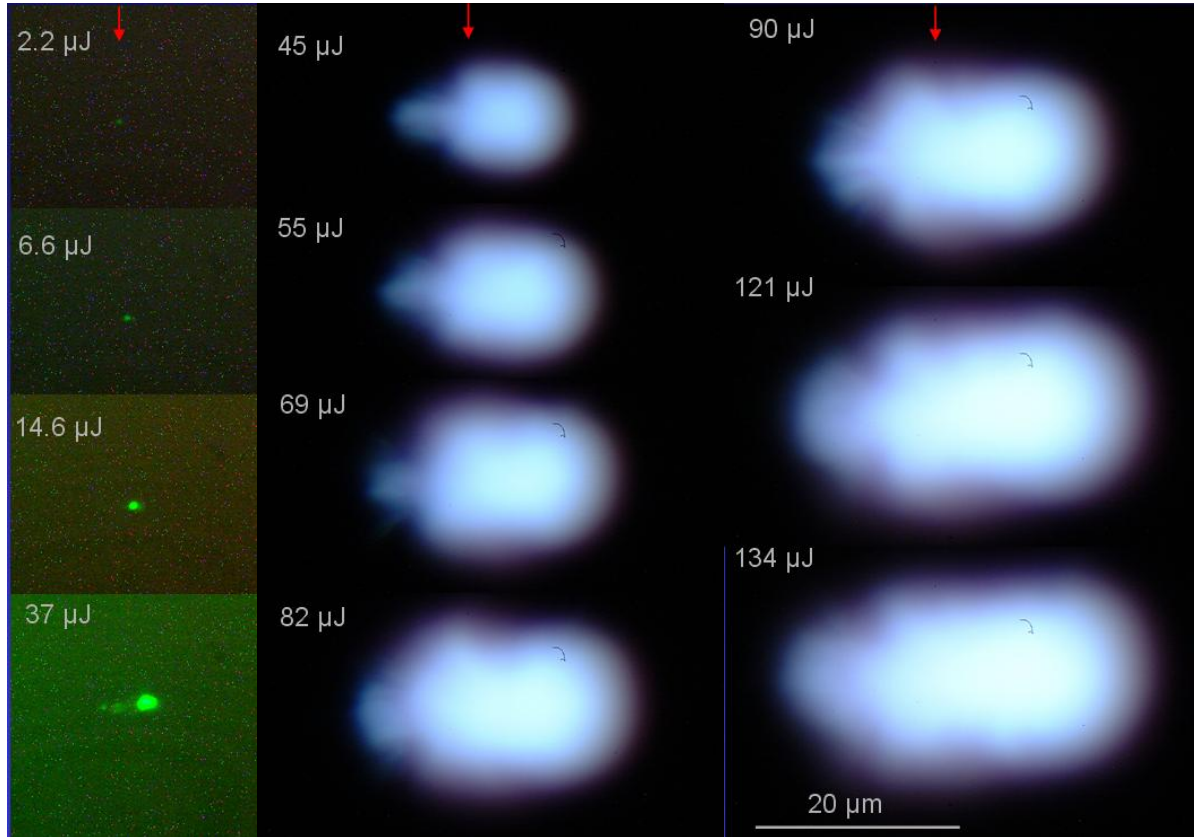
Figure 5.1 Photographs of plasmas produced by slm 355-nm, 6.8-ns pulses of various energies focused at $NA = 0.8$.
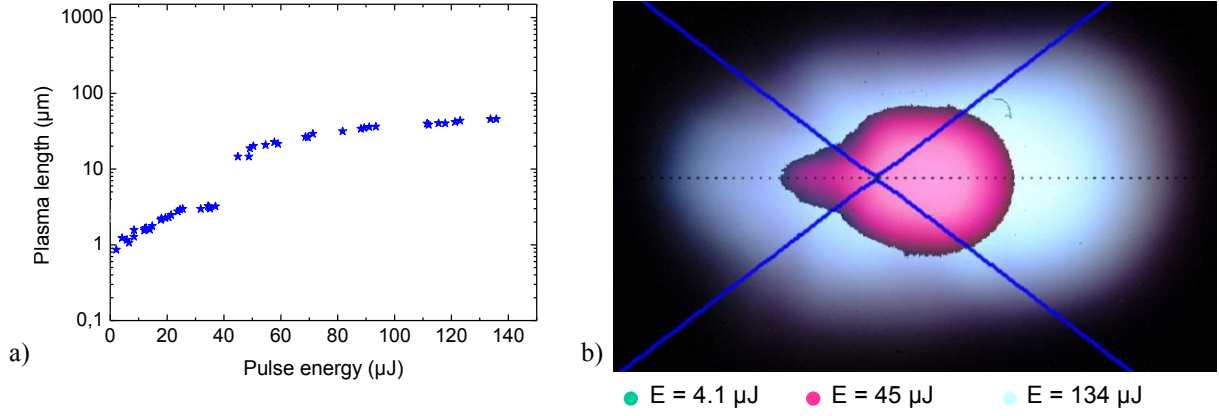
Figure 5.2 a) Plasma length as a function of laser pulse energy for 6.8-ns pulses at 355 nm wavelength focused at *NA* = 0.8. b) shows an overlay of plasma photographs at various pulse energies, and the laser cone angle.

Figure 5.2 illustrates the enormous jump in plasma size at the BPL threshold. Above this threshold, the plasma luminescence extends beyond the beam waist and into regions outside the cone angle of the laser beam. **Figure 5.3** and **Fig. 5.4** show that the extent of luminescence beyond the cone angle is a general feature of nanosecond optical breakdown at large *NA* because it is observed for all laser wavelengths investigated.
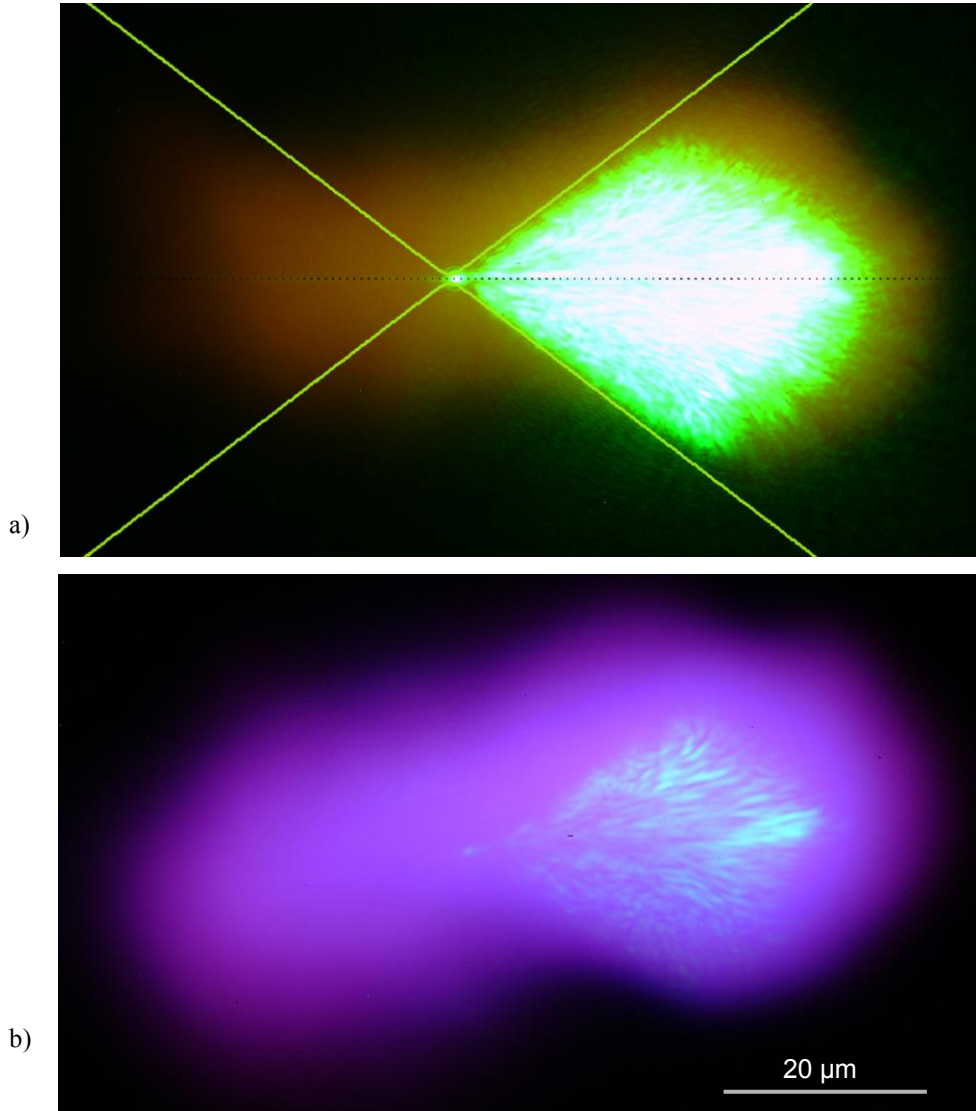
Figure 5.3 Plasma luminescence produced by 8.8-ns slm pulses of 532 nm wavelength and 0.73 mJ energy focused at *NA* = 0.8. To attenuate the scattered laser light, we used a) a color glass filter, and b) a dichroic blocking filter for 532 nm
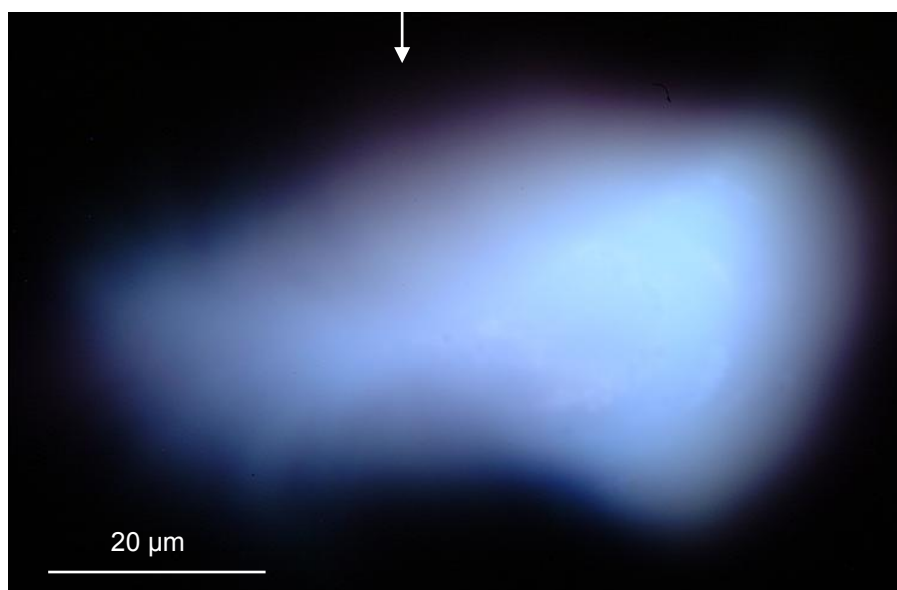
Figure 5.4 Plasma luminescence produced by an 11.2-ns, 1064-nm slm pulse of 0.59 mJ energy focused at *NA* = 0.8. Plasma luminescence is brighter within the cone angle of the laser beam both in front and behind the beam waist (arrow).

Plasma photographs are time-integrated images taken with open shutter in a dark room. Scattering of ‚pump‚‚ laser light by regions with large free-electron density ρ reveals filament-like plasma structures formed during the laser pulse within the cone angle of the incident laser beam. The region from which laser light is scattered defines the zone of initial energy deposition. How do the filaments form and grow towards the incoming laser beam? We assume that small spatial fluctuations in free electron density nucleate spatial insta-bilities in the highly nonlinear plasma formation process. Regions with larger free-electron density ρ exhibit a larger avalanche ionization rate ($\propto \rho$) and exceed earlier the threshold for AI&TI runaway. Therefore, locally a hotter plasma with faster electron diffusion into neighboring regions is formed and breakdown occurs preferentially in regions adjacent to filaments. Shielding of downstream regions by already existing plasma favors filament growth towards the incoming laser beam.

Scattering of ‚pump‚‚ laser light originates only from regions within the laser cone angle as evident from Fig. 5.3. By contrast, diffuse plasma luminescence is emitted from a much larger region extending 20-30 µm beyond the laser cone angle, especially in forward direction. The asymmetry of the diffuse halo indicates that it is not caused by the hydrodynamic plasma expansion. What are the mechanisms of energy transport from the high-density filaments into the diffusely emitting plasma? Why does the energy transport occur preferentially in forward direction? To be able to give a tentative answer to these questions, we need to consider the penetration depth of optical radiation and X rays in water in **Fig. 5.5** and look at the photographs of plasma luminescence at smaller numerical apertures in **Fig. 5.6** and **Fig. 5.7**.

a)   b)
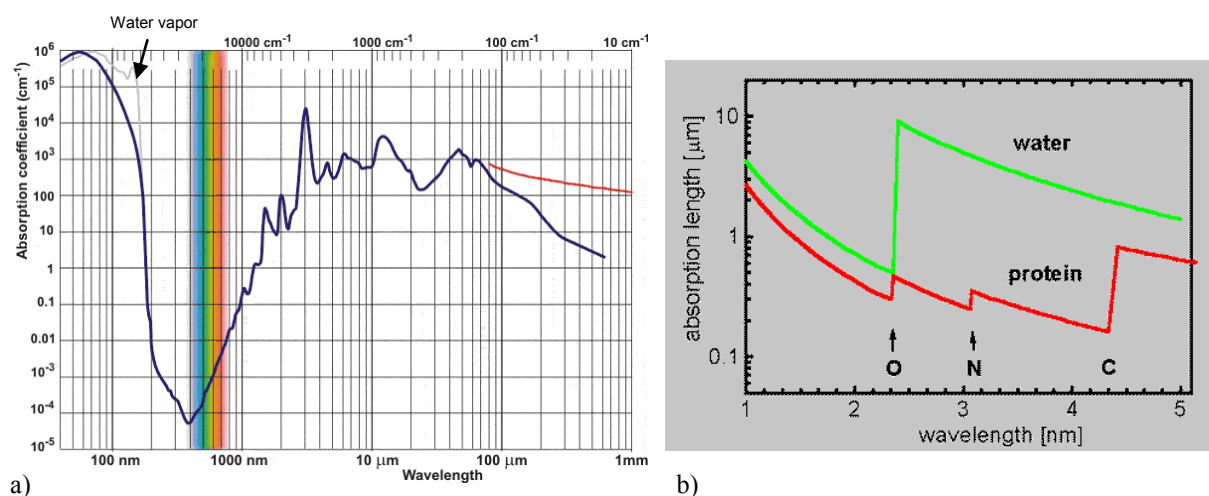
Figure 5.5 Penetration depth of a) optical radiation in water (source: http://www.lsbu.ac.uk/water/vibrat.html) and b) X rays in water (source: H. Stiel, Max Born Institut Berlin: e-mail: stiel@mbi-berlin.de)
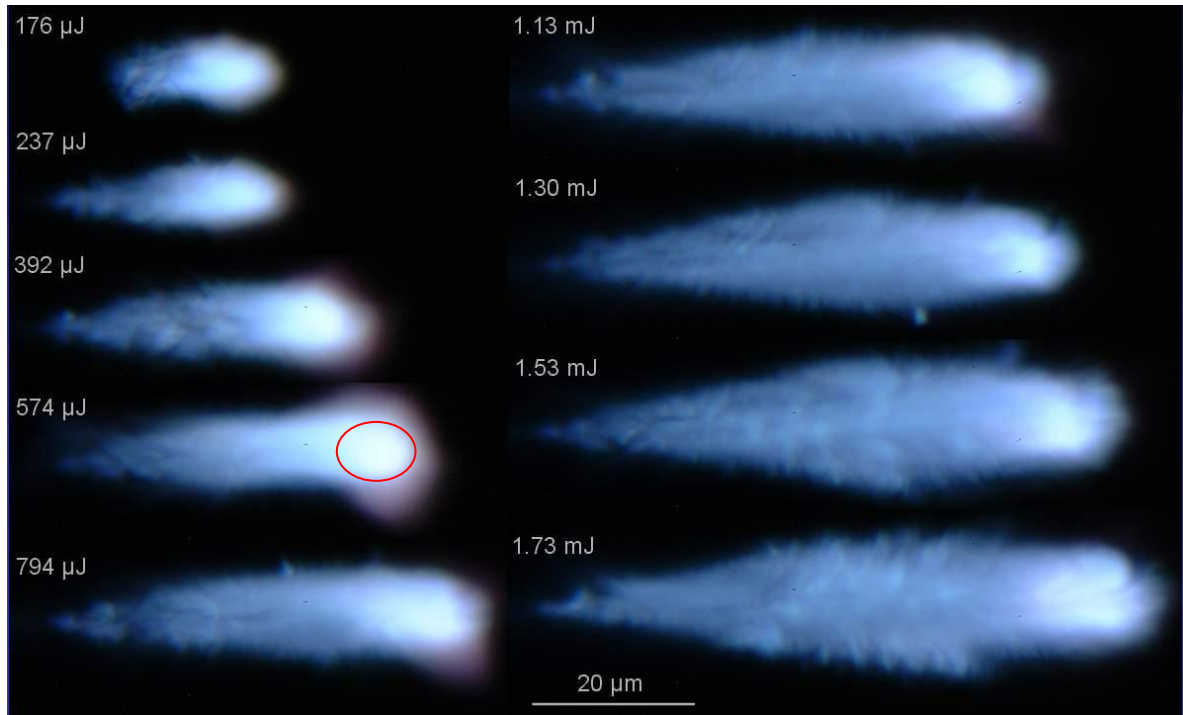
Figure 5.6 Plasma luminescence produced by 6.8-ns, 355-nm slm pulses of various energies focused at *NA* < 0.3. The energy density within the bright spot (marked red) most likely exceeds 270 kJ/cm^3 . We arrive to this conclusion by assuming the plasma growth ceases at the peak of the laser pulse, and afterwards all energy is deposited in the upstream part of the plasma creating the very brightly luminescent volume. This implies that half of the pulse energy must be absorbed in the bright region.
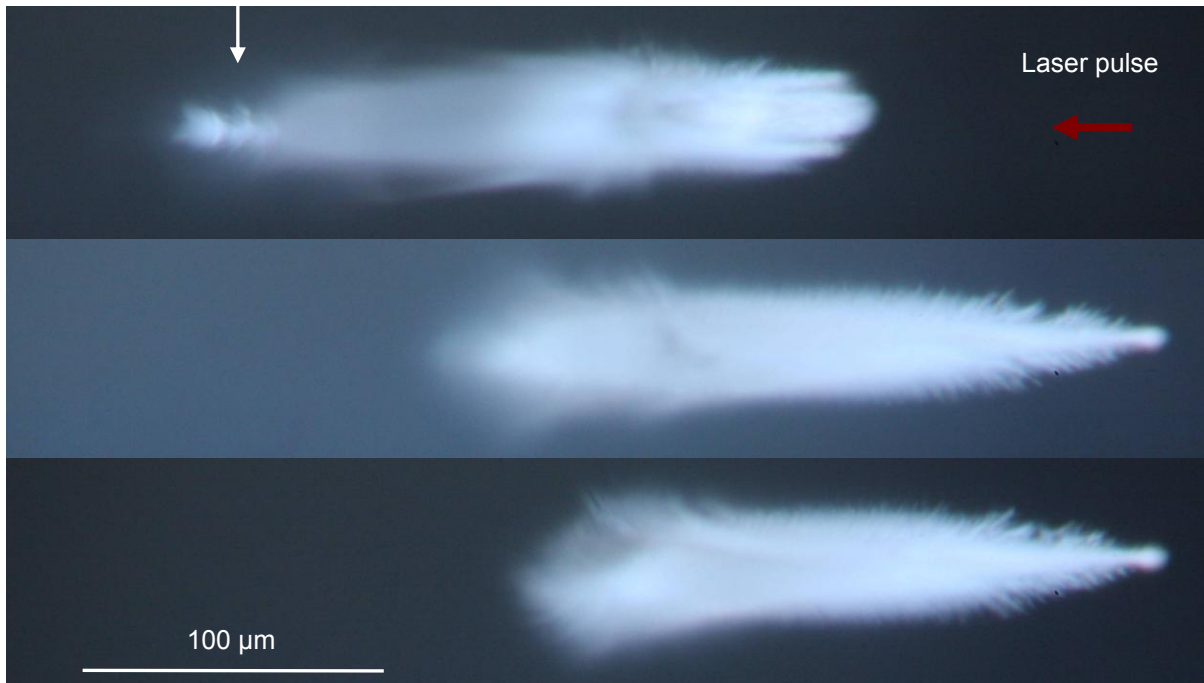
Figure 5.7 Plasma luminescence produced by 11.2-ns, 1064-nm slm pulses of 4.62 mJ focused at *NA* = 0.1. The breakdown dynamics at this small numerical aperture is influenced by stimulated Brillouin scattering (SBS) and, due to the linear absorption of water at 1064 nm (Fig. .5.5a), by thermal self-focusing of the light reflected by SBS. This produces a hot spot of large irradiance upstream from the beam waist, which is marked by an arrow.

Candidates for the mechanism of energy transport from the high-density filaments into the diffusely emitting plasma regions outside the laser cone angle and behind the beam waist are 1. diffusion of ‚hot‚ electrons (β radiation), 2. ionization via UV or X-ray radiation; either blackbody radiation, or bremsstrahlung. Since the penetration depth of free electrons in water is below 1 μm [Gru00], it cannot explain the extended halo, and the only explanation left is radiative energy transport by photons [Rob96]. The penetration depth of UV radiation in water is very small – about 10-100 nm for wavelengths between 40 and 100 nm (Fig. 5.5a). The photon penetration depth increases with decresasing wavelength [Gru00]. For soft x-rays of $\approx$ 2.5 nm wavelength (hv $\approx$ 500 eV), it is about 10 μm (Fig. 5.5b).

It is unlikely that the (hypothetical) x-ray radiation is blackbody radiation because in that case the diffuse halo should be homogeneously distributed around the energy deposition region, with no preference in forward direction. Blackbody radiation is probably seen around the ‚hot spots‚ in Fig. 5.6. Here an approximately isotropic halo with a red shift towards it‚s periphery is observed. The plasma emission from the hot spots likely continues during the plasma expansion, leading to the red shift because of the adiabatic cooling within the expanding plasma. By contrast, the diffuse halo around high-density plasmas produced at large *NA* (Fig. 5.1) is bluish everywhere.

Alternatively, X-rays could be produced by Bremsstrahlung from hot electrons within the filaments. This would explain the forward direction of the extent of the halo because the electrons should carry the photon impulse of the incident laser radiation that is imparted during inverse Bremsstrahlungs absorption. Multiple scattering would explain components under 90° and in backward direction. Note that the forward direction of the radiative energy transport can be seen in many images - not only in Fig. 5.3 but also in Fig. 5.1 and even in Fig. 5.6 where a halo extends from the hot spot towards the tip of the plasma at the beam waist but is obscured by the other plasma radiation.

When X-rays are absorbed in the halo region, their energy creates a cascade of electrons of lower energy that, in turn, can produce radiation of longer wavelength - either by Bremsstrahlung, or by heating and blackbody radiation. Thus, the visible plasma luminescence is the long-wavelength tail either of bremsstrahlung, or of blackbody radiation emitted from the halo region. This tail can escape the water cell as soon as wavelengths with sufficiently large optical penetration depth are produced.

The filaments visible in Fig. 5.3 provide good laser-plasma coupling efficiency because they are thin ($\approx$ 1 μm), and evanescent waves can couple energy into these ‚fractal‚ structures even when the free-electron density already exceeds the critical density at which plasma becomes both strongly reflective and absorbing [God72, God79, God95]. Moreover, the filaments act as an energy trap with immediate re-absorption of Bremsstrahlung in the UV region of the optical spectrum. Once the free-electron temperature (energy) in the filements becomes sufficiently large for generation of soft X-rays, these can escape and produce the halo.

In IR breakdown at lower *NA* (Fig. 5.7), the filaments are sharply demarcated without a surrounding halo because no energy can leave the ‚trap‚ due to a smaller free electron temperature in the plasma. The critical plasma density is smaller for longer wavelengths and, therefore, the laser-plasma coupling is weaker, the free-electron temperature remains lower, and no halo is produced. At larger *NA*s, the plasma energy density is generally higher [Vog96b, Vog99a], an a halo can be produced even with IR laser pulses (Fig. 5.4).

The sharp borders of the plasma luminescence in Fig. 5.7 and the structures within the weakly luminescent plasma regions in Fig. 5.6 indicate that the luminescence in these regions is, most likely, not caused by blackbody radiation. If it was blackbody radiation, blurring should occur such as around the bright ‚hot‚ spot in Fig. 5.6 where the emission continues during the plasma expansion. The bluish radiation in the weakly luminescent parts could possibly be Bremsstrahlung, or recombination radiation. It is difficult to resolve these questions spectroscopically because of the re-absorption of short wavelength radiation in the water.

Experimental evidence for large energy densities in the high-density filaments or in hot spots is provided in Fig. 5.6: If we assume that the energy deposition occurs in accordance to the moving breakdown described in section 2.2, the plasma growth ceases at the peak of the laser pulse, and afterwards all energy is deposited in the upstream part of the plasma. This implies that half of the pulse energy must be absorbed in the brightly luminescent, red encircled region. Following this assumption, we obtain an energy density of $\approx$ 270 kJ cm^{-3}, which is more than hundred times the vaporization enthalpy of water. Using the equation of state (EOS) for high energy-density water by Mattsson and Desjarlais [Mat06, Mat07], we can relate the energy density to pressure and temperature, as shown in **Fig. 5.8.**
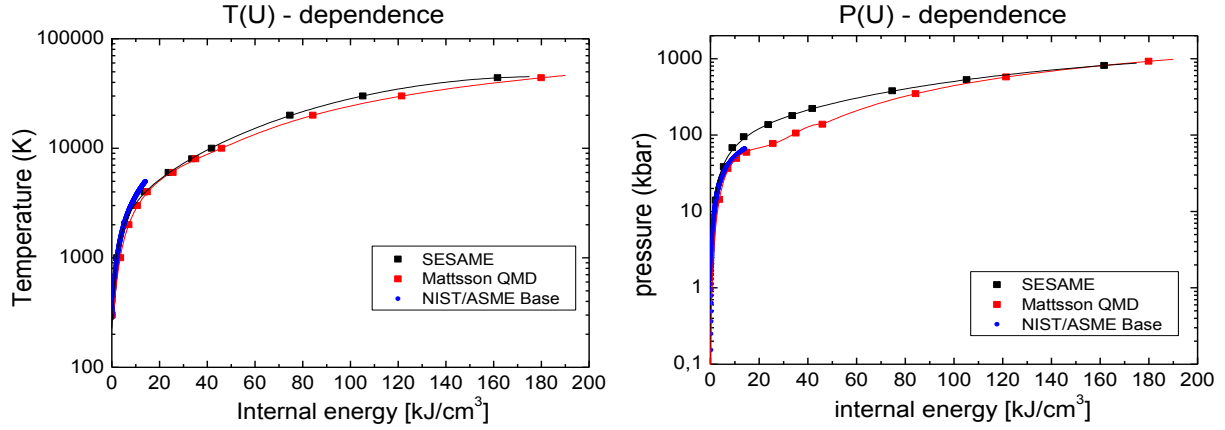
Figure 5.8 Dependence of temperature and pressure on internal energy for high energy-density water. The NIST equation of state (EOS) does not cover the high energy-density region [NIS05]. Data are available from the SESAME data base (Los Alamos National Laboratories) and from the recently established EOS by Mattsson and Desjarlais that is based on quantum mechanical molecular dynamics simulations [Mat07]. SESAME overestimates the pressure in an intermediate energy density region because it overestimates dissociation. Therefore, we use the EOS of Mattsson and Desjarlais.

The value of 270 kJ cm^{-3} is outside the range of the EOS data covered in Fig. 5.8. By extrapolation, we obtain a corresponding a temperature of $\approx 10^5$ K and a peak pressure > 1 Mbar, i.e. > 100 GPa. If we assumed that the plasma radiation is pure blackbody radiation, this would imply the existence of a thermal equilibrium between electrons and ions. In that case, temperatures well exceeding 10^5 K are required to produce 2.5-nm radiation. However, if the electron temperature is higher than the ion temperature, 2.5-nm radiation can be produced already at lower average energy density and temperature, and conditions corresponding to an average temperature of $\approx 10^5$ K may suffice to produce the radiative energy transport resulting in the halo. Vogt and coworkers already showed experimentally that soft x-rays can be produced by focusing nanosecond laser pulses onto a water jet [Vogt01]. Thus, our hypothesis does not seem too far-fetched.

It must be emphasized that pressure and temperature can be deduced from internal energy only if the density of the medium is known. The density is known for optical breakdown in water whenever the energy deposition is isochoric, i.e. stress confined. This is always the case for ultra-short pulse breakdown because in that case the thermalization time is much shorter that the acoustic transit time through the focal volume even for sub-micrometer plasma diameters. Ns optical breakdown is nearly stress-confined for plasmas > 10 μm that are produced only at energies well above the optical breakdown threshold.

The largest plasma pressure values measured so far were 8-12 GPa at the plasma rim for IR breakdown produced by unseeded 6-ns pulses [Noa98]. Nevertheless, the much larger value > 100 GPa obtained in the above estimate may be realistic because it refers to a hot spot within a plasma produced by a UV pulse. Laser-plasma coupling is much better for UV pulses than for IR pulses because the critical free electron density above which plasma becomes reflective is 9 times larger at 355 nm than at 1064 nm (Eq. 2.6). Moreover, energy is rapidly dissipated at shock fronts exhibiting a very large pressure jump [Duv63, Vog96a], and the pressure at the plasma rim may, hence, be considerably lower than at hot spots within the plasma.

Figure 5.9 presents photographs of the luminescent plasmas produced by slm 0.55-ns laser pulses of 355 nm wavelength that were focused at different *NA*. For all *NA*s, plasma formation starts at the beam waist and grows with increasing pulse energy predominantly towards the incident laser pulse. In addition, a sharp tip is formed that extends beyond the beam waist in propagation direction of the laser beam. The absolute length of the tip increases with decreasing NA, but the ratio (tip length)/(overall plasma length) is similar for all NAs.

The plasmas produced at low *NA* exhibit a relatively homogeneous brightness distribution while the plasmas produced at NA = 0.8 show bright luminescence especially in the rear part of the plasma. Since the plasma growth by a moving breakdown wave ceases when the peak power in the laser pulse is reached, all energy contained in the second half of the pulse is deposited into the already existing plasma [Doc88, Vog96]. This explains the origin of the bright spot and suggests that at least half of the absorbed energy is deposited in this region. For smaller NA, this effect gets smaller but for NA = 0.3 a small bright rim is still visible at the right side of the plasma, oriented towards the incoming laser pulse.
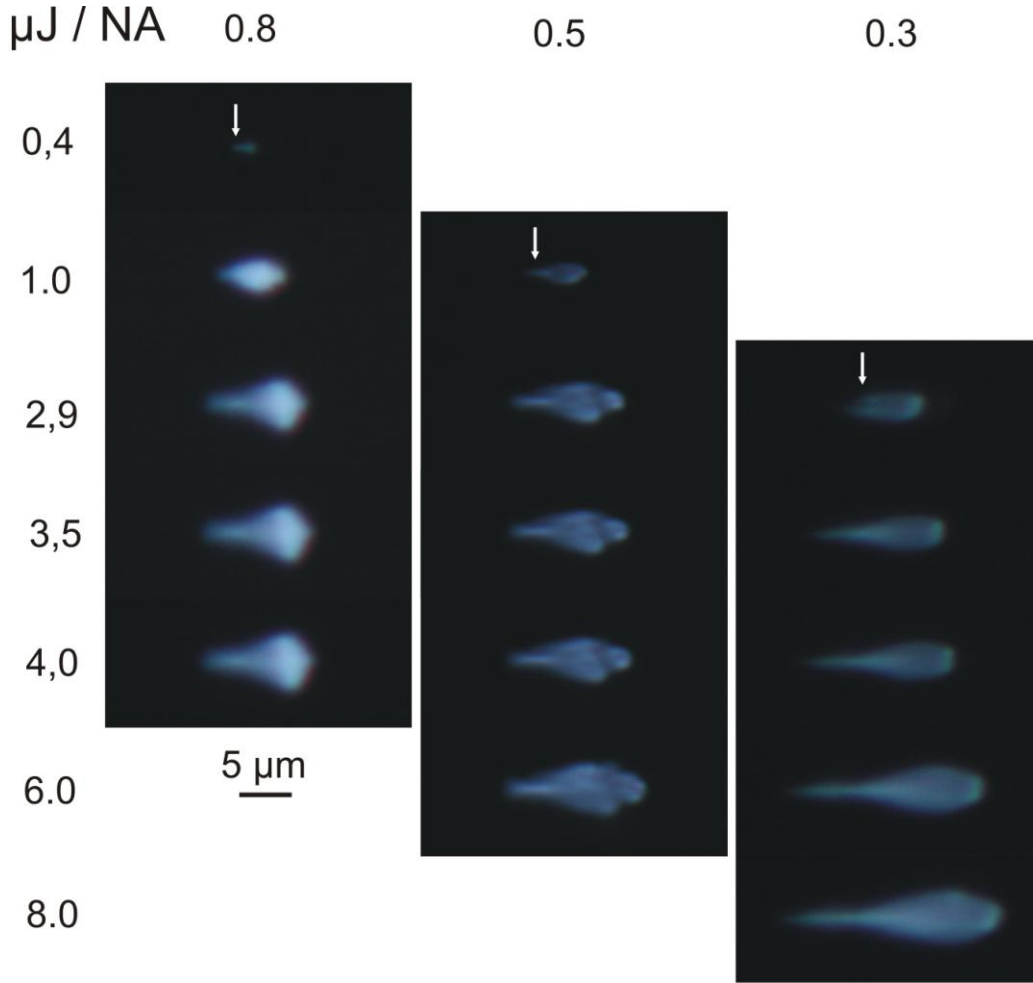
Figure 5.9 Photographs of the plasma luminescence produced when 0.55-ns laser pulses of 355 nm wavelength are focused at *NA* = 0.8, *NA* = 0.5, and *NA* = 0.3. The rows correspond to equal energy for the different focusing geometries. All photographs were integrated over 10 laser pulses. The laser light is incident from the right. The white arrows mark the position of the beam waist of the focused laser pulse.

The filamentation-like plasma tip that extends well beyond the beam waist must be related to some kind of nonlinear beam propagation. The critical power for catastrophic beam collapse is [Liu03]

$$P'_{cr} = \frac{3.72 \cdot \lambda^2 \pi}{8\pi \, n_0 \gamma} \, , \tag{5.1}$$

with $n_0 = 1.33$, $\gamma \approx 4 \cdot 10^{16}$ cm²/W for water. For $\lambda = 355$ nm, we obtain $P'_{cr} = 0.355$ MW, and, with $\tau = 550$ ps, $E'_{cr} = 195$ µJ. Thus the critical energy for self-focusing is much larger than the energies of 1-8 µJ that produce the filamentation in Fig. 5.9. Plasma defocusing [Fei74, Cou07] is the only mechanism that can explain the observed filamentation. The refractive index of plasma is smaller than that of normal water, and the plasma thus acts as diverging lens for the transmitted part of the incident laser light. The free electron density distribution in the plasma reflects the resulting laser intensity distribution in the beam waist. In the center part close to the optical axis, most of the incident laser light is absorbed by high-density plasma, whereas the boundary of the plasma with low density leads to a defocusing of the laser pulse. This defocused laser light will be focused slightly behind the original position of the beam waist. Here it creates additional plasma, which then contributes to further defocusing. Thus, nonlinear beam propagation effects may influence plasma-mediated energy deposition well below the self-focusing threshold.

We conclude that the spatio-temporal dynamics of plasma formation is, especially for long laser pulse durations, much more complex than previously assumed and by far not yet completely understood. Time-resolved investigations of nanosecond breakdown by time-gated photography can provide further insight.

5.1.2. Photographs of femtosecond breakdown

Figure 5.10 shows that plasma luminescence can be detected when 1040-nm femtosecond laser pulses with energies of approximately 90 - 570 nJ are focused into water at a numerical aperture of 0.8. This finding is very remarkable because plasma luminescence has never been observed when femtosecond pulses were focused at smaller numerical apertures (NA ≤ 0.3) and beam propagation was strongly influenced by nonlinear beam propagation and shielding effects [Vog99, Ham96]. White-light plasma emission was first observed when 25-µm water droplets were irradiated by powerful femtosecond laser pulses and breakdown generated by Mie-backscattering within the droplet that focused the scattered radiation at large *NA* [Fav02, Cour03].

$E = 48$ nJ, $\beta = 1.93$, $l = 1.8$ µm $E = 95$ nJ, $\beta = 3.81$, $l = 3.6$ µm

$E = 165$ nJ, $\beta = 6.6$, $l = 5.1$ µm $E = 323.8$ nJ, $\beta = 13.0$, $l = 6.5$ µm

$E = 458.6$ nJ, $\beta = 18.4$, $l = 7.3$ µm $E = 570.4$ nJ, $\beta = 22.8$, $l = 7.6$ µm
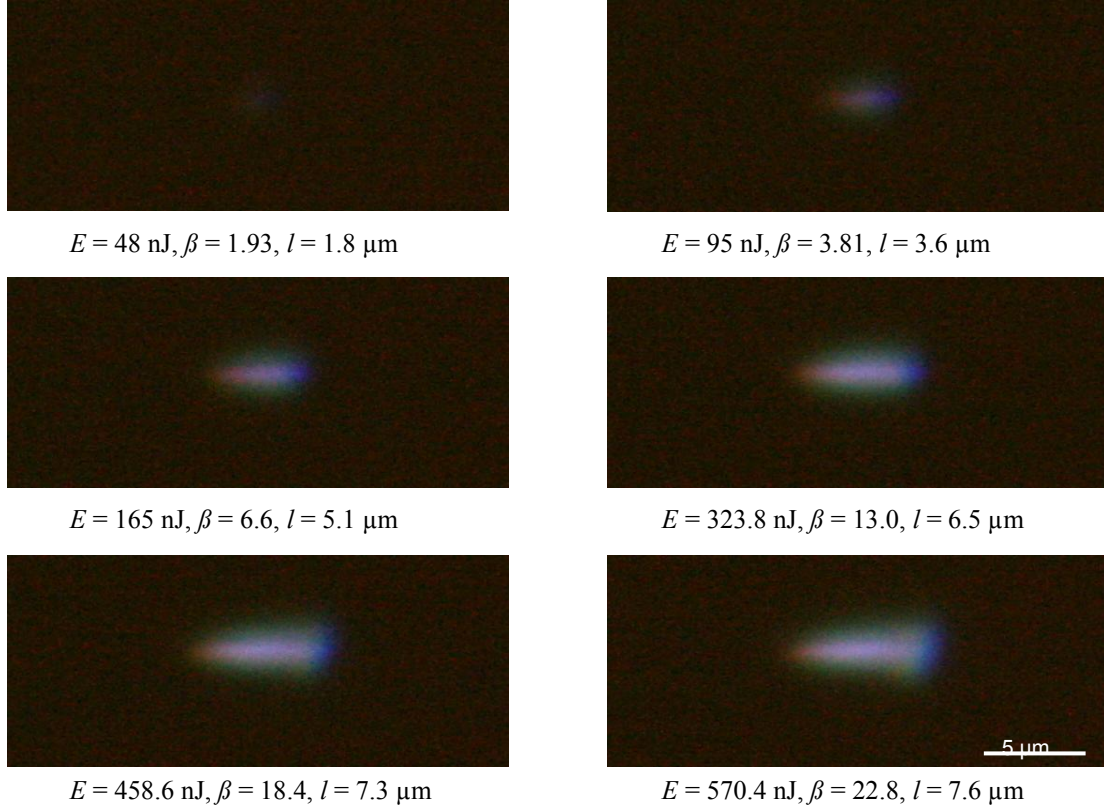
Figure 5.10 Photos of luminescent plasmas produced by 350-fs laser pulses with 1040 nm wavelength focused at NA = 0.8. The values of the pulse energy E, normalized energy $\beta = E/E_{th}$, and plasma length l are given below each frame. The laser light is incident from the right. All photographs are integrated over 70 laser pulses at ISO 3200 and auto white balance.

Figure 5.11 demonstrates that in femtosecond breakdown at large NA the plasma grows from the beam waist towards the incoming pulse as described by the classical "moving breakdown" model (section 2.2 and [Doc88,Vog96]). This is possible because the entire plasma length is only ≈ 5 µm, compared to a pulse length of ≈ 100 µm for $\tau_L = 350$ fs. By contrast, for small NAs and breakdown regions longer than the pulse length, the breakdown wave moves with the femtosecond laser pulse [Ham97, Arn05].
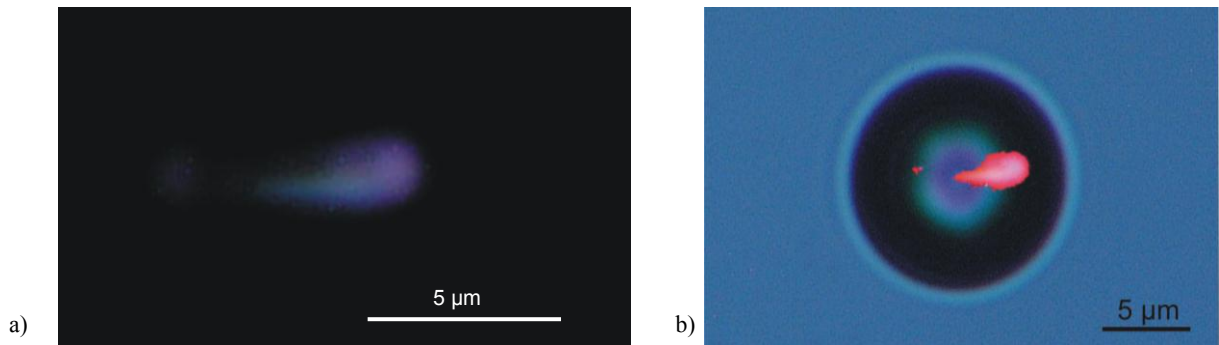
Figure 5.11 a) Plasma luminescence produced by a 350-fs, 1040-nm laser pulse with 160 nJ energy ($\beta = 7$) at NA = 0.8; the photograph was integrated over 150 laser pulses. b) Overlay of the plasma luminescence with a photograph of the bubble produced close to the breakdown threshold. The laser beam waist is presumably located at the center of the bubble. The plasma has grown from the beam waist towards the incoming laser beam.

Even though the light emitted by the plasma was collected with a numerical aperture of NA = 0.5, the plasma emission could be recorded only through integration over 70-150 pulses at an ISO setting of 3200. This is partially due to the large magnification employed (M = 175) but mostly to the weakness of the plasma emission. Since the emission is too weak for a spectral analysis to be performed, we are not yet sure whether it is blackbody radiation, Bremsstrahlung, or some kind of recombination radiation. We can exclude direct recombination radiation with photon energy of approximately 6.5 eV because such radiation would be immediately reabsorbed. However, in water, recombination is usually not a one-step process but consists in hydration of a free electron within about 300 fs and subsequent decay of the hydrated state that has an average lifetime of approximately 300 ns [Nik83]. Recombination radiation emitted during the decay of the hydrated state has a larger wavelength that may be able to leave the water cell. However, it seems unlikely that it is bright enough to be detected by the CCD chip of the digital camera. Moreover, if it could be detected, it should also be observable when the pump laser pulse is focused at smaller NAs, in contrast to previous experimental findings. A specific feature of the focusing at large NA, for which plasma luminescence was now first observed, is the highly localized energy deposition, leading to a highly compact plasma shape and large free-electron and energy densities. This would be consistent with an interpretation of the plasma emission as blackbody radiation.

Another feature of the plasma emission consistent with blackbody radiation is the color distribution from reddish at the beam waist through whitish at the center towards bluish at the upstream end. Since the plasma growth ceases when the peak power in the laser pulse is reached, energy contained in the second half of the pulse is deposited mainly into the upstream part of the already existing plasma while the beam waist is shielded. The resulting energy density distribution corresponds to the expected color temperature of blackbody radiation.

We used measured data sets of photographically determined plasma size and corresponding plasma transmission to determine the volumetric energy density (see slso section 5.3), and obtained a value of $\varepsilon \approx 10$ kJ/cm^3. Femtosecond optical breakdown is isochoric because the free-electron energy is thermalized only after the end of the laser pulse. Therefore, the liquid density ρ_0 at the end of the pulse is known, and from ρ_0 together with the measured value for the plasma energy density, we can calculate pressure and temperature using EOS data for high energy-density water [Mat06, Mat07], as already discussed in the previous section. For $\varepsilon \approx 10$ kJ/cm^3, we obtain an average temperature of T = 2800 K (consistent with a peak temperature of $T \approx 6000$ K and whitish luminescence in the plasma center) and $p = 4.8 \times 10^3$ MPa. Independently, we calculated p and T from the plasma volume and the measured maximum bubble radius R_{max} using the Gilmore model of bubble dynamics [Gil52]. For a plasma radius R_0 = 1.3 µm, max. bubble radius R_{max} = 36 µm, and equilibrium radius R_n (2.45 µm), the predicted breakdown pressure is $p = 1.35 \times 10^3$ MPa, less than the value obtained using the EOS [Mat06, Mat97].

We conclude that the states of matter upon femtosecond breakdown are much less extreme than postulated by Juodkazis and coworkers who claim that pressures up to 10^7 MPa such as in nuclear explosions are produced when 100-nJ femtosecond pulses are focused into sapphire [Juo06]. These authors did not measure the plasma size but just assume that is produced in a 20-50 nm thin skin layer such as in surface ablation.

While femtosecond breakdown in bulk transparent media corresponds to relatively low energy densities, temperatures and pressures, we found experimental evidence that very large energy densities ≥ 270 kJ/cm^3 can be produced in nanosecond breakdown. The strong difference in extent, energy density, and brightness of ns and fs plasmas is due to the different dynamics of free electron generation. In femtosecond breakdown, only one "set" of free electrons is produced and their energy is thermalized within a few picoseconds after the end of the laser pulse. In nanosecond breakdown, the thermalization time of the free electrons is only a small fraction of the laser pulse duration and, therefore, electrons are generated and recombine continuously during the laser pulse. Compared to one generation/thermalization cycle in femtosecond breakdown, this cycle can be repeated a thousand times during a nanosecond pulse. This way, very high plasma energy densities can be produced that will result in radiative energy transfer from the energy deposition region which ‚inflates' the plasma size, as seen in **Fig. 5.12.**
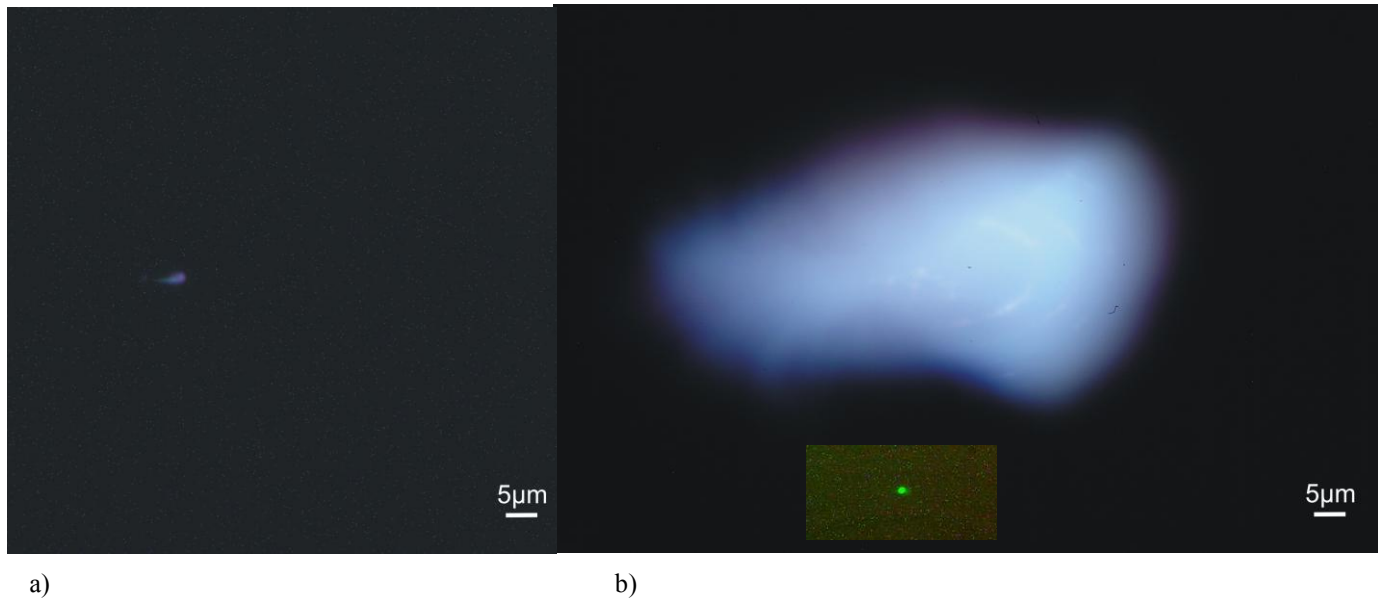
Figure 5.12 Plasma luminescence produced by IR femtosecond and nanosecond laser pulses, printed at equal magnification. a) 350-fs, 1040-nm laser pulse 7 times above bubble formation threshold (E = 160 nJ), b) 11-ns, 1064 nm laser pulse 7 times above BPL threshold (E = 590 µJ). For comparison, the insert in b) shows the low-density plasma produced by a 6.8-ns, 355 nm pulse 7 times above bubble formation threshold (E = 14.6 µJ). In all cases, the laser pulses were focused at $NA = 0.8$.

5.1.3. Plasma length and volume

Plots of plasma length and volume for all investigated combinations of laser pulse duration and wavelength are presented in Figs. 11.30 to 11.34 of the appendix. Here, in **Figs. 5.13 to 5.15**, we summarize the plasma length data for different wavelengths in one plot for each pulse duration and use a logarithmic scale to explore the respective scaling laws of plasma length with pulse energy. The moving breakdown model presented in section 2.2 predicts a scaling law of $l \propto (\beta-1)^{0.5}$. Agreement with this prediction is rarely seen; very often the slope of the $l(\beta-1)$ curve is less steep.

300 fs
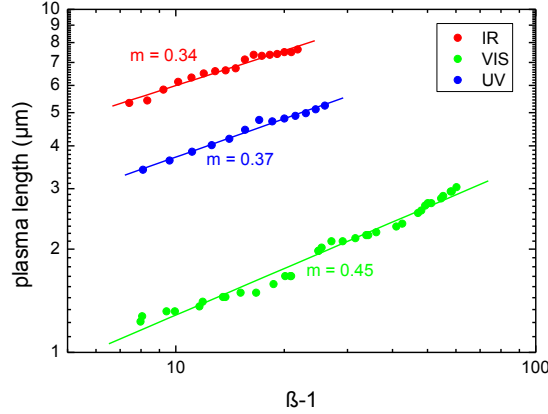
Figure 5.13 Length of luminescent plasmas produced by 352-fs laser pulses with 1040 nm wavelength, 306-fs laser pulses with 520 nm wavelength, and 280-fs laser pulses with 347 nm wavelength focused through a 40x water immersion objective (NA = 0.8), normalized to $\beta - 1$ with $\beta = E/E_{th}$.

1 ns, Gaussian
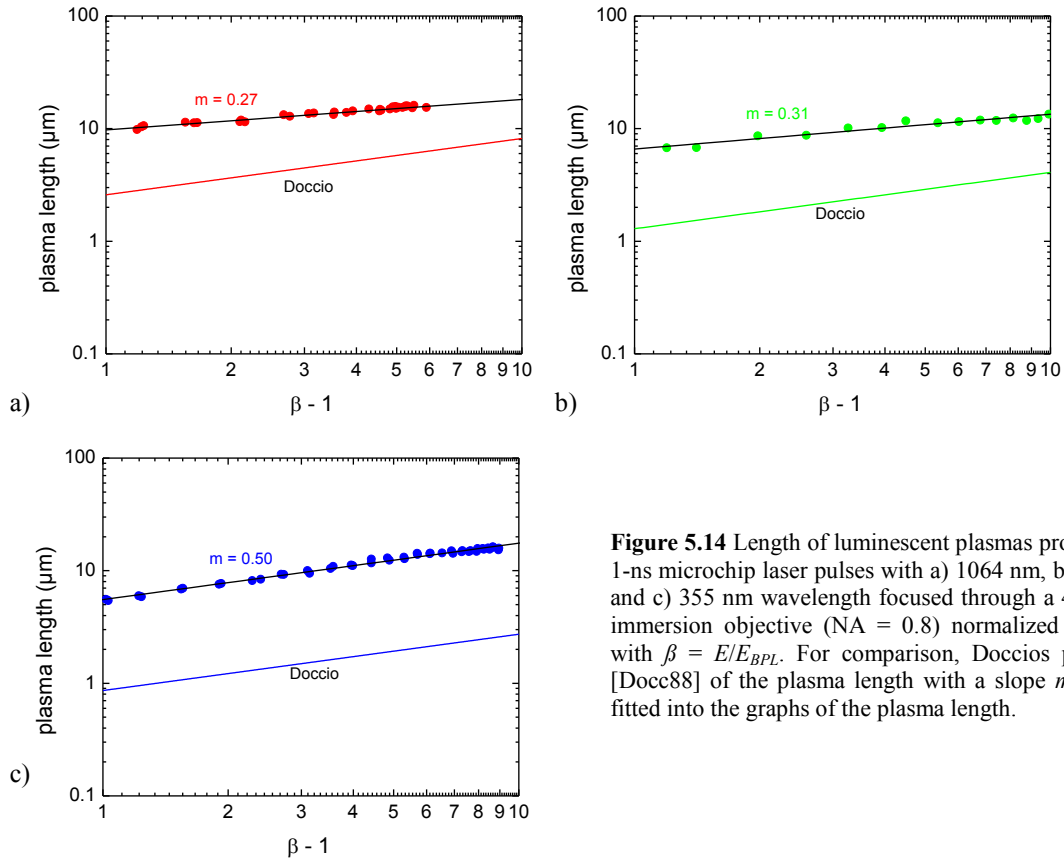
Figure 5.14 Length of luminescent plasmas produced by 1-ns microchip laser pulses with a) 1064 nm, b) 532 nm, and c) 355 nm wavelength focused through a 40x water immersion objective (NA = 0.8) normalized to $\beta - 1$ with $\beta = E/E_{BPL}$. For comparison, Doccios prediction [Docc88] of the plasma length with a slope $m = 0.5$ is fitted into the graphs of the plasma length.

7-11 ns, slm & unseeded
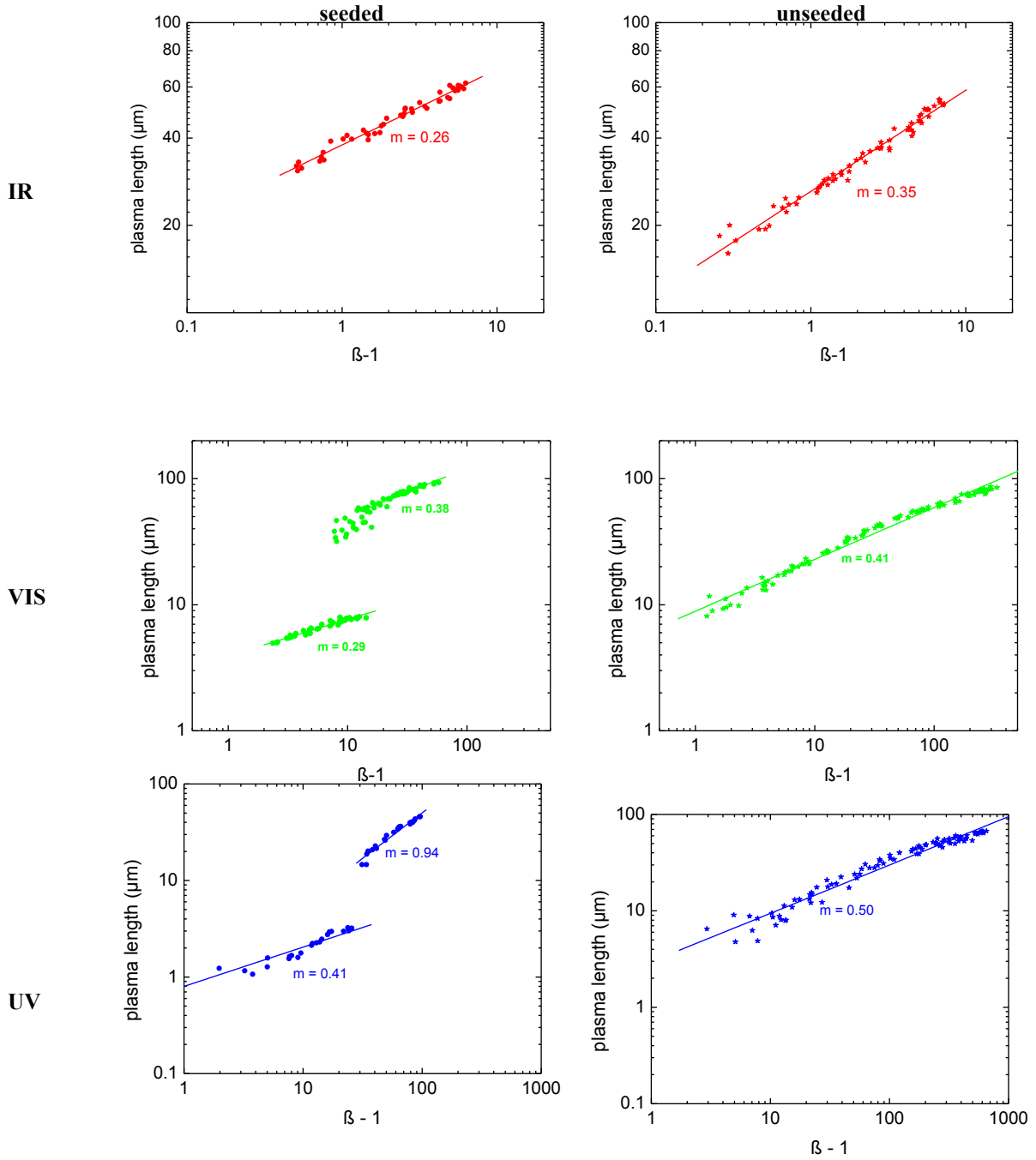
Figure 5.15 Length of luminescent plasmas produced by seeded and unseeded 11.2-ns laser pulses with 1064 nm wavelength, 8.8-ns laser pulses with 532 nm wavelength, and 6.8-ns laser pulses with 355 nm wavelength focused through a 40x water immersion objective (NA = 0.8) normalized to $\beta - 1$ with $\beta = E/E_{Bubble}$.

The most important deviation between the predictions of the moving breakdown model and the measurement data relate to the absolute values of the plasma length. Fig. 5.14 shows that the actual values often exceed the predicted values by a factor of ≈ 5, and Fig. 5.16 below demonstrates that for longer IR laser pulses of 11.2 ns duration, the factor is even ≈ 5. The reason for this deviation is that the moving breakdown model does not consider the plasma enlargement by radiative energy transfer from the region into which the laser energy is deposited. This enlargement is most pronounced at large NA, as investigated in this study. For smaller NAs that were explored in a previous study [Vog96b], the discrepancy also exists but is much less pronounced.
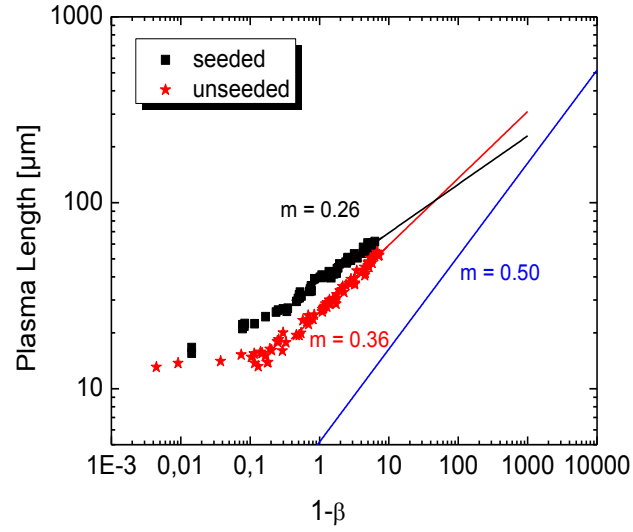
Figure 5.16 Length of luminescent plasmas produced by seeded and unseeded 11.2-ns laser pulses with 1064 nm wavelength, focused at NA = 0.8, compared to the prediction of the moving breakdown model (blue line).

5.2. Plasma transmission

The total plasma transmission was measured with the experimental setup described in section 3. The detailed results of the transmission measurements are presented in Figs. 11.35-11.39 in the appendix. Here, in **Fig. 5.17**, we summarize the transmission data for different wavelengths in one plot for each pulse duration. We plot the transmission data as a function of dimensionless energy β to facilitate the comparison between wavelengths for which the absolute threshold energies are different.
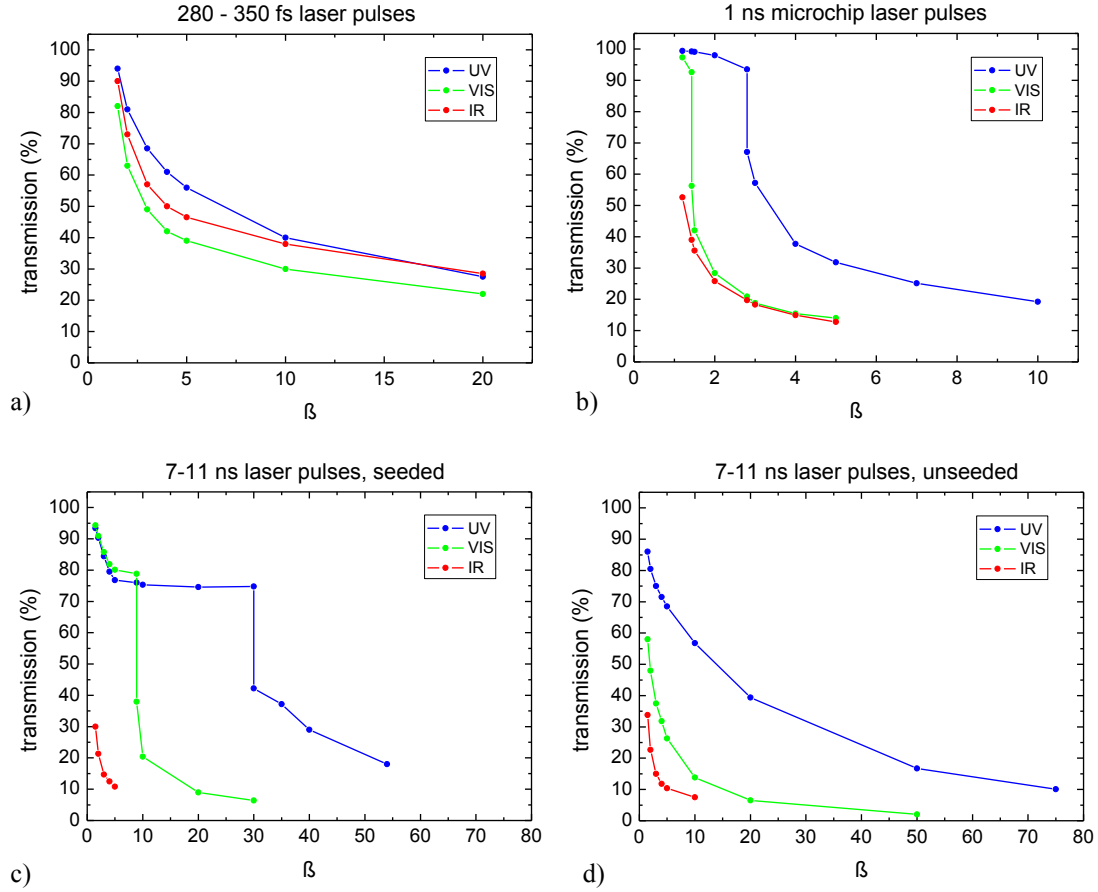
Figure 5.17 Plasma transmission as a function of the normalized laser pulse energy $\beta = E/E_{th}$ for a) 300-fs laser pulses, b) 1-ns microchip laser pulses, c) seeded 7-11 ns laser pulses, and d) unseeded 7-11 ns laser pulses at UV, VIS, and IR wavelengths. The pulses were focused at NA = 0.8.

At equal dimensionless energy, transmission is usually largest for the UV wavelength and smallest for the IR wavelength. This is partially due to the vigorous avalanche at IR breakdown but partially also related to the fact that the energy thresholds are smaller for UV breakdown and, correspondingly, also the plasma length and plasma absorption.

For nanosecond pulses with smooth temporal profile, the transmission curves reflect the 2-step behavior of breakdown with separate thresholds for bubble formation and BPL.

5.3. Plasma energy density

From the plasma transmission data, we estimated the absorbed energy deposited in the focal volume, using the simplifying assumption that the entire transmission loss corresponds to absorption: $A = 1 - T$ (see 3.2.8.). This assumption neglects scattering and reflection which were, for luminescent plasmas, shown to be small in previous studies with IR and VIS wavelengths [Nah96]. Detailed results are presented in figures 11.40 to 11.44 of the appendix. For the calculation of the plasma energy density, the measured data were fitted using the TableCurve2D computer program.

The plasma energy density was determined by calculating the ratio of absorbed energy to the corresponding plasma volume. We cannot calculate the energy values for individual laser exposures because the absorbed energy and the plasma volume were experimentally determined in different measurement series. Therefore, we relied on the fit functions for plasma volume $V(E)$ and absorbed energy $A(E)$. Division of the fit function $A(E)$ by $V(E)$ yielded the function for the plasma energy density $\varepsilon(E)$. The plasma energy densities are plotted in **Fig. 5.18** for all three wavelengths. We plot the data as a function of dimensionless energy β to facilitate the comparison between wavelengths for which the absolute threshold energies are different.
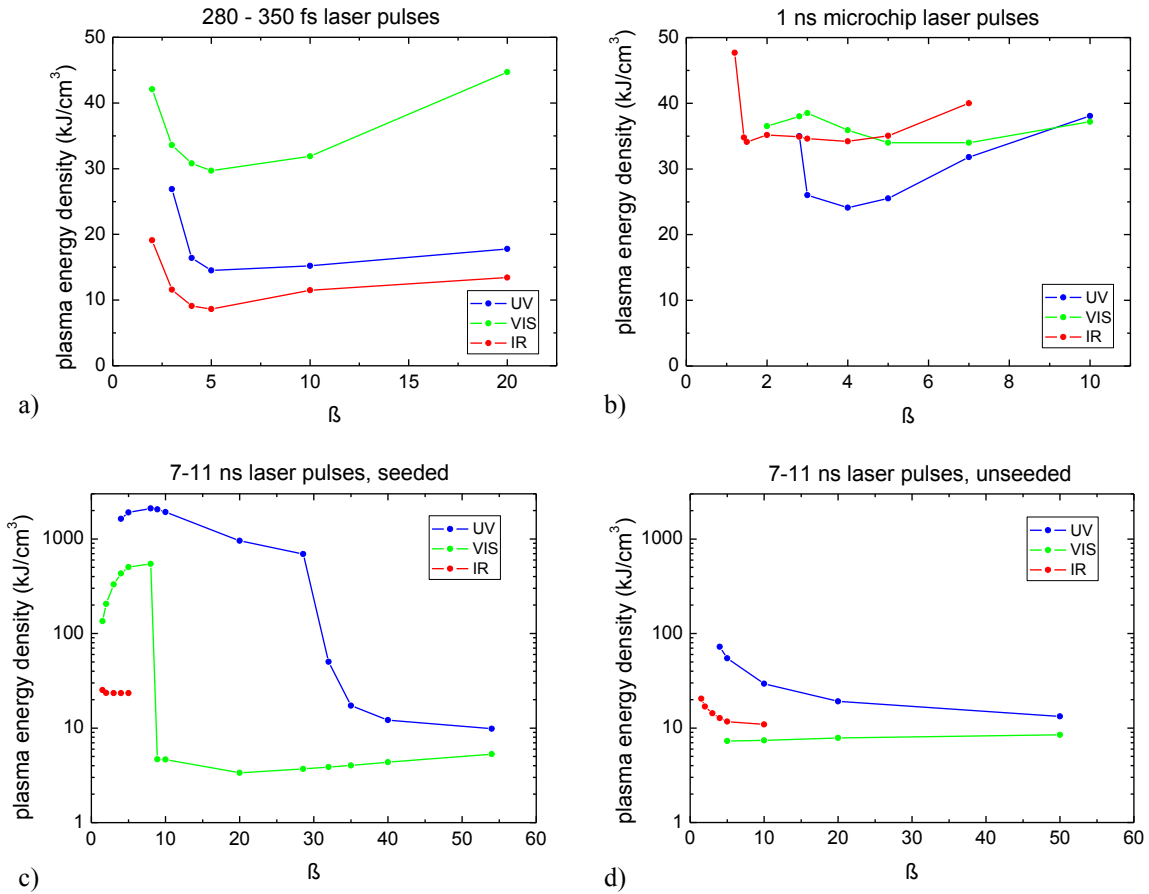
Figure 5.18 Plasma energy density as a function of the normalized laser pulse energy $\beta = E/E_{th}$ for a) 300-fs laser pulses, b) 1-ns microchip laser pulses, c) seeded 7-11 ns laser pulses, and d) unseeded 7-11 ns laser pulses at UV, VIS, and IR wavelengths. The energy density for ns plasmas is plotted on a logarithmic scale. The pulses were focused at NA = 0.8.

Quite obviously, the assumption $A = 1 - T$ is only fulfilled in the BPL range but not for low-density plasma close to the bubble formation threshold. In this region, where low-density plasmas are produced, scattering is apparently much stronger than plasma absorption. Calculation of the energy density based on $A = 1 - T$ thus leads to a dramatic overestimation of the energy density close to the bubble formation threshold.

In the BPL region, we obtain average energy density values between 5 and 45 kJ/cm^3. For comparison: the vaporization enthalpy of water is 2.5 kJ/cm^3; the energy density of the explosive TNT is 6.9 kJ/cm^3. Uncertainties arise because of the sometimes arbitrary delineation of the plasma shape on the photographs that depend on subjective estimates of brightness contours. The energy density in hot spots can always be larger than the average values given in Fig. 5.18. Moreover, the size of the entire luminescent region is, in the BPL range of

nanosecond breakdown, considerably larger than the volume in which the laser energy is deposited (Fig. 5.3). Thus the peak plasma energy density will thus be larger than the average density within the luminescent region.

Well above threshold, the average energy density in the entire plasma volume usually remains fairly constant with increasing laser pulse energy. This is probably due to the fact that redistribution of the deposited energy by radiative energy transfer will cease when the energy density in the source region drops under a critical value.

The above considerations with regard to radiative energy transfer apply to photographs taken at large $NA \geq 0.8$ for which the plasma luminescence extends well beyond the laser cone angle. For UV breakdown at $NA \leq 0.3$, a pulse duration of 6.7 ns, and well above threshold, the plasma luminescence remains within the laser cone angle, and volumetric energy densities of up to 250 kJ/cm^3 could be identified in bright spots within the plasma (Fig. 5.6).

Laser plasma coupling

In fs breakdown, a large plasma energy density must be associated with a large free electron density because only one "set" of free electrons is produced the energy of which is thermalized during a few ps after the end of the pulse. Temperatures of several thousand Kelvin required to produce visible plasma radiation can only be achieved with free electron densities of approximately 10^{22} cm^{-3} (A free electron density of $1.0 \cdot 10^{22}$ cm^{-3} corresponds to a temperature of 6000 K for 1040 nm and NA=0.8, assuming a constant value of the heat capacity C_p). This is a very interesting finding because some researchers state that above the critical density for which the plasma frequency exceeds the light frequency, the plasma becomes 100% reflecting and further coupling into the plasma in completely impaired [Fei04]. For $\lambda = 1040$ nm, the critical free electron density amounts to approximately 1.0×10^{21} cm^{-3}. Our results, even though still preliminary, indicate that the free electron density produced in the bulk of transparent dielectrics, can be at least one order of magnitude larger.

The Drude model predicts a steep rise of both plasma reflectivity and absorption for free electron densities above the critical plasma density [Feit04, Jia06]. However, the reflectivity does not reach 100 % but remains in the order of 70% [Jia06] which implies that laser energy can still be coupled into the plasma. Further considerations explaining efficient laser-plasma coupling at large free-electron densities are given in a series of papers by Godwin [God72, God79, God95]. The observation of strongly scattering streaks of large free electron density within the luminescent plasma [Lin07] and the pronounced plasma ‚inflation' that is indicative for radiative energy transport beyond the regions into which the laser energy is deposited both suggest that very high free-electron densities and energy densities are reached within the plasma.

6. Cavitation bubble size as a function of laser energy

Shock wave emission and cavitation bubble formation are consequences of the rapid expansion of the laser-produced plasmas that both are important for material processing [Vog96a, Vog03, Vog05]. While shock wave amplitude and energy are difficult to measure, especially for low-density plasmas produced at large NA and very small laser pulse energies, we have developed a precise technique for the determination of the maximum cavitation bubble radius that yields results almost in real time (section 3.2.4 and [Vog08]). In previous studies on the energy partitioning in optical breakdown, we found evidence that the ratio of deposited energy going into acoustic transient emission and bubble formation remains fairly constant over a large range of laser parameters, especially for plasmas well above the optical breakdown threshold (the ratio acoustic energy : bubble energy is about 2:1) [Vog99a]. Therefore, we use the cavitation bubble energy as convenient marker for the conversion of incident and deposited laser pulse energy, respectively, into mechanical energy. Knowledge of these conversion rates helps understanding the conditions for precise laser surgery and materials processing, especially when compared to the amount of energy spent on inducing a phase transition of the material within the plasma volume.

6.1. Bubble size at specific UV/VIS/IR wavelengths for various pulse durations

Our results on bubble formation by laser pulses with smooth temporal shape are summarized in **Fig. 6.1** for all investigated pulse durations comprising an energy range of 6 orders of magnitude. The experimental data are plotted on a double logarithmic scale, because the laser pulse energy ranges between 4 nJ and 1000 µJ (more than 5 orders of magnitude) and the bubble energy extends over 11 orders of magnitude. For comparison, **Fig. 6.2** presents the results obtained with regular, nonseeded Nd:YAG laser pulses of 7-11 ns duration.
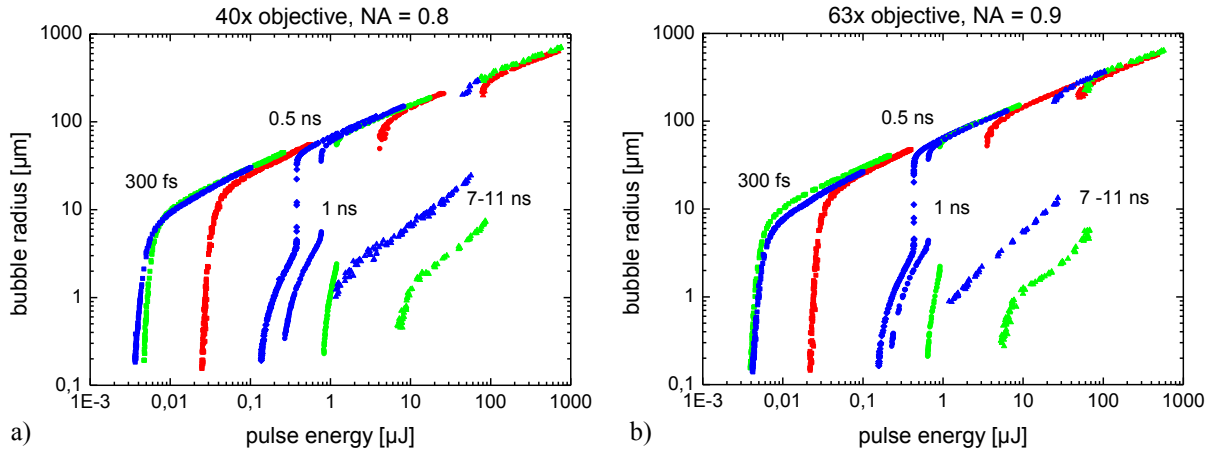
Figure 6.1 Maximum bubble radius as a function of incident laser pulse energy for different pulse durations, wavelengths, and energies focused through a) a 40x (*NA* = 0.8) water immersion objective and b) a 63x (*NA* = 0.9) objective. The colors denote different wavelengths: blue = UV (347 nm and 355 nm for fs- and ns-pulses, respectively), green = VIS (520 nm and 532 nm), red = IR (1040 nm and 1064 nm). The data for 7-11 ns pulse duration were obtained with seeded (slm) laser pulses.
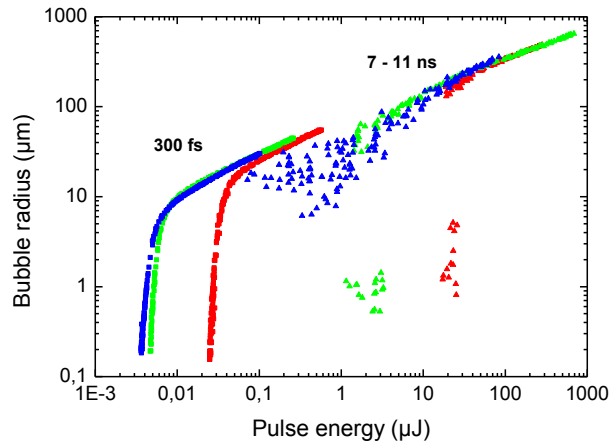
Figure 6.2 Maximum bubble radius as a function of incident laser pulse energy for different pulse durations, wavelengths, and energies focused through a 40x (*NA* = 0.8) water immersion objective. The colors denote different wavelengths as in Fig. 6.1. The data for 7-11 ns pulse duration were obtained with regular, unseeded laser pulses.

For all laser pulses with a smooth temporal shape, VIS or UV wavelengths, and $\tau \geq 500$ ps, the optical breakdown is a two-step process. In the first step, very small bubbles with maximum radii between 150 nm and 30 μm are generated in a low-density plasma regime, and no visible plasma luminescence can be observed. The bubbles in this regime are as small as femtosecond-laser-induced bubbles. The nano-and microbubble regime corresponds to irradiances in which avalanche ionization is balanced by recombination, preventing full ionization to be reached (see section 4.2.2.2).

The second breakdown step occurs abruptly at energies 1.5 to 30 times larger than the bubble formation threshold (depending on pulse duration and wavelength). At the steps, the plasma suddenly assumes a much larger size, bright plasma luminescence (BPL) is observed, and much larger bubbles are produced. The coincidence of these two changes is shown in **Fig. 6.3** for 6.8-ns pulses at 355 nm wavelength. The steps are indicative for the runaway process driven by avalanche ionization in conjunction with thermal ionization (4.2.2.2). The energy range between bubble formation threshold and bright plasma luminescence threshold increases for shorter wavelengths and longer pulse duration. The ratio E_{BPL}/E_B is 24 for 6.8-ns UV pulses, 11 for 8.8-ns VIS pulses, 2.8 for 0.93-ns UV pulses, 1.4 for 0.95-ns VIS pulses, and 2.7 for 0.55-ns UV pulses.
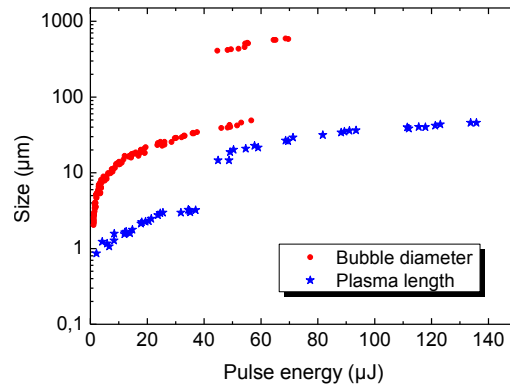
Figure 6.3 Maximum bubble diameter and plasma length as a function of incident laser pulse energy for 6.8-ns pulses at 355 nm wavelength focused through a 40x (*NA* = 0.8) water immersion objective.

For unseeded Nd:YAG laser pulses exhibiting intensity spikes in their temporal pulse shape, no reproducible nanobubble regime is observed (Fig. 6.2) but breakdown is usually associated with luminescent plasmas and the formation of large bubbles. **Fig. 6.4** demonstrates that within the BPL regime at equal pulse energy, bubbles produced by unseeded IR pulses are larger than those created by slm pulses. The intensity spikes in unseeded pulses cause surges of intense photoionization of seed electrons that push the ionization avalanche.
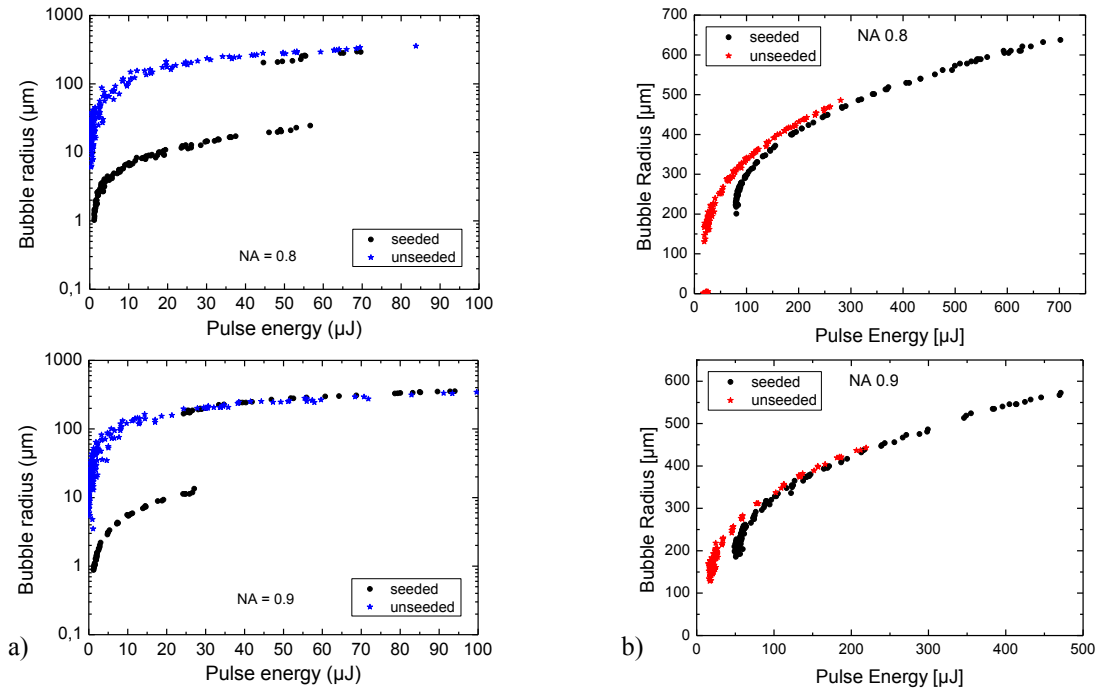
Figure 6.4 Maximum bubble radius as a function of incident laser pulse energy for a) 6.8-ns pulses at 355 nm wavelength and b) 11.1-ns pulses at 1064 nm wavelength. The pulses were focused at *NA* = 0.8 (top) and *NA* = 0.9 (bottom).

The bubble volume increases at the step between the microbubble regime and BPL abruptly by a factor of 1000 for 6.8-ns UV pulses, and even 50 000-fold for the 8.8-ns VIS pulses. The respective values for the microchip laser pulses are 200 for the 0.93-ns UV pulses and 8000 for the 0.95-ns VIS pulses. The stronger increase of bubble size at BPL threshold for the VIS wavelength could be related to the fact that the rate of avalanche ionization is smaller at shorter wavelengths. Thus, the free electron density increases more slowly with energy for UV than VIS, and a larger dimensionless energy E/E_{th} is required to produce the temperature leading to thermal runaway. This explains the larger bubble size before the onset of the runaway. Thermal runaway itself progresses also more slowly for UV than VIS because it relies of an interplay of avalanche ionization, heating and thermal ionization (section 4.2.2.2).

The optical breakdown with IR ns laser pulses is a one step process in which both bubble formation and the appearance of plasma luminescence coincide. The minimum bubble radius is 50 µm and therefore much larger than the smallest bubbles in VIS and UV breakdown. For IR wavelengths, the irradiance threshold for producing seed electrons by multiphoton ionization is very large due to the higher order of the multiphoton process ($k = 6$). At the same time, the rate of avalanche ionization is very high. Therefore, once the avalanche is initiated, there is no regime in which it can be balanced by recombination as for UV and VIS but already at threshold it progresses into the runaway regime where high-density plasma and large bubbles are produced.

Figure 6.5 demonstrates that the 2-step behavior for nanosecond breakdown at short wavelengths occurs within a large range of numerical apertures (at least $0.3 \leq NA \leq 0.9$).
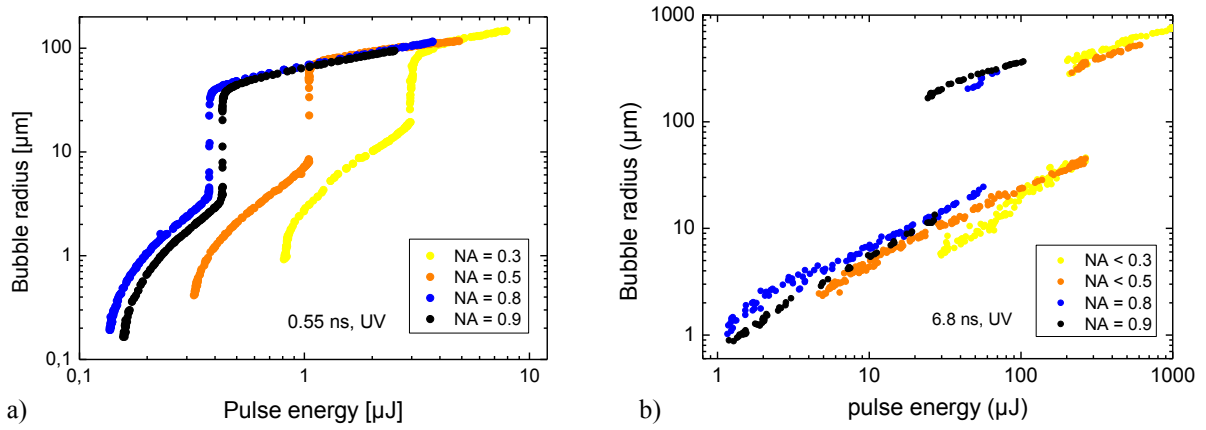
Figure 6.5 Maximum cavitation bubble radii for UV laser pulses focused at different NA. The pulse duration was a) 0.55-ns, and b) 6.8 ns.

In **Fig. 6.6**, the bubble radius is plotted against the normalized pulse energy E/E_{th} because the latter presentation facilitates a comparison of the respective ranges of low density plasma formation. The low-density plasma range with small bubbles increases first with decreasing NA because of enhanced plasma shielding but the bubble size increases as well because of the larger breakdown threshold. For the 6.8-ns pulses, the range first increases with decreasing NA but then decreases again when the NA is further reduced from 0.5 to 0.3.
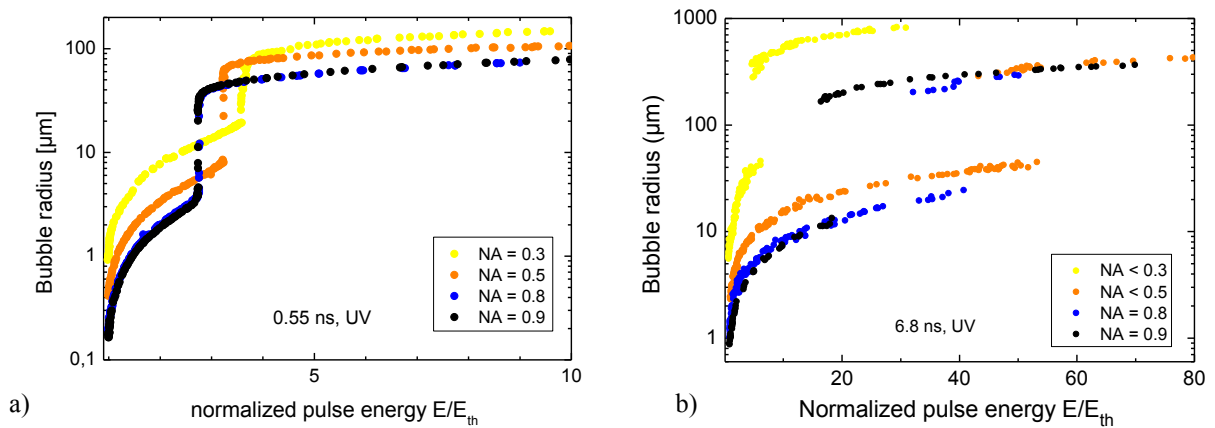
Figure 6.6 Maximum cavitation bubble radii R_{max} for UV laser pulses focused at different NA, plotted as a function of the normalized pulse energy E/E_{th}. The pulse duration was a) 0.55-ns, and b) 6.8 ns.
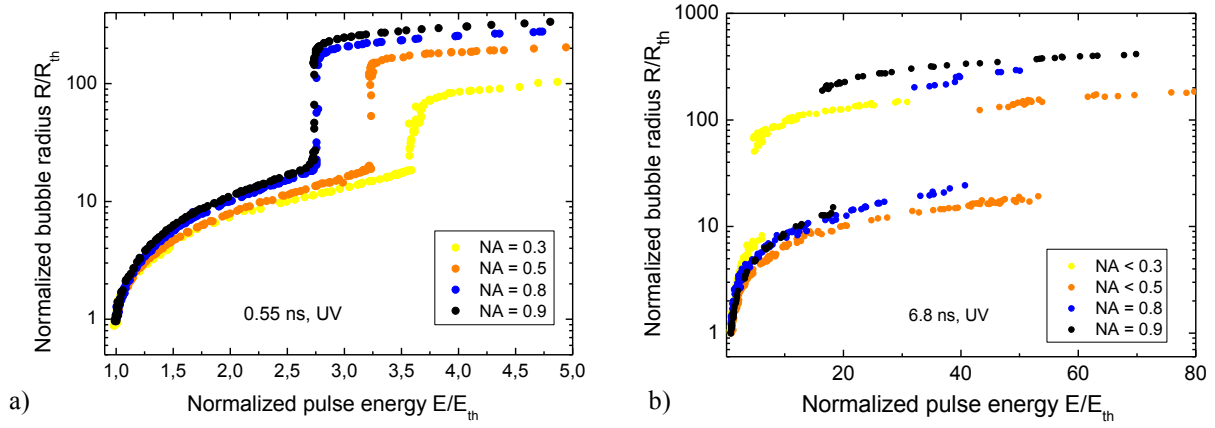
Figure 6.7 Normalized maximum bubble radii R/R_{th} for 0.55-ns microchip laser pulses with UV wavelength focused at different NA in dependence on the normalized pulse energy E/E_{th}. The pulse duration was a) 0.55-ns, and b) 6.8 ns.

The relative increase of the bubble size at threshold, R/R_{th}, is shown in **Fig. 6.7**. For the microchip laser pulses (τ_L = 550 ps), the bubble radius is for all objectives about 20x larger at the BPL threshold than at the bubble threshold. This corresponds to an 8000-fold increase of the bubble volume. The relative increase in bubble radius at the BPL threshold is largest (10x) for $NA = 0.9$, and decreases to 3x for $NA = 0.3$. For much smaller NA, the 2-step behavior will probably disappear.

For the longer slm nanosecond pulses (τ_L = 6.8 ns), the relative increase in bubble radius at the BPL threshold decreases also for lower NAs but the most remarkable feature is the reduction of the energy range for low-density plasma formation and the rapid increase of bubble size with decreasing NA (Fig. 6.6b)

Disappearance of the 2-step behavior at low NA < 0.3 is probably one of the reasons why it has not been observed previously because most of the early work on nanosecond optical breakdown was done using relatively small focusing angles in order to avoid aberrations upon focusing the pulses into the medium of interest.

Using microchip laser pulses of 550 ps duration focused at $NA = 0.9$, we can produce minute bubbles with a maximum radius of only 150 nm, i.e. below the optical diffraction limit (Fig. 6.5a). The minimum bubble radius above the BPL threshold is 30 μm, which corresponds to an 8 million times larger volume. This implies that it is now possible to produce ns laser effects that are 8 million times finer than previously assumed.

6.2. Bubble size in OPO measurements of nanosecond and femtosecond breakdown

Figure 6.8 presents the maximum bubble radii for all nanosecond slm OPO laser pulses ($\tau_L \approx 2$ ns) with wavelengths ranging from 725 nm to 1025 nm.
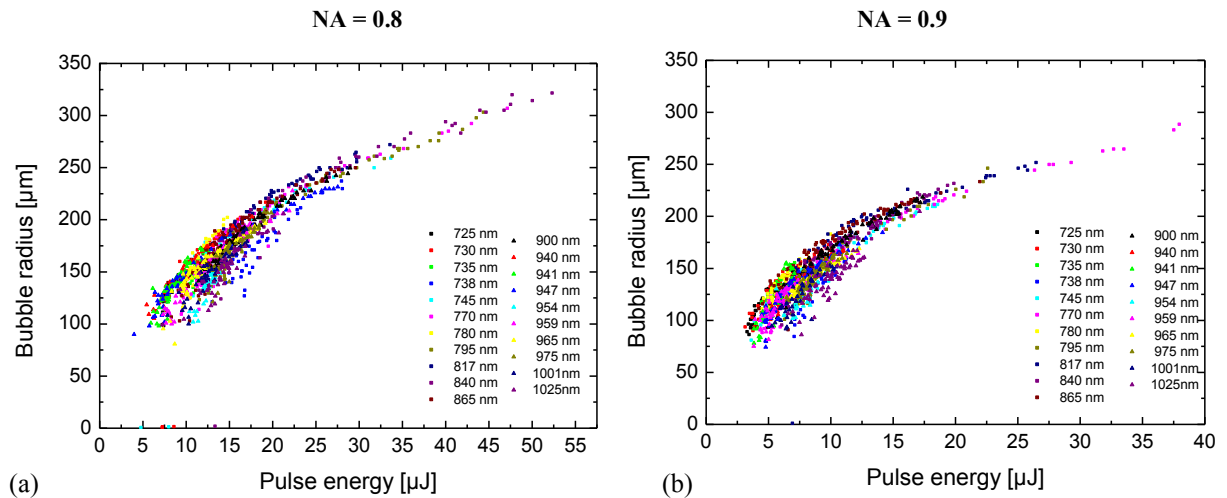
Figure 6.8 Maximum bubble radius as a function of pulse energy for nanosecond slm OPO laser pulses ($\tau_L \approx 2$ ns) of wavelengths ranging from 725 nm to 1025 nm focused at a) $NA = 0.8$, and b) $NA = 0.9$.

For all wavelengths investigated, large bubbles of about 80 – 100 μm radius were produced already at threshold. Small bubbles with R_B < 2 μm were generated with less than 2 % probability. This indicates that optical breakdown is a one-step process for IR wavelengths down to 725 nm. The transition to a two-step process must occur somewhere between 725 nm and 532 nm.

The dependence of the maximum bubble radius on laser pulse energy in Fig. 6.8 exhibits a larger scatter of than observed at fixed wavelengths (Figs. 6.1 and 6.5 – 6.7). This is due to fluctuations of the laser pulse duration after new OPO alignments that were necessary after every change of wavelength and due to thermally induced drifts of the system performance, to pulse-to pulse fluctuations of the beam profile, and finally due to the occasional small spikes on the temporal pulse profile shown in Fig. 3.7.

Figure 6.9 presents the maximum bubble radii for femtosecond OPA laser pulses at selected wavelengths within the range between 347 nm and 1064.
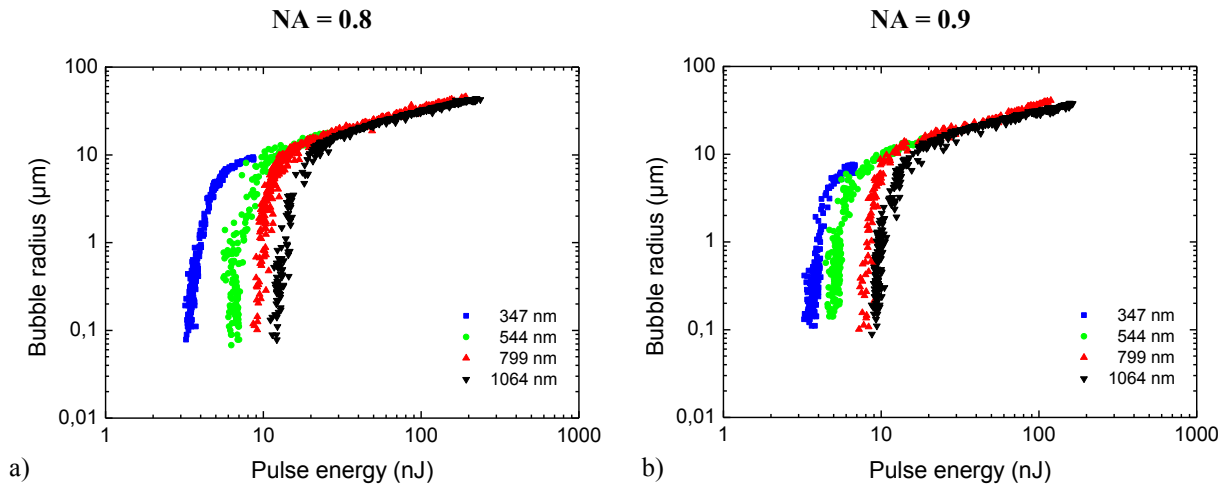
Figure 6.9 Maximum bubble radius as a function of pulse energy for femtosecond OPA laser pulses of wavelengths ranging from 347 nm to 1064 nm focused at a) *NA* = 0.8), and b) *NA* = 0.9.

For all wavelengths investigated, very small bubbles below 100 nm radius were produced already at threshold, similar to the measurements using fixed wavelengths (Fig. 6.1). The bubble size increases rapidly with increasing laser pulse energy. The energy threshold for bubble formation increases considerably with increasing wavelength because the focal spot size increases with wavelength while the irradiance threshold decreases only slightly (Fig. 4.26). The bubble size at threshold remains fairly constant for all wavelengths between UV and IR, in agreement with previous observations at fixed wavelengths [Vog08]. This is expected because the bubble threshold is defined by the temperature rise for which the spinodal limit is exceeded at the focus center, and the bubble size is determined by the thermoelastic stress transient produced under these conditions [Vog05, Vog08]. Both the temperature of the spinodal limit and the thermoelastic stress generation do not depend on laser wavelength, and the bubble size at threshold should thus not vary with wavelength.

6.3. Conversion efficiency of laser energy into bubble energy

Figure 6.10 presents an overview of the conversion efficiency of incident laser energy into bubble energy for the same irradiation parameters as in Fig. 6.1a for *NA* = 0.8, and **Fig. 6.11** shows the dependence on *NA* for UV 0.55-ns microchip laser pulses. The bubble energy is given by

$$E_{B\sigma} = \frac{4}{3}\pi\left[(p_\infty - p_v) + p_\sigma(R_{\max\sigma})\right]R_{\max\sigma}^3 \quad , \tag{6.1}$$

where $p_\infty = 0.1\,\text{MPa}$, $p_v = 2300\,\text{Pa}$, and $p_\sigma(R_{\max\sigma}) = 2\sigma/R_{\max}$, $\sigma = 0.073$ N/m.

It becomes evident from Fig. 6.10 that the creation of nano-effects is always associated with a very low conversion rate of laser energy into mechanical energy, especially for nanosecond pulses. This is partially due to a low absorption of the laser energy at the bubble threshold (section 5.2), and partially due to a small conversion rate of absorbed energy into mechanical energy. The conversion rate rapidly increases with pulse energy due to the increase of peak temperature in the focal volume and the corresponding rise of plasma pressure.
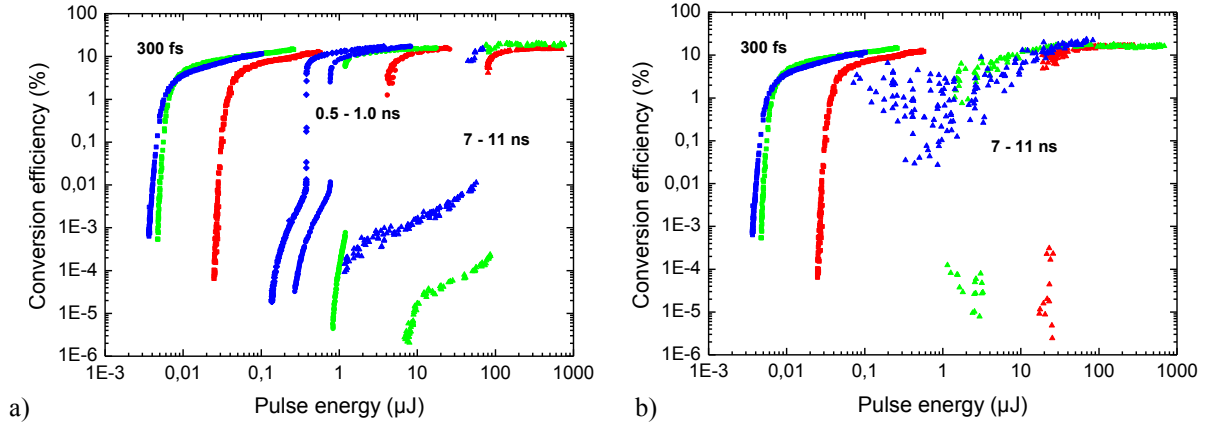
Figure 6.10 Conversion efficiency of incident laser energy into bubble energy for different pulse durations, wavelengths, and energies focused through a 40x (*NA* = 0.8) water immersion objective. Blue stands for UV wavelengths (347 nm and 355 nm for fs- and ns-pulses, respectively), green = VIS (520 nm and 532 nm), red = IR (1040 nm and 1064 nm). a) Same parameters as in Fig. 6.1a. The data for 7-11 ns pulse duration were obtained with seeded (slm) laser pulses. b) Data for ns pulses of 7-11 ns pulse duration refer to unseeded laser operation.

The increase of conversion efficiency is more gradual for femtosecond breakdown but fairly abrupt at the BPL threshold of nanosecond breakdown. This difference is partially due to the slower drop of plasma transmission for fs pulses (5.2) and partially reflects that the $R_{max}(I/I_{th})$ and $T_{max}(I/I_{th})$ curves in Figs. 4.5 – 4.8 in section 4.2.2.2 also increase gradually for femtosecond breakdown but abruptly at the BPL threshold of nanosecond breakdown.

For large E/E_{th} values, the conversion efficiency of incident laser energy into bubble energy approaches a value of about 20% for all pulse durations, wavelengths and numerical apertures investigated. This value would be slightly larger if the conversion efficiency would be calculated using the absorbed rather than the incident energy. At large E/E_{th} values, plasma temperature and pressure are very large, and the Carnot efficiency $\eta = 1 - (T_{Cold}/T_{Hot})$ for the conversion of thermal energy into mechanical energy is close to its upper limit. Therefore, universal laws of energy partitioning for strong explosions in liquid media apply – similar to those described previously by Taylor [Tay50] and Sedov [59] for strong explosions in gases, and by Cole for underwater explosions [Col48]. Of particular interest is here the partitioning into bubble and shock wave energy because other contributions such as plasma radiation are very small [Vog99].

The dependence of conversion efficiency on laser pulse energy is for Gaussian laser pulses fairly deterministic. By contrast, for unseeded nanosecond laser pulses with ps spikes we observe the typical stochastic behavior that is usually attributed to ns optical breakdown [Liu97]. Our results show that this is not an intrinsic feature of the breakdown process but rather related to the statistics of laser emission. Pulses with smooth temporal profile have, at threshold, smaller conversion efficiency than unseeded, spiky pulses. While the small conversion efficiency close to threshold is the prerequisite for the creation of nano-effects in cells, the rapid rise of the conversion efficiency above threshold explains why the laser pulses can also be used to create small voids in solid dielectrics such as glass, quartz, or sapphire for which much larger forces are required than for bubble generation in water.
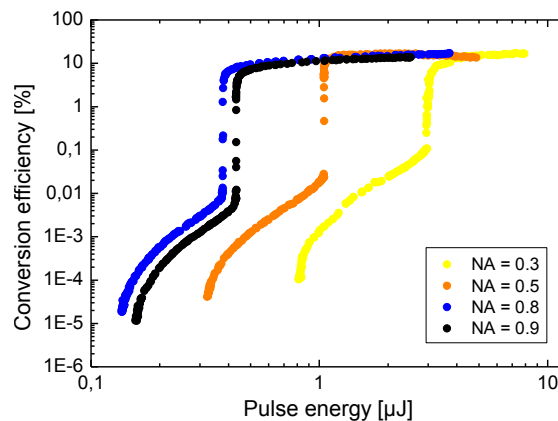
Figure 6.11 Conversion efficiency of laser pulse energy into bubble energy for UV 0.55-ns microchip laser pulses focused at different NA as a function of incident laser pulse energy.

6.4. Shape of the laser-produced bubbles

Diffraction limited focusing at large NA produces compact plasmas and, therefore, very round cavitation bubbles. Right at the breakdown threshold, the shape of the laser-produced bubbles may be ellipsoidal because the shape of the plasma itself is ellipsoidal ([Vog05], section 3.2), and the measured bubble radius is below 150 nm for $NA = 0.9$ (Fig. 6.1b). However, for energies well above threshold, the bubbles rapidly assume an approximately spherical shape.

It has been shown theoretically that any deviations from the spherical shape are amplified during the collapse phase [Str71] and lead to jetting and bubble splitting [God99]. A large number of rebounds of a collapsing bubble is, therefore, indicative for a highly spherical bubble shape. As seen in **Fig. 6.12a**, we observed 8 rebounds after the first bubble oscillation, when a fs pulse with 520 nm wavelength and an energy 6 times above the bubble formation threshold was focused into water at $NA = 0.8$. A similar number of rebound oscillations after a violent bubble collapse has previously been observed only in the context of single bubble luminescence [Bar97, Bre02]. Slight deviations from spherical shape reduce the number of rebounds as shown in Figs, 6.12b and c. The oblate spheroidal shape of the expanded bubble is due to the elongated plasma shape. In the final stages of the collapse, the aspherical bubble shape leads first to the evolution of an equatorial jet and then to two axial jets propagating in opposite direction [Bla97, Bru01] that result in bubble splitting which reduces the number of rebounds.

The largest number of oscillations is observed for small bubbles with $R_{max} < 50$ μm because under these conditions surface tension stabilizes the spherical shape. An extreme case in which the bubble performs more than 100 oscillations is shown in **Fig. 6.13**.
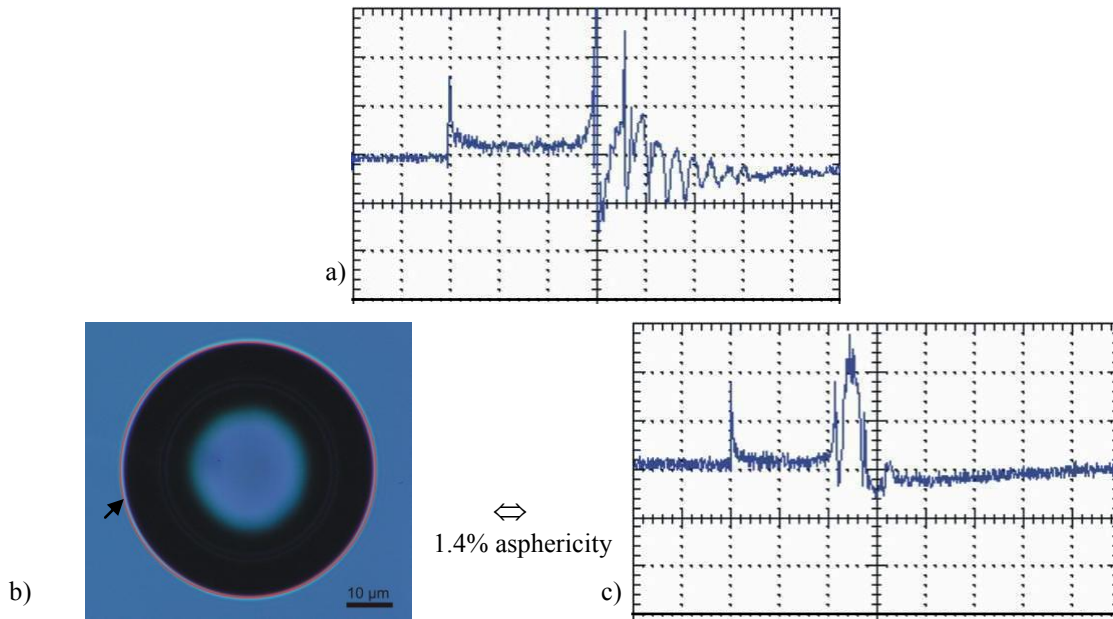
Figure 6.12 a) Scattering signal of a highly spherical bubble produced by a 306-fs laser pulse of 520 nm wavelength focused at NA = 0.8. The bubble oscillation time is 3000 ns, corresponding to a radius of 16.6 μm. The larger bubble in b) exhibits 1.4% deviation from a spherical shape, leading to a collapse with fewer rebounds, as seen in c).
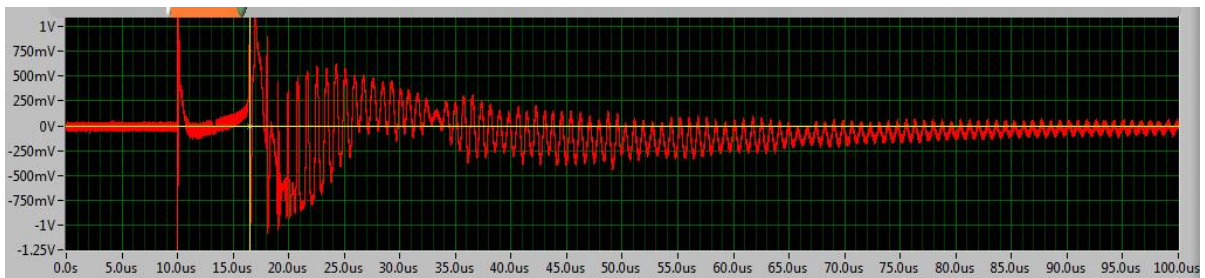
Figure 6.13 Scattering signal of a highly spherical bubble produced by a 265-fs laser pulse of 755 nm wavelength and 157 nJ energy focused at NA= 0.9. The bubble oscillation time is 6.43 μs, corresponding to a radius $R_{max} = 34.8$ μm. The bubble oscillates more than 100 times. Initial nonlinear cavitation bubble oscillation of large amplitude are damped by acoustic transient emission, and the remaining gas bubble later performs small linear oscillation

The highly spherical shape of the bubble produced at large NAs using laser pulse energies well above the breakdown threshold is due to a short length l_p of the laser plasma compared to the maximum bubble radius R_{max}. The dependence between plasma length and focusing angle was derived in section 2.2, Eq. 2.66. Expressed in terms of numerical aperture it is

$$l_p = \frac{\lambda}{\pi\, NA^2}\sqrt{\beta-1} \quad , \qquad \text{with} \quad \beta = E/E_{th} \tag{6.2}$$

It is obvious from equation (6.2) that for a given β - value l_p decreases and R_{max}/l_p increases with increasing NA.

Bubbles with highly spherical shape produced by aberration-free focusing of laser pulses at large NA using objectives with long working distance may serve as perfect model systems for the experimental investigation of initially spherical voids both in free liquids and with nearby rigid or elastic structures.

6.5. Modeling results for nanocavitation close to threshold

In 2005, we presented a theoretical analysis of femtosecond laser-driven bubble formation [Vog05], at a time when measurement results on the size of the laser-produced bubbles were not yet available. We are now able to compare the results of our fs breakdown model to the experimental data presented in this report [Vog08]. For this purpose, we will shortly recapitulate the line of reasoning in our analysis.

We first calculate the dependence of free electron density ρ_{max} at the end of the laser pulse on irradiance I using a rate equation model. Multiplication of ρ_{max} by the average energy of a free electron then yields the volumetric energy density $\varepsilon = \rho_{max}(\widetilde{\Delta} + \overline{E}_{kin})$, where $\widetilde{\Delta}$ is the ionization potential, and $\overline{E}_{kin} = (5/4)\widetilde{\Delta}$ is the average kinetic energy of the free electrons. The temperature rise produced by thermalization of the free electron energy is given by $\Delta T = \varepsilon/(\rho_0 C_p)$, where C_p is the heat capacity and ρ_0 the mass density of the medium, and the final temperature is $T = 20°C + \Delta T$. We take an ellipsoidal temperature distribution $T(x,y,z) \propto \rho_{max}(x,y,z)$ as starting point for the calculation of the thermoelastic stress evolution. Because of the predominance of multiphoton ionization, the $\rho(I)$ dependence is, in this distribution, simplified to $\rho_{max} \propto I^k$. When the compressive stress in the focus center relaxes, a tensile wave evolves that results in a phase change once the tensile stress amplitude exceeds the stability limit (rupture threshold) of the superheated water. We assume that this occurs in the entire volume in which the kinetic spinodal limit as defined by Kiselev [Kis99] is exceeded. This volume is taken as bubble nucleus, and the subsequent dynamics driven by tensile stress and vapor pressure inside the bubble is calculated using the Gilmore model [Gil52]. The influence of heat exchange between bubble content and surrounding liquid is assessed by distinguishing between isothermal and adiabatic conditions. **Figure 6.14** shows the numerical results for 1040 nm and $NA = 0.8$. Assuming a thermalization time of 10 ps [10,15], we obtain a threshold temperature and pressure of $T_{th} = 167.7°C$ and $p_{th} = -62.8\,\text{MPa}$. Results for T_{th} are largely independent of wavelength because the shape of the focal irradiance distribution remains the same. However, with increasing NA, the focus becomes less elongated, the tensile stress wave more strongly focused, and T_{th} decreases to 151.5°C at $NA = 1.3$ [Vog05].

To compare the experimental $R_{max}(E_L)$ values with model predictions for $R_{max}(T)$, we equate the experimental and theoretical thresholds E_{th} and T_{th}, and transform the E_L–scale into a temperature scale as described above. As shown in **Figure 6.14**, we obtain an excellent agreement between predicted and measured bubble radii at the bubble formation threshold. With increasing temperature, the theoretical R_{max} values grow initially slightly faster than the measured ones because we calculate the bubble expansion using the stress evolution in the focus center that originates in a situation without bubble formation. This approach neglects the clipping of the tensile stress amplitude upon rupture of the liquid, and overrates the force acting on the bubble wall that is actually located at a distance from the focus center.

Under isothermal conditions, when temperature T_B and vapor pressure p_v inside the bubble decay only by heat diffusion within the liquid surrounding the bubble, R_{max} is only slightly larger than under adiabatic conditions, when T_B and p_v drop rapidly upon bubble expansion (Fig. 6.14). The adiabatic bubble motion is, in turn, almost identical to the case where p_v is not at all taken into account (not shown). We conclude that, near threshold, fs laser-induced bubble formation is largely driven by tensile thermoelastic stress with little contri-
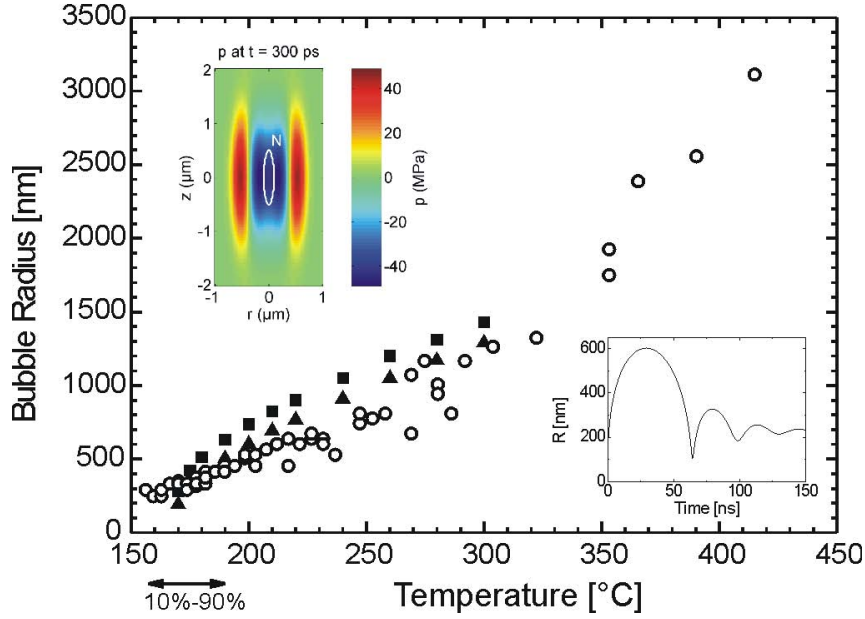
Figure 6.14 Measured bubble radii R_{max} (o) compared to predictions for isothermal (■) and adiabatic (▲) conditions of the bubble content with respect to the surrounding liquid. All data refer to 1040-nm pulses focused at $NA = 0.8$. Arrows mark the region from 10 % to 90 % breakdown probability. The insets show the calculated thermoelastic stress distribution with bubble nucleus (N), and the adiabatic bubble oscillation for a peak temperature of $T = 200°C$. Figure taken from [Vog08].

bution from vapor pressure. However, for $T > 300$ °C, a steep increase of R_{max} is observed, corresponding to the increase in Fig 3.25 for $E_L > 25$ nJ that starts about 11% above E_{th}. Since at $T \approx 300$ °C the spinodal limit is crossed at ambient pressure [16], no tensile stress is required any more for $T > 300$ °C to induce a phase transition, and bubble formation progresses as explosive vaporization. For nanosecond breakdown, which is not stress-confined at the bubble formation threshold, bubble formation always progresses as explosive vaporization.

Modeling of the bubble formation for temperatures above 300 °C requires a different approach from that appropriate close to threshold. When the amount of deposited energy and the plasma size are known, the subsequent hydrodynamic development consisting of acoustic transient emission and bubble formation can be modeled by hydrodynamic codes based on tabulated equation-of-state data. This has previously demonstrated on ps optical breakdown using the MESA code developed at Los Alamos National Laboratories and measurement data from our laboratory [Cha97]. However, such calculations are numerically costly, and the codes are not easily accessible. In the following section we present a simpler approach in which the nonlinear energy deposition is estimated using our breakdown model and the conversion into mechanical energy is assessed in a simple approximation based on Carnot cycle considerations. The calculated dependence between the mechanical energy produced during breakdown and incident laser energy is then compared with the experimental data on bubble energy versus incident energy.

6.6 Modeling results on energy deposition compared to energy dependence of bubble size

The advanced breakdown model presented in section 2.1 enables to calculate the time evolution of the plasma energy density and the temperature in the focal volume. This ability creates a much closer link between model predictions and experimentally measurable data on material modification than previous models, which provided only the time evolution of the free electron density. For example, if we assume that the calculated temperature rise in the focal volume is a measure for the energy deposited in the breakdown process, we can compare this prediction to the experimentally determined bubble energy. This comparison is presented in **Fig. 6.15** for UV, VIS and IR femtosecond breakdown (τ_L = 340 fs) and in **Fig. 6.16** for nanosecond breakdown produced by a microchip laser (τ_L = 1.0 ns). The bubble energy E_B is calculated according to Eq. (6.1).

In the left column of Figs. 6.15 and 6.16, the peak temperature rise in the focal volume is plotted as a function of the incident laser energy. Our breakdown model originally yields the focal temperature T_{max} as a function of irradiance. The conversion into energy is done using equations (4.1) and (4.3) from section 4.2.2.5. As already discussed in section 4.2.2.2, the T_{max} values above the BPL threshold are unrealistically high because our model does not consider the plasma growth with increasing irradiance that shields the focal region but assumes that the entire laser energy reaches the beam waist even at energies well above the BPL threshold. Moreover, the model does not consider the enlargement of the plasma volume beyond the laser cone angle by radiative energy transport (section 5.4) and the plasma expansion that leads to a rapid adiabatic cooling. For irradiance values up to the bubble threshold, the model predictions of T_{max} are realistic. For $I_{bubble} < I < I_{BPL}$, the predicted T_{max} value rises faster with irradiance than in reality because the model neglects plasma growth and shielding. It will be a challenge for future modeling to include all spatio-temporal aspects required to derive a realistic temperature distribution in the focal region. However, in the present context, where we simply use the temperature rise from ambient temperature to T_{max} as a measure for the energy deposition during plasma formation, it does not matter that the absolute values are partially much too high.

The $T_{max}(E_L)$ curves in the left column of Figs. 6.15 and 6.16 cannot be directly compared to the $E_B(E_L)$ curves in the right column because we have to consider the conversion efficiency from thermal into mechanical energy. In a first approximation, we use the efficiency derived for a Carnot cycle in equilibrium thermodynamics

$$\eta = \frac{W}{Q_H} = \frac{T_{Hot} - T_{Cold}}{T_{Hot}} , \tag{6.3}$$

and obtain

$$E_{mech} \propto \eta \, (T_{Hot} - T_{Cold}) = \frac{T_{Hot} - T_{Cold}}{T_{Hot}} \times (T_{Hot} - T_{Cold}) = \frac{\Delta T^2}{T_{Hot}} . \tag{6.4}$$

Here W denotes the mechanical energy exiting the system as work, Q_H is the heat energy entering the system via nonlinear energy deposition, T_{Cold} is the temperature of the cold reservoir (in our case the ambient temperature), and T_{Hot} is the temperature of the hot reservoir (in our case the temperature in the focal volume). Consideration of the Carnot efficiency leads to a value scaling with mechanical energy plotted in the middle column. To obtain real energy values, one needs to integrate over the $\eta \times \Delta T$ distribution in the focal volume and consider the heat capacity, which is beyond the scope of the present report. However, the scaling with E_L will not change by this integration, and we can thus compare the shape of the calculated $E_{mech}(E_L)$ in the middle column with the shape of the $E_B(E_L)$ curves in the right column. Note that in performing this comparison, we implicitly assume that the partitioning of mechanical energy into acoustic energy and bubble energy remains approximately constant for varying focus temperature. However, this seems to be a reasonable assumption.

Considering the many simplifications made in our model of conversion of plasma energy into mechanical energy, the agreement between model predictions for $E_{mech}(E_L)$ and measured $E_B(E_L)$ curves is excellent both with regard to the general shape of the curves and the energy values for bubble and BPL thresholds. However, there is a difference in the vertical scale. In all cases, the experimentally determined bubble energy spans a larger range than in the model predictions. We attribute this discrepancy to the fact that the model does not consider the plasma growth during the laser pulse for $E > E_{th}$. Therefore, it cannot properly account for the entire deposited energy.
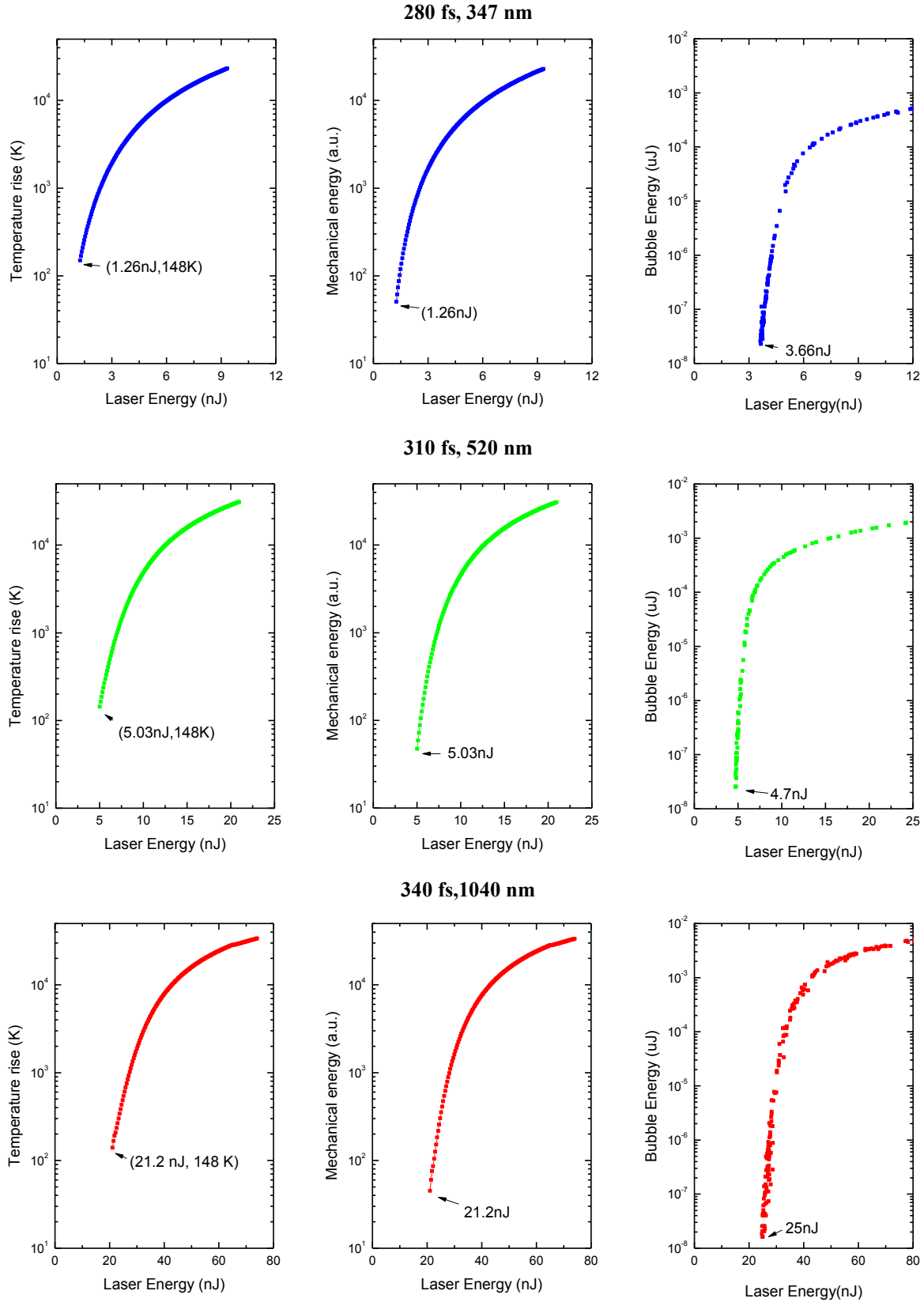
Figure 6.15 Comparison of modeling results on energy deposition with the experimentally determined energy dependence of cavitation bubble size for femtosecond breakdown at different wavelengths. Left column: Calculated focal peak temperature T_{max} as a function of laser energy E_L for energies above the bubble formation threshold. Middle column: $\eta \times T_{max}$ (E_L) as a measure of the breakdown-induced mechanical energy. Right column: measure cavitation bubble size E_B (E_L). The calculations were performed for 340 fs pulse duration, T_{cr} = 441 K (i.e. ΔT = 148 K), 1.6 fs collision time, a band gap of 6.55 eV, and a seed electron density $\rho_{ini} = 2 \times 10^{13}$ cm^{-3}.

1 ns, 355 nm

1 ns, 532 nm

1 ns, 1064 nm
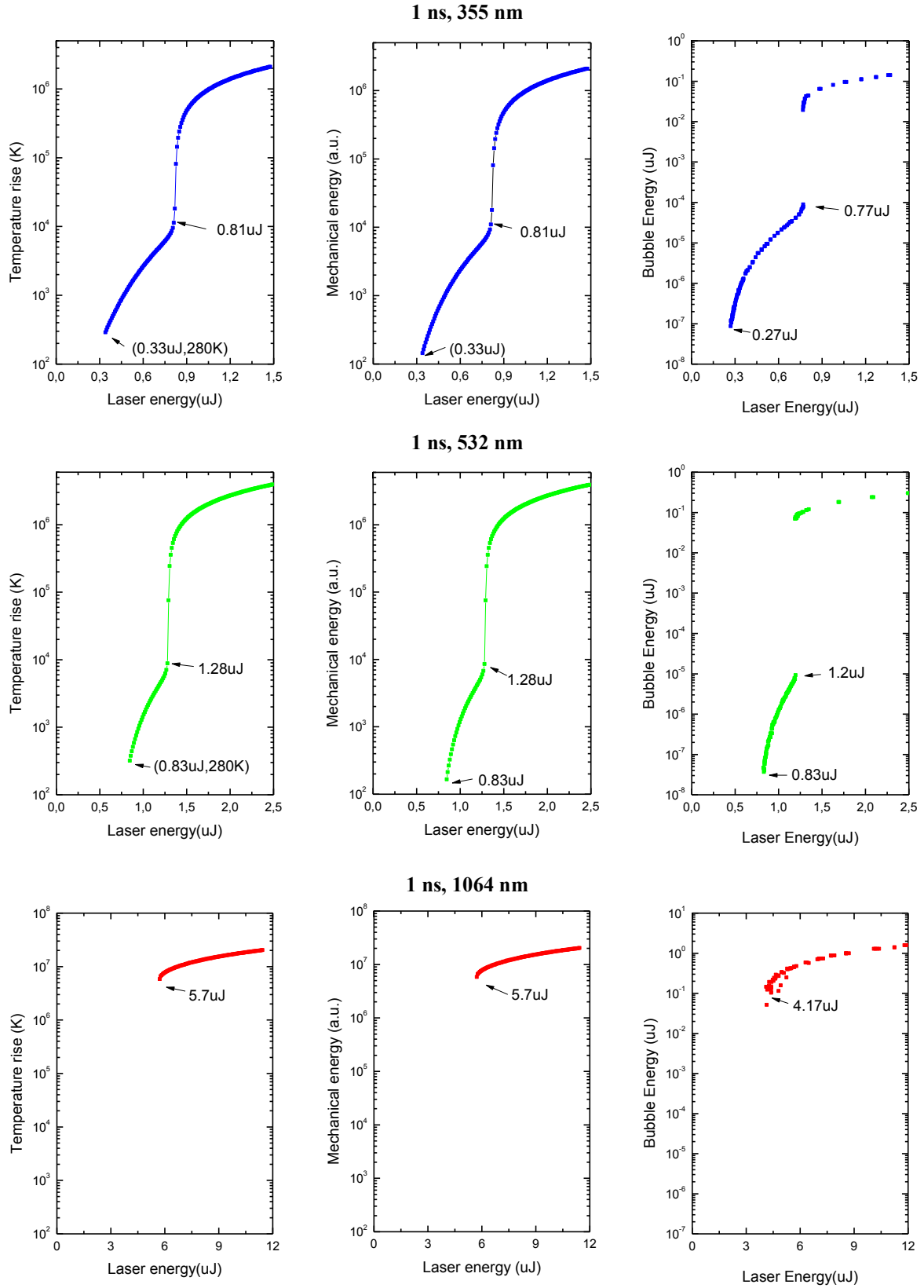
Figure 6.16 Comparison of modeling results on energy deposition with the experimentally determined energy dependence of cavitation bubble size for nanosecond breakdown at different wavelengths. Left column: Calculated focal peak temperature T_{max} as a function of laser energy E_L for energies above the bubble formation threshold. Middle column: $\eta \times T_{max}$ (E_L) as a measure of the breakdown-induced mechanical energy. Right column: measure cavitation bubble size E_B (E_L). The calculations were performed for 1.0 ns pulse duration, $T_{cr} = 573$ K (i.e. $\Delta T = 280$ K), 3.0 fs collision time, a band gap of 6.55 eV, and a seed electron density $\rho_{ini} = 2 \times 10^{13}$ cm^{-3}.

7. Implications for laser nanosurgery and materials processing

Our project did not aim at improving specific techniques for laser surgery of cells and tissues or material processing. However, our findings do have important implications for improving the cost-effectiveness of some of these techniques, and provide guidelines for parameter selection. These implications are briefly summarized in the following.

7.1. Link of plasma modeling to material processing and delineation of a parameter space for controlled nonlinear energy deposition

The incorporation of all ionization mechanisms including thermal ionization into the theoretical treatment of breakdown together with the consideration of losses by recombination, free electron diffusion and heat diffusion has enabled us to go beyond a mere calculation of breakdown thresholds by modeling the gradual increase of energy deposition with increasing laser pulse energy. The introduction of temperature-related breakdown criteria directly links plasma modeling to changes in the target relevant for laser surgery and material processing, such as bubble formation or plasma luminescence. Based on these criteria, we created a ‚tunability' map of the (λ-τ_L) parameter space presenting the dependence of the laser-produced temperature on the incident laser energy. This map can guide the choice of laser parameters appropriate for different types of applications employing nonlinear energy deposition. It is useful not only for laser surgery of cells and tissues but guiding material modification (for example waveguide writing) and ablation of all kinds of transparent dielectrics.

Our approach will develop its full potential when the spatio-temporal aspect of the breakdown dynamics (plasma growth and shielding, nonlinear beam propagation) are incorporated into the modelling. Before that, the enrgy range in which the laser effects can be tuned will be underestimated.

7.2. Cost-effective nanosurgery and material processing by means of UV- and VIS nanosecond laser pulses

The sensitive probe beam scattering technique developed for the detection of the bubble formation threshold at large numerical aperture led us to the discovery that nano-effects can be produced not only by femtosecond laser pulses but also if UV- and VIS nanosecond laser pulses with smooth temporal profile and pulse energies below the threshold for bright plasma luminescence are employed. Such laser pulses are delivered from microchip lasers, which provides a cost-effective alternative to ultrashort pulse lasers.

The creation of nano- and micro-effects close to the bubble formation threshold is of particular interest for laser surgery in cells and small organisms [Vog05, Vog08]. Therefore, we display the microcavitation range of the data of Fig. 6.1 again in **Fig. 7.1**. The radii are plotted as a function of the dimensionless pulse energy $\beta = E/E_{th}$ to facilitate the comparison of the effects arising from different laser wavelengths.

a)   b)
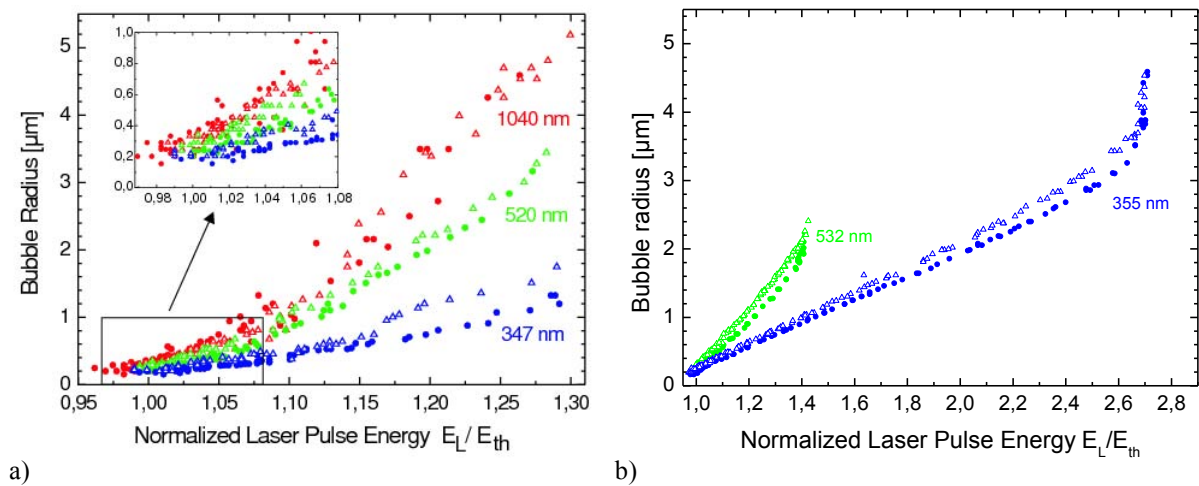
Figure 7.1 Bubble radius R_{max} in the low-density plasma regime a) for 300-fs pulses, and b) for microchip laser pulses of 0.55 ns and 0.93 ns duration. The radii are plotted as a function of the normalized pulse energy E/E_{th} for different wavelengths at $NA = 0.9$ (•) and NA = 0.8 (Δ).

Figure 7.1 shows that the bubbles produced by microchip-laser nanosecond pulses are as small as those produced by femtosecond pulses. However, the energy range in which small bubbles can be generated is broader for the ns laser pulses (note the different axis in a) and b)). Regardless of pulse duration, near-UV wavelengths are best suited for nanosurgery because R_{max} is smallest at threshold and increases most slowly with E_L. The low order of multiphoton processes at short wavelengths translates into a relatively slow increase of ρ_{max} and, consequently, R_{max} with E_L, which provides a good adjustability of the surgical effect. Nevertheless, the $R_{max}(E_L)$ dependence is generally fairly strong. An online control of the bubble size based on our probe beam scattering technique could thus further improve the surgical precision (section 7.3).

Figs. 7.2 and 7.3 shows an example in which UV nanosecond pulses from a microchip laser are used for a purpose for which previously only femtosecond lasers have been employed. The SEM micrograph shows a corneal flap such as required for LASIK refractive surgery. The cut is very precise, the bed is smooth, and no thermal damage is observed. **Figure 7.4** presents the logo of the University of Luebeck inside a microscope glass slide.
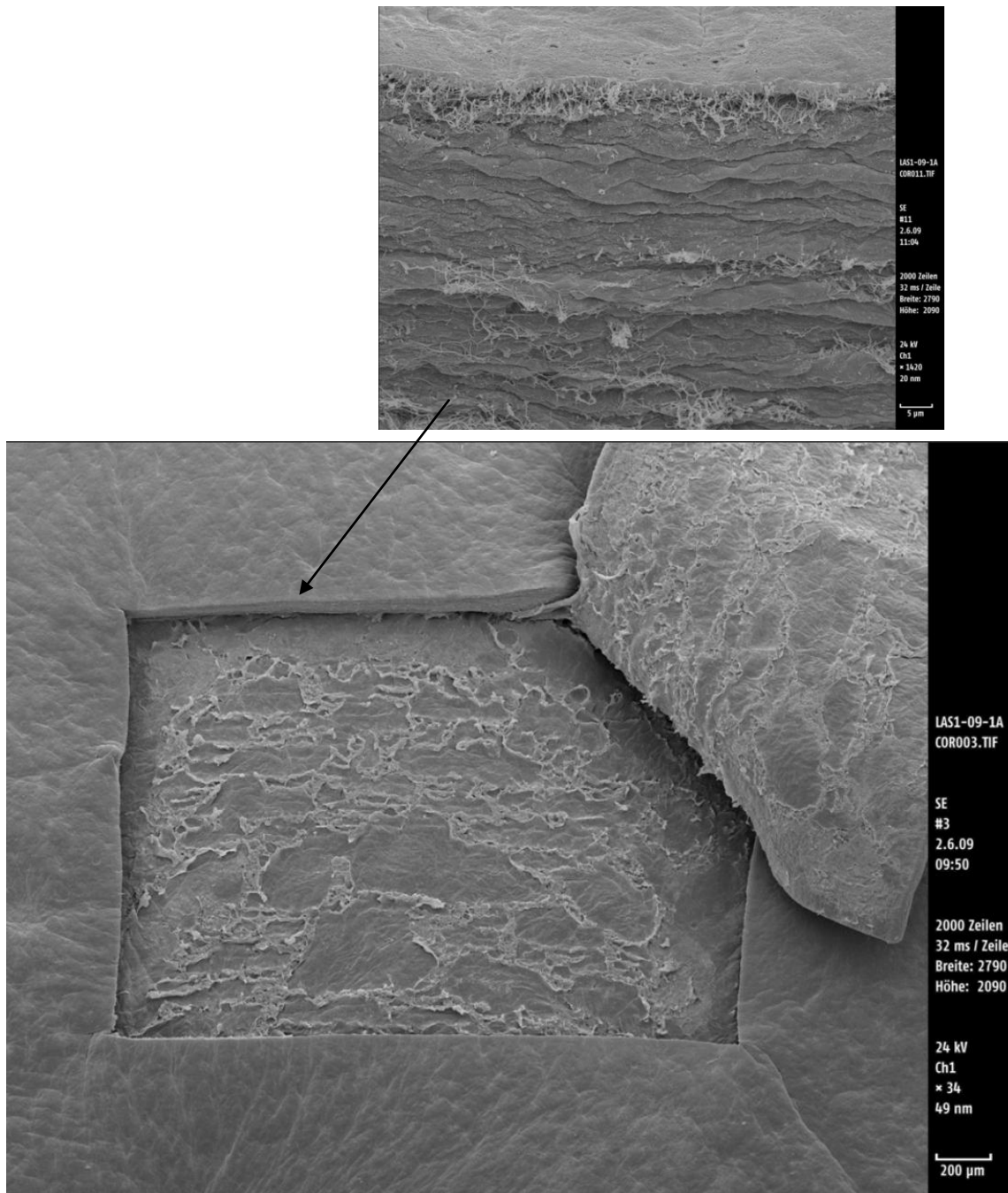
Figure 7.2 Scanning electron micrograph of a corneal flap produced using UV laser pulses of 355 nm wavelength and 0.6 ns duration. The pulses were focused at NA = 0.75 about 150 μm below the corneal surface in an ex-vivo porcine eye.
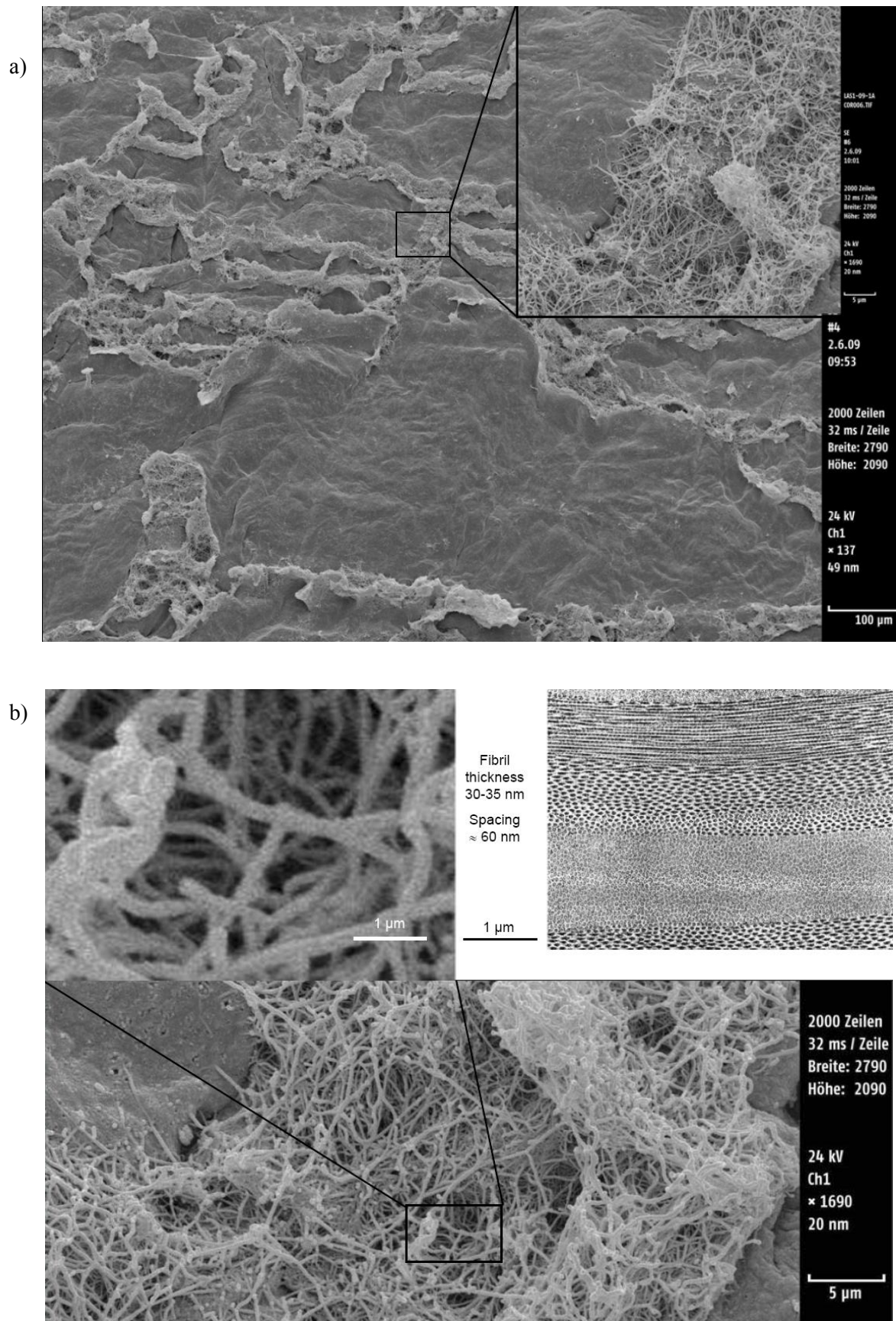
Figure 7.3 Enlarged section of the bed of the flap in Fig. 7.2. The detail shown in a) is presented in larger magnification again in b), together with a transmission electron microscopic image of the collagen fibrils of the corneal stroma. The intact fibrils are indicative for the lack of thermal damage.

Figure 7.4 Logo of the University of Luebeck composed of micro-cavities created inside a microscope glass slide. Image height: 4 mm.

Figures 7.1 – 7.4 show examples for precise material processing inside of transparent dielectrics because this is the field in which UV and VIS nanosecond pulses have their largest potential and can best compete with femtosecond laser pulses.

For surface ablation, the optical penetration depth in metals is very small (< 30 nm), and the thermal confinement time is thus very short, in the range of a few picoseconds to a few tens of picoseconds. Energy is deposited in a very thin layer even upon irradiation of transparent dielectrics because of the rapid increase of nonlinear absorption with increasing free electron density. For $\rho > \rho cr$, a skin layer develops, and electrons within this skin layer may be heated to large temperatures. Because of the small thickness of the deposition layer, an increase of the heat affected zone via electron and heat diffusion has been observed for pulse duration above ≈ 10 ps, i.e. for pulse durations longer than the thermalization time of the free electron energy. For pulse durations < 10 ps, the extent of the heat affected zone depends more on pulse energy rather than on pulse duration. For sufficiently high energies, large thermally affected zones have been observed at pulse durations as short as 100 fs [Mom96, Ben07] but for energies close to threshold, highly precise nano-effects could be created using pulse durations of 800 fs [Jog04].

The situation is quite different for energy deposition into the bulk of transparent dielectrics. Here, the entire focal volume defines the zone of energy deposition, and the breakdown front can, at superthreshold energies, move towards the direction of the incoming laser beam. Because of the larger volume with dimensions > 100 nm the thermalization time is in the order of several nanoseconds for water and slightly less for fused silica (depending on the heat diffusivity). Thus, thermal confinement can be achieved even with nanosecond pulses. Therefore, the precision of the laser effects is not as soon limited by heat conduction as for surface ablation.

Shielding of the target by a plasma plume in front of the target is an issue for surface ablation but not in the same way for processing in the bulk of transparent materials. In surface ablation, avoidance of shielding requires the use of ultra-short pulse durations shorter than the hydrodynamic response time. Inside transparent materials, plasma growth and shielding in front of the laser focus occur both for nanosecond and femtosecond pulses, i.e. it brings no advantage to use ultra-short pulses.

The energy deposition into the bulk of transparent materials may be influenced by nonlinear beam propagation, especially when small focusing angles are used. Such effects depend on the peak power while the material modification is related to the deposited energy. Nonlinear beam propagation effects are, hence, less pronounced for longer pulse durations, which favors the use of nanosecond pulses.

7.3. Online control of cell and tissue surgery

We demonstrated in Figs. 6.1 and 7.1 that the bubble size grows fairly rapidly with laser pulse energy and showed In section 6.3, Figs. 6.10 and 6.11 that the conversion efficiency of laser light energy into cavitation bubble energy rises even more rapidly. An online control of the bubble size based on our probe beam scattering technique could thus further improve the precision in cell and tissue surgery, especially when the light transmission in the beam path depends on the optical properties in the surrounding of the treatment location. Under these circumstances on cannot work with a pre-selected laser pulse energy to achieve a desired laser effects but needs to adjust the energy. Online control of the bubble size is a rapid technique for measuring the magnitude of the produced laser effect and thus well-suited for automated dosimetry. We created an algorithm for automatic evaluation of the probe beam scattering signals that presently runs at repetition rates up to 30 Hz with 10000 data point per scattering signal trace. By reducing the recorded data points, we can easily reach 300 Hz; and with additional improvements, online control at 1 kHz is feasible. This algorithm allows for an online dosimetry of high-throughput cell and tissue surgery and thus nicely complements the discovery of cost-effective controlled nonlinear energy deposition.

8. Future perspectives

In the following we will give a brief list of challenging tasks for future experimental work and modeling efforts, accomplishment of which would further improve our understanding of optical breakdown.

8.1 Experimental investigations

1. Investigation of nonlinear beam propagation and its influence on plasma formation at small and medium numerical apertures.

2. Investigation of thresholds for low- and high-density ns plasmas in the full range from small to large NAs ($0.05 \leq NA \leq 0.9$)

3. Determination of the influence of linear absorption and inter-band excitation levels in biological cells and tissues on the breakdown threshold, comparison to the values in water.

4. Investigation of plasma formation and mechanical effects (shock wave emission and bubble formation) in fs breakdown in water at medium NAs ($0.1 \leq NA \leq 0.9$) with high (fs) temporal resolution by means of pump-probe Schlieren photography and scattering techniques.

5. Time-resolved investigations of the spatio-temporal dynamics of nanosecond breakdown with 200 ps time resolution using a time-gated intensified CCD camera; analysis of the evolution of the streaks of high-density plasma and of the diffuse luminescence indicative for radiative energy transport.

6. Time-resolved investigations of the dynamics of breakdown-induced cavities in cells and transparent tissues at medium and large NAs; analysis of the changes compared to bubble formation in water.

8.2 Modeling

1. Incorporation of the spatio-temporal evolution of breakdown, i.e. plasma growth and distributed shielding at superthreshold energies. For NAs at which nonlinear beam propagation can be neglected, this can be done based on the approach described by Jiao et al (2009).

2. Incorporation of nonlinear beam propagation taking into account nonparaxial and vectorial effects. This could be done based on the approach described by Arnold et al. (2007).

3. Consideration of the changes in laser plasma coupling at large free-electron densities such as reached well above the bubble formation threshold when part of the incident energy is reflected at the plasma produced earlier during the pulse.

4. Consideration of field-induced electron drift and radiative energy transport from high-density plasma regions such as produced in nanosecond breakdown.

5. Incorporation of centers with reduced excitation energy into the model, and investigation of the interplay of local avalanches arising from individual seed electrons and their fusion to "global" breakdown in order to consider the role of impurities.

6. Consideration of plasma expansion and the resulting stress wave emission and hydrodynamics effects. This aspect is particularly important for nanosecond breakdown in which the expansion starts already during the laser pulse, influencing the laser-plasma coupling.

7. Consideration of the change of collision rates and band structure with increasing plasma temperature during pico- and nanosecond breakdown

8. Modeling of breakdown effects with tailored femtosecond laser pulses, based on our capability to implement arbitrary pulse shapes.

In pursuing each of the mentioned tasks, one needs to compare experimental and modeling results. The improved understanding of controlled nonlinear energy deposition will be useful for numerous practical applications in laser surgery, material modification, and ablation of and within transparent dielectrics.

9. Acknowledgements

10. References

[Amm86]   **Ammosov M V, Delone N B, Krainov V P** (1986) Theory of laser-induced free-electron heating and impact ionization in wide-band-gap solids. *Sov Phys JETP* **64**:1191-1194

[Arn92]   **Arnold D, Cartier E** (1992) Tunnel ionization of complex atoms and of atomic ions in an alternating electromagnetic field. *Phys Rev B* **46**:15102-15115

[Arn05]   **Arnold CL, Heisterkamp A, Ertmer W, Lubatschowski H** (2005) Streak formation as side effect of optical breakdown during processing the bulk of transparent Kerr media with ultrashort laser pulses. *Appl. Phys. B* **80**:247-253

[Arn07]   **Arnold C, Heisterkamp A, Ertmer W, Lubatschowski H** (2007) Computational model for nonlinear plasma formation in high NA micromachining of transparent materials and biological cells. *Opt. Express* **15**:10303

[Bar97]   **Barber B P, Hiller R A, Löfstedt R, Putterman S J, Weninger K R** (1997) Defining the unknowns of sonoluminescence. *Phys Reports* **281**:65-143

[Bas72]   **Bass M, Barrett H H** (1972) Avalanche breakdown and the probabilistic nature of laser-induced damage. *IEEE J Quantum Electron* **8**:338-343

[Ben07]   **Ben-Yakar A, Harkin A, Ashmore J, Byer RL, Stone HA** (2007) Thermal and fluid process of a thin melt zone during femtosecond laser ablation of glass: the formation of rims by single laser pulses. *J Phys D Appl Phys* **40**: 447-1459

[Bla97]   **Blake J R, Hooton M C, Robinson P B, Tong R P** (1997) Collapsing cavities, toroidal bubbles and jet impact. *Phil Trans R Soc Lond A* **355**:537-550

[Bar68]   **Barnes P A, Rieckhoff K E** (1968) Laser induced underwater sparks. *Appl Phys Lett* (13) 282-284

[Blo74]   **Bloembergen N** (1974) Laser-induced electric breakdown in solids. *IEEE J Quantum Electron* **10**:375-386

[Bor70]   **Born M, Wolf E** (1970) Principles of Optics. *Pergamon Press:* Oxford

[Bos93]   **Bosenberg W R, Guyer D R** (1993) Broadly tunable, single-frequency optical parametric frequency-conversation system. *J Opt Soc Am B* **10**:1716-1722

[Bre02]   **Brenner M P, Hilgenfeldt S, Lohse D** (2002) Single-bubble sonoluminescence. *Rev Mod Phys* **74**:425

[Bre64]   **Brewer R G, Rieckhoff K E** (1964) Stimulated brillouin scattering in liquids. *Phys Rev Lett* **13**: 334-336

[Bro89]   **Bronstein I N, Semendjajew K A** (1989) Taschenbuch der Mathematik. *Harri Deutsch:* Thun

[Bru01]   **Brujan E A, Nahen K, Schmidt P, Vogel A** (2001) Dynamics of laser-induced cavitation bubbles near an elastic boundary. *J Fluid Mech* **433**:251-281

[Bul04]   **Bulgakova N M, Stoian R, Rosenfeld A, Hertel I V, Campbell E B** (2004) Electronic transport and consequences for material removal in ultrafast pulsed laser ablation of materials. *Phys Rev B* **69**:054102-1-12

[Car59]   **Carslaw H S, Jaeger J C** (1959) *Conduction of Heat in Solids*, 2nd ed. Oxford University Press: Oxford

[Cha97]   **Chapyak E J, Godwin R P, Vogel A** (1997) Comparison of numerical simulations and laboratory studies of shock waves and cavitation bubble growth produced by optical breakdown in water. *SPIE Proc* **2975**:335-342

[Col48]   **Cole RH** (1948) *Underwater Explosions*. Princeton University Press, Princeton, NJ

[Cou07]   **Couairon A, Mysyrowicz A** (2007) Femtosecond filamentation in transparent media. *Physics Reports* **441**:47 – 189

[Cour03]   **Courvoisier F, Boutou V, Favre C, Hill SC, Wolf J-P** (2003) Plasma formation dynamics within a water microdroplet on femtosecond time scales. *Opt Lett* **28**:206-208

[Dai67]   **Daiber JW, Thompson HM** (1967) Laser-driven detonation waves in gases, *Phys Fluids* **10**, 1162-1169

[deM69]   **DeMichelis C** (1969) Laser induced gas breakdown: a bibliographical review. *IEEE J Quantum Electron* **QE5**:188-202

[Doc88a] **Docchio F, Regondi P, Capon M R C, Mellerio J** (1988) Study of the temporal and spatial dynamics of plasma induced in liquids by nanosecond Nd:YAG laser pulses I – Analysis of the plasma starting times. *Appl Opt* **27**:3661-3668

[Doc88b] **Docchio F, Regondi P, Capon M R C, Mellerio J** (1988) Study of the temporal and spatial dynamics of plasma induced in liquids by nanosecond Nd:YAG laser pulses II – Plasma luminescence and shielding. *Appl Opt* **27**:3669-3674

[Doc88c] **Docchio F** (1988) Lifetimes of plasmas induced in liquids and ocular media by single Nd:YAG pulses of different duration. *Europhys Lett* **6**:407-412

[Doc91] **Doccio F** (1991) Spatial and temporal dynamics of light attenuation and transmission by plasmas induced in liquids by nanosecond Nd:YAG laser pulses. *Il Nuovo Cimento* **13**:87-98

[Du96] **Du D, Liu X, Mourou G** (1996) Reduction of multi-photon ionization in dielectrics due to collisions. *ApplPhys B* **63**:617-621

[Duv63] **Duvall GE, Fowles GR** (1963) Shock waves, in: Bradley RS, ed., *High Pressure Physics and Chemistry*, Academic Press, New York, pp. 209-291.

[Fan02] **Fan HC, Sun J, Longtin JP** (2002) Breakdown threshold and localized electron density in water induced by ultrashort laser pulses. *J Appl Phys* **91**:2530-2536

[Fav02] **Favre C, Boutou V, Hill SC, Zimmer W, Krenz M, Lambrecht H, Yu J, Chang R, Woeste L, Wolf J-P** (2002) White-light nanosource with directional emission. *Phys Rev Lett* **89**:035002

[Fei74] **Feit M D, Fleck JA** (1974) Effect of refraction on spot size dependence of laser-induced breakdown. *Appl Phys Lett* **24**:169-172

[Fei04] **Feit M D, Komashko A M, Rubenchik A M** (2004) Ultra-short pulse laser interaction with transparent dielectrics. *Appl Phys A* **79**:1657-1661

[Fen97] **Feng Q, Moloney J V, Newell A C, Wright E M, Cook K, Kennedy P K, Hammer D X, Rockwell B A, Thompson C R** (1997) Theory and simulation on the threshold of water breakdown induced by focused ultrashort laser pulses. *IEEE J Quantum Electron* **33**:127-137

[Gil52] **Gilmore F R** (1952) *Calif Inst Techn Rep* **26-4**

[Gle84] **Glebov L B, Efimov O M, Petrovskii G T, Rogovtsev** (1984) Influence of the mode composition of laser radiation on the optical breakdown of silicate glasses. *Sov J Quantum Electron* **14**:226-229

[God72] **Godwin R P** (1972) Optical mechanism for enhanced absorption of laser energy incident on solid targets. *Phys Rev Lett* **28**:85-87

[God79] **Godwin R P** (1979) Absorption in laser-produced plasma experiments: a personal view. *Appl Opt* **18**:3555-3561

[God95] **Godwin R P** (1995) Multilayer optics provides laser-plasma-coupling insight. *Appl Opt* **34**:572-580

[God99] **Godwin R, Chapyak E, Noack J, Vogel A** (1999) Aspherical bubble dynamics and oscillation times. *SPIE Proc* **3601**:225-236

[Gra79] **Grand D, Bernas A, Amouyal E** (1979) Photoionization of aqueous indole; conduction band edge and energy gap in liquid water. *Chem Phys* **44**:73

[Gri99] **Grill S, Stelzer E H K** (1999) Method to calculate lateral and axial gain factors of optical setups with a large solid angle. *J Opt Soc Am A* **16**:2658-2665

[Gre75] **Grey Morgan C** (1975) Laser induced breakdown in gases. *Rep Prog Phys* **38**:621-665

[Gru00] **Grupen C** (2000) *Grundkurs Strahlenschutz*. Vieweg, Braunschweig & Wiesbaden (in German).

[Gru07a] **Gruzdev VE, Chen JK** (2007) Laser-induced ionization and intrinsic breakdown of wide band-gap solids. *Appl Phys A* **90**:255-261

[Gru07b] **Gruzdev VE** (2007) Photoionization range in wide band-gap crystals. Phys Rev B 75:205106

[Ham96] **Hammer D X, Thomas R J, Noojin G D, Rockwell B A, Kennedy P A, Roach W P** (1996) Experimental investigation of ultrashort pulse laser-induced breakdown thresholds in aqueous media. *IEEE J Quantum Electron* **3**:670-678

[Ham97] **Hammer DX, Jansen ED, Frenz M, Noojin GD, Thomas RJ, Noack J, Vogel A, Rockwell BA, Welch AJ** (1997) Shielding properties of laser-induced breakdown in water for pulse durations from 5 ns to 125 fs. *Appl Opt* **36**:5630-5640

[Hut07] **Hutson MS, Ma X** (2007) Plasma and cavitation dynamics during pulsed laser microsurgery in vivo. *Phys Rev Lett* **99**:158104

[Jia06]   **Jia T Q, Chen H X, Huang M, Zhao F L, Li X X, Xu S Z, Sun H Y, Feng D H, Li C B, Wang X F, Li R X, Xu Z Z, He X K, Kuroda H** (2006) Ultraviolet-infrared femtosecond laser-induced damage in fused silica and CaF_2 crystals. *Phys Rev B* **73**:054105

[Jiao09]   **Jiao J, Guo Z, Mitra K** (2009) Modeling of USP laser ablation in water. *Proc. ASME 2009 Int. Mech. Eng. Congress and Expos.* IMECE2009-10405 (in print)

[Jog03]   **Joglekar AP, Liu H, Spooner GJ, Meyhöfer E, Mourou G, Hunt AJ** (2003) A study of the deterministic character of optical damage by femtosecond laser pulses and applications to nanomachining. *Appl Phys B* **77**:25-30

[Jog04]   **Joglekar AP, Liu H, Meyhöfer E, Mourou G, Hunt AJ** (2004) Optics at critical intensity: applications to nanomorphing. *Proc. Nat. Acad. Sci.* **101**:5856-5861

[Juo06]   **Juodkazis S, Nishimura K, Tanaka S, Misawa H, Gamaly EG, Luther-Davies B, Hallo L, Nicolai P, Tikhonchuk VT** (2006) Laser-induced micoexplosion confined in the bulk of a sapphire crystal: evidence of multimagabar pressure. *Phys Rev Lett* **96**:166101.

[Kai00]   **Kaiser A, Rethfeld B, Vicanek M, Simon G** (2000) Microscopic processes in dielectrics under irradiation by subpicosecond laser pulses. *Phys Rev B* **61**:11437-11450

[Ken95a]   **Kennedy P K** (1995) A first-order model for computation of laser-induced breakdown thresholds in ocular and aqueous media: Part I – Theory *IEEE J. Quantum Electron* **31**:2241-2249

[Ken95b]   **Kennedy P K** (1995) A first-order model for computation of laser-induced breakdown thresholds in ocular and aqueous media: Part II – Comparison to experiment *IEEE J. Quantum Electron* **31**:2250-2257

[Ken97]   **Kennedy PK, Hammer DX, Rockwell BA** (1997) Laser-induced breakdown in aqueous media, Progr Quantum Electron **21**:155-248

[Kel60]   **Keldysh L V** (1960) Kinetic theory of impact ionization in semiconductors. *Sov Phys JETP* **11**:509-518

[Kel65]   **Keldysh L V** (1965) Ionization in the field of a strong electromagnetic wave. *Sov Phys JETP* **20**:1307-1314

[Ker69]   **Kerker M** (1969) The scattering of light and other electromagnetic radiation. *Academic:* New York

[Kis99]   **Kiselev S B** (1999) Kinetic boundary of metastable states in superheated and stretched liquids. *Physica A* **269 2**:252-268

[Kit76]   **Kittel C** (1976) *Einführung in die Festkörperphysik.* R. Oldenbourg Verlag München Wien

[Kna71]   **Knapp R T, Daily J W, Hammitt F G** (1971) *Cavitation.* McGraw-Hill: New York, 117-131

[Lau03]   **Lauterborn W, Kurz T** (2003) *Coherent Optics. Fundamentals and Applications.* Springer: Berlin, Heidelberg, New York, 346 pp

[Lei05]   **Leica Microsystems CMS GmbH, Ahrberg H** (2005) personal communication by E-mail correspondence 15.09.2005

[Len98]   **Lenzner U, Krüger J, Sartina S, Cheng Z, Spielmann C, Mourou G, Kautek W, Krausz F** (1998) Femtosecond optical breakdown in dielectrica. *Phys Rev Lett* **80**:4076-4079

[Lig04]   **Light Conversion** (2004) TOPAS manual.

[Liu97]   **Liu X, Du D, Mourou G** (1997) Laser ablation and micromachining with ultrashort laser pulses. *IEEE J Quantum Electr* **33**:1706-1716

[Liu03]   **Liu W, Kosareva O, Golubtsov I S, Iwasaki A, Becker A, Kandidov V P, Chin S** (2003) Femtosecond laser pulse filamentation versus optical breakdown in H_2O. *Appl Phys B* **76**:215-229

[Mao04]   **Mao S S, Quéré F, Guizard S. Mao X, Russo E, Petite G, Martin P** (2004) Dynamics of femtosecond laser interactions with dielectrics. *Appl Phys A* **79**:1695-1709

[Mar75]   **Marburger J H** (1975) Self focusing: Theory. *Prog Quant Electron* **4**:35-110

[Mat06]   **Mattsson TR, Desjarlais MP** (2006) Phase diagram and electrical conductivity of high energy-density water from density functional theory. *Phys Rev Lett* **97**:017801

[Mat07]   **Mattsson TR, Desjarlais MP** (2007) High energy-density water: Density density functional theory calculations of structure and electrical conductivity. *Sandia Report* SAND2006-7539

[Mie08]   **Mie G** (1908) Beiträge zur Optik trüber Medien, speziell kolloidaler Metallösungen. *Ann Phys Leipzig* **25**:377-445

[Mom96]   **Momma C, Chichkov BN, Nolte S, von Alvensleben F, Tünnermann A, Welling H, Wellegehausen B** (1996) Short-pule laser ablation of solid targets. *Opt Comm* **129**:134-142

[Nah96] **Nahen K, Vogel A** (1996) Plasma Formation in Water by Picosecond and Nanosecond Nd:YAG Laser Pulses – Part II: Transmission, Scattering, and Reflection. *IEEE J Quantum Electron* **2**:861-871

[Nik83] **Nikogosyan D N, Oraevsky A A, Rupasov V** (1983) Two-photon ionization and dissociation of liquid water by powerful laser UV irradiation. *Chem Phys* **77**:131-143

[Nis05] **NIST** (2005) Thermophysical properties of fluid systems. *National Institute of Standards Chemistry Web book: http://webbook.nist.gov/chemistry/fluid*

[Noa98a] **Noack J, Hammer DX, Noojin GD, Rockwell BA, Vogel A** (1998) Influence of pulse duration on mechanical effects after laser-induced breakdown in water. *J Appl Phys* **83**:7488-7495

[Noa98b] **Noack J, Vogel A** (1998) Single-shot spatially resolved characterization of laser-induced shock waves in water. *Appl Opt* **37**:4092-4099.

[Noa99] **Noack J, Vogel A** (1999) Laser-induced plasma formation in water at nanosecond to femtosecond time scales: Calculation of thresholds, absorption coefficients, and energy density. *IEEE J. Quantum Electron* **35:**1156-1167

[Oli08] **Olivié G, Giguère D, Vidal F, Ozaki T, Kieffer J C, Nada O, Brunette I** (2008) Wavelength dependence of femtosecond laser ablation threshold of corneal stroma. *Opt Expr* **16**:4121

[Ore06] **Oregon Medical Laser Center** (2006) Mie scattering calculations. *http://omlc.ogi.edu/calc/mie_calc.html*

[Pal96] **Paltauf G, Schmidt-Kloiber H** (1996) Microcavity dynamics during laser-induced spallation of liquids and gels. *Appl Phys A* **62**:303-311

[Pal03] **Paltauf G, Dyer P E** (2003) Photomechanical processes and effects in ablation. *Chem Rev* **103**:487-518

[Rai65] **Raizer Yu P** (1965) Heating of a gas by a powerful light pulse. *Sov Phys JETP* **48**:1508-1519

[Rai66] **Raizer Yu P** (1966) Breakdown and heating of gases under the influence of a laser beam. *Sov Phys JETP* **8**:87-103

[Ram64] **Ramsden SA, Savic P** (1964) A radiative detonation model for the development of a laser-induced spark in air. *Nature* **302**:1217-1219

[Ray17] **Rayleigh L** (1917) On the pressure developed in a liquid during the collapse of a spherical cavity. *Philos Mag* **34**:94-98

[Rea71] **Ready J F** (1971) *Effects of High Power Laser Radiation*. Academic press, Orlando 261-262

[Ret04] **Rethfeld B** (2004) Unified model for the free-electron avalanche in laser-irradiated dielectrics. *Phys Rev Lett* **92**:187401

[Rid99] **Ridley B K** (1999) *Quantum Processes in Semiconductors*. Oxford University Press, Oxford

[Rob96] **Roberts RM, Cook JA, Rogers RL, Gieeson AM, Griffy TA** (1996) The energy partition of underwater sparks. *J Acoust Soc Am* **99**:3465-3475

[Sac91] **Sacchi C A** (1991) Laser-induced electric breakdown in water. *J Opt Soc Am B* **8**:337

[Sar06] **Sarpe-Tudoran C, Assion A, Wollenhaupt M, Winter M, Baumert T** (2006) Plasma dynamics of water breakdown at a water surface induced by femtosecond laser pulses. *App Phys Lett* **88**:261109

[Sch01] **Schaffer C B, Brodeur A, Garcia J F, Mazur E** (2001) Micromachining bulk glass by use of femtosecond laser pulses with nanojoule energy. *Optics Lett* **26**:93-95

[Sch02] **Schaffer CB, Nishimura N, Glezer EN, Kim AMT, Mazur E** (2002) Dynamics of femtosecond laser-induced breakdown in water from femtoseconds to nanoseconds. *Opt. Express* **10**:196

[Sed59] **Sedov L I** (1959) Similarity and dimensional methods in mechanics. *Academic Press*: New York

[Set01] **Settles G S** (2001) *Schlieren and Shadowgraph Techniques*. Springer, Berlin, Heidelberg, New York, 376 pp

[She84] **Shen Y R** (1984) *The Principles of Nonlinear Optics*. Wiley, New York

[Smi76] **Smith D C, Meyerand Jr R G** (1976) Laser radiation induced gas breakdown. *Principles of laser plasma.* Wiley, New York*:457-507

[Smi77] **Smith D C, Meyerand R G** (1977) Superbroadening in H_2O and D_2O by self-focused picosecond pulses from a YAIG:Nd laser. *Phys Rev Lett A* **15**:2396-2403

[Soi89] **Soileau MJ, Williams WF, Mansour N, Van Stryland EW** (1989) Laser-induced damage and the role of self-focusing. *Opt Eng* **28**:1133-1144.

[Spa81]   **Sparks M, Mill D L, Warren R, Holstein T, Maradudin A A, Sham L J, Loh E Jr, King D F** (1981) Theory of electron-avalanche breakdown in solids. *Phys Rev B* **24**:3519-3536

[Sto95]   **Stolarski D J, Hardman J, Bramlette C M, Noojin G D, Thomas R J, Rockwell B A, Roach W P** (1996) Integrated light spectroscopy of laser induced breakdown in aqueous media. *Proc SPIE* **2391**:100-109

[Str71]   **Strube H W** (1971) Numerische Untersuchung zur Stabilität nichtsphärisch schwingender Blasen. *Acustica* **25**:289-303

[Stu95]   **Stuart B C, Feit M D, Rubenchick A M, Shore B W, Perry M D** (1995) Laser-induced damage in dielectrics with nanosecond to subpicosecond pulses. *Phys Rev Lett* **74**:2248-2251

[Stu96]   **Stuart B C, Feit M D, Hermann S, Rubenchick A M, Shore B W, Perry M D** (1996) Nanosecond to femtosecond laser-induced breakdown in dielectrics. *Phys Rev B* **53**:1749-1761

[Sud02]   **Sudrie L, Couairon A, Franco M, Lamouroux, Prade B , Tzortzakis S, Mysyrowicz A** (2002) Femtosecond Laser-Induced Damage and Filamentary Propagation in Fused Silica. *Phys Rev Lett* **89**:186601

[Sun05]   **Sun Q, Jiang H, Liu Y, Wu Z, Yang H, Gong Q** (2005) Measurement of the collision time of dense electronic plasma induced by a femtosecond laser in fused silica. *Opt Lett* **30**:320-322

[Tay50]   **Taylor G** (1950) The formation of a blast wave by a very intense explosion. I Theoretical discussion. *Proc. Roy. Soc. A* **201**:159-186

[Tho81]   **Thornber K K** (1981) Applications of scaling to problems in high-field electronic transport. *J Appl Phys* **52**:279-290

[Tie99]   **Tien A C, Backus S, Kapteyn H, Murnane M, Mourou G** (1999) Short-pulse laser damage in transparent materials as a function of pulse duration. *Phys Rev Lett* **82**:3883-3886

[Tri04]   **Trickl T, Vogelmann H** (2004) A powerful widely tunable single-mode laser system for lidar sounding of water vapor throughout the free troposphere. *Reviewed and Revised Papers Presented at the 22nd International Laser and Radar Conference, Volume 1* Matera, Italy 175-178

[Tzo01]   **Tzortzakis S, Sudrie L, Franco M, Prade B, Mysyrowicz A, Couairon A, Bergé L** (2001) Self-Guided Propagation of Ultrashort IR Laser Pulses in Fused Silica. *Phys Rev Lett* **87**:213902

[Ven02]   **Venugopalan V, Guerra III A, Nahen K, Vogel A** (2002) Role of Laser-Induced Plasma Formation in Pulsed Cellular Microsurgery and Micromanipulation. *Phys Rev Lett* **88**:78103 1-4

[Vog96a]   **Vogel A**, **Busch S, Parlitz U** (1996) Shock wave emission and cavitation bubble generation by picoseconds and nanosecond optical breakdown in water. *J Acoust Soc Am* **100**:148-165

[Vog96b]   **Vogel A**, **Nahen K, Theisen D, Noack J** (1996) Plasma Formation in Water by Picosecond and nanosecond Nd:YAG Laser Pulses – Part I: Optical Breakdown at Threshold and Superthreshold Irradiance. *IEEEJ Quantum Electron* **2**:847-890

[Vog99a]   **Vogel A**, **Noack J, Nahen K, Theisen D, Busch S, Parlitz U, Hammer D X, Noojin G D, Rockwell B A, Bringruber R** (1999) Energy balance of optical breakdown in water at nanosecond to femtosecond time scales. *Appl Phys B* **68**:271-280

[Vog99b]   **Vogel A, Nahen K, Theisen D, Birngruber R, Thomas RJ, Rockwell BA** (1999) Influence of optical aberrations on laser-induced plasma formation in water, and their consequences for intraocular photodisruption. *Appl Opt* **38**:3636–3643

[Vog01]   **Vogel A**, **Noack J** (2001) Numerical simulation of optical breakdown for cellular surgery at nanosecond to femtosecond time scales. *Proc SPIE Functional Imaging and Optical Manipulation of Living Cells and Tissues* **4260**:83-93

[Vog03]   **Vogel A**, **Venugopalan V** (2003) Mechanisms of pulsed laser ablation of biological tissues. *Chem Rev* **103**:577-644

[Vog05]   **Vogel A**, **Noack J, Huettmann G, Paltauf G** (2005) Mechanisms of femtosecond laser nanosurgery of cells and tissue. *Appl Phys B* **81**:1015-1047

[Vog06]   **Vogel A, Apitz I, Freidank S, Dijkink R** (2006) Sensitive high-resolution white-light Schlieren technique with a large dynamic range for the investigation of ablation dynamics. *Opt. Lett.* **31**:1812-1814

[Vog08]   **Vogel A, Linz N, Freidank S, Paltauf G** (2008) Femtosecond laser induced nanocavitation in water: implications for optical breakdown threshold and cell surgery. *Phys Rev Lett* **100**:038102.

[Vogl08]   **Vogelmann H, Trickl T** (2008) Wide-range sounding of free-tropospheric water vapor with a differential-absorption lidar (DIAL) at high-altitude station. *Appl Opt* **47**:2116-2132

[Vogt01] **Vogt U, Stiel H, Will I, Kickles PV, Sandner W, Wieleand M, Wilhein T** (2001) Influence of laser intensity and pulse duration on the extreme ultraviolet yield from a water jet target laser plasma. *Appl Phys Lett* 79:2336-2338

[Wea88] **Weast R C** (1988) *CRS Handbook of Chemistry and Physics*. CRC Press, Boca Raton

[Wey89] **Weyl G M** (1989) Physics of laser-induced breakdown: An update. In Radziemski LJ, Cremers DA (eds) *Laser-induced plasmas and applications*. Marcel Dekker, New York 1-67

[Wil76] **Williams F, Varama S P, Hillenius S** (1976) Liquid water as a lone-pair amorphous semiconductor. *J Chem Phys* **64**:1549-1554

11. Appendix

11.1 Breakdown probability curves

11.1.1. Fixed wavelengths, 315 fs
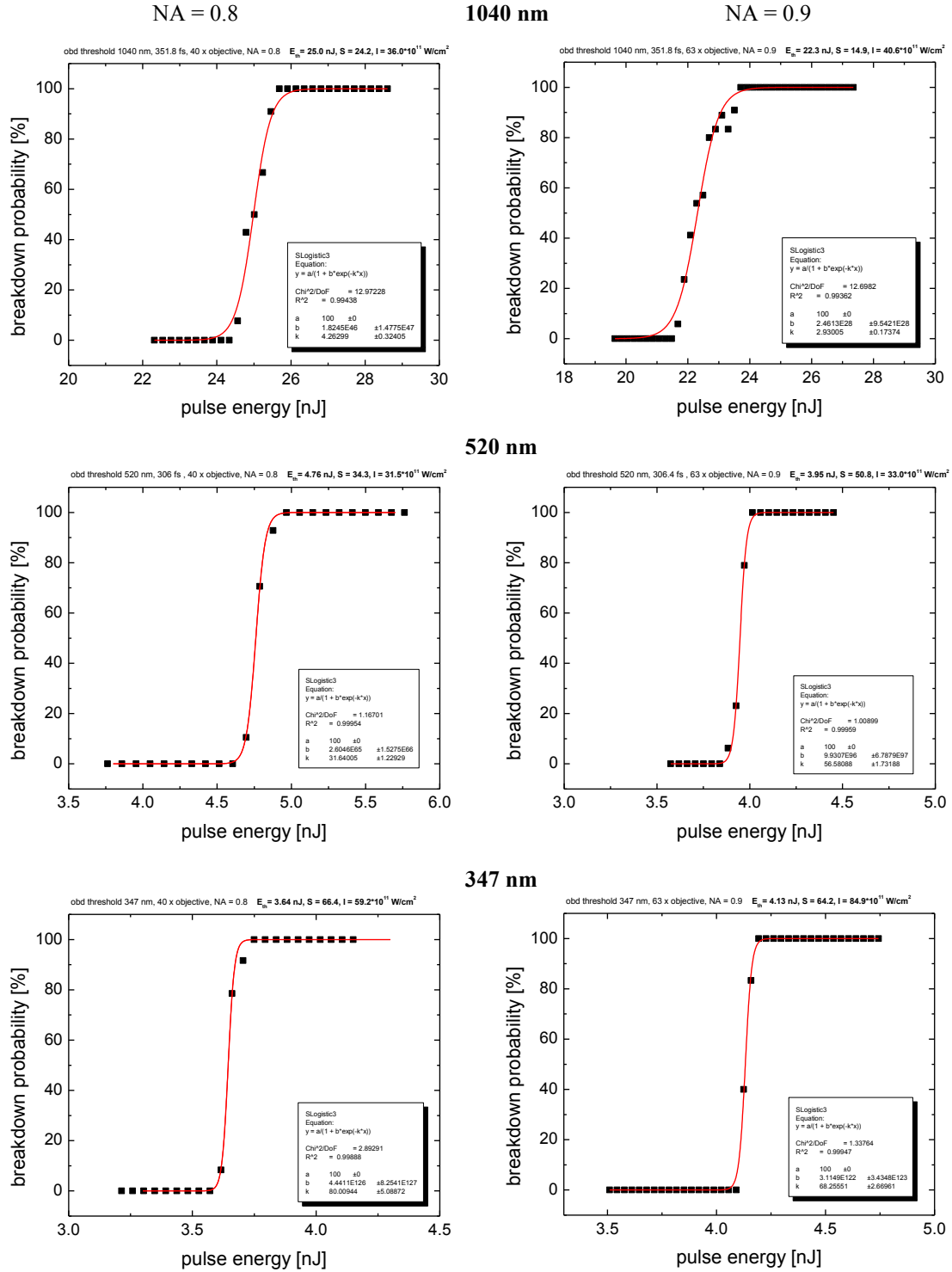
Figure 11.1 Probability for optical breakdown in water induced by 315-fs laser pulses with 1040 nm wavelength (top), 520 nm (middle), and 346 nm (bottom). The laser pulses were focused through a 63 x water immersion objective, NA = 0.9 (left) and a 40 x objective, NA = 0.8 (right).

11.1.2. Fixed wavelengths, 30 ps

1064 nm
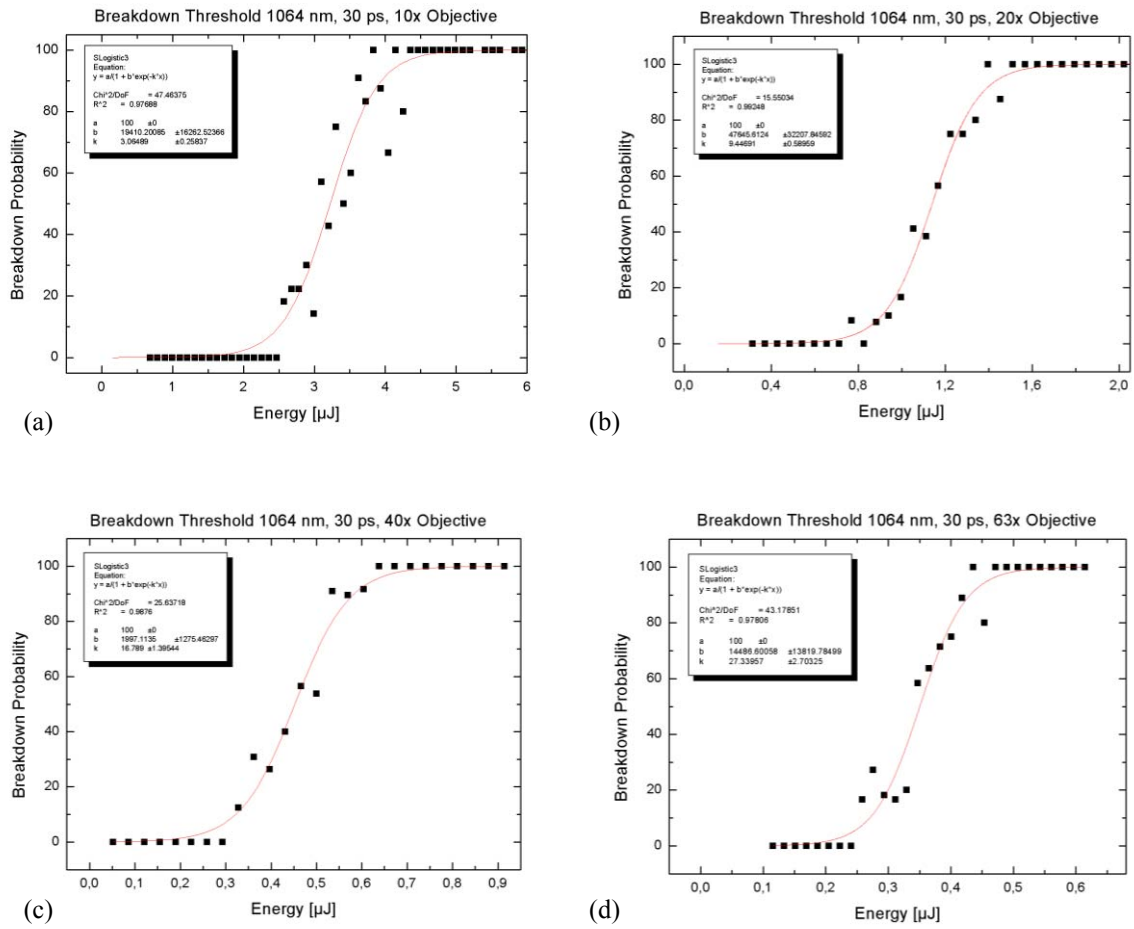
Figure 11.2 Probability for optical breakdown in water induced by 30-ps laser pulses with 1064 nm wavelength for different water immersion objectives: (a) 10 x, NA = 0,3 (b) 20 x, NA = 0,5 (c) 40 x, NA = 0,8 (d) 63 x, NA = 0,9.

532 nm
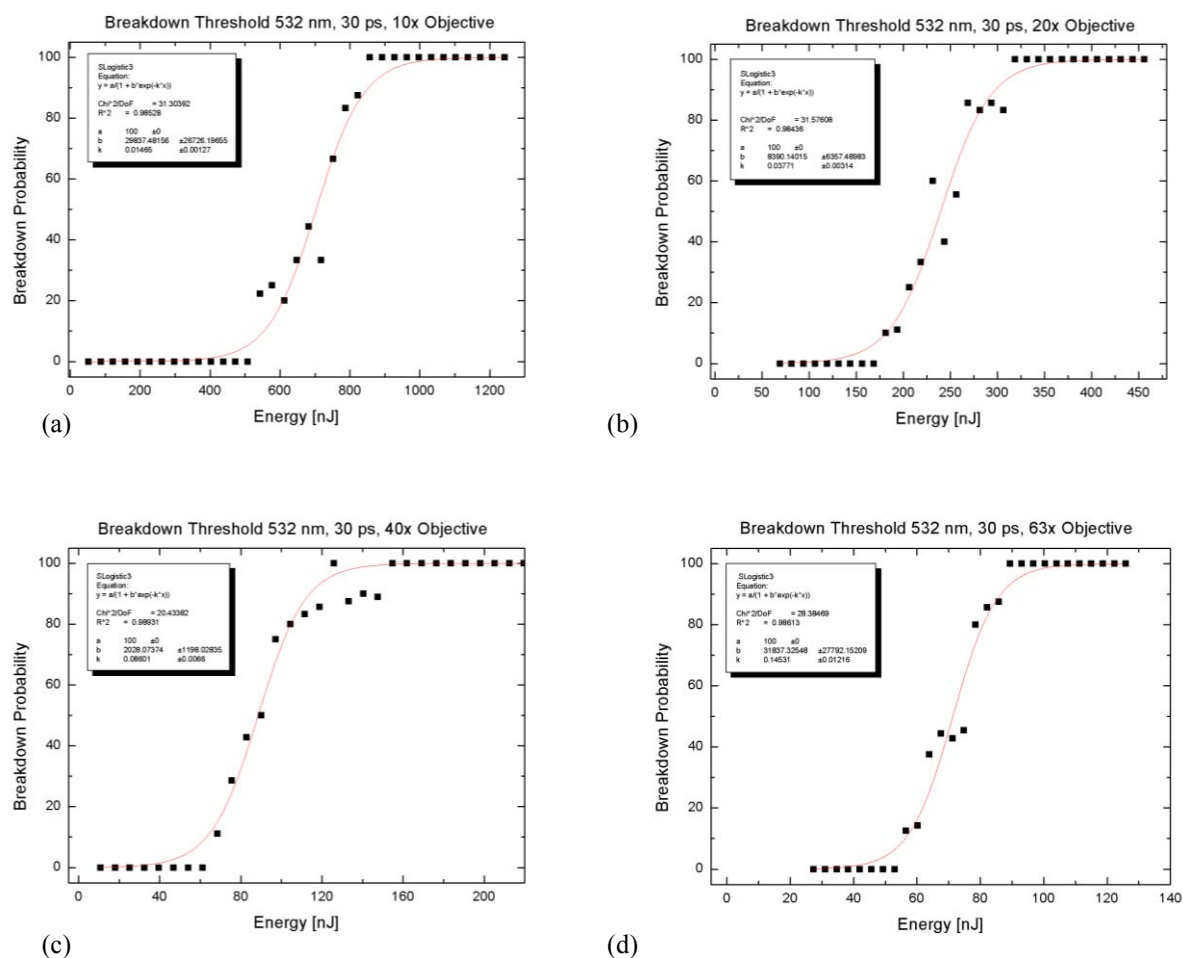
Figure 11.3 Probability for optical breakdown in water induced by 30-ps laser pulses with 532 nm wavelength for different water immersion objectives: (a) 10 x, NA = 0,3 (b) 20 x, NA = 0,5 (c) 40 x, NA = 0,8 (d) 63 x, NA = 0,9.

355 nm

(a)

(b)

(c)

(d)
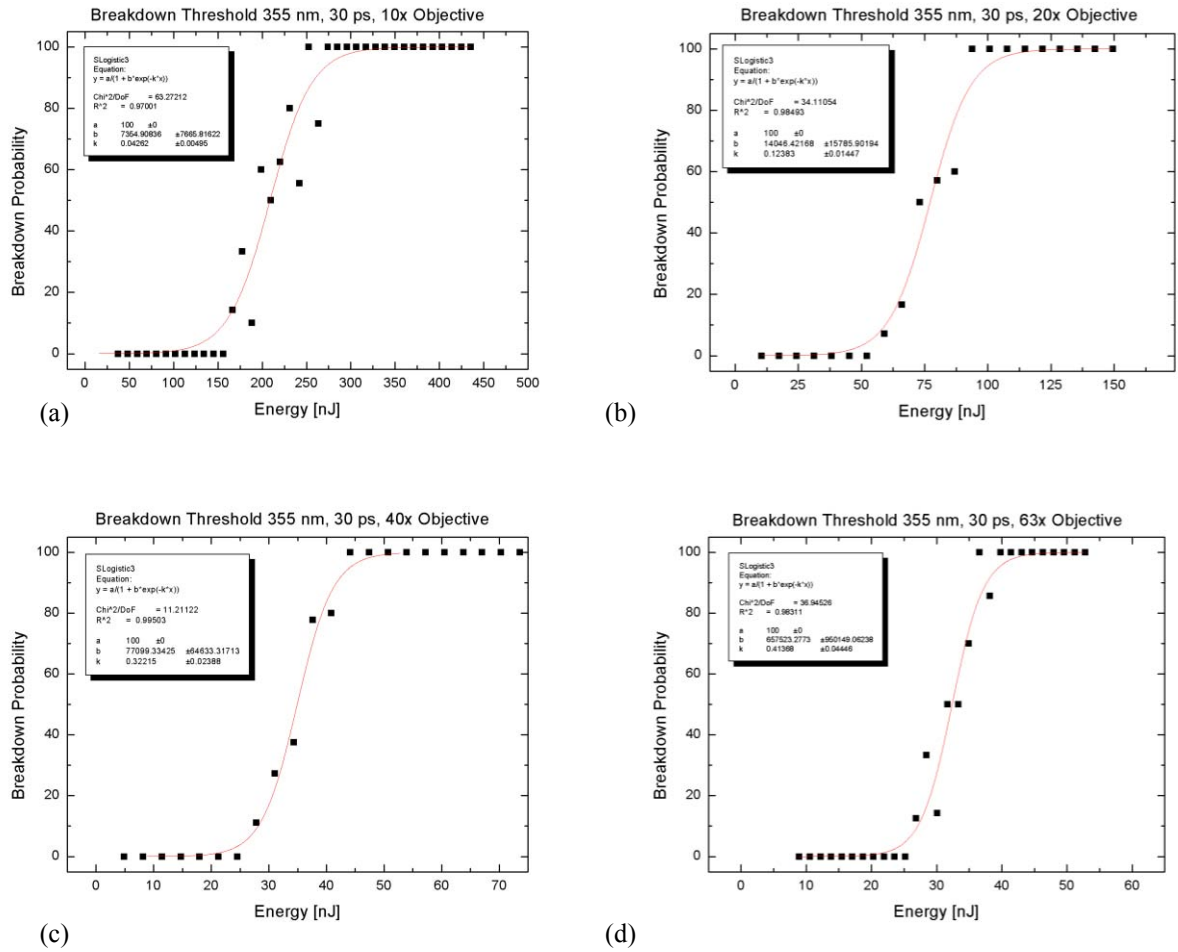
Figure 11.4 Probability for optical breakdown in water induced by 30-ps laser pulses with 355 nm wavelength for different water immersion objectives: (a) 10 x, NA = 0,3 (b) 20 x, NA = 0,5 (c) 40 x, NA = 0,8 (d) 63 x, NA = 0,9.

11.1.3. Fixed wavelengths, 6-11 ns

1064 nm, seeded

(a)

(b)

1064 nm, unseeded

(c)
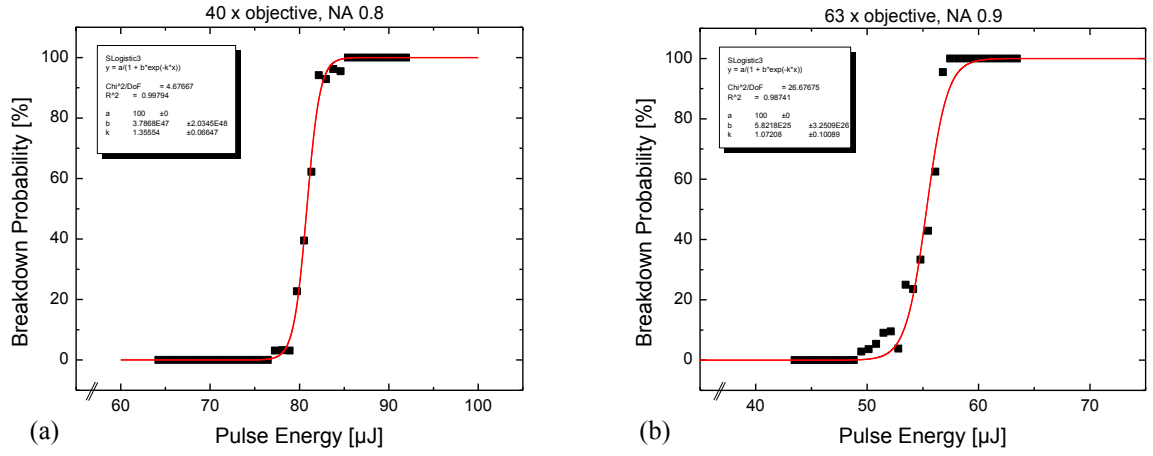
(d)
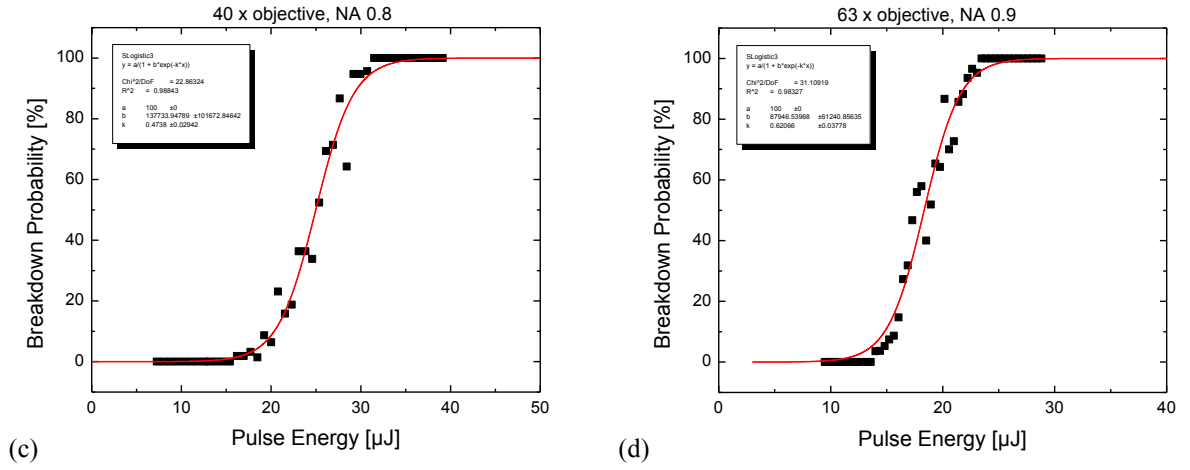
Figure 11.5 Probability for optical breakdown in water induced by seeded/unseeded 11-ns laser pulses with 1064 nm wavelength focused through water immersion objectives: seeded: (a) 40 x objective, NA = 0.8 (b) 63 x objective, NA = 0.9; unseeded: (c) 40 x objective, NA = 0.8 (d) 63 x objective, NA = 0.9. Both for seeded and unseeded operation, bubble and BPL thresholds coincide.

532 nm, seeded

Bubble formation   **Bright plasma luminescence (BPL)**
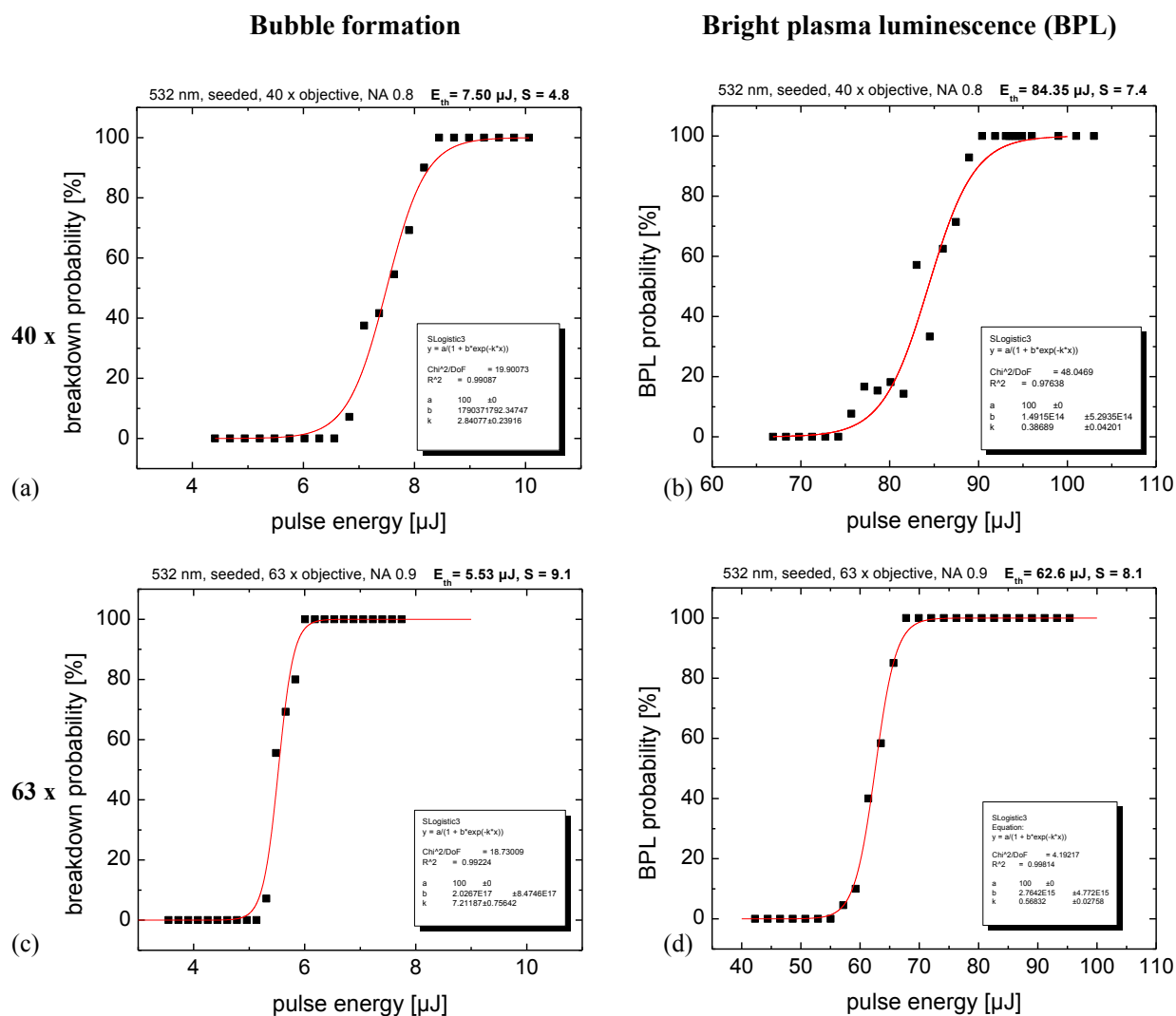
Figure 11.6 Probability for optical breakdown in water induced by seeded 8.8-ns laser pulses with 532 nm wavelength focused through two water immersion objectives. The optical breakdown with seeded laser pulses is a two step process with two thresholds: (a), (c) the bubble formation threshold, and (b), (d) the bright plasma luminescence (BPL) threshold for the 40 x objective, NA = 0.8, and for the 63 x objective, NA = 0.9, respectively.

532 nm, unseeded
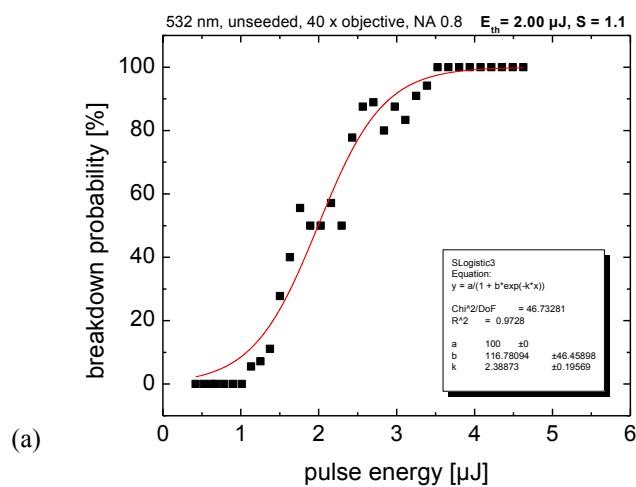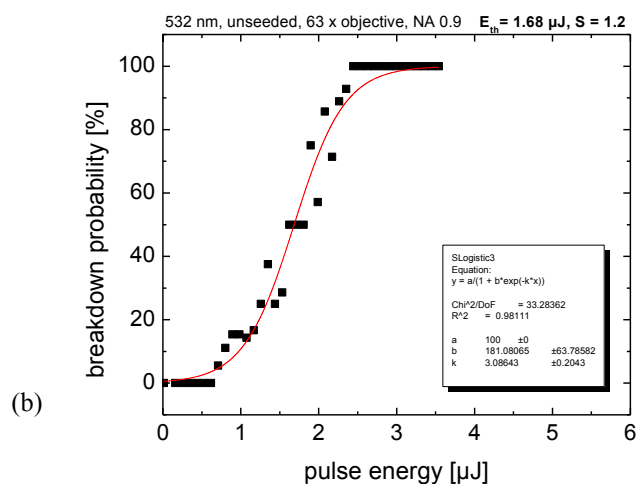
Figure 11.7 Probability for optical breakdown in water induced by unseeded 8.8-ns laser pulses with 532 nm wavelength focused through two water immersion objectives: (a) 40 x objective, NA = 0.8 (b) 63 x objective, NA = 0.9. For unseeded laser pulses, no clear distinction between bubble and BPL threshold exists.

355 nm, seeded

Bubble formation

355 nm, seeded, 40 x objective, NA 0.8   E$_{th}$ = 1.39 µJ, S = 2.1

40 x

(a)

Bright plasma luminescence (BPL)

355 nm, seeded, 40 x objective, NA 0.8   E$_{th}$ = 42.42 µJ, S = 9.1

(b)

355 nm, seeded, 63 x objective, NA 0.9   E$_{th}$ = 1.49 µJ, S = 4.5

63 x

(c)

355 nm, seeded, 63 x objective, NA 0.9   E$_{th}$ = 25.4 µJ, S = 12.1

(d)
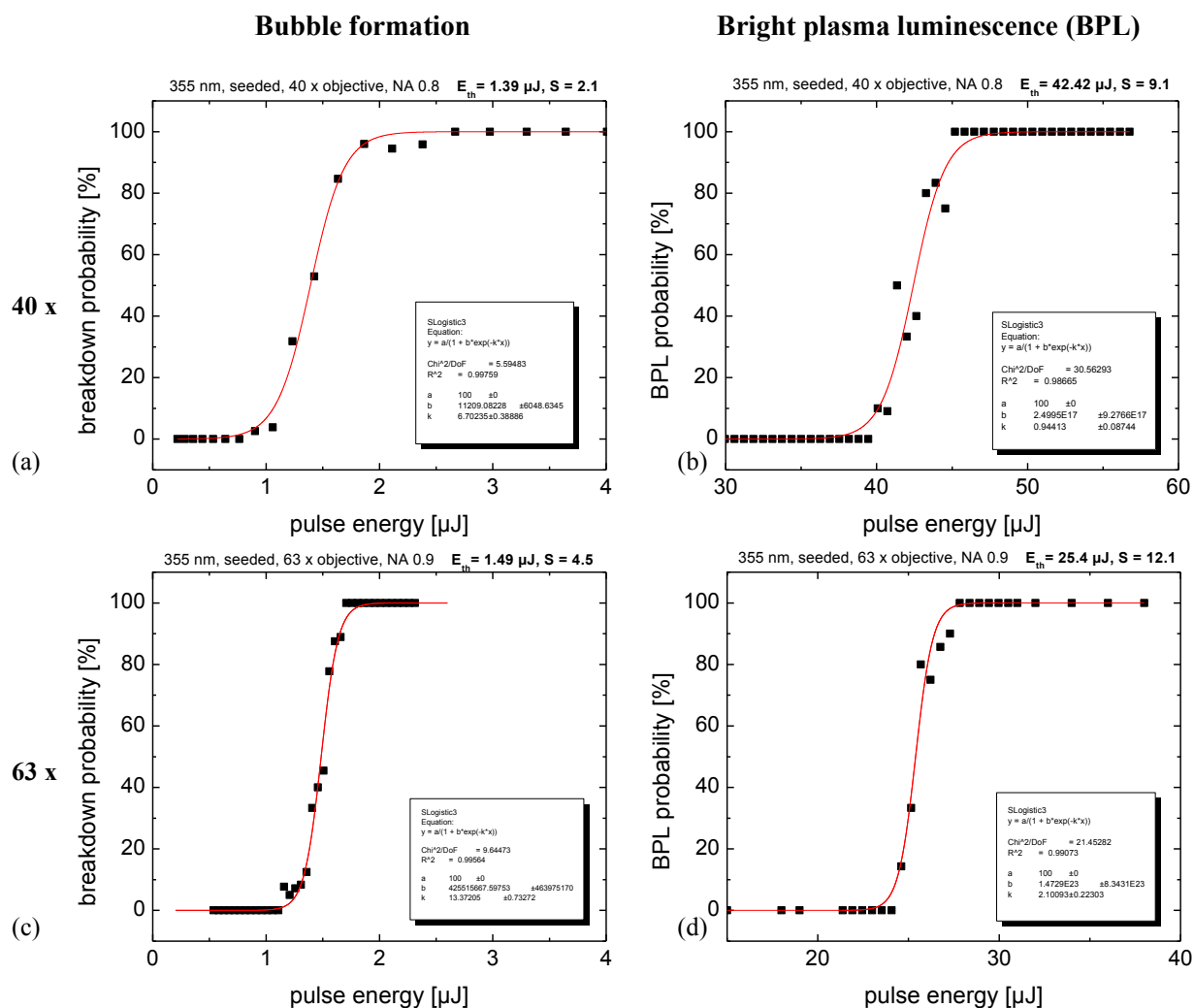
Figure 11.8 Probability for optical breakdown in water induced by seeded 6.8-ns laser pulses with 355 nm wavelength focused through two water immersion objectives. The optical breakdown with seeded laser pulses is a two step process with two thresholds (a), (c) the bubble formation threshold, and (b), (d) the bright plasma luminescence (BPL) threshold for the 40 x objective,   NA = 0.8, and the 63 x objective, NA = 0.9, respectively.

355 nm, unseeded

355 nm, unseeded, 40 x objective, NA 0.8   E$_{th}$= 0.60 µJ, S = 0.7

40 x, NA 0.8

(a)

Model: SLogistic3
Equation:
y = a/(1 + b*exp(-k*x))

Chi^2/DoF   = 39.93548
R^2   = 0.97962

a   100   ±0
b   18.25332   ±3.68114
k   4.83326   ±0.34658

355 nm, unseeded, 63 x objective, NA 0.9   E$_{th}$= 0.50 µJ, S = 0.7

63 x, NA 0.9

(b)

SLogistic3
Equation:
y = a/(1 + b*exp(-k*x))

Chi^2/DoF   = 53.36629
R^2   = 0.97152

a   100   ±0
b   17.76974   ±2.87411
k   5.79635   ±0.33208

breakdown probability [%]

pulse energy [µJ]
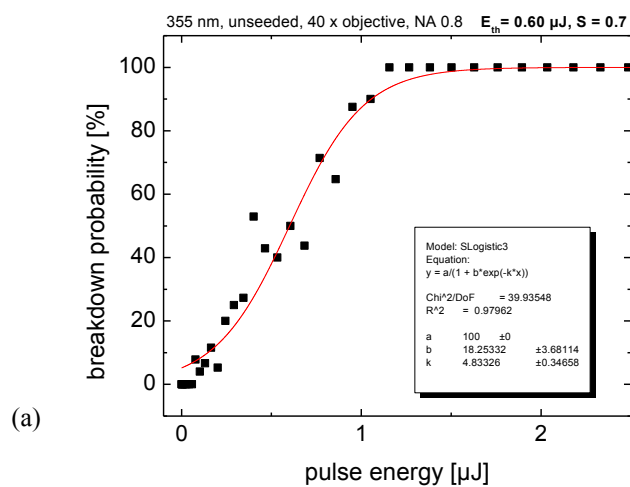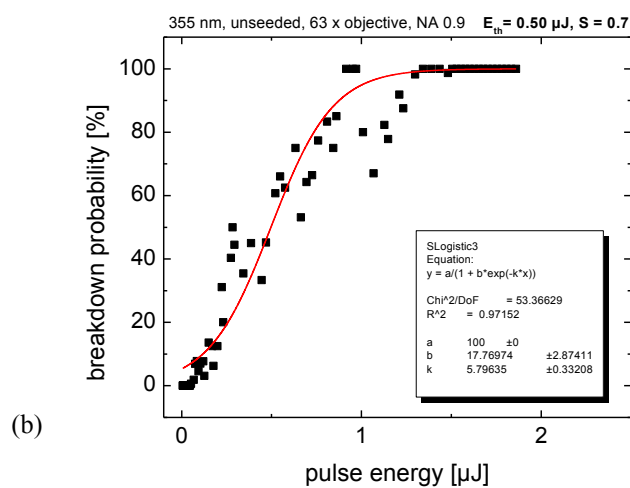
Figure 11.9 Probability for optical breakdown in water induced by unseeded 6.8-ns laser pulses with 355 nm wavelength focused through water immersion objectives: (a) 40 x objective, NA = 0.8 (b) 63 x objective, NA = 0.9. For unseeded laser pulses, no clear distinction between bubble and BPL threshold exists.

11.1.4. Microchip lasers of fixed wavelengths, 0.5 -1.0 ns

1064 nm, Gaussian

40 x, NA 0.8

(a)

63 x, NA 0.9

(b)
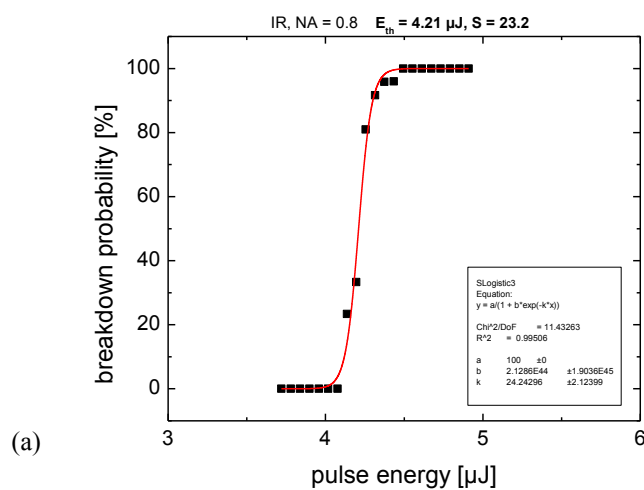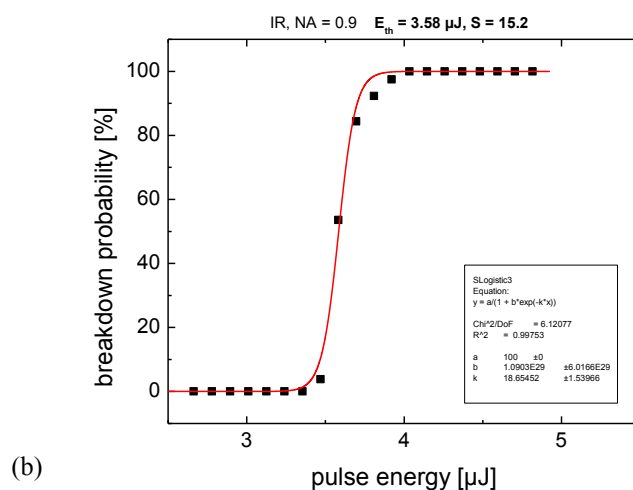
Figure 11.10 Probability for optical breakdown in water induced by 1.01-ns laser pulses with 1064 nm wavelength focused through water immersion objectives: (a) 40 x objective, NA = 0.8 (b) 63 x objective, NA = 0.9. Bubble and BPL thresholds coincide.

532 nm, Gaussian

Bubble formation **Bright plasma luminescence (BPL)**
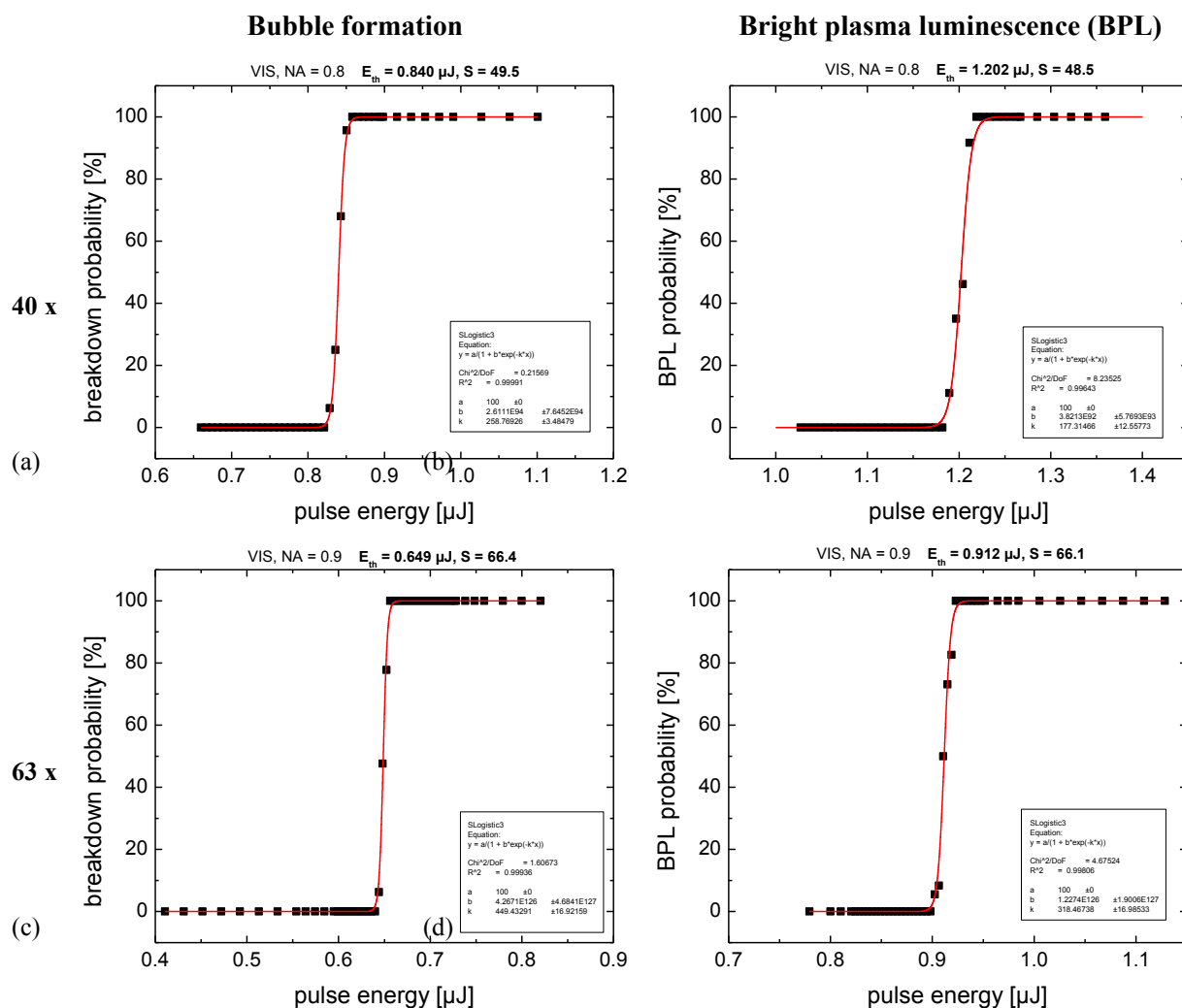
Figure 11.11 Probability for optical breakdown in water induced by 0.95-ns laser pulses with 532 nm wavelength focused through two water immersion objectives. The optical breakdown with laser pulses is a two step process with two thresholds: (a), (c) show the bubble formation threshold, and (b), (d) the bright plasma luminescence (BPL) threshold for a 40 x objective, NA = 0.8, and a 63 x objective, NA = 0.9, respectively.

355 nm, Gaussian

Bubble formation

Bright plasma luminescence (BPL)
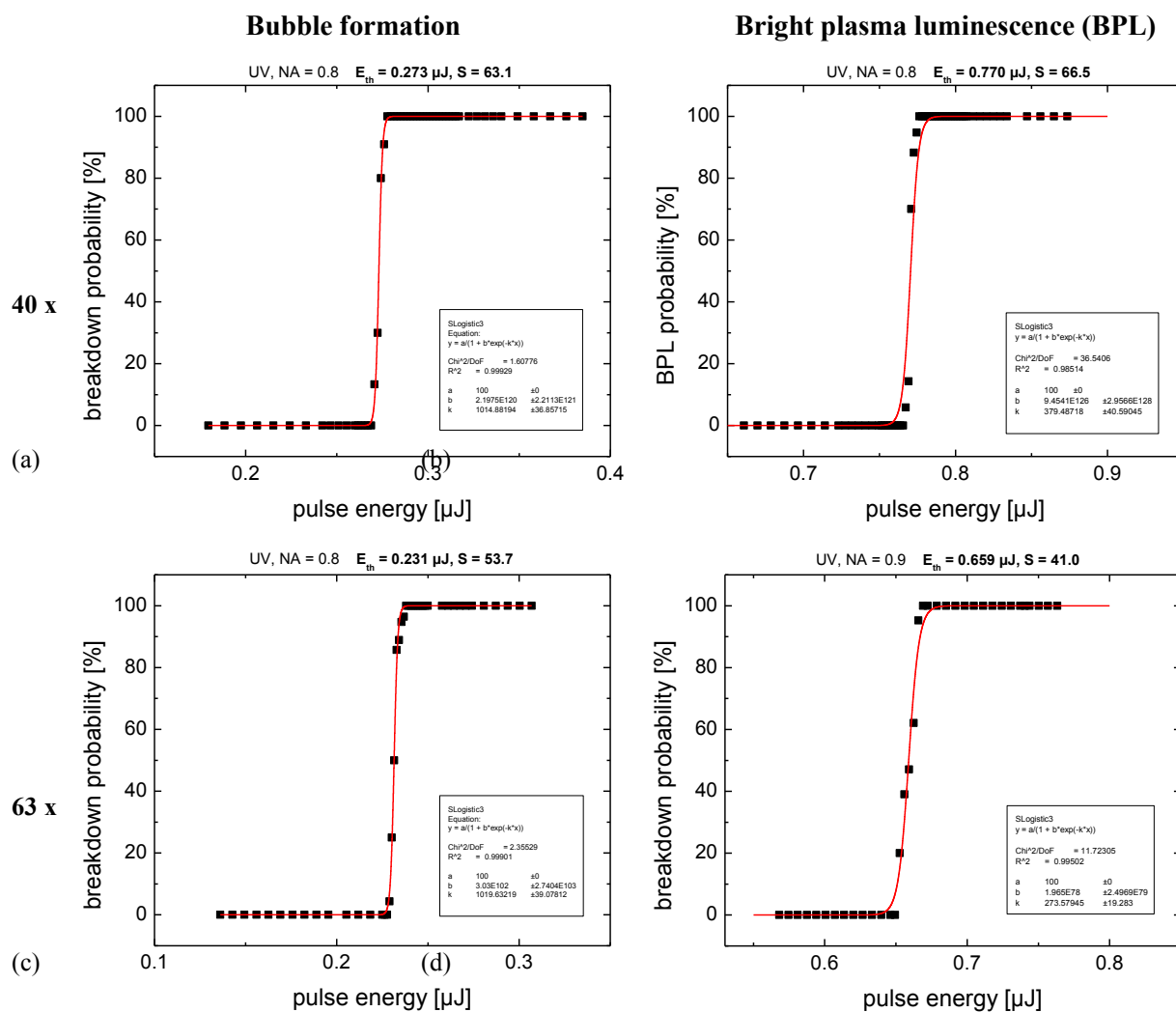
Figure 11.12 Probability for optical breakdown in water induced by 0.93-ns laser pulses with 355 nm wavelength focused through two different water immersion objectives. The optical breakdown with laser pulses is a two step process with two thresholds: (a), (c) show the bubble formation threshold, and (b), (d) the bright plasma luminescence (BPL) threshold for the 40 x objective, NA = 0.8, and the 63 x objective, NA = 0.9, respectively.

355 nm, Gaussian, 560 ps

Bubble threshold

BPL threshold
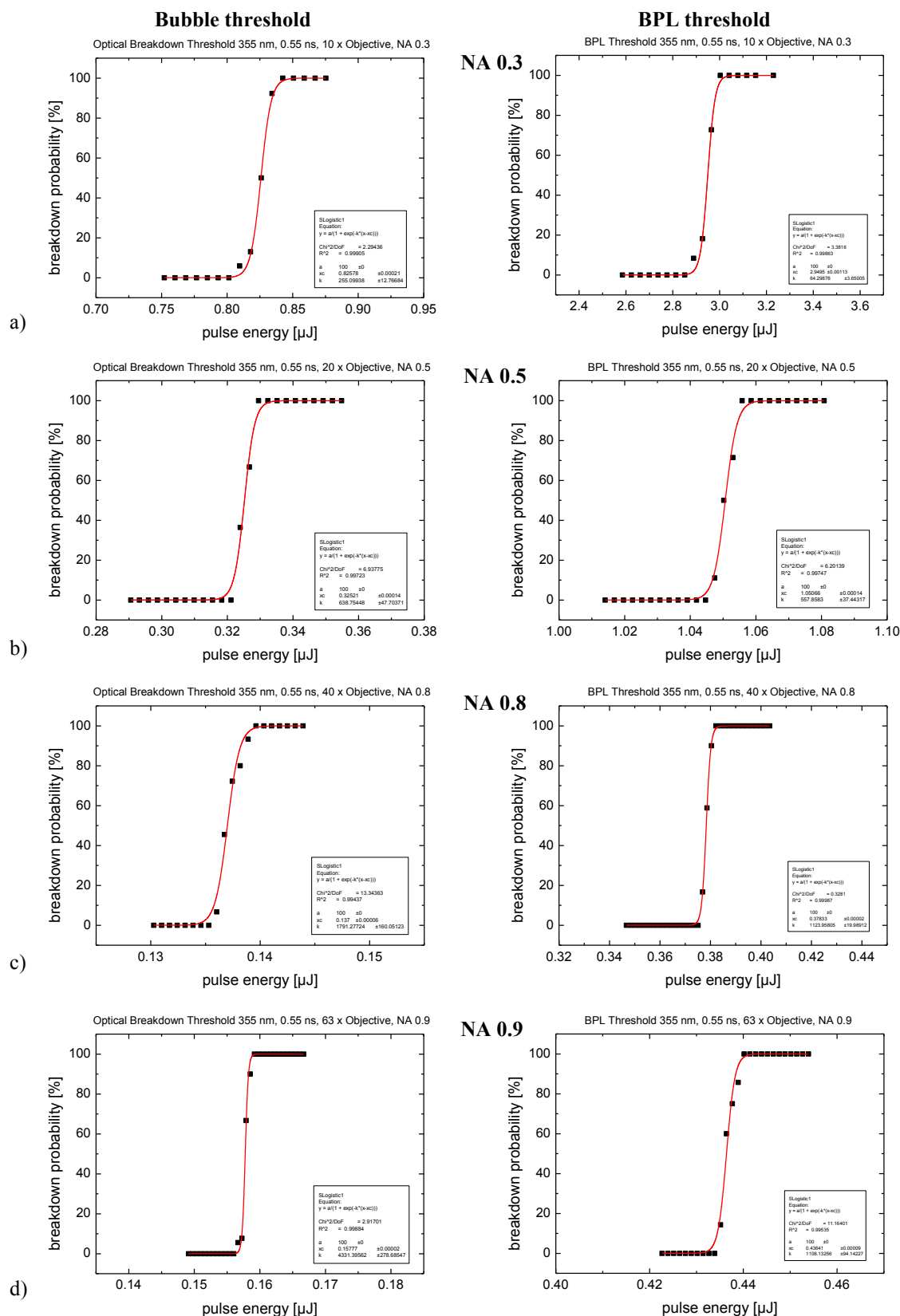
Figure 11.13 Probability curves for optical breakdown in water produced by 0.55-ns laser pulses with 355 nm wavelength focused through water immersion objectives with different NAs: a) 10x objective, NA = 0.3, b) 20x objective, NA = 0.5, c) 40x objective, NA = 0.8, and the d) 63x objective, NA = 0.9. For each NA, measurement data are displayed both for the bubble formation threshold and the bright plasma luminescence (BPL) threshold.

11.1.5. OPO, 2 ns

40x, NA 0.8   **63x, NA 0.9**

725 nm

obd threshold 725 nm, 40 x objective, NA = 0.8   T = 1.71 ns, E_{th} = 7.30 µJ, S = 19.4, I = 4.46*10^{11} W/cm^2

obd threshold 725nm, 63 x objective, NA = 0.9   T = 1.89 ns, E_{th} = 3.45 µJ, S = 8.5, I = 2.41*10^{11} W/cm^2

a)

730 nm

obd threshold 729.85 nm, 40 x objective, NA = 0.8   T = 2.17 ns, E_{th} = 9.21 µJ, S = 6.0, I = 4.36*10^{11} W/cm^2

obd threshold 729.85 nm, 63 x objective, NA = 0.9   T = 2.17 ns, E_{th} = 4.00 µJ, S = 3.2, I = 2.40*10^{11} W/cm^2

b)

734.5 nm

obd threshold 734.5 nm, 40 x objective, NA = 0.8   T = 2.06 ns, E_{th} = 10.44 µJ, S = 9.9, I = 5.14*10^{11} W/cm^2

obd threshold 734.5 nm, 63 x objective, NA = 0.9   T = 1.88 ns, E_{th} = 4.71 µJ, S = 7.9, I = 3.23*10^{11} W/cm^2

c)

738 nm

obd threshold 738 nm, 40 x objective, NA = 0.8   T = 2.25 ns, E_{th} = 14.73 µJ, S = 5.3, I = 6.58*10^{11} W/cm^2

obd threshold 738 nm, 63 x objective, NA = 0.9   T = 2.25 ns, E_{th} = 7.56 µJ, S = 5.8, I = 4.28*10^{11} W/cm^2

d)

40x, NA 0.8

63x, NA 0.9

745 nm

e)

770 nm

f)

780 nm

g)

795 nm

h)

40x, NA 0.8

63x, NA 0.9

817 nm

obd threshold 817 nm, 40 x objective, NA = 0.8   T = 2.49 ns, E_{th}= 12.00 µJ, S = 9.6, I = 3.95*10^{11} W/cm^2

obd threshold 817 nm, 63 x objective, NA = 0.9   T = 2.49 ns, E_{th}= 6.93 µJ, S = 6.2, I = 2.89*10^{11} W/cm^2

i)

SLogistic3
Equation:
y = a/(1 + b*exp(-k*x))

Chi^2/DoF   = 7.08537
R^2   = 0.997

a   100   ±0
b   1.88E18   ±4.6912E18
k   3.50696   ±0.20787

SLogistic3
Equation:
y = a/(1 + b*exp(-k*x))

Chi^2/DoF   = 10.85095
R^2   = 0.99515

a   100   ±0
b   686436481461.98657   ±1.1857E12
k   3.93134   ±0.24897

840 nm

obd threshold 840 nm, 40 x objective, NA = 0.8   T = 2.73 ns, E_{th}= 13.59 µJ, S = 3.3, I = 3.86*10^{11} W/cm^2

obd threshold 840 nm, 63 x objective, NA = 0.9   T = 2.73 ns, E_{th}= 7.40 µJ, S = 3.5, I = 2.66*10^{11} W/cm^2

j)

SLogistic3
Equation:
y = a/(1 + b*exp(-k*x))

Chi^2/DoF   = 26.50449
R^2   = 0.98663

a   100   ±0
b   1987011.9356   ±1906949.76964
k   1.0669   ±0.07035

SLogistic3
Equation:
y = a/(1 + b*exp(-k*x))

Chi^2/DoF   = 23.63218
R^2   = 0.98732

a   100   ±0
b   5241561.20488   ±5716140.48307
k   2.09085   ±0.14687

865 nm

obd threshold 865 nm, 40 x objective, NA = 0.8   T = 1.98 ns, E_{th}= 10.64 µJ, S = 3.5, I = 3.93*10^{11} W/cm^2

obd threshold 865 nm, 63 x objective, NA = 0.9   T = 1.98 ns, E_{th}= 5.02 µJ, S = 3.4, I = 2.35*10^{11} W/cm^2

k)

SLogistic3
Equation:
y = a/(1 + b*exp(-k*x))

Chi^2/DoF   = 7.46419
R^2   = 0.99639

a   100   ±0
b   4889580.85821   ±3955111.28632
k   1.44759   ±0.07558

SLogistic3
Equation:
y = a/(1 + b*exp(-k*x))

Chi^2/DoF   = 9.84116
R^2   = 0.99536

a   100   ±0
b   2621342.53246   ±2666869.84101
k   2.94669   ±0.20217

900 nm

obd threshold 900 nm, 40 x objective, NA = 0.8   T = 2.43 ns, E_{th}= 11.97 µJ, S = 8.9, I = 3.33*10^{11} W/cm^2

obd threshold 900 nm, 63 x objective, NA = 0.9   T = 2.43 ns, E_{th}= 6.06 µJ, S = 3.2, I = 2.13*10^{11} W/cm^2

l)

SLogistic3
Equation:
y = a/(1 + b*exp(-k*x))

Chi^2/DoF   = 0.56647
R^2   = 0.99978

a   100   ±0
b   9.0415E16   ±8.084E16
k   3.2615   ±0.07476

SLogistic3
Equation:
y = a/(1 + b*exp(-k*x))

Chi^2/DoF   = 20.81222
R^2   = 0.99092

a   100   ±0
b   1525079.89851   ±2411227.2974
k   2.34847   ±0.25977

40x, NA 0.8   **63x, NA 0.9**

930 nm

obd threshold 930 nm, 40 x objective, NA = 0.8   T = 1.63 ns, E$_{th}$ = 6.18 μJ, S = 3.2, I = 2.40*10^{11} W/cm^2

obd threshold 930 nm, 63 x objective, NA = 0.9   T = 1.96 ns, E$_{th}$ = 5.10 μJ, S = 15.2, I = 2.08*10^{11} W/cm^2

m)

940 nm

obd threshold 940.8 nm, 40 x objective, NA = 0.8   T = 1.84 ns, E$_{th}$ = 6.56 μJ, S = 3.7, I = 2.21*10^{11} W/cm^2

obd threshold 940 nm, 63 x objective, NA = 0.9   T = 1.74 ns, E$_{th}$ = 3.94 μJ, S = 6.9, I = 1.77*10^{11} W/cm^2

n)

947 nm

obd threshold 947 nm, 40 x objective, NA = 0.8   T = 1.78 ns, E$_{th}$ = 5.90 μJ, S = 5.5, I = 2.02*10^{11} W/cm^2

obd threshold 947 nm, 63 x objective, NA = 0.9   T = 2.19 ns, E$_{th}$ = 4.53 μJ, S = 5.0, I = 1.60*10^{11} W/cm^2

o)

954 nm

obd threshold 954 nm, 40 x objective, NA = 0.8   T = 2.61 ns, E$_{th}$ = 10.97 μJ, S = 5.2, I = 2.53*10^{11} W/cm^2

obd threshold 954 nm, 63x objective, NA = 0.9   T = 2.61 ns, E$_{th}$ = 6.92 μJ, S = 4.9, I = 2.02*10^{11} W/cm^2

p)

40x, NA 0.8

63x, NA 0.9

959 nm

q)

965 nm

r)

975 nm

s)

1001 nm

t)

40x, NA 0.8

63x, NA 0.9

1025 nm

u)

Figure 11.14 Probability curves for optical breakdown in water produced by slm OPO ns laser pulses of ≈ 2 ns duration for 21 wavelengths ranging from 725 nm to 1025 nm (a) – u)). The pulses were focused through water immersion objectives with two different NAs. Left column: 40 x objective, NA = 0.8, right column: 63 x objective, NA = 0.9.

Figure 11.15 (next 12 pages) Probability for optical breakdown in water induced by OPO fs laser pulses for 48 (a) – vv)) wavelengths ranging from 334 nm to 1085 nm focused through two different water immersion objectives: (left column) 40 x objective, NA = 0.8, (right column) 63 x objective, NA = 0.9.

11.1.6. OPA, 265 fs

40x, NA 0.8   **63x, NA 0.9**

334 nm

a)

347 nm

b)

359.5 nm

c)

373 nm

d)

40x, NA 0.8 **63x, NA 0.9**

389 nm

e)

410 nm

f)

425 nm

g)

441 nm

h)

40x, NA 0.8 **63x, NA 0.9**

456 nm

i)

471 nm

j)

485 nm

k)

498 nm

l)

40x, NA 0.8　　　　　　　　　　　**63x, NA 0.9**

513 nm

Optical Breakdown Threshold 513 nm, 40x objective, NA 0.8

Optical Breakdown Threshold 513 nm, 63x objective, NA 0.9

m)

529 nm

Optical Breakdown Threshold 529 nm, 40x objective, NA 0.8
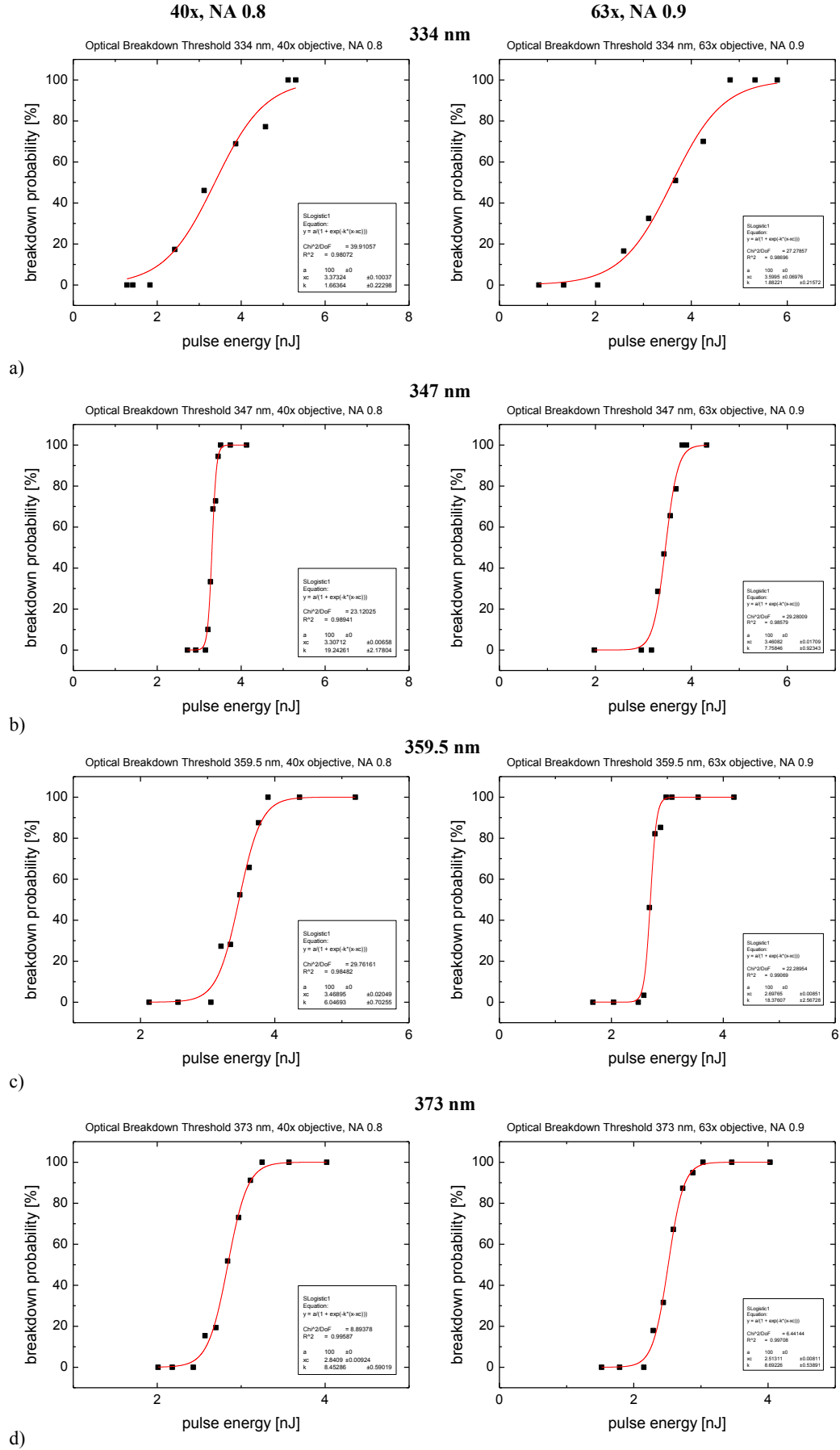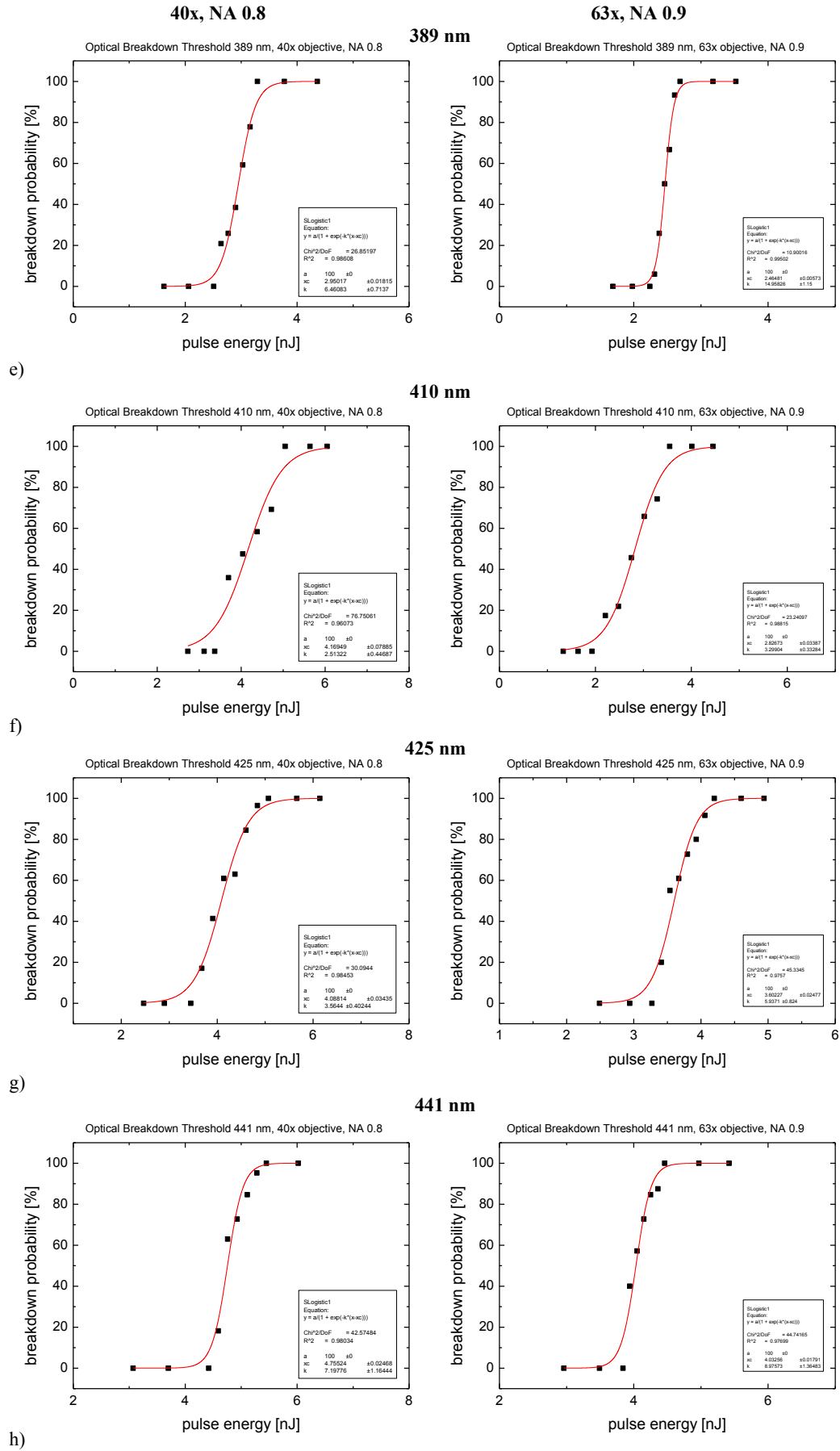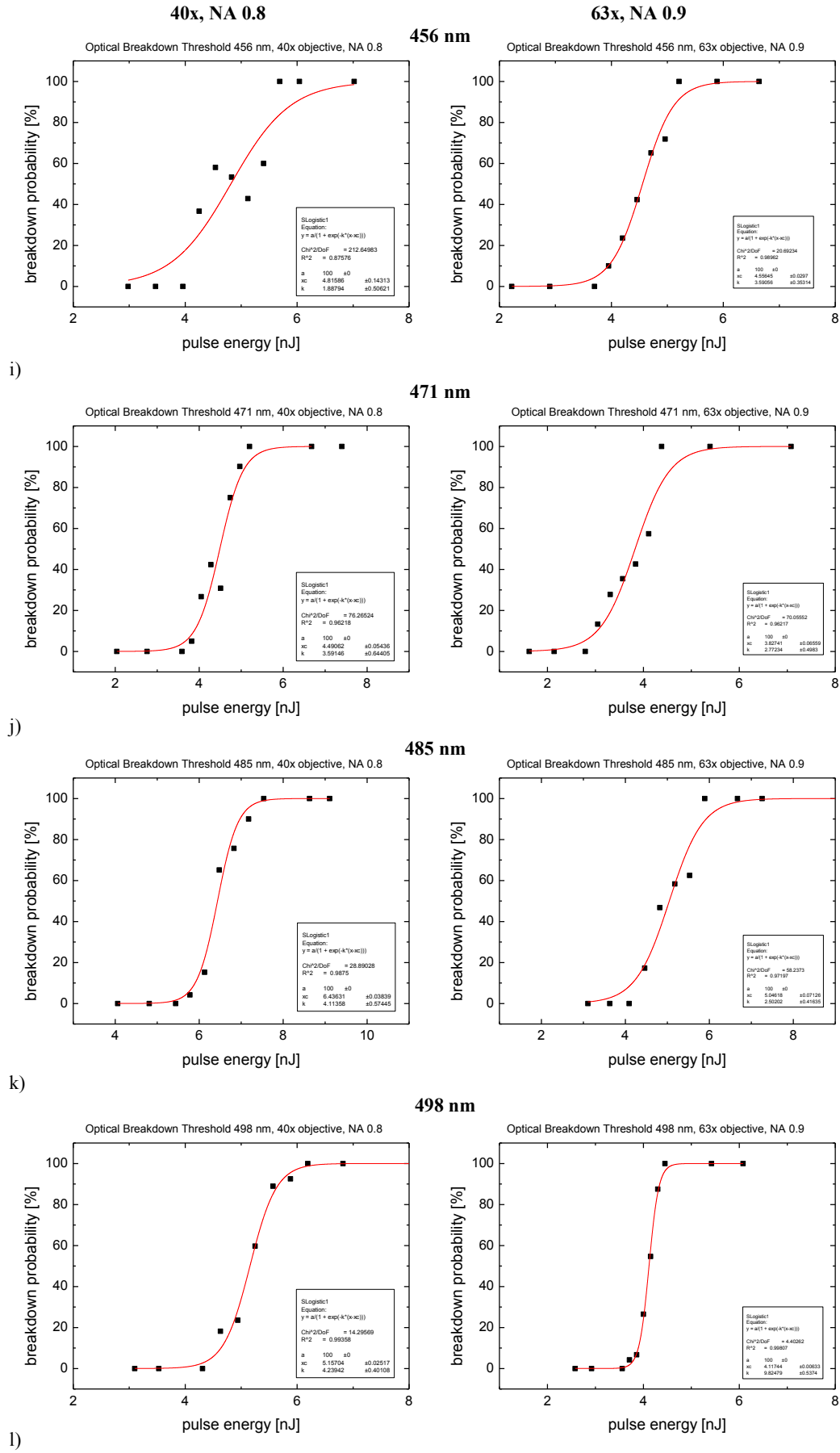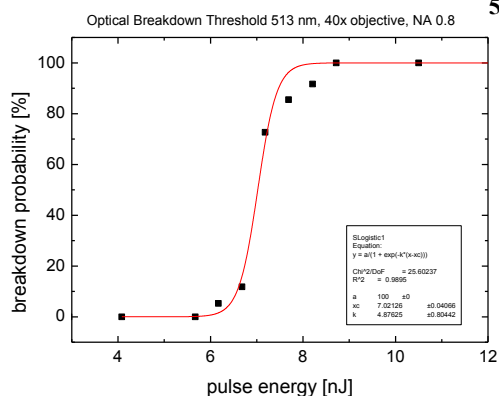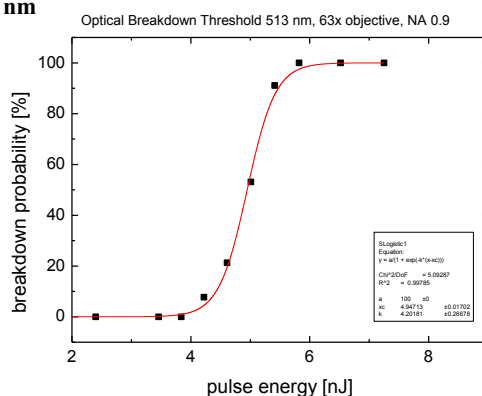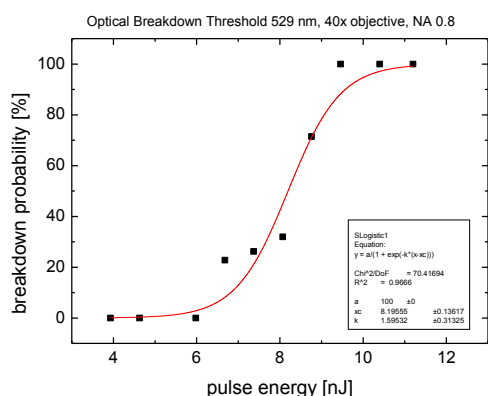
Optical Breakdown Threshold 529 nm, 63x objective, NA 0.9

n)

544 nm

Optical Breakdown Threshold 544 nm, 40x objective, NA 0.8
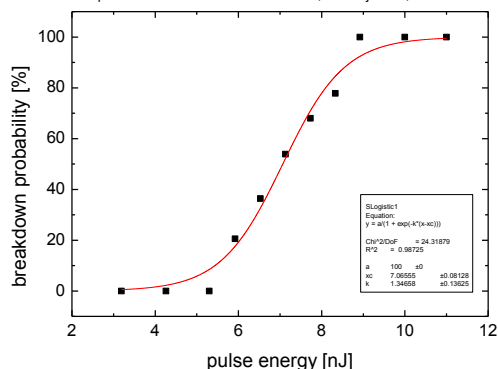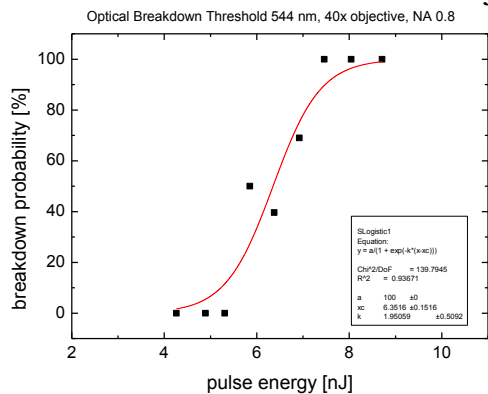
Optical Breakdown Threshold 544 nm, 63x objective, NA 0.9

o)

560 nm

Optical Breakdown Threshold 560 nm, 40x objective, NA 0.8
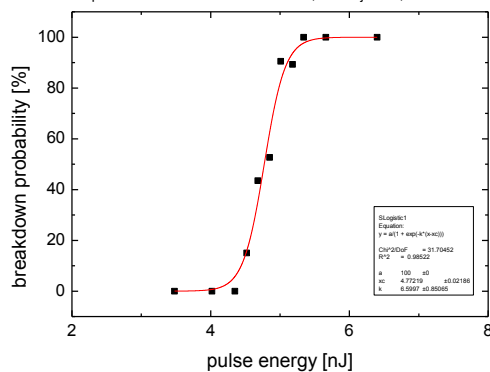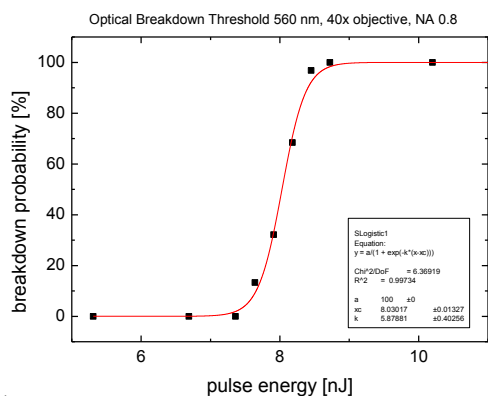
Optical Breakdown Threshold 560 nm, 63x objective, NA 0.9
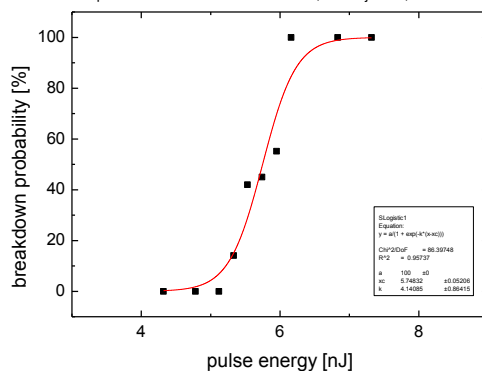
p)
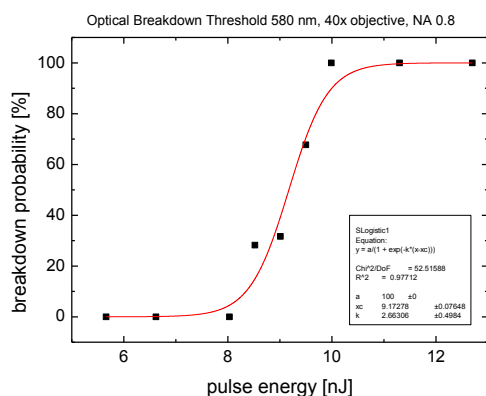
40x, NA 0.8 **63x, NA 0.9**

580 nm
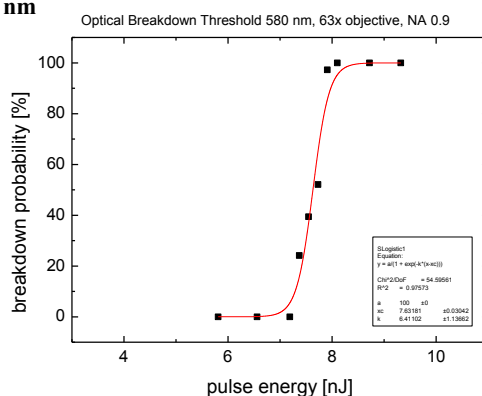
q)

595 nm
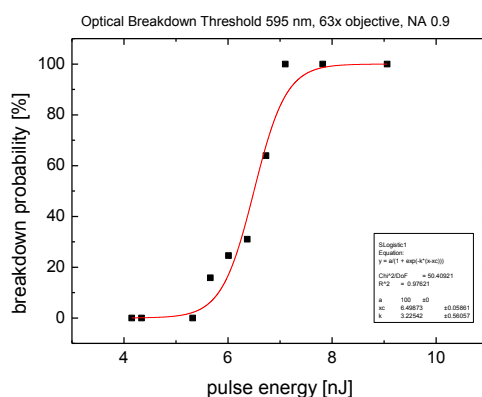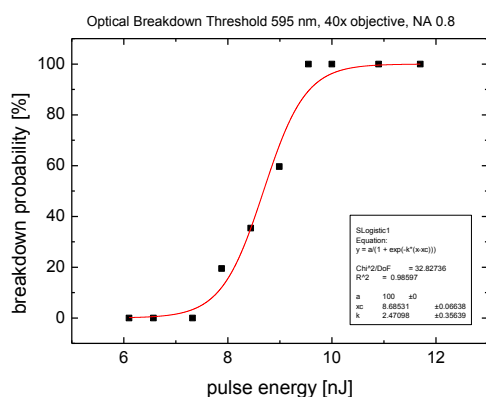
r)

610 nm
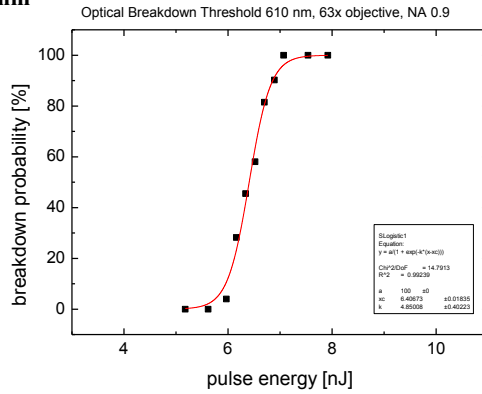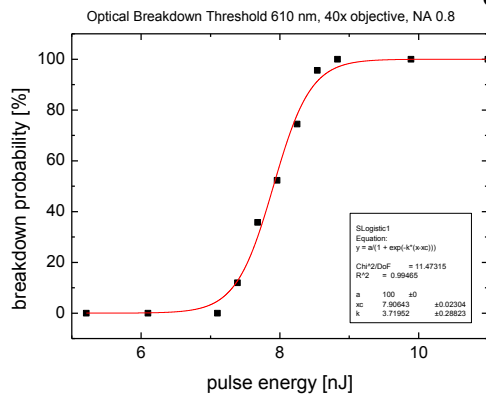
s)

627 nm
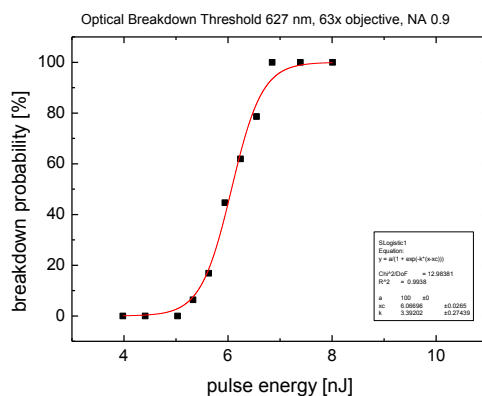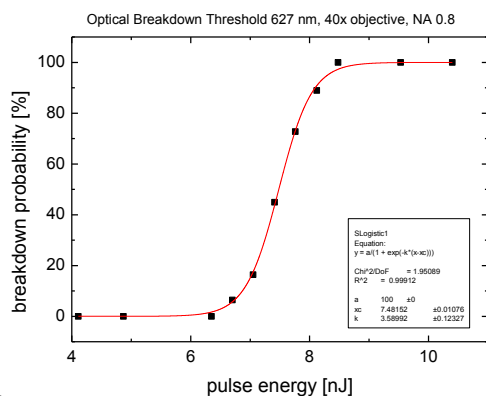
t)

40x, NA 0.8
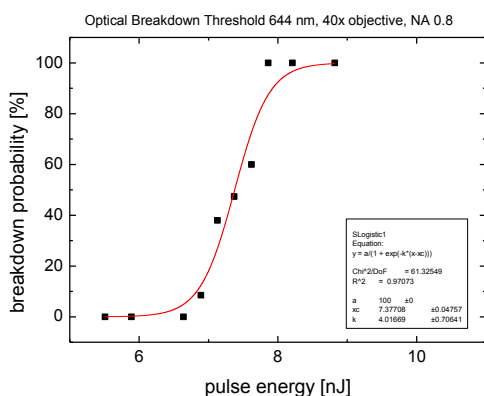
63x, NA 0.9

644 nm
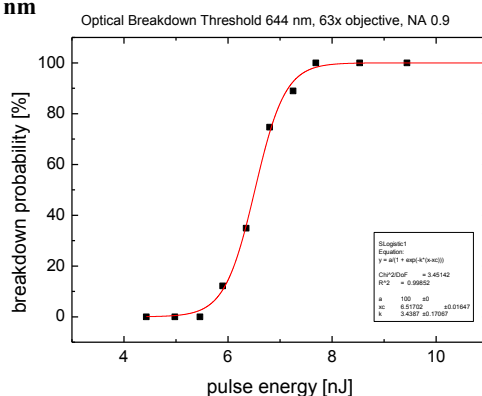
u)

660 nm
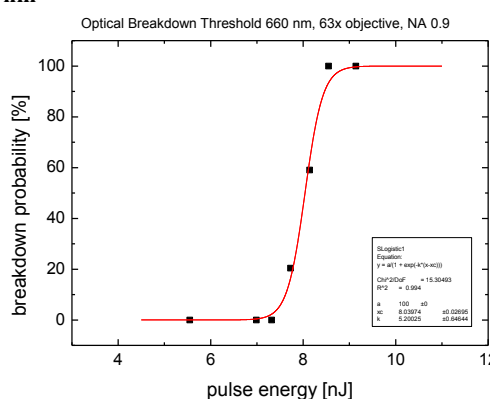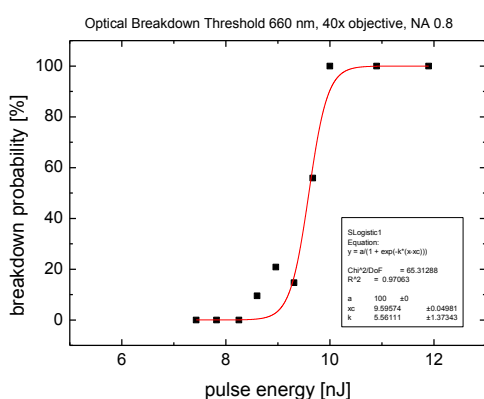
v)

677 nm

w)

708.8 nm

x)

40x, NA 0.8 **63x, NA 0.9**

725 nm

y)

740.2 nm

z)

755

aa)

770 nm

bb)
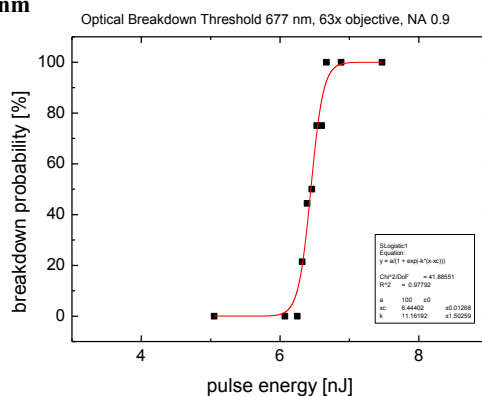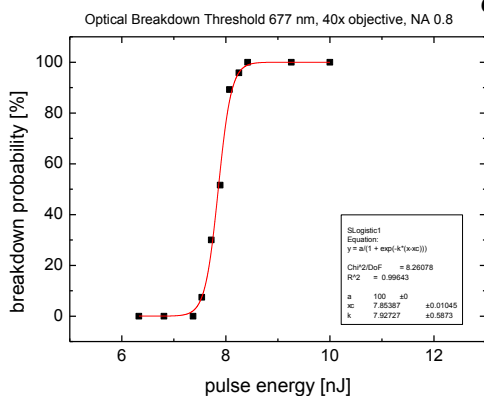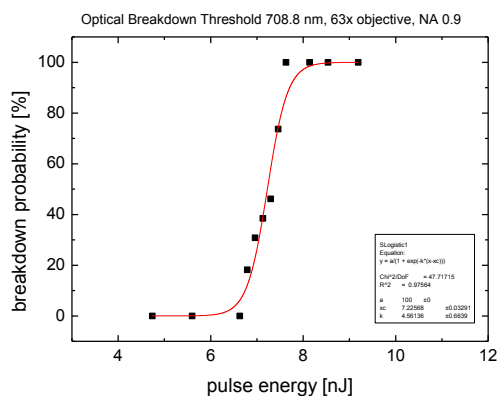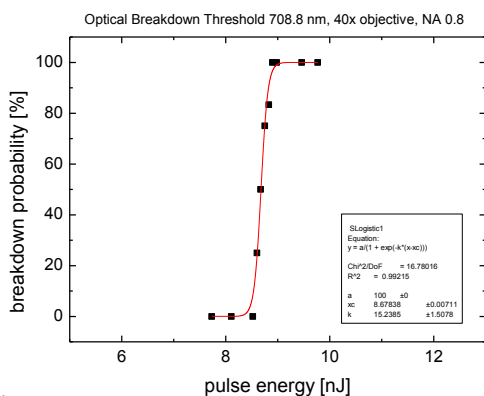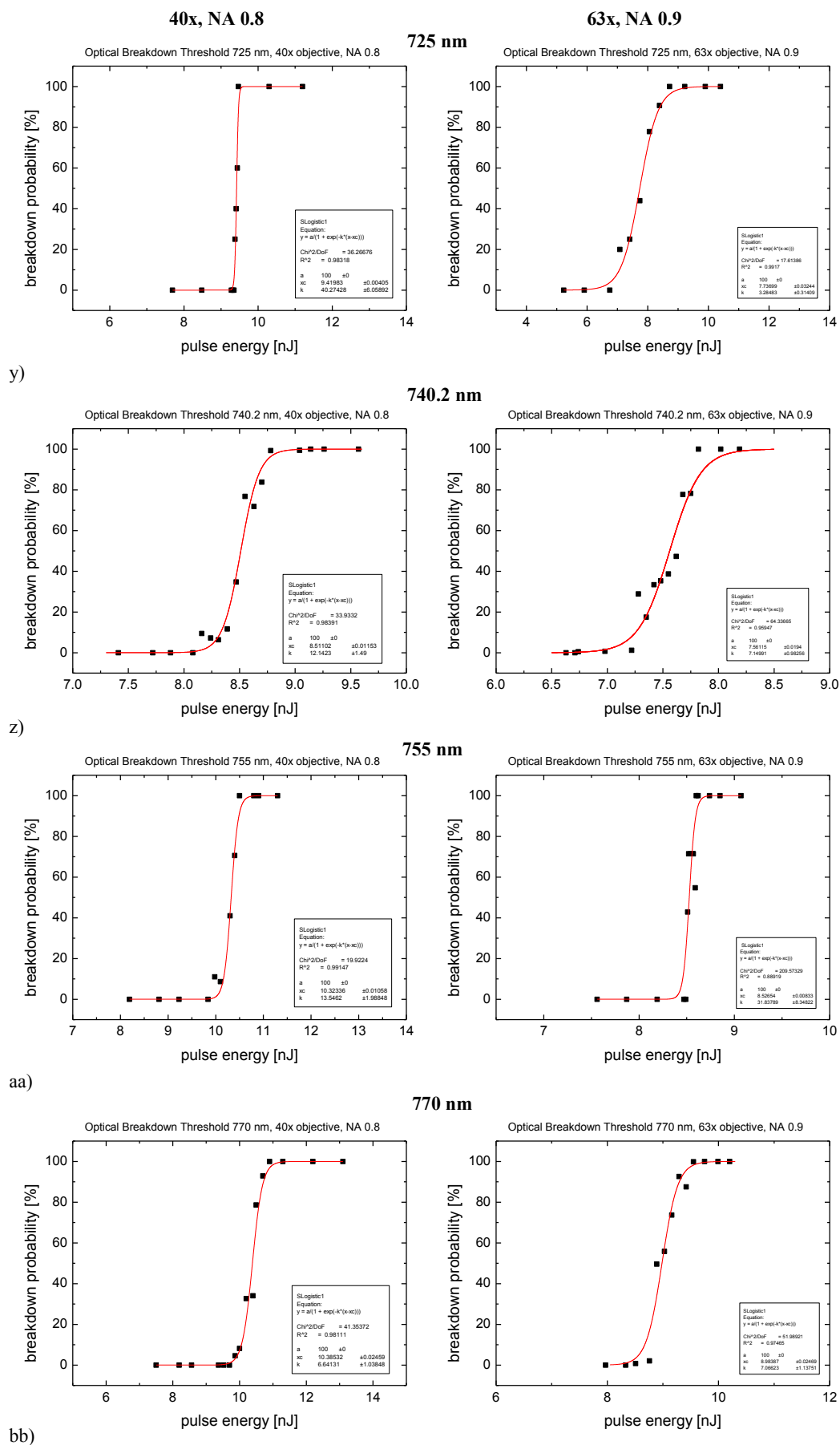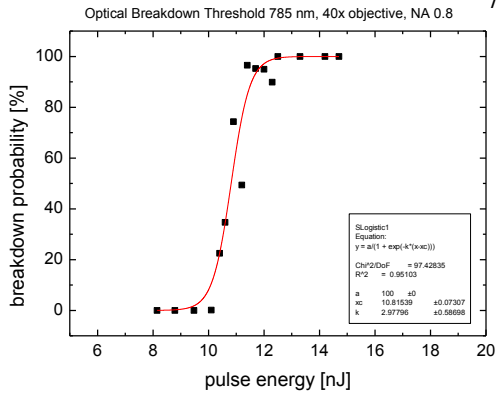
40x, NA 0.8   **63x, NA 0.9**

785 nm
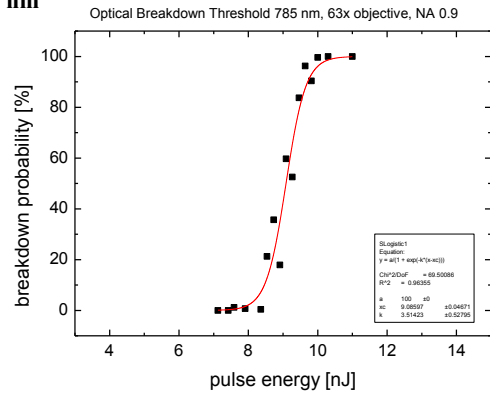
cc)

799 nm
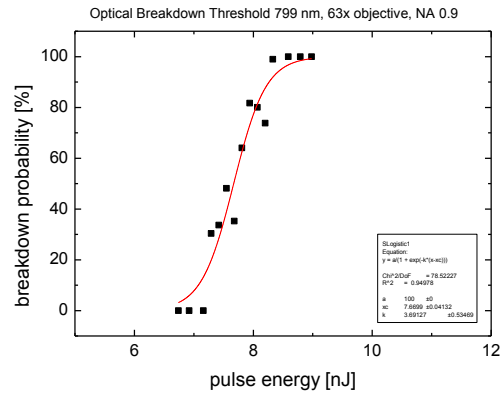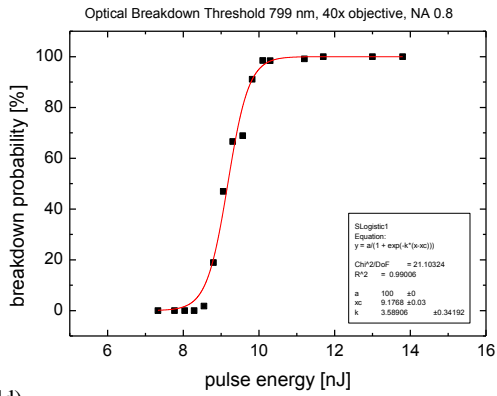
dd)

814 nm
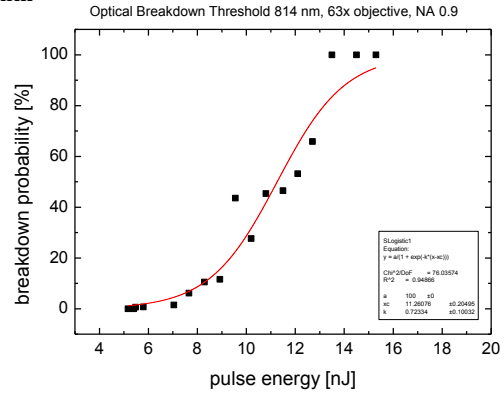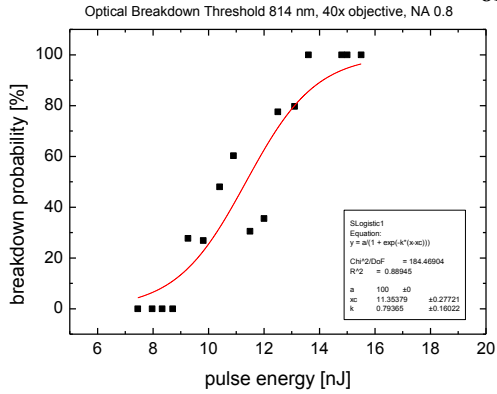
ee)

834.8 nm

ff)
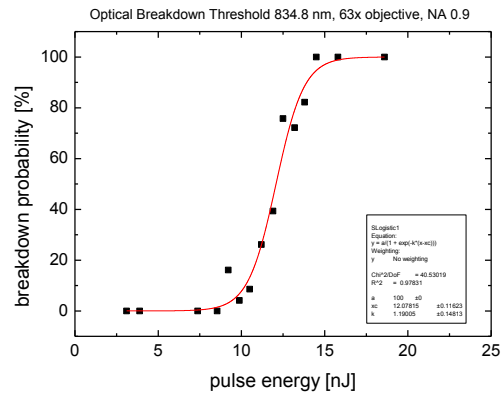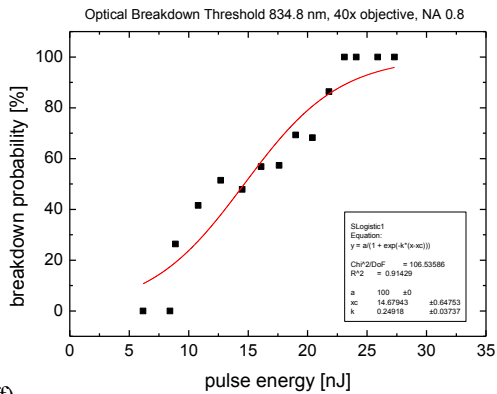
40x, NA 0.8 **63x, NA 0.9**
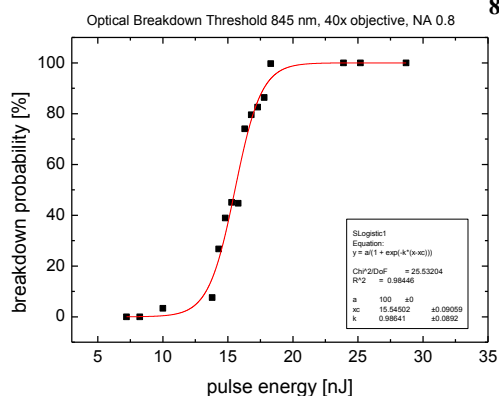
845 nm
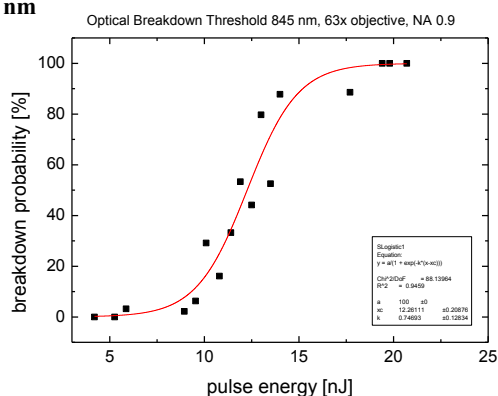
gg)

865 nm
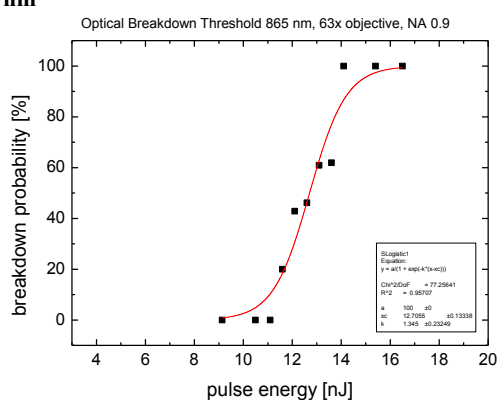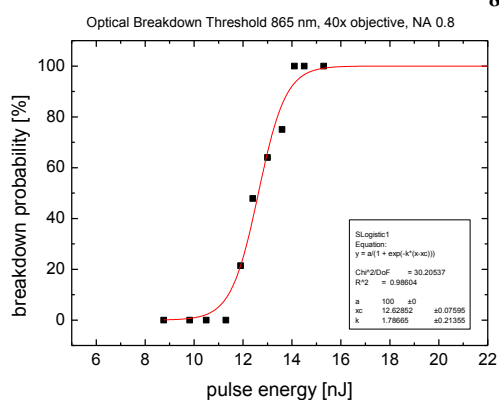
hh)

882.9 nm

ii)

903 nm

jj)

40x, NA 0.8 **63x, NA 0.9**

923.8 nm

Optical Breakdown Threshold 923.8 nm, 40x objective, NA 0.8

Optical Breakdown Threshold 923.8 nm, 63x objective, NA 0.9

kk)

942 nm

Optical Breakdown Threshold 942 nm, 40x objective, NA 0.8

Optical Breakdown Threshold 942 nm, 63x objective, NA 0.9

ll)

956.8 nm

Optical Breakdown Threshold 956.8 nm, 40x objective, NA 0.8

Optical Breakdown Threshold 956.8 nm, 63x objective, NA 0.9

mm)

973 nm

Optical Breakdown Threshold 973 nm, 40x objective, NA 0.8

Optical Breakdown Threshold 973 nm, 63x objective, NA 0.9

nn)

40x, NA 0.8 **63x, NA 0.9**

993 nm

oo)

1005 nm

pp)

1020.5 nm
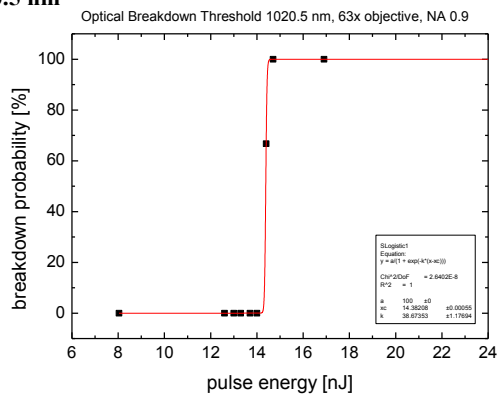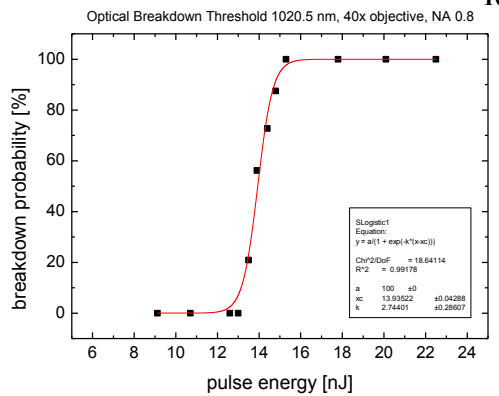
qq)

1035.6 nm

rr)

40x, NA 0.8

63x, NA 0.9

1051 nm

Optical Breakdown Threshold 1051 nm, 40x objective, NA 0.8

Optical Breakdown Threshold 1051 nm, 63x objective, NA 0.9

ss)

1063.4 nm

Optical Breakdown Threshold 1063.4 nm, 40x objective, NA 0.8

Optical Breakdown Threshold 1063.4 nm, 63x objective, NA 0.9

tt)

1072.6 nm

Optical Breakdown Threshold 1072.6 nm, 40x objective, NA 0.8

Optical Breakdown Threshold 1072.6 nm, 63x objective, NA 0.9

uu)

1085 nm

Optical Breakdown Threshold 1085 nm, 40x objective, NA 0.8

Optical Breakdown Threshold 1085 nm, 63x objective, NA 0.9

vv)

Figure 11.15 (previous 12 pages) Probability for optical breakdown in water induced by OPO fs laser pulses for 48 (a) – vv)) wavelengths ranging from 334 nm to 1085 nm focused through two different water immersion objectives: (left column) 40 x objective, NA = 0.8, (right column) 63 x objective, NA = 0.9.

11.2 Plasma photographs

11.2.1. Fixed wavelengths, 315 fs

IR

E = 48.3 nJ, ß = 1.93, l = 1.8 μm   E = 95.2 nJ, ß = 3.81, l = 3.6 μm

E = 164.7 nJ, ß = 6.6, l = 5.1 μm   E = 323.8 nJ, ß = 13.0, l = 6.5 μm

E = 458.6 nJ, ß = 18.4, l = 7.3 μm   E = 570.4 nJ, ß = 22.8, l = 7.6 μm
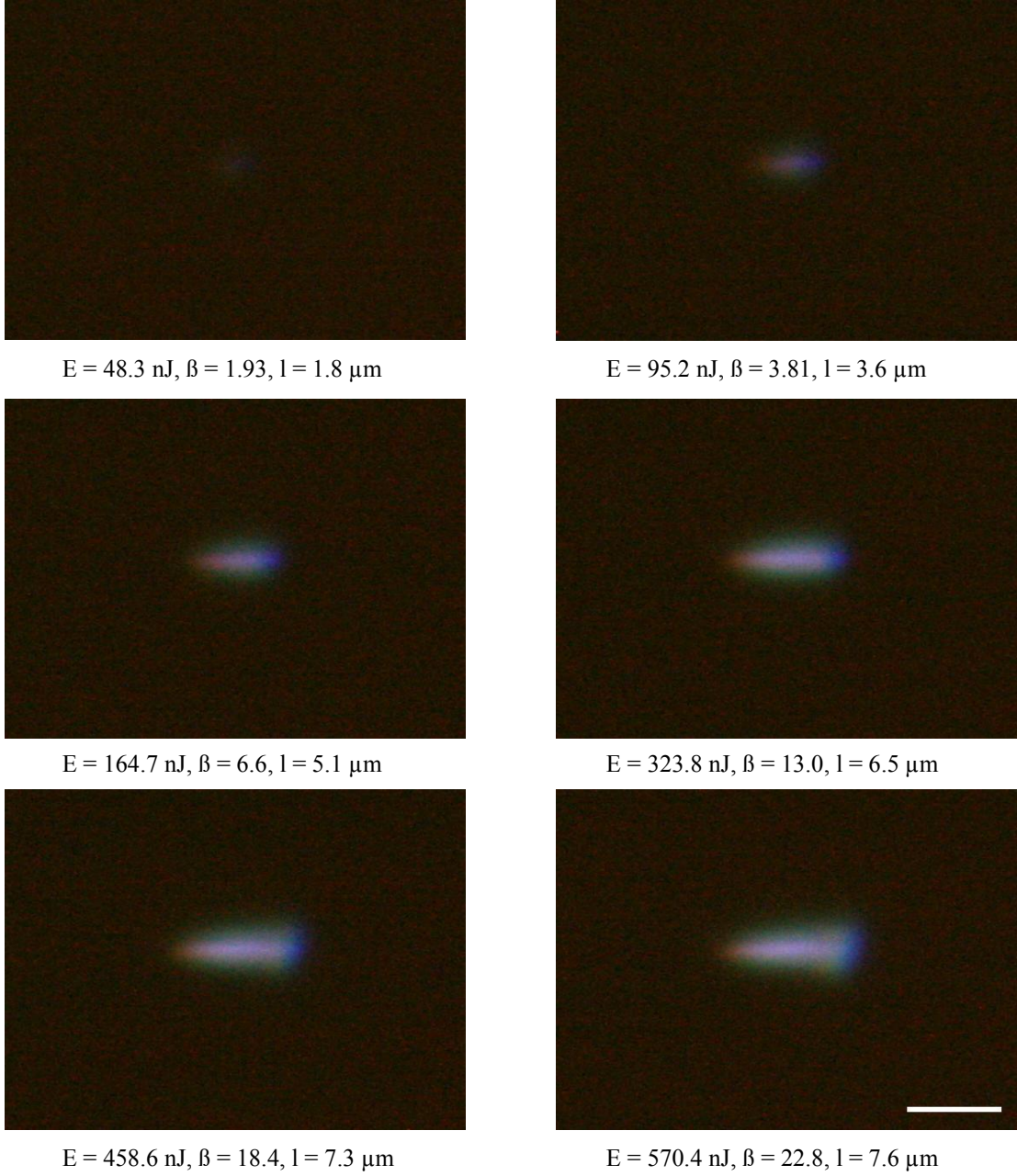
Figure 11.16 Photos of luminescent plasmas produced by 352-fs laser pulses with 1040 nm wavelength focused at NA = 0.8. The values of the pulse energy E, normalized energy $\beta = E/E_{th}$, and plasma length are given below each frame. The laser light is incident from the right. The white bar represents 5 μm. The photographs are integrated over 70 laser pulses, the camera Canon EOS 5D was set to ISO 3200 and auto white balance.

VIS without filter

E = 7.0 nJ, ß = 1.5

E = 10.9 nJ, ß = 2.3

E = 21.2 nJ, ß = 4.5

E = 48.2 nJ, ß = 10.1

E = 78.0 nJ, ß = 16.4

E = 105.0 nJ, ß = 22.1

E = 131.6 nJ, ß = 27.7

E = 149.9 nJ, ß = 31.5

E = 163.0 nJ, ß = 34.3

E = 194.1 nJ, ß = 40.8

E = 201.3 nJ, ß = 42.3

E = 233.7, ß = 49.1
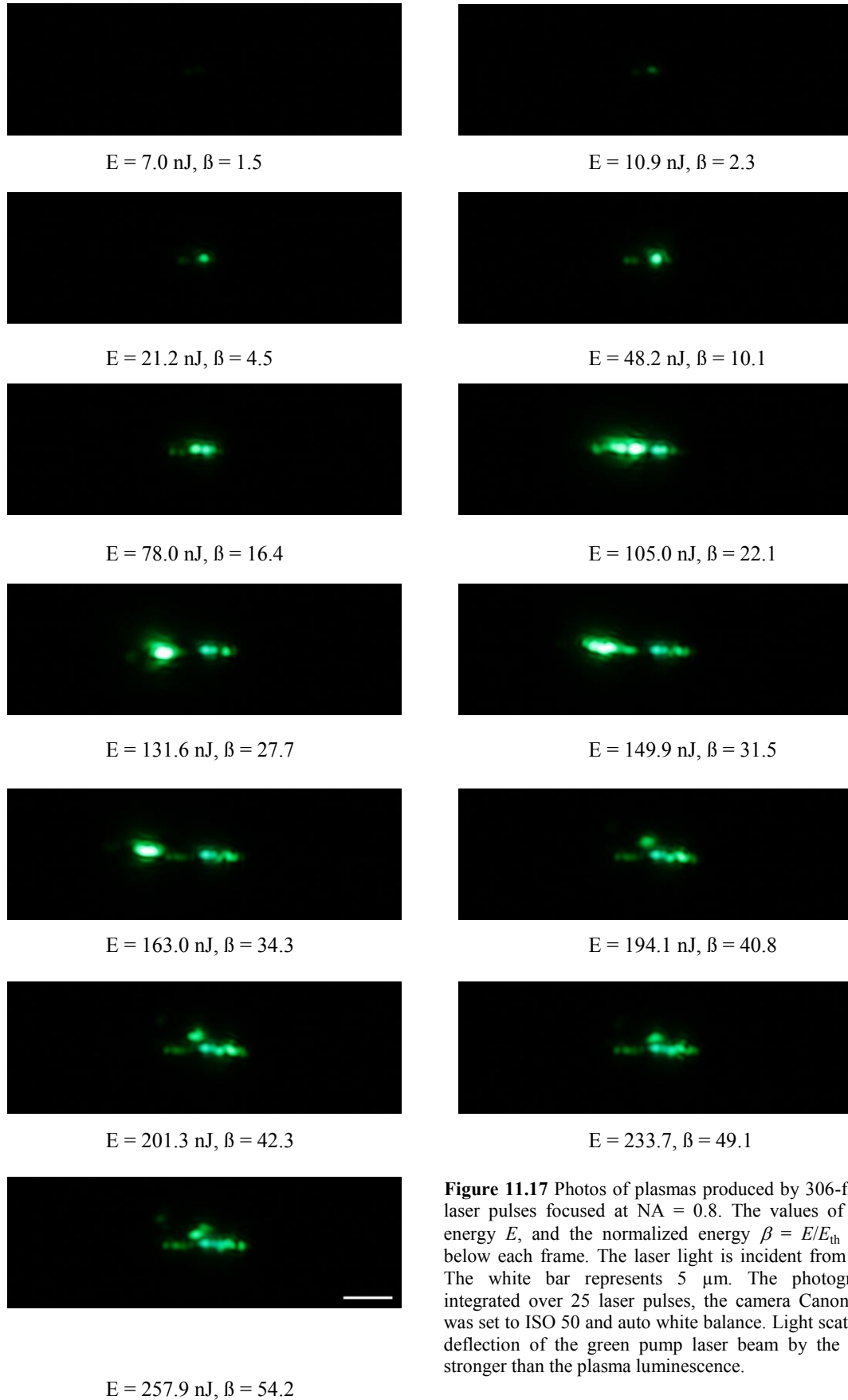
Figure 11.17 Photos of plasmas produced by 306-fs, 520-nm laser pulses focused at NA = 0.8. The values of the pulse energy E, and the normalized energy $\beta = E/E_{th}$ are given below each frame. The laser light is incident from the right. The white bar represents 5 μm. The photographs are integrated over 25 laser pulses, the camera Canon EOS 5D was set to ISO 50 and auto white balance. Light scattering and deflection of the green pump laser beam by the plasma is stronger than the plasma luminescence.

E = 257.9 nJ, ß = 54.2

VIS with filter

E = 12.1 nJ, ß = 2.5, l = 0.70 µm

E = 16.7 nJ, ß = 3.5, l = 0.92 µm

E = 25.2 nJ, ß = 5.3, l = 1.14 µm

E = 34.2 nJ, ß = 7.2, l = 1.19 µm

E = 52.1 nJ, ß = 10.9, l = 1.32 µm

E = 76.8 nJ, ß = 16.1, l = 1.9 µm

E = 104.3 nJ, ß = 21.9, l = 1.67 µm

E = 133.6 nJ, ß = 28.1, l = 2.11 µm

E = 176.4 nJ, ß = 37.0, l = 2.24 µm

E = 239.5 nJ, ß = 50.3, l = 2.68 µm

E = 291.7 nJ, ß = 61.3, l = 3.03 µm
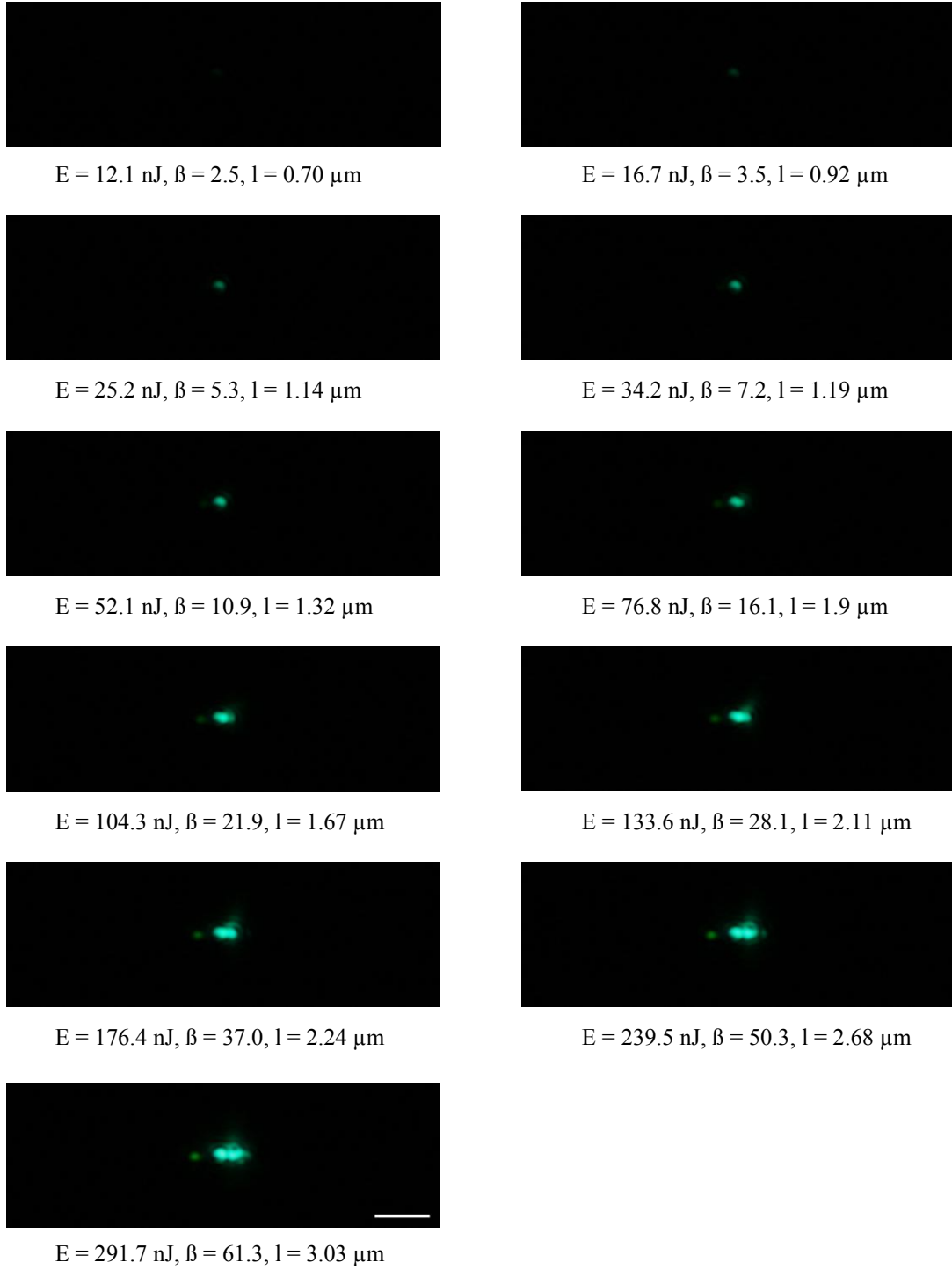
Figure 11.18 Photos of luminescent plasmas produced by 306-fs laser pulses with 520 nm wavelength focused at NA = 0.8. The values of the pulse energy E, normalized energy $\beta = E/E_{th}$, and plasma length are given below each frame. The laser light is incident from the right. The white bar represents 5 µm. The photographs are integrated over 25 laser pulses, the camera Canon EOS 5D was set to ISO 400 and auto white balance. We used a dielectric blocking filter for the laser wavelength to eliminate scattered probe laser light.

UV

E = 11.1 nJ, ß = 3.1, l = 1.0 µm

E = 22.2 nJ, ß = 6.1, l = 2.2 µm

E = 44.0 nJ, ß = 12.1, l = 3.8 µm

E = 60.3 nJ, ß = 16.6, l = 4.5µm

E = 76.5 nJ, ß = 21.0, l = 4,8 µm
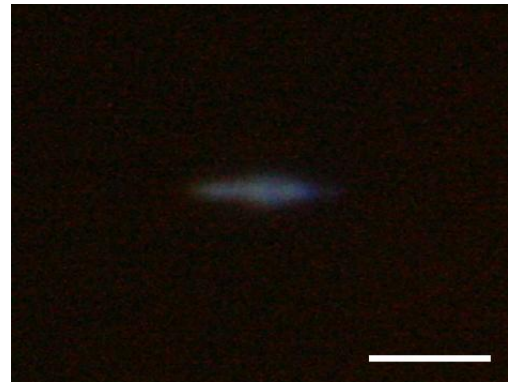
E = 98.1 nJ, ß = 27.0, l = 5.2 µm

Figure 11.19 Photos of luminescent plasmas produced by 280-fs laser pulses with 347 nm wavelength focused at NA = 0.8. The values of the pulse energy E, normalized energy $\beta = E/E_{th}$, and plasma length are given below each frame. The laser light is incident from the right. The white bar represents 5 µm. The photographs are integrated over 70 laser pulses, the camera Canon EOS 5D was set to ISO 3200 and auto white balance.
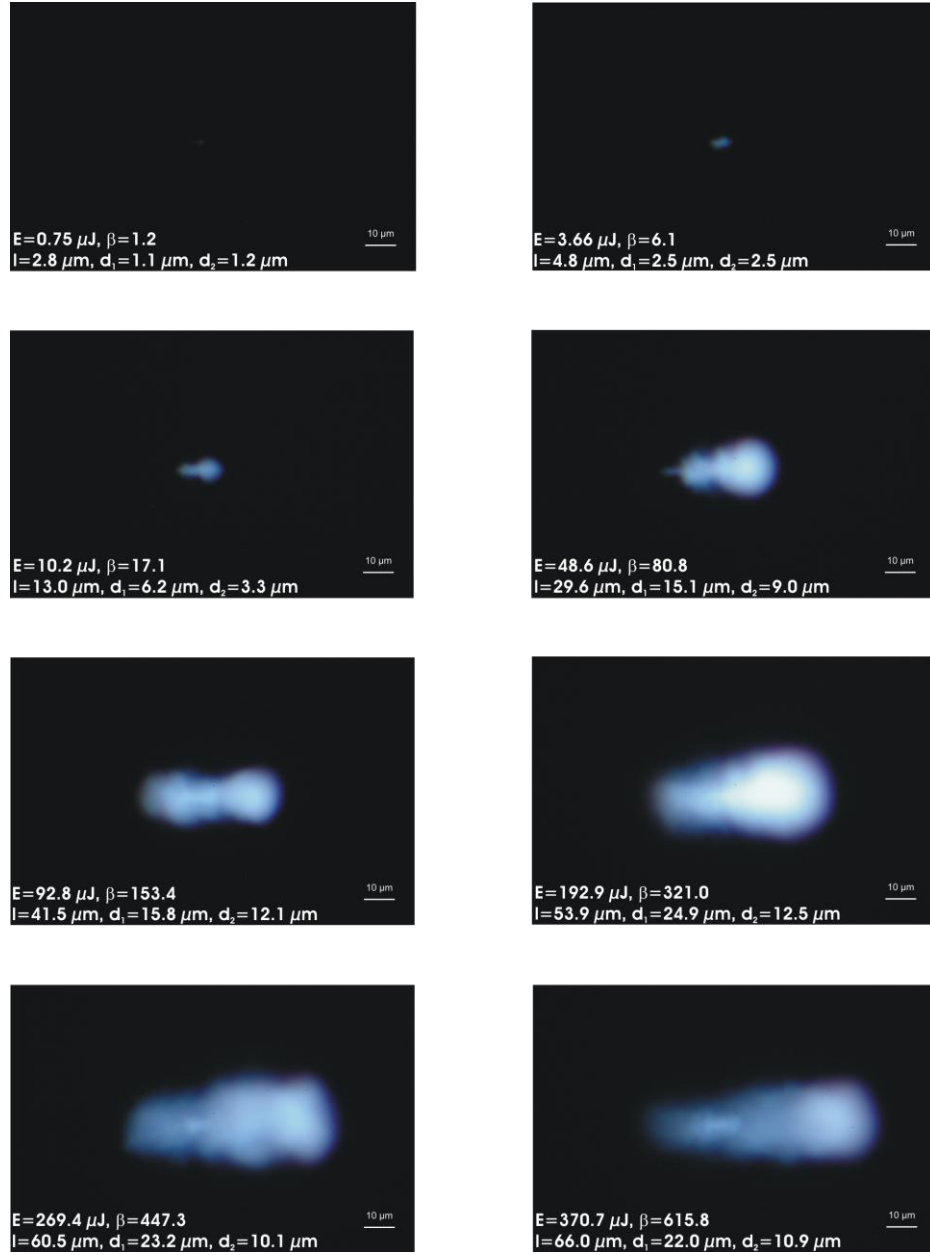
11.2.2. Fixed wavelengths, 6-11 ns

IR, unseeded

Figure 11.20 Photos of luminescent plasmas produced by unseeded 11-ns laser pulses with 1064 nm wavelength focused at NA = 0.8. The focal volume is imaged with 175x magnification. The values of the pulse energy, the plasma length and diameters are indicated on each frame. The light is incident from the right.

IR, seeded

Figure 11.21 Photos of luminescent plasmas produced by seeded 11-ns laser pulses with 1064 nm wavelength focused at NA = 0.8. The values of the pulse energy, the plasma length and diameters are indicated on each frame. The light is incident from the right.

VIS, unseeded, with filter
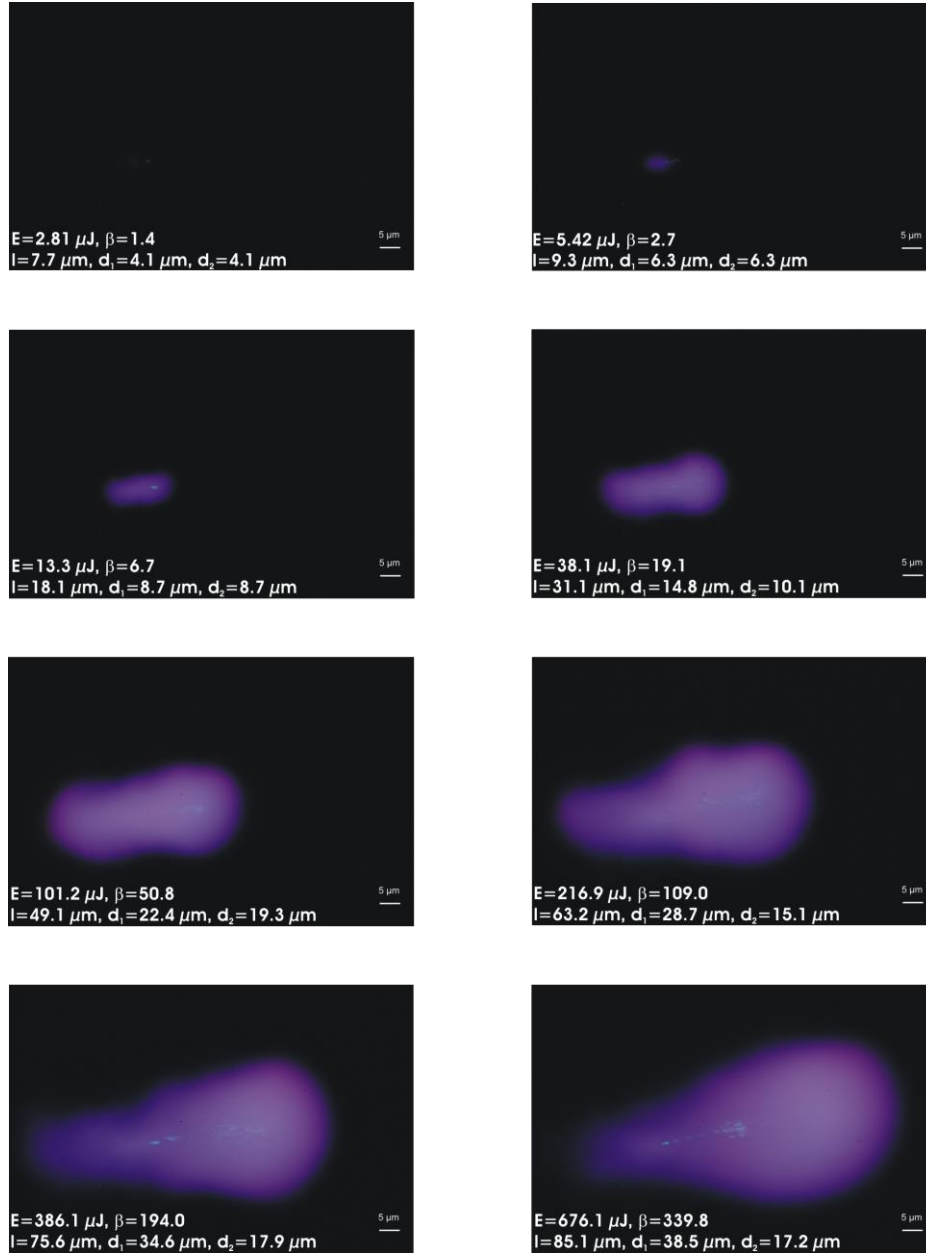
Figure 11.22 Photos of luminescent plasmas produced by unseeded 8.8-ns laser pulses with 532 nm wavelength focused at NA = 0.8. A dichroic mirror in front of the digital camera was used to block the scattered green laser light. Therefore the plasma luminescence appears purple. The values of the absolute pulse energy E, normalized energy $\beta = E/E_{th}$, plasma length and diameter are indicated on each frame. The laser light is incident from the right. The white bar represents 5 μm.

VIS, seeded, bubble range with filter
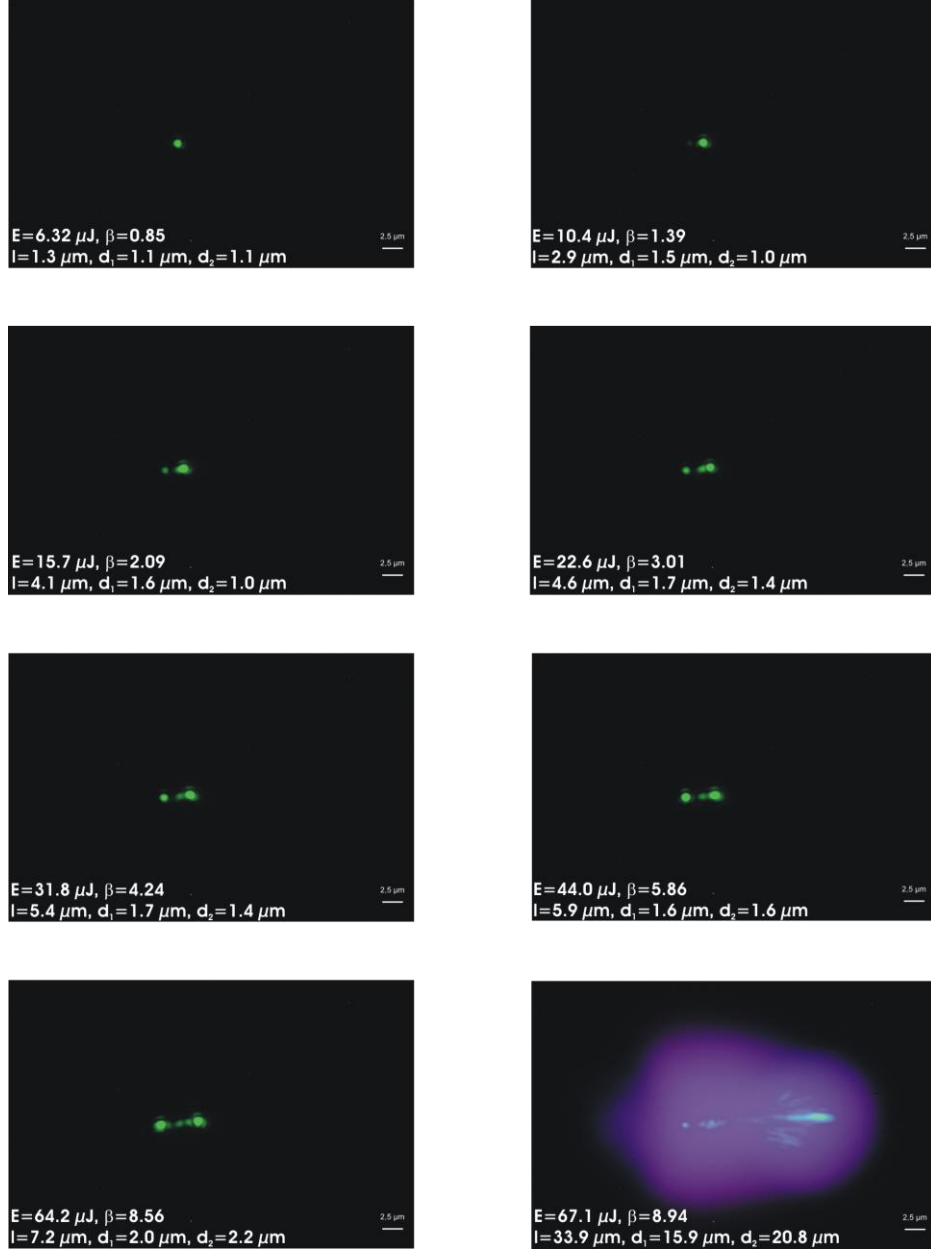
Figure 11.23 Photos of plasmas produced by seeded 8.8-ns laser pulses with 532 nm wavelength focused at NA = 0.8. The values of the absolute pulse energy E, normalized energy $\beta = E/E_{th}$, plasma length and diameter are indicated on each frame. The laser light is incident from the right. The white bar represents 2.5 μm.

VIS, seeded, BPL range with filter
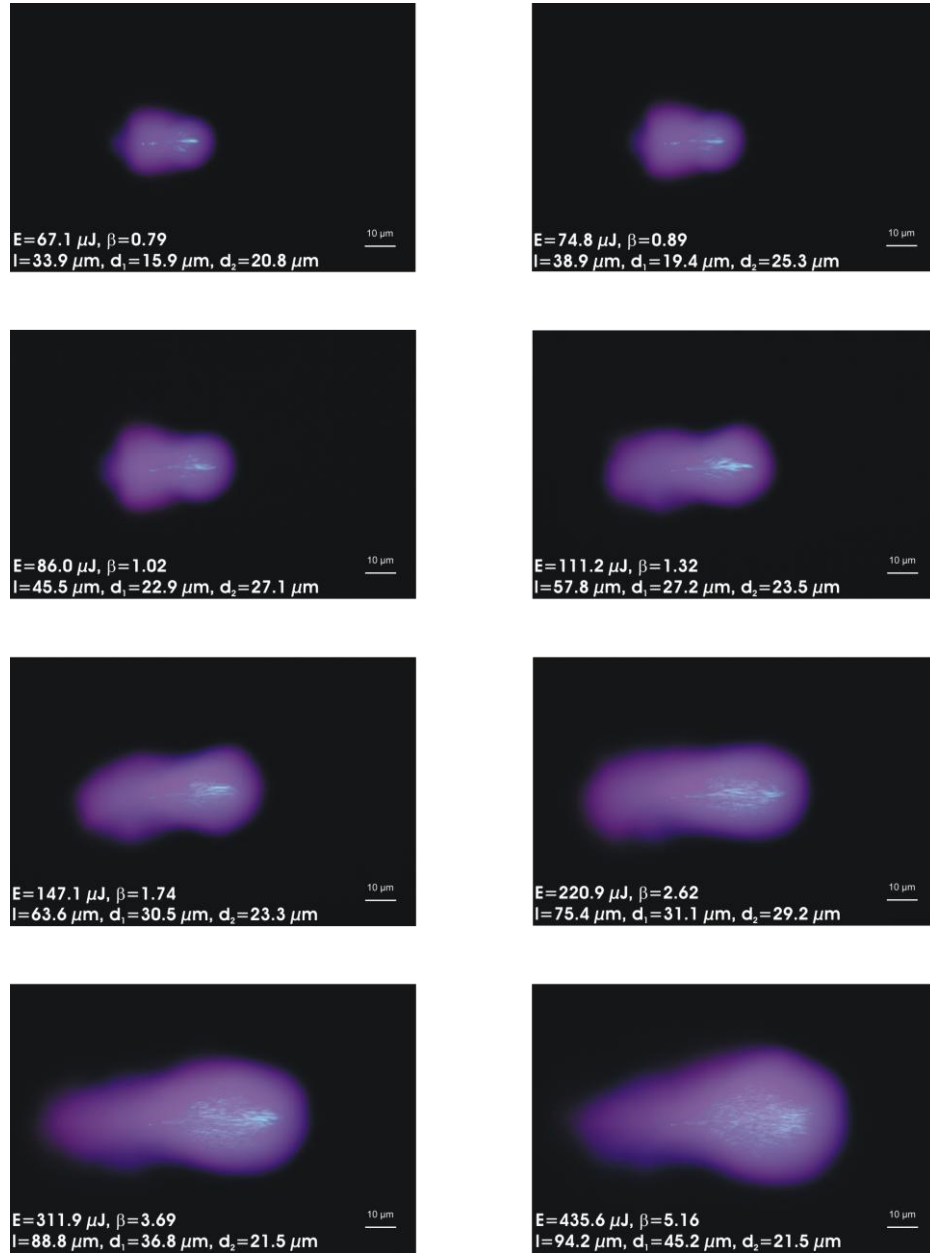
Figure 11.24 Photos of the bright luminescent plasmas produced by seeded 8.8-ns laser pulses with 532 nm wavelength focused at NA = 0.8. A dichroic mirror in front of the digital camera was used to block the scattered green laser light. Therefore the plasma luminescence appears purple. The values of the absolute pulse energy E, normalized energy $\beta = E/E_{th}$, plasma length and diameter are indicated on each frame. The laser light is incident from the right. The white bar represents 10 μm.

UV, unseeded

Figure 11.25 Photos of luminescent plasmas produced by unseeded 6.8-ns laser pulses with 355 nm wavelength focused at NA = 0.8. The values of the pulse energy E, normalized energy $\beta = E/E_{\text{th}}$, plasma length and diameter are given on each frame. The laser light is incident from the right. The white bar represents 10 μm.

UV, seeded, bubble range
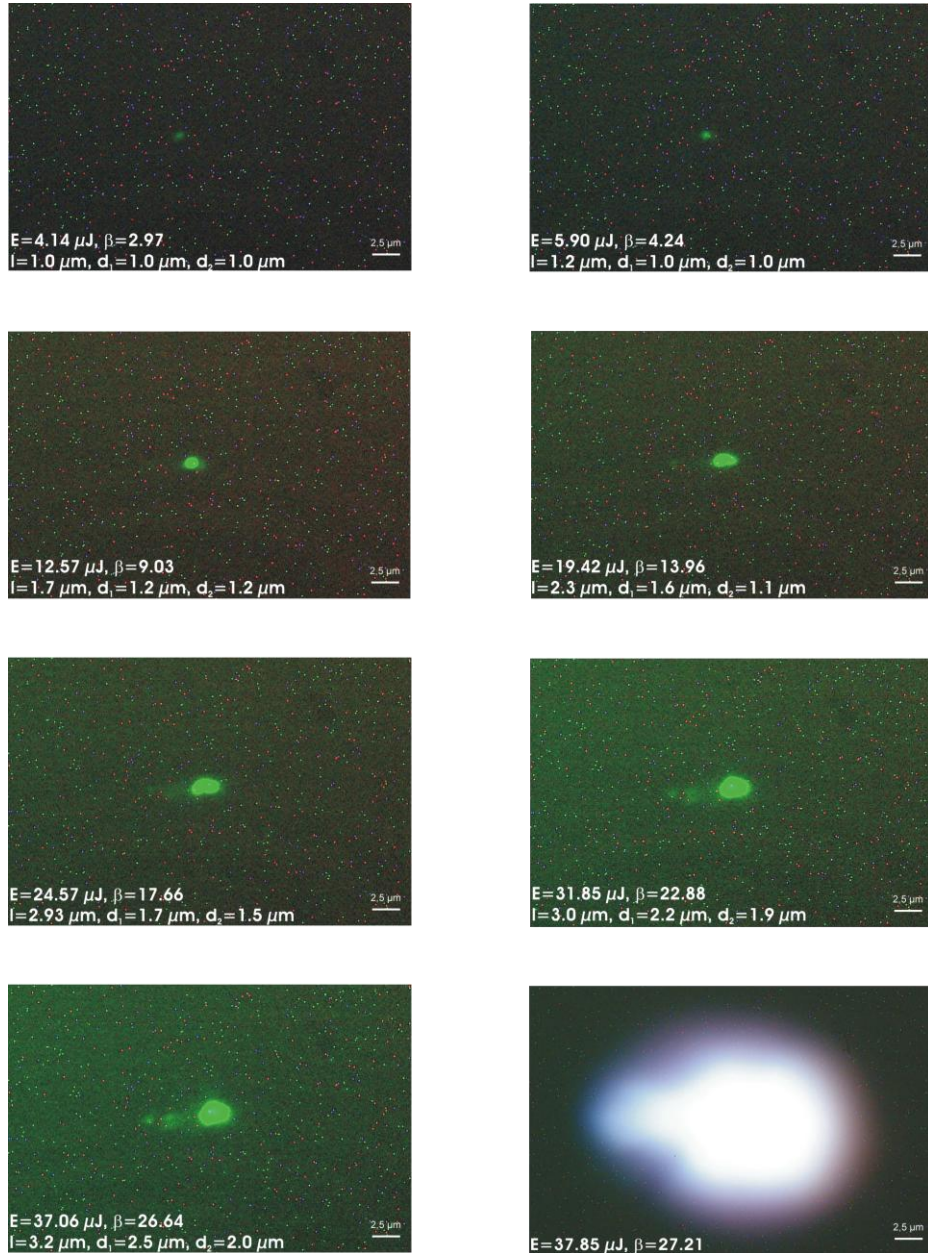
Figure 11.26 Photos of plasmas produced by seeded 6.8-ns laser pulses with 355 nm wavelength focused at NA = 0.8. All images are integrated over 100 laser exposures. The values of the pulse energy E, normalized energy $\beta = E/E_{th}$, plasma length and diameter are given on each frame. The laser light is incident from the right. The white bar represents 2.5 µm.

UV, seeded, BPL range
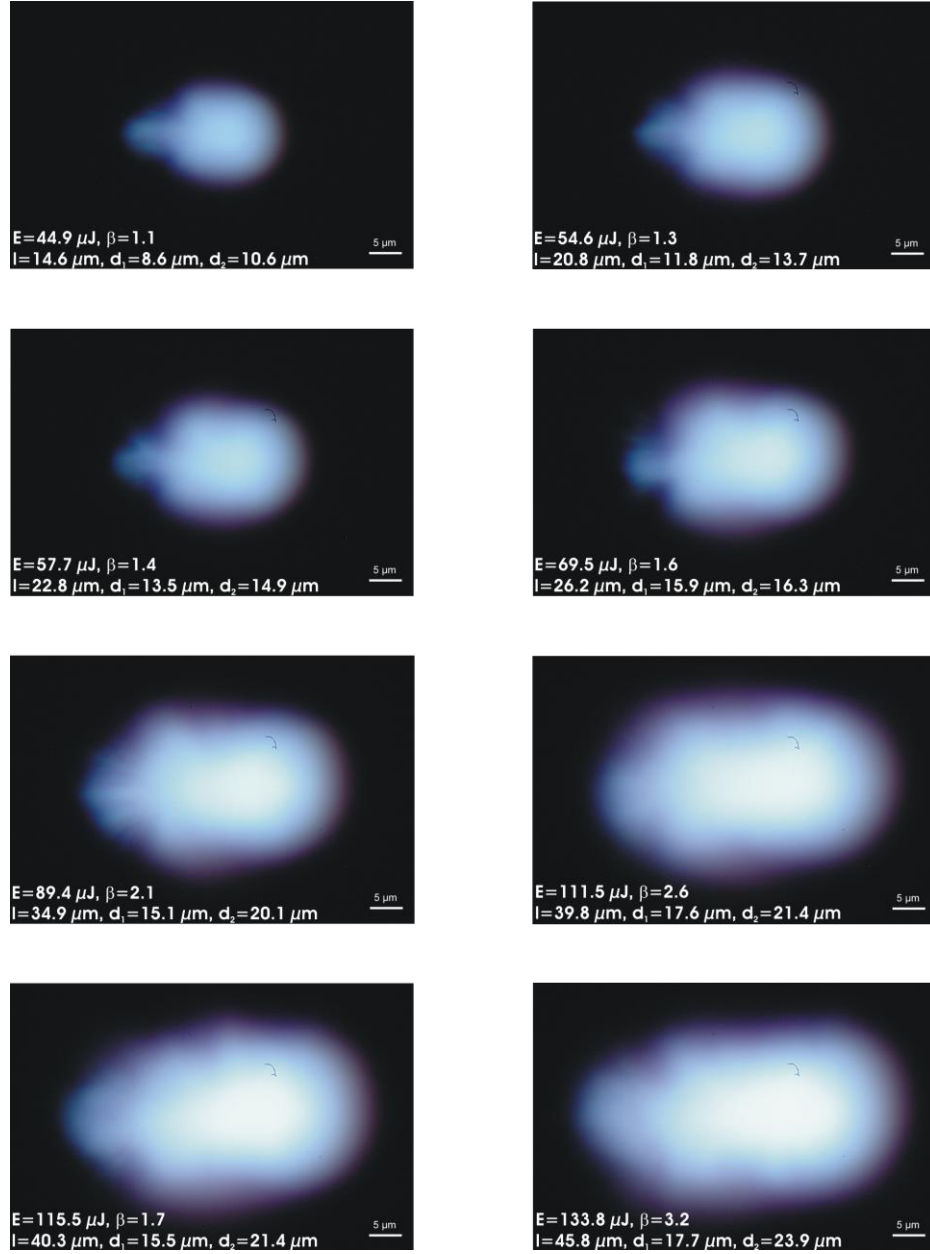
Figure 11.27 Single exposure photographs of the bright luminescent plasmas produced by seeded 6.8-ns laser pulses with 355 nm wavelength focused at NA = 0.8. The values of the pulse energy E, normalized energy $\beta = E/E_{th}$, plasma length and diameter are given on each frame. The laser light is incident from the right. The white bar represents 5 µm.

11.2.3. Microchip lasers of fixed wavelengths, 0.5 -1.0 ns

Crylas laser, 1 ns, IR, VIS, and UV wavelengths
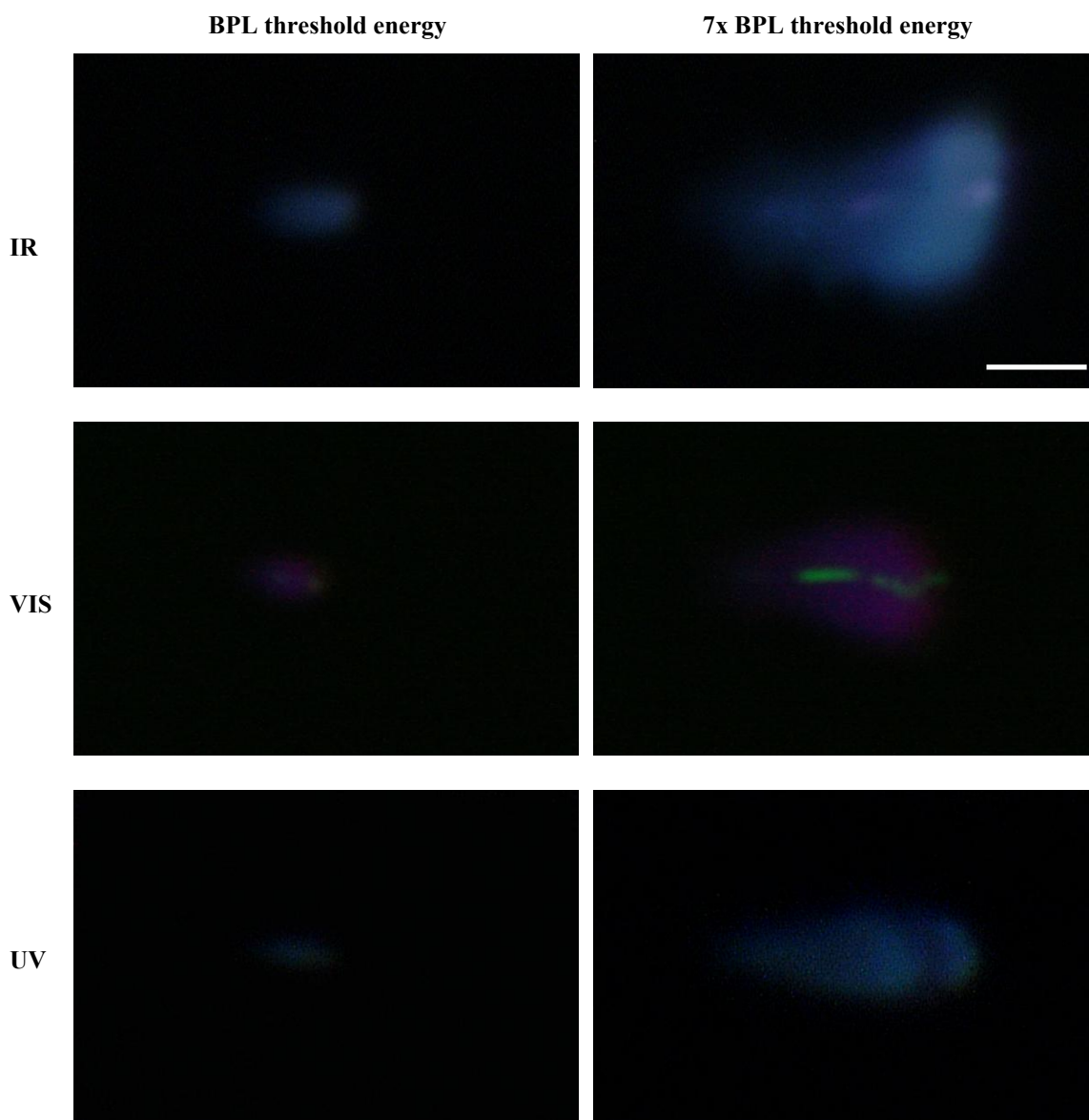
Figure 11.28 Single exposure photographs of the bright luminescent plasmas produced by ns laser pulses with IR, VIS, and UV wavelengths focused at NA = 0.8. The photographs in the left column portray the plasma size at the threshold for plasma luminescence, the photographs in the right column show the plasma size at approximately 7 times BPL threshold energy. The laser light is incident from the right. The white bar represents 5 μm.

Powerchip laser, 0.55 ns, UV wavelength
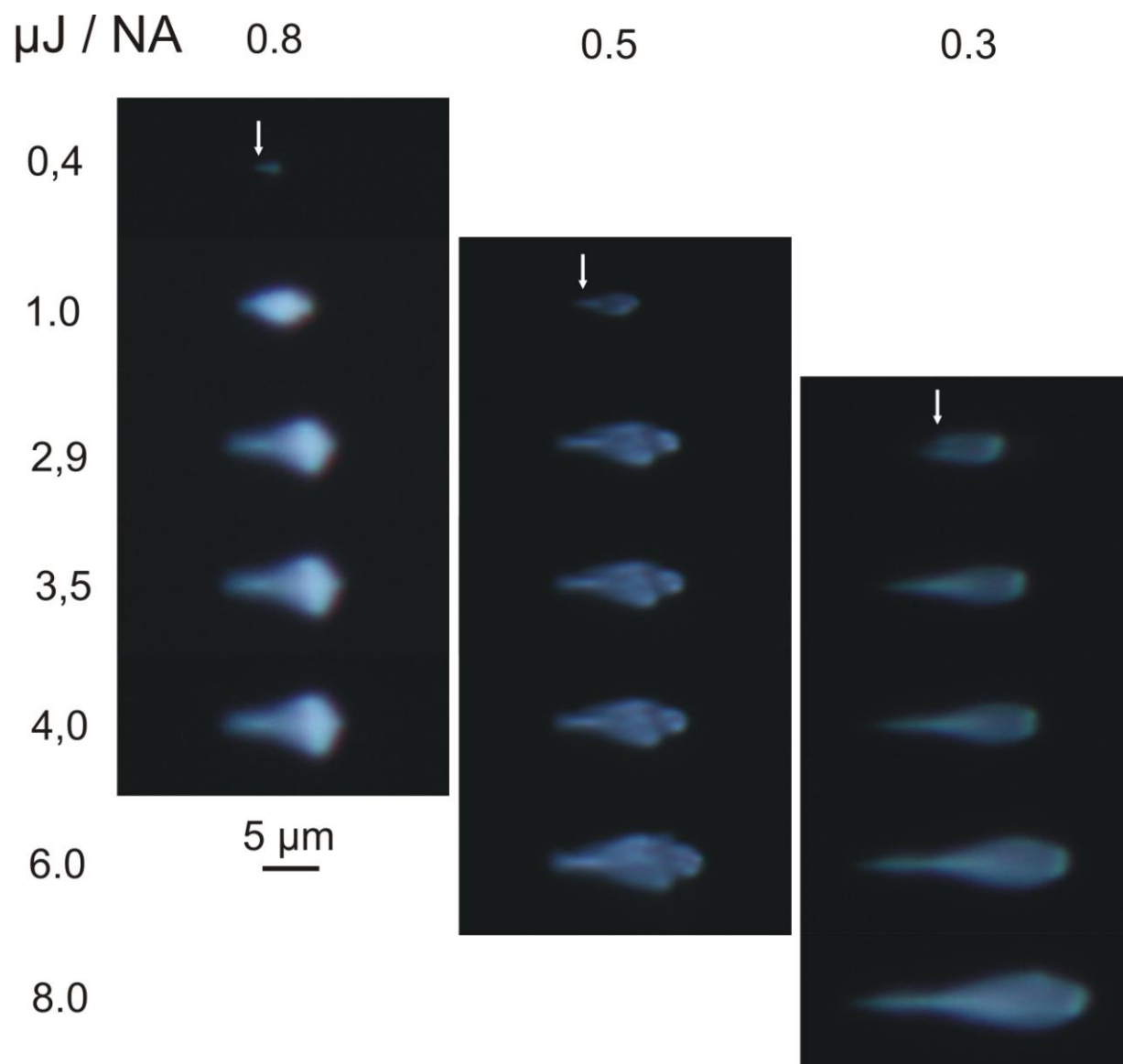
Figure 11.29 Photographs of the plasma luminescence produced when 0.55-ns laser pulses of 355 nm wavelength are focused through the 40x objective (NA = 0.8), 20x objective (NA = 0.5), and 10x objective (NA = 0.3). The rows correspond to equal energy for the different focusing geometries. The photographs were integrated over 10 laser pulses. The laser light is incident from the right. The white arrows mark the position of the beam waist of the focused laser pulse.

Note the nonlinear beam propagation effects leading to a filament reaching beyond the laser beam waist. This filament is exclusively due to plasma defocusing because the laser power remains well below the self-focusing threshold.

11.3 Plasma length and volume

11.3.1. Fixed wavelengths, 280-350 fs
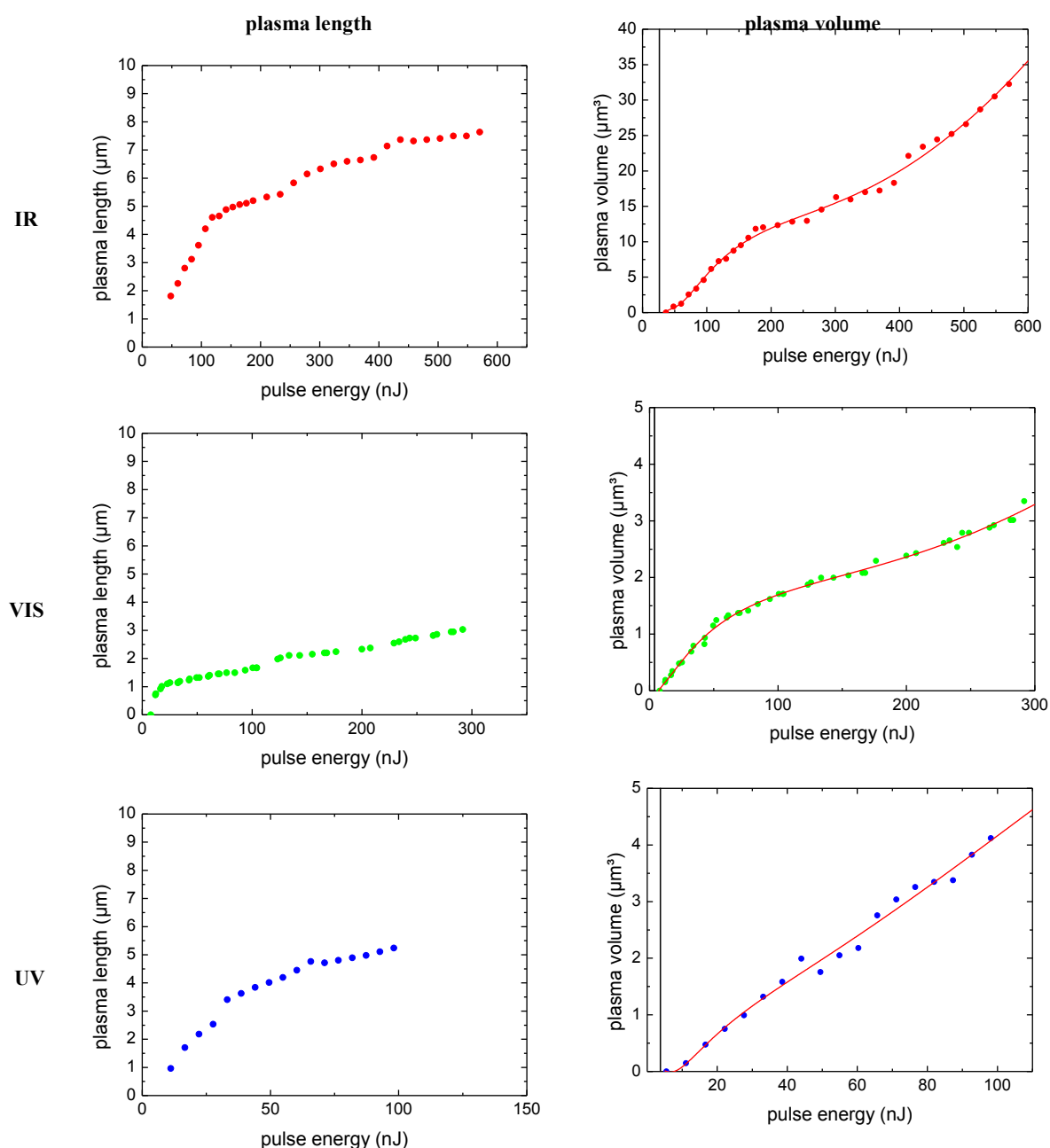
Figure 11.30: Length and volume of luminescent plasmas produced by 352-fs laser pulses with 1040 nm wavelength, 306-fs laser pulses with 520 nm wavelength, and 280-fs laser pulses with 347 nm wavelength focused through a 40x water immersion objective (NA = 0.8). The plasma size was evaluated from the photos by measuring the size of the bright luminescence of the plasma. The measured plasma volume data were fitted by a function V(E) to be able to interpolate the plasma volume for any specific laser pulse energy E using the computer program TableCurve2D.

11.3.2. Fixed wavelengths, 6-11 ns
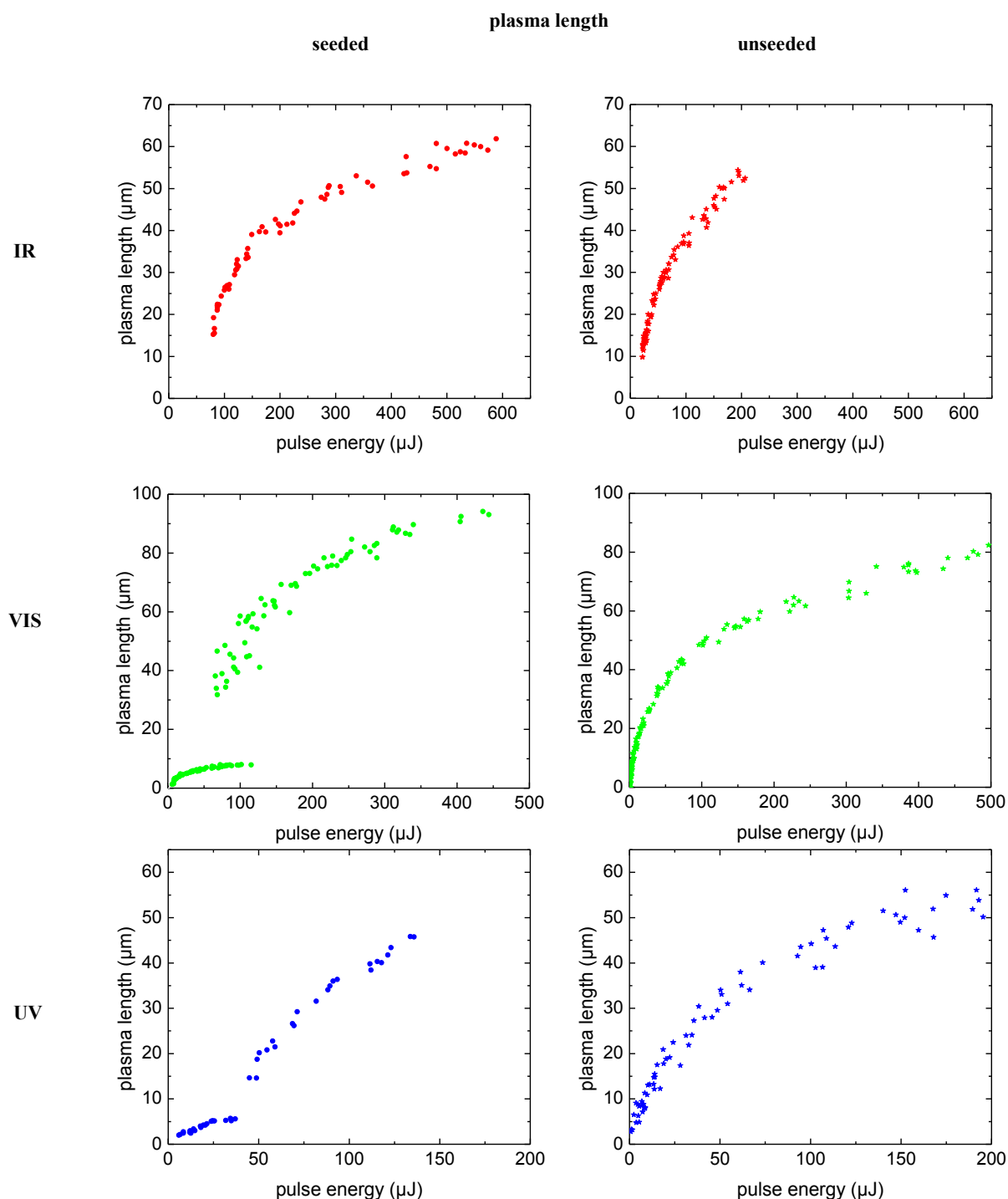
Figure 11.31: Length of luminescent plasmas produced by seeded and unseeded 11.2-ns laser pulses with 1064 nm wavelength, 8.8-ns laser pulses with 532 nm wavelength, and 6.8-ns laser pulses with 355 nm wavelength focused through a 40x water immersion objective (NA = 0.8). The plasma size was evaluated from the photos by measuring the size of the bright luminescence in the inner part of the plasma. For seeded laser pulses with energies below the BPL threshold, the plasma size was identified with the size of the green scattering region on the photographs.
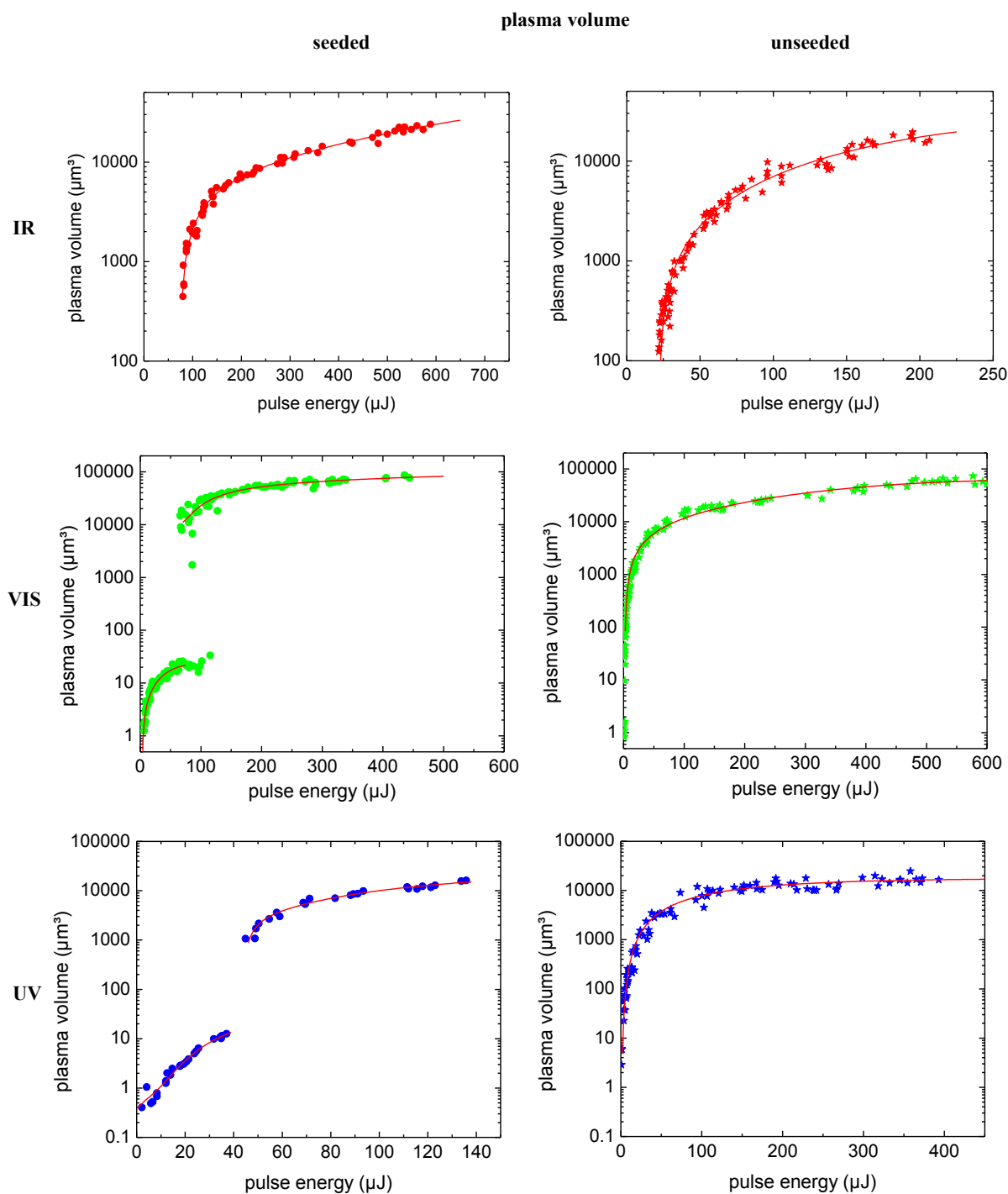
Figure 11.32: Volume of luminescent plasmas produced by seeded and unseeded 11.2-ns laser pulses with IR wavelength, 8.8-ns laser pulses with VIS wavelength, and 6.8-ns laser pulses with UV wavelength focused through a 40x water immersion objective (NA = 0.8). The measured data were fitted by a function V(E) to be able to interpolate the plasma volume for any specific laser pulse energy E using the computer program TableCurve2D.

11.3.3. Microchip laser of fixed wavelengths, 1 ns

plasma length　　　　　　　**plasma volume**
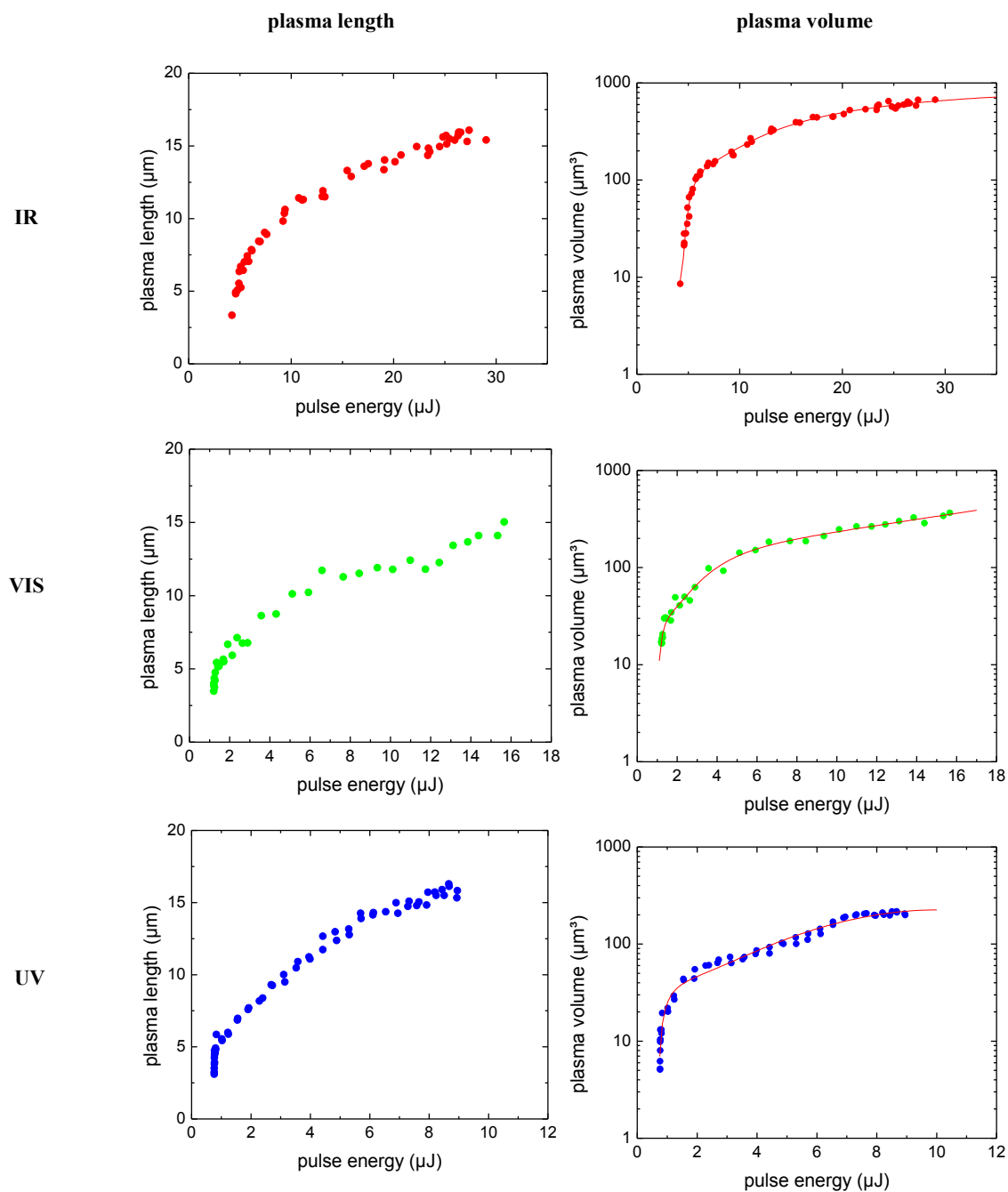
Figure 11.33: Plasma length and volume of luminescent plasmas produced by 1-ns microchip laser pulses with 1064 nm, 532 nm, and 355 nm wavelength focused through a 40x water immersion objective (NA = 0.8). An analytic function (red line) was fitted to the experimental data of the plasma volume using the computer program TableCurve2D.

11.3.4. Microchip 0.5 ns UV laser at different NA
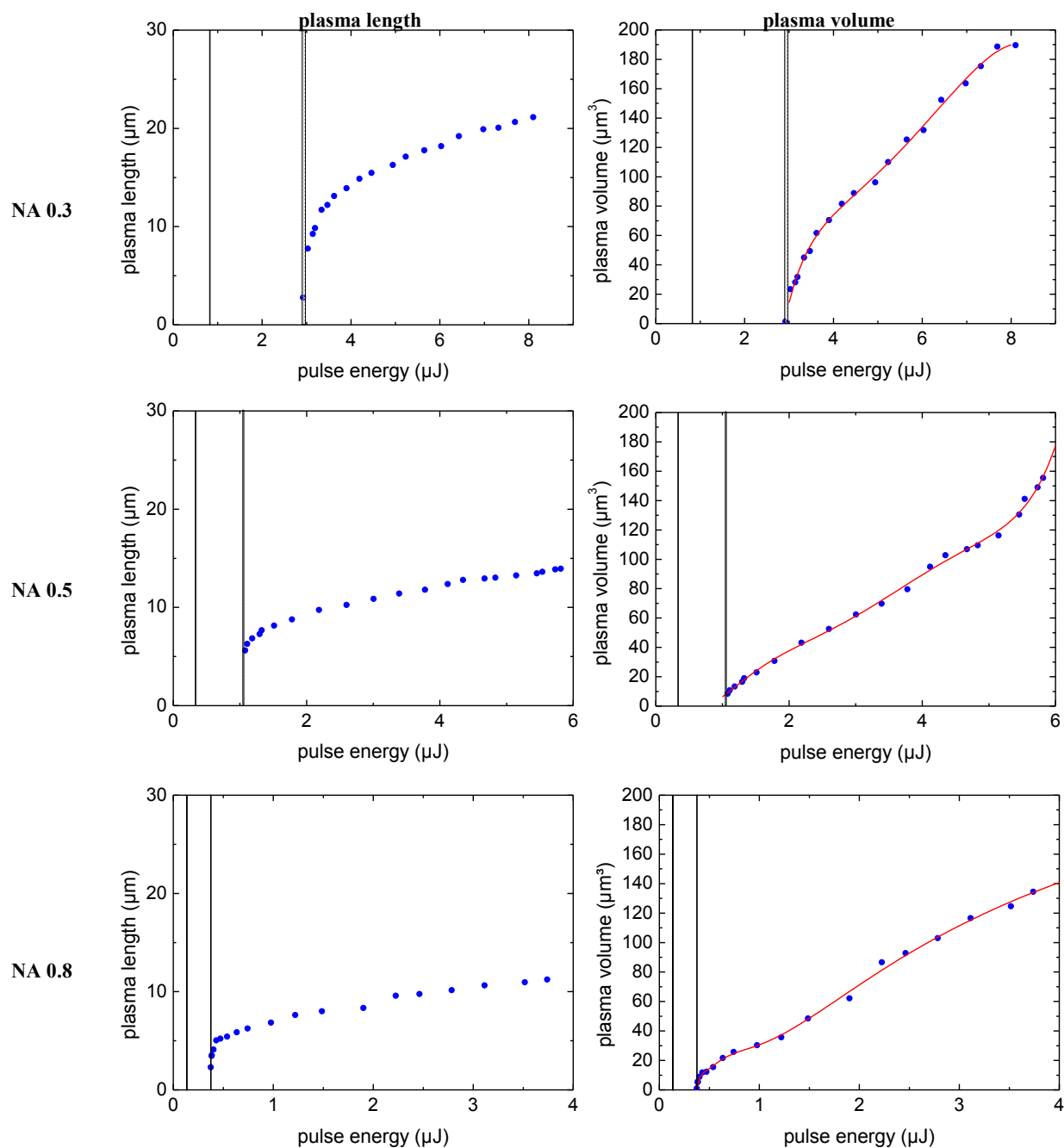
Figure 11.34: Plasma length and volume of luminescent plasmas produced by 0.5–ns microchip laser pulses with 355 nm wavelength focused through a 10x water immersion objective (NA = 0.3), a 20x water immersion objective (NA = 0.5), and a 40x water immersion objective (NA = 0.8). An analytic function (red line) was fitted to the experimental data of the plasma volume using the computer program TableCurve2D.

11.4 Plasma transmission

11.4.1. Fixed wavelengths, 280-350 fs
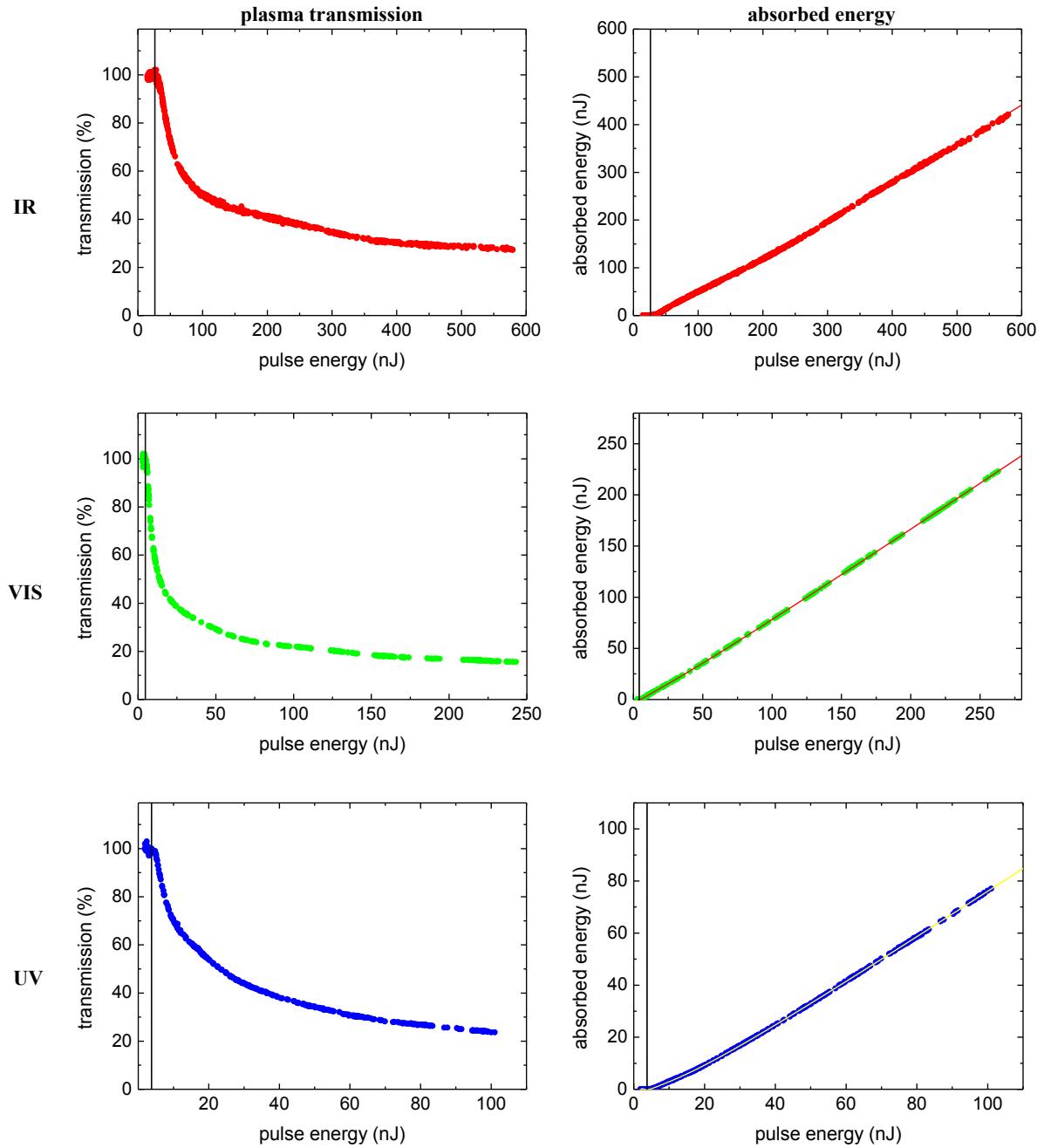
Figure 11.35: Plasma transmission and absorbed energy assuming $A = 1 - T$ as a function of incident laser pulse energy 352-fs laser pulses with 1040 nm wavelength, 306-fs laser pulses with 520 nm wavelength, and 280-fs laser pulses with 347 nm wavelength focused through a 40x water immersion objective (NA = 0.8). The energy intervals between 10 % and 90 % breakdown probability are indicated as shaded region.

11.4.2. Fixed wavelengths, 6-11 ns
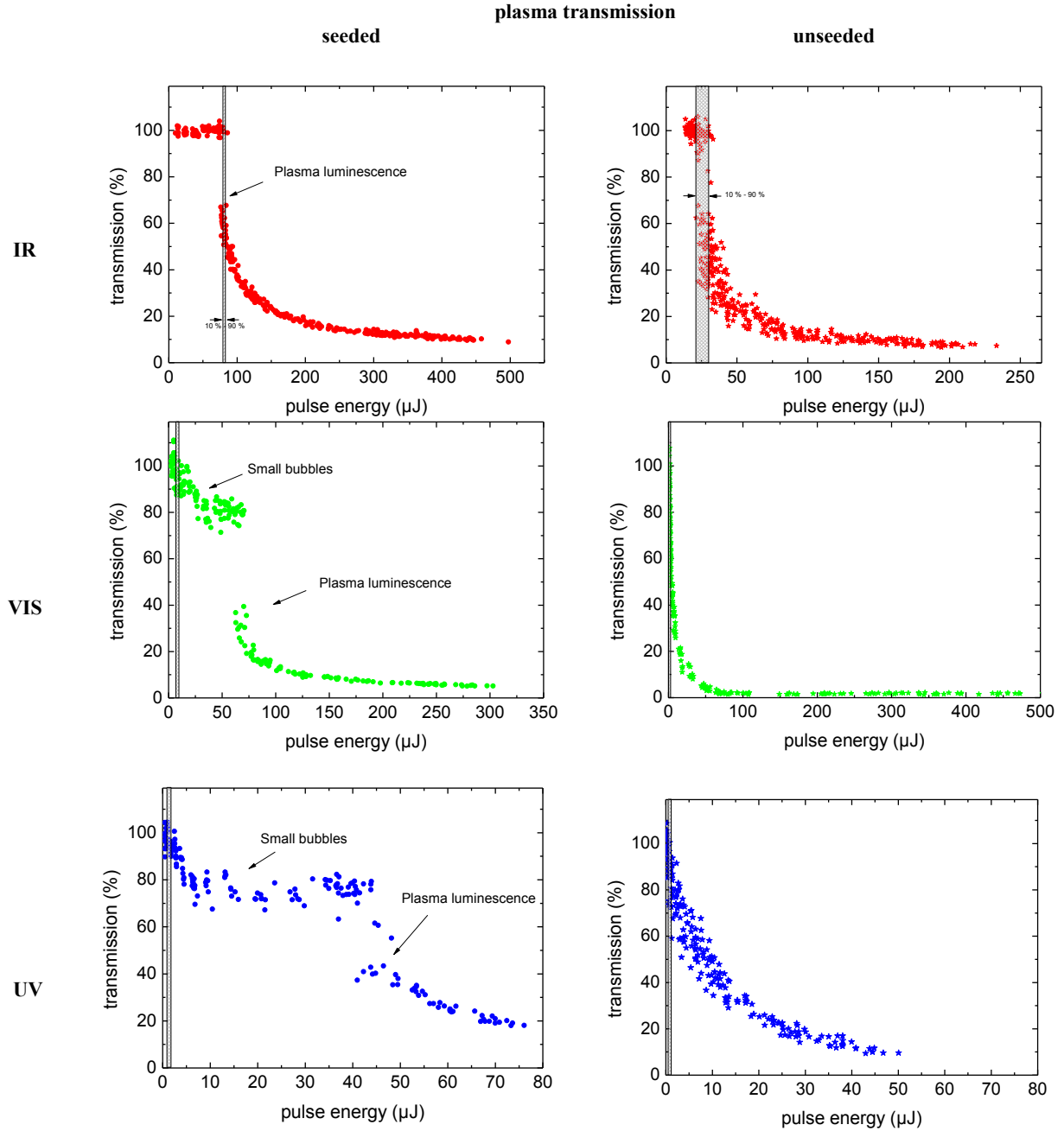
Figure 11.36: Plasma transmission as a function of incident laser pulse energy for unseeded and seeded 11.2-ns laser pulses with 1064 nm wavelength, 8.8-ns laser pulses with 532 nm wavelength, and 6.8-ns laser pulses with 355 nm wavelength focused through a 40x water immersion objective (NA = 0.8). The marked area indicates the optical breakdown threshold region between 10 % and 90 % breakdown probability. E_{th} (50 % breakdown probability) lies in the center of the marked area.
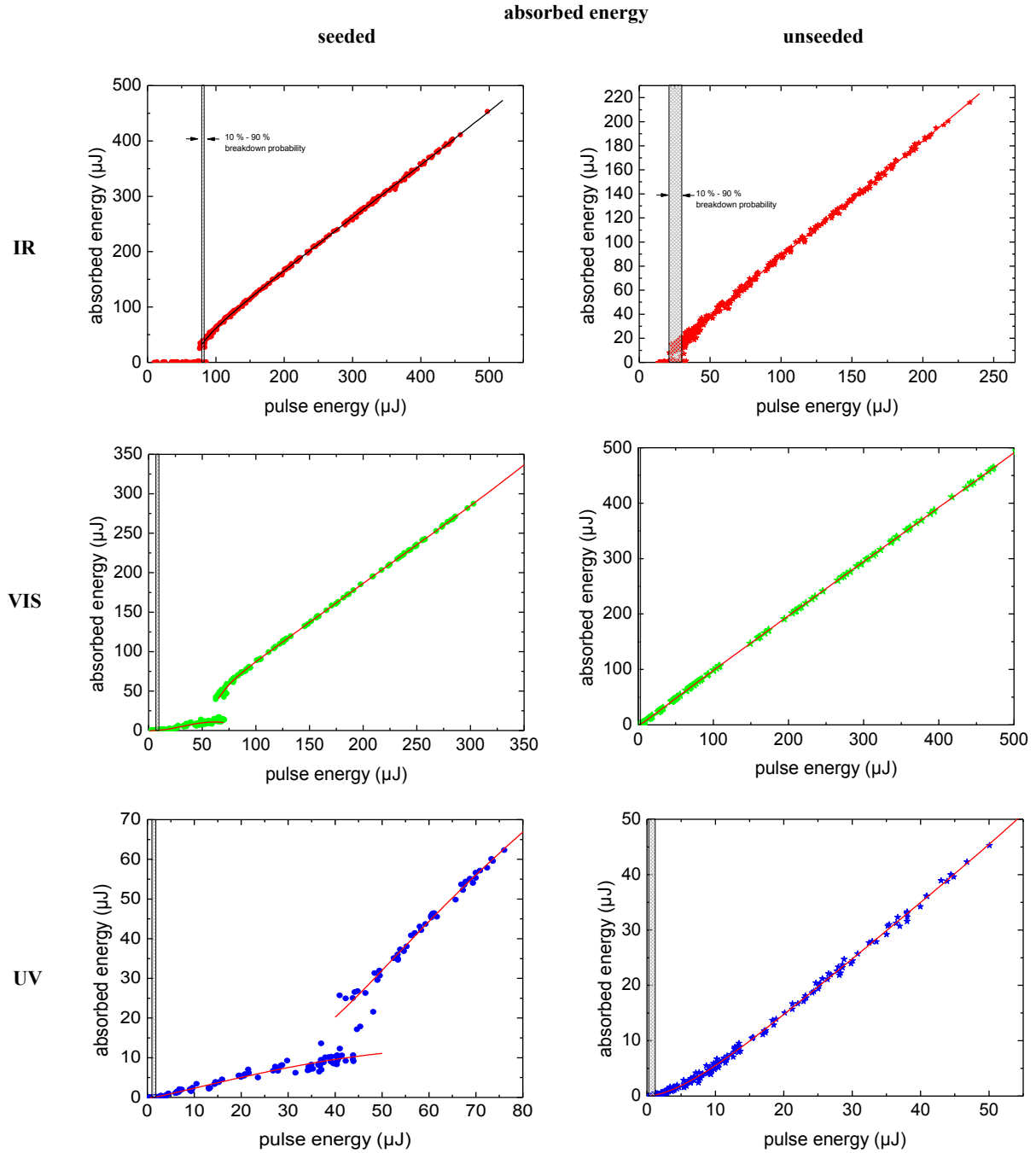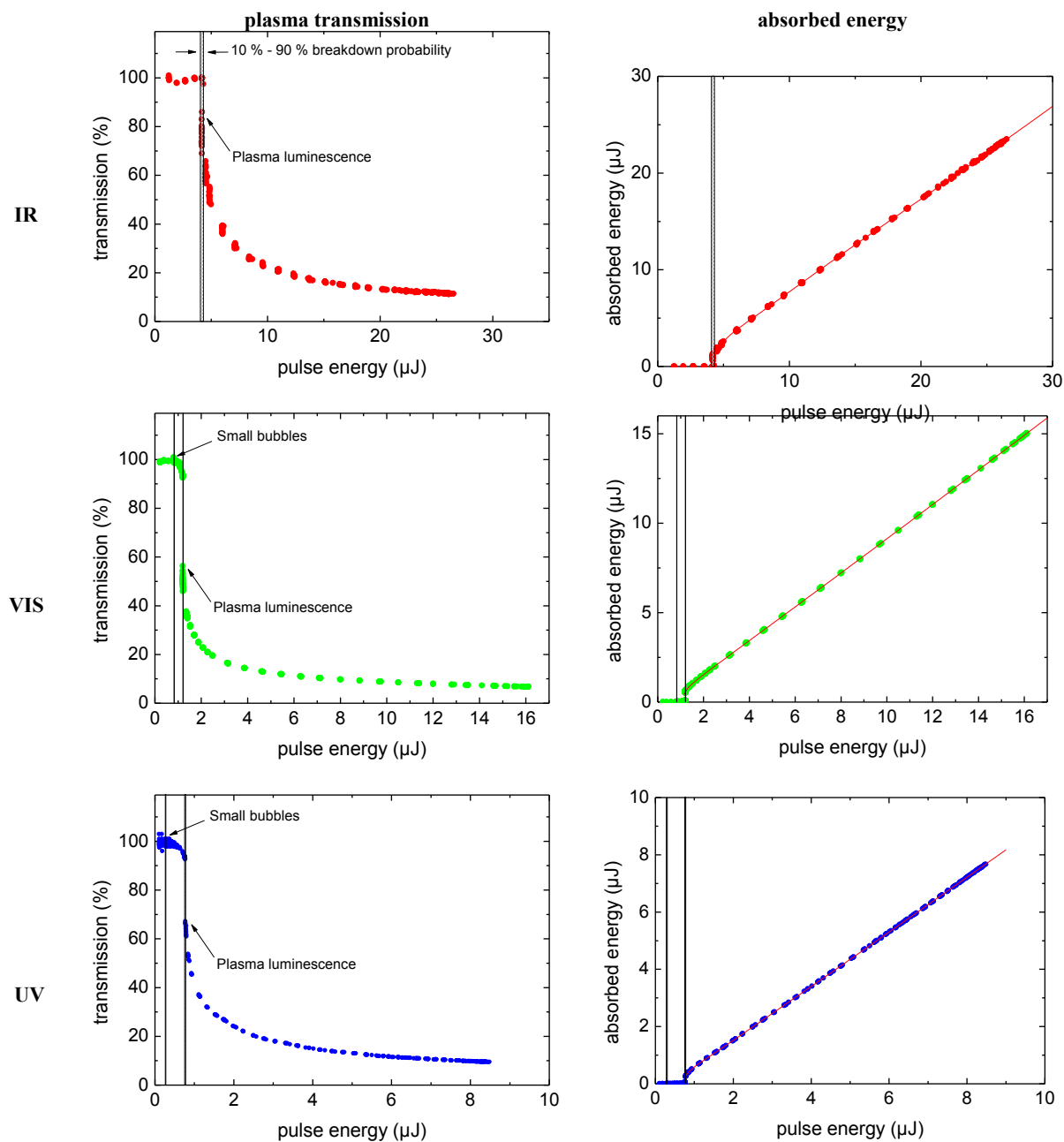
Figure 11.37: Absorbed energy as a function of incident laser pulse energy calculated from the data in figure 11.22 assuming *A* = 1 - *T* for unseeded and seeded 11.2-ns laser pulses with 1064 nm wavelength, 8.8-ns laser pulses with 532 nm wavelength, and 6.8-ns laser pulses with 355 nm wavelength focused through a 40x water immersion objective (NA = 0.8). The marked area indicates the optical breakdown threshold region between 10 % and 90 % breakdown probability. E_{th} (50 % breakdown probability) lies in the center of the marked area.

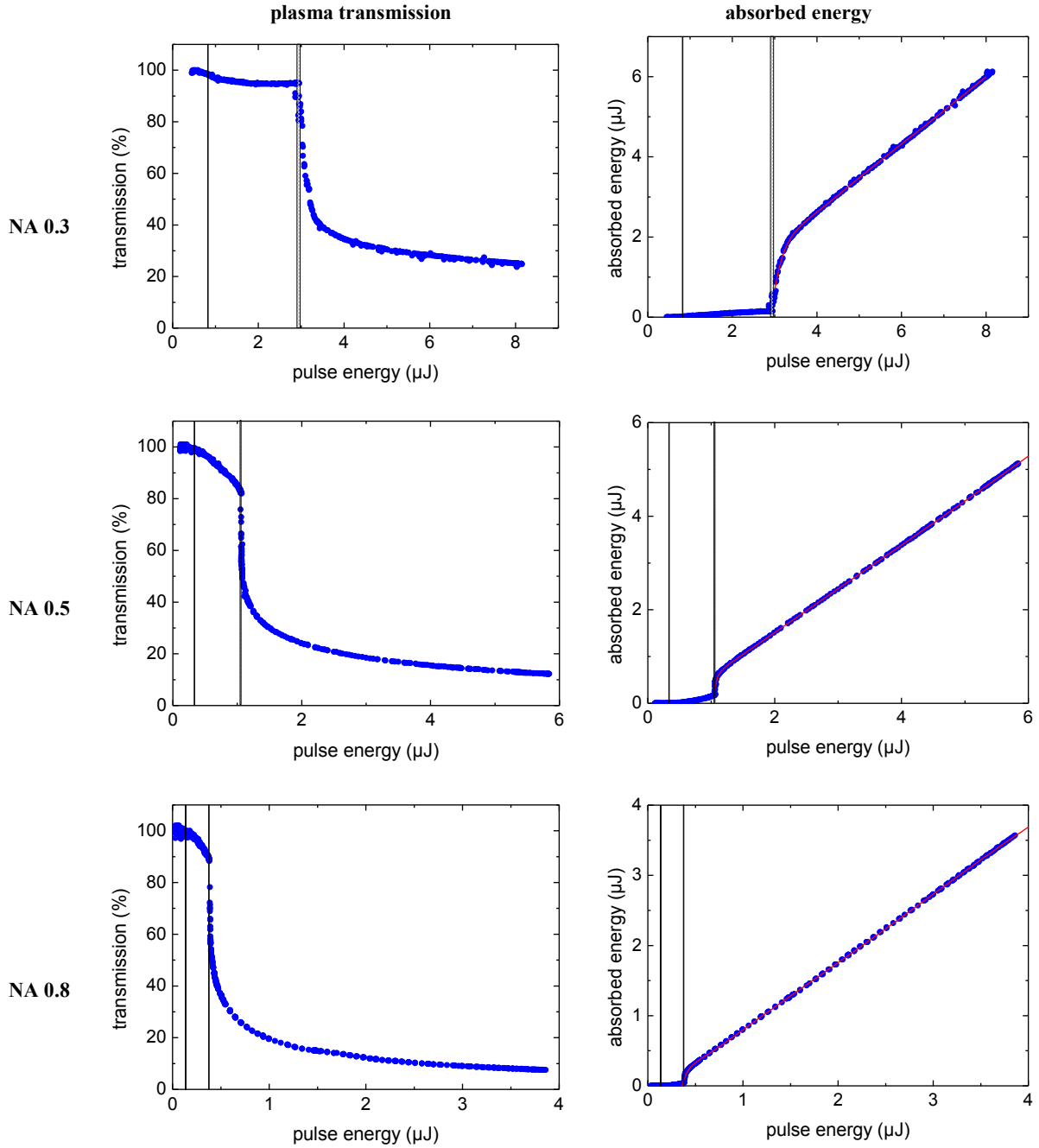### 11.4.3. Microchip laser of fixed wavelengths, 1 ns

Figure 11.38: Plasma transmission and absorbed energy assuming $A = 1 - T$ as a function of incident laser pulse energy for 1 - ns microchip laser pulses with 1064 nm, 532 nm, and 355 nm wavelength focused through a 40x water immersion objective (NA = 0.8). The energy intervals between 10 % and 90 % breakdown probability are indicated as shaded region or lines, respectively, for both the bubble formation and BPL threshold.

11.4.4. Microchip 0.5 ns UV laser at different NA

Figure 11.39: Plasma transmission and absorbed energy assuming $A = 1 - T$ as a function of incident laser pulse energy for 0.5 - ns microchip laser pulses at 355 nm wavelength focused through a 10x water immersion objective (NA = 0.3), a 20x objective (NA = 0.5), and a 40x objective (NA = 0.8). The energy intervals between 10 % and 90 % breakdown probability are indicated as shaded region or lines, respectively, for both the bubble formation and BPL threshold.

11.5 Plasma energy density

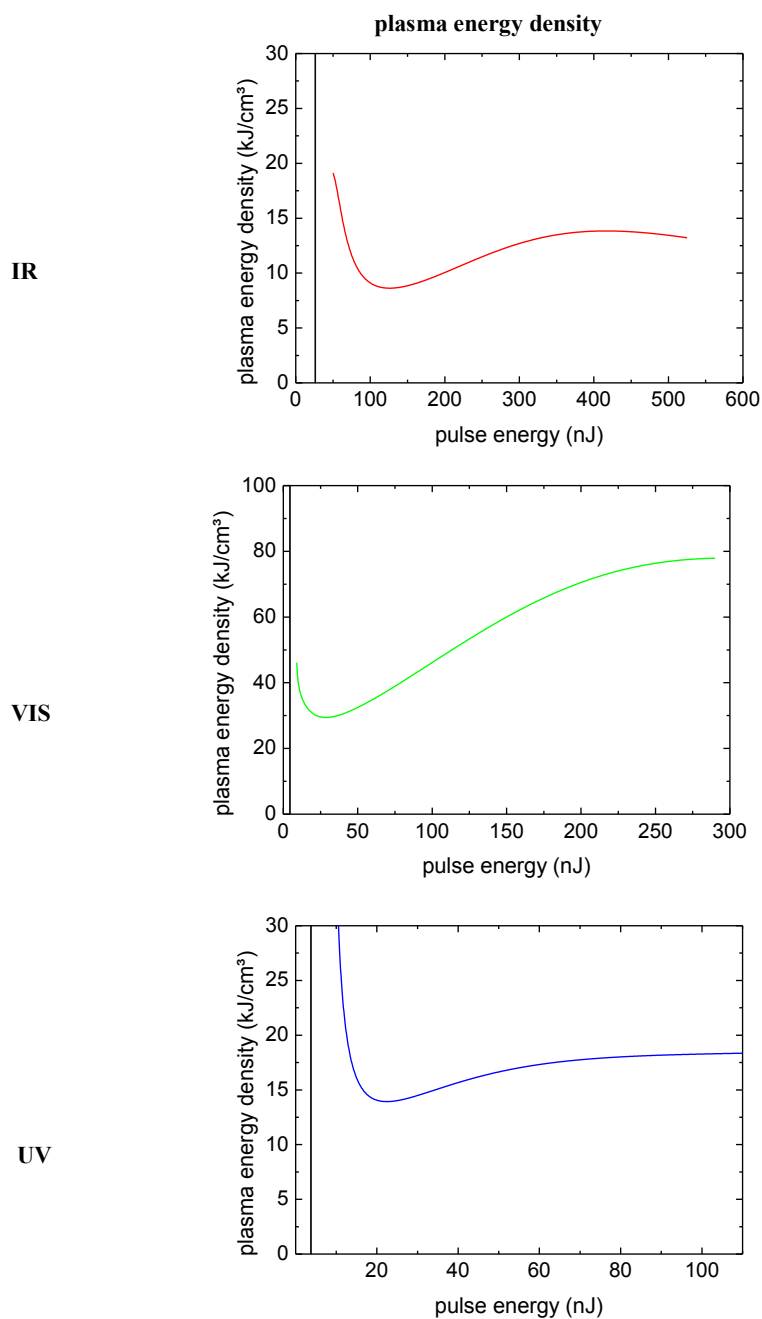### 11.5.1. Fixed wavelengths, 280-350 fs

Figure 11.40: Plasma energy density as a function of incident laser pulse energy for fs laser pulses with 1040 nm, 520 nm, and 347 nm wavelength focused through a 40x water immersion objective (NA = 0.8). The energy intervals between 10 % and 90 % breakdown probability are indicated as shaded region.

11.5.2. Fixed wavelengths, 6-11 ns
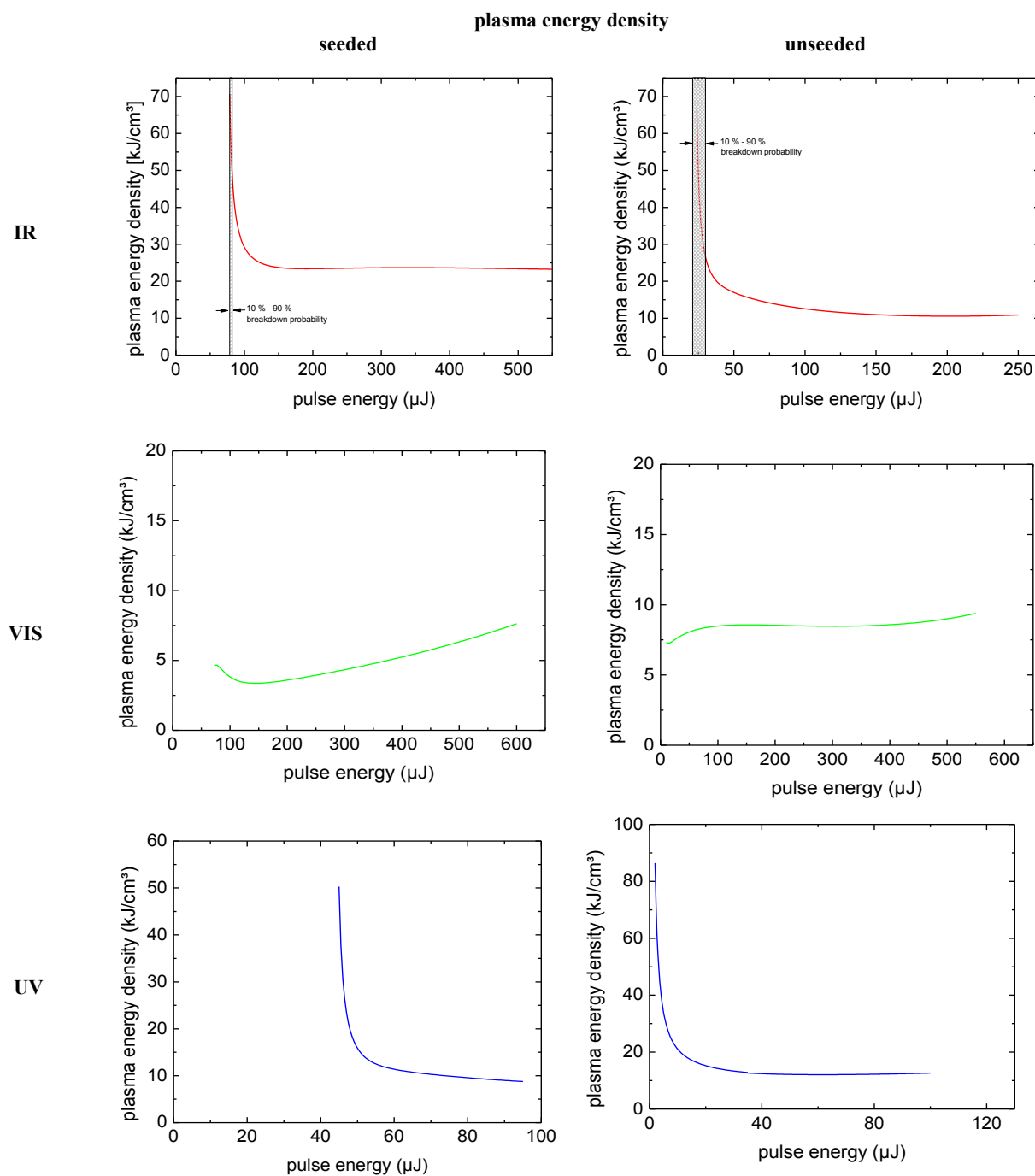
plasma energy density

Figure 11.41: Plasma energy density as a function of incident laser pulse energy above BPL threshold for unseeded and seeded 11.2-ns laser pulses with 1064 nm wavelength, 8.8-ns laser pulses with 532 nm wavelength, and 6.8-ns laser pulses with 355 nm wavelength focused through a 40x water immersion objective (NA = 0.8).
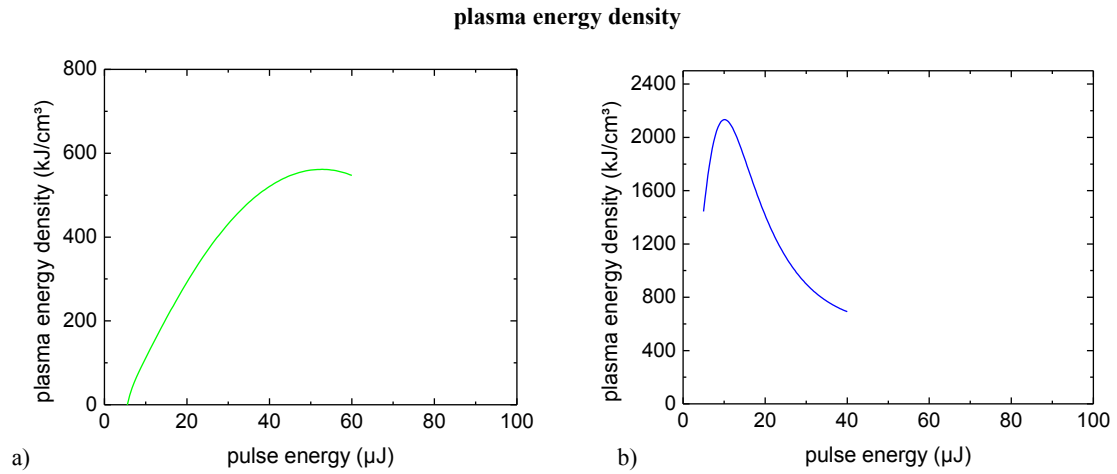
plasma energy density

Figure 11.42: Plasma energy density as a function of incident laser pulse energy below BPL threshold for (a) seeded 8.8-ns laser pulses with 532 nm wavelength, and (b) seeded 6.8-ns laser pulses with 355 nm wavelength focused through a 40x water immersion objective (NA = 0.8).

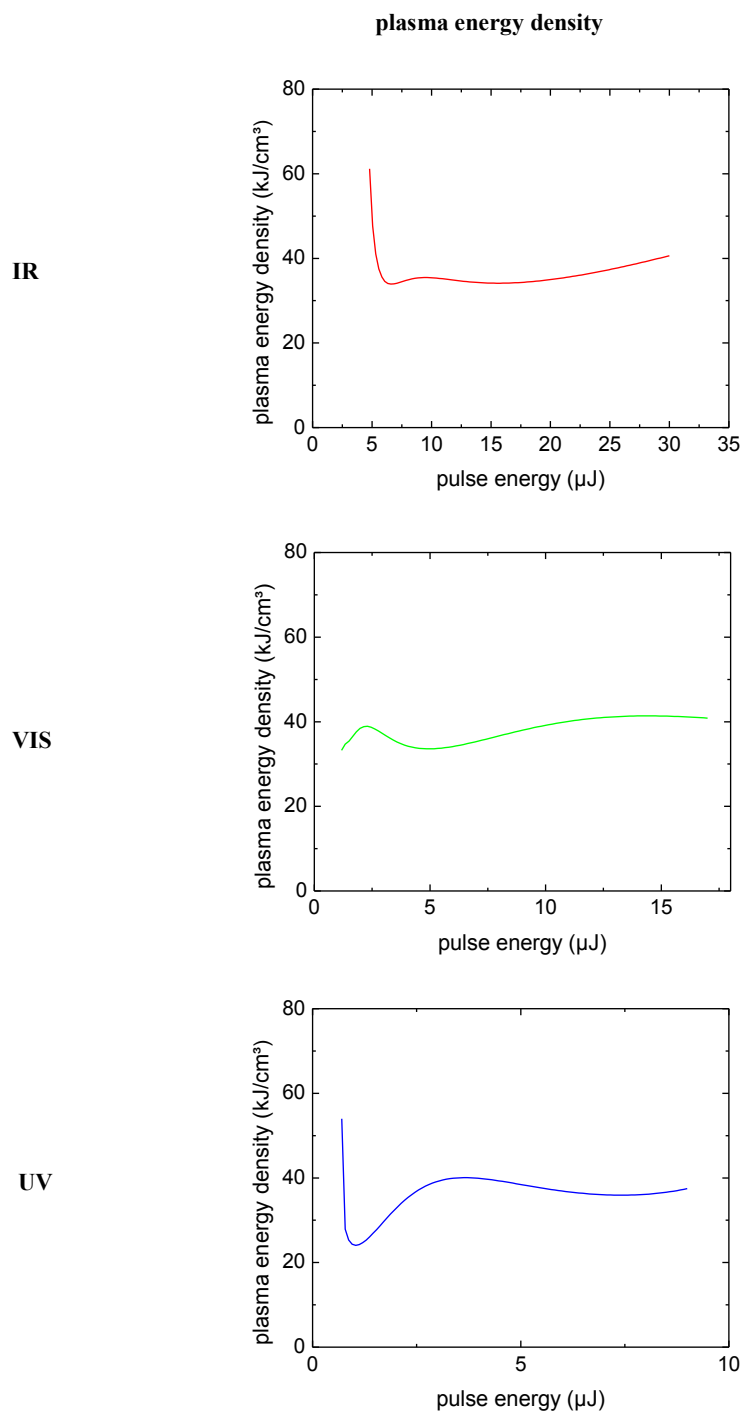## 11.5.3. Microchip laser of fixed wavelengths, 1 ns

Figure 11.43: Plasma energy density as a function of incident laser pulse energy for 1 - ns microchip laser pulses with 1064 nm, 532 nm, and 355 nm wavelength focused through a 40x water immersion objective (NA = 0.8).

11.5.4. Microchip 0.5 ns UV laser at different NA

plasma energy density
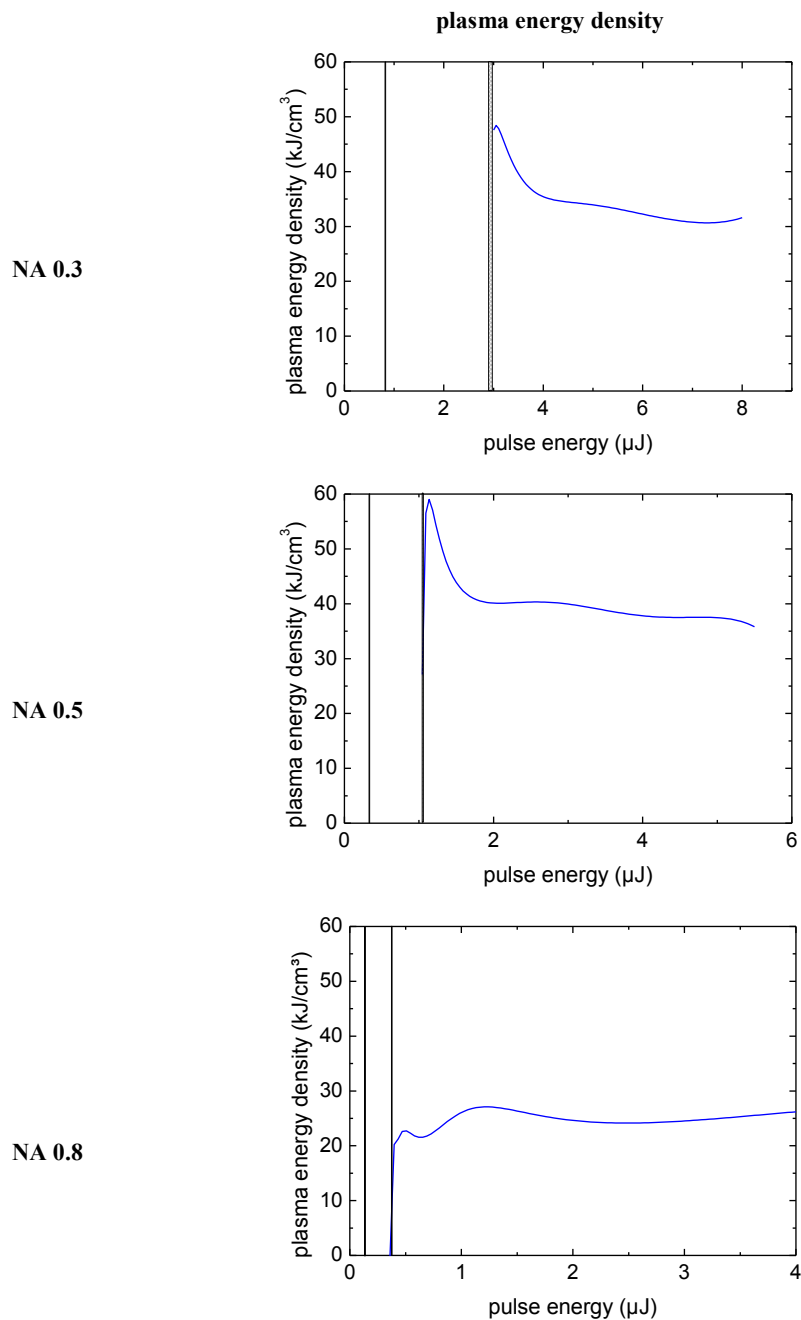
NA 0.3

NA 0.5

NA 0.8

Figure 11.44: Plasma energy density as a function of incident laser pulse energy for 0.5 - ns microchip laser pulses at 355 nm wavelength focused through a 10x water immersion objective (NA = 0.3), a 20x objective (NA = 0.5), and a 40x objective (NA = 0.8). The energy intervals between 10 % and 90 % breakdown probability are indicated as shaded region or lines, respectively, for both the bubble formation and BPL threshold.